

THE DYNAMICS OF DRILLING FLUID RHEOLOGY, WELLBORE FLOW, AND
FORMATION PRESSURE IN WELL CONTROL

A Dissertation

by

PEDRO CAVALCANTI DE SOUSA

Submitted to the Office of Graduate and Professional Studies of
Texas A&M University
in partial fulfillment of the requirements for the degree of

DOCTOR OF PHILOSOPHY

Chair of Committee,	Jerome Schubert
Committee Members,	Maria Barrufet
	Ibere Nascentes Alves
	Samuel Noynaert
	Paulo Waltrich
Head of Department,	Jeff Spath

May 2020

Major Subject: Petroleum Engineering

Copyright 2020 Pedro Cavalcanti de Sousa

ABSTRACT

Drillers dedicate many hours to well control training, where they learn how to identify a kick by looking at drilling parameters and comparing them to the planned values. In HPHT wells, UBD and other advanced drilling techniques, however, standard well-control operations and assumptions may lead to inaccurate influx size estimates and inappropriate handling of the kick.

A limited number of studies on the rheological properties of drilling fluids in HPHT conditions is available. Initial works modeled density and viscosity of muds based on empiric-mechanistical models, but were limited to 350 °F and 20,000 psig. A large number of models are used to describe mud rheological behavior in HPHT, with no model being universally accepted. By modifying and upgrading a HPHT viscometer, we thoroughly analyze how well different models represent the experimental data in a wide range of pressure and temperature.

Upward, gas-liquid flow studies are generally focused on describing flow in pipes. The same happens with larger diameter pipes where slug flow has been reported not to take place. In that slugless domain, only a handful of works takes in consideration the flow in annuli. Thus, we designed a flow loop circulating oil and air to explore the virtually untapped slugless regime in concentric and eccentric annuli.

Additionally, estimating the intensity of a kick generally implies a tradeoff between computationally expensive and inaccurate (or improperly-used) methods. Here, we developed a computationally inexpensive tool capable of coupling the response of

the producing formation to the changes in bottomhole pressure due to the dynamics of wellbore flow.

Our drilling fluid characterization and test methodology of uncontaminated and gas-cut muds helps delivering an accurate description of the frictional pressure losses during circulation of formation-fluid influxes. With the flow loop, we are able to give a better description of upward, gas-liquid flow behavior in slugless annuli, which is crucial in understanding the dynamics of wellbore during well control. Furthermore, the coupled wellbore-formation tool developed here accurately describes fluid influxes, being especially useful for managed pressure and underbalanced drilling. This work serves as the basis for more advanced well-control procedures, training, and understanding.

DEDICATION

To my parents, Joaquim Francisco de Sousa Neto and Laélia Cavalcanti de Sousa, and my wife, Breanne Sousa, for their love and support.

ACKNOWLEDGEMENTS

I would like to thank my committee chair, Dr. Jerome Schubert, and the other committee members, Drs. Maria Barrufet, Samuel Noynaert, Ibere Nascentes Alves, and Paulo Waltrich for their support and guidance throughout the course of this research. I am equally grateful to the National Academies for funding the Gulf Research Program, which allowed me to conclude this project.

I want to thank all my friends, and current and former colleagues, especially Maria Cláudia Alves and Florent Baudier, Johannes Alvares, Dinara Dussenova, Renato Coutinho, Érika Pagan, Rodolfo Santos, and Francisco Tovar for making my time at Texas A&M University a great experience. I am especially thankful to Artur Posenato Garcia for his friendship and intellectual contributions to this work, and to Omer Kaldirim for his companionship and help through the long hours of lab work.

Also, I would like to thank the Petroleum Engineering staff at Texas A&M for their work, especially John Maldonado for his friendship, and help. I am also thankful to all student workers that helped me at one point or another, especially Shaun Stephen and Ashton Haass.

Finally, I want to thank my parents and my wife for being understanding, supporting, and making all the effort put into this work a lot easier.

To all those who help, influenced, and inspired me, thank you!

CONTRIBUTORS AND FUNDING SOURCES

Contributors

This work was supported by a dissertation committee composed of Professor Jerome Schubert, Samuel Noynaert and Ibere Nascente Alves of the Department of Petroleum Engineering, Professor Maria Barrufet of the Departments of Chemical and Petroleum Engineering, and Professor Paulo Waltrich from the Petroleum Engineering Department of the Louisiana State University.

All work for the dissertation was completed independently by the student.

Funding Sources

Graduate study was supported by the Gulf Research Program from the National Academies of Science, Engineering, and Medicine.

NOMENCLATURE

Acronyms

ACV	Air flow control valve
APCV	Automated pressure control valve
API	American Petroleum Institute
APT	Gauge pressure transducer
ASV	Air solenoid valve
BHP	Bottomhole pressure
BP	Bingham plastic rheological model
BPAPI	Bingham plastic model according to API recommendations
CAF	Coriolis air flowmeter
CLF	Coriolis liquid flowmeter
CSB	Caetano, Shoham, and Brill pressure gradient model
DIM	Dynamic influx model
DIPR	Dynamic IPR
DPT	Differential pressure transducer
EPRV	Emergency pressure relief valve
GCV	Gas control valve
GFM	Gas flowmeter
GIV	Gas injection valve
HB	Herschel-Bulkley rheological model

HPHT	High-pressure/high-temperature
HVV	Hydraulic oil pressurization vessel valve
ID	Inner diameter
IPR	Inflow performance relationship
LCV	Liquid flow control valve
MD	Measured depth
MPD	Managed pressure drilling
MSF	Mix-to-separator valve
NADF	Non-aqueous drilling fluid
OBM	Oil-based mud
OD	Outer diameter
O&G	Oil and gas
PI	Productivity index
PL	Power law rheological model
PLAPI	Power law rheological model according to API recommendations
PSS	Pseudosteady-state
PV	Plastic viscosity
RCWD	Reservoir characterization while drilling
ROP	Rate of penetration
RPM	Rotations per minute
SBM	Synthetic-based mud
SC	Standard conditions

SIV	Shut-in valve
SS	Steady-state
SSD	Schlegel, Hibiki, and Ishii pressure gradient for small diameters
SSL	Schlegel, Hibiki, and Ishii pressure gradient for large diameters
TPV	Test vessel pressurization valve
TVD	True vertical depth
UBD	Underbalanced drilling
WBM	Water-based mud
YP	Yield point
YPL	Yield power law, or Herschel-Bulkley rheological model
ZH	Zhao and Hibiki pressure gradient model

Variables and Parameters

a_j	j-th pressure coefficient in Dynamic IPR model
A_{wf}	Amplitude of sinusoidal bottomhole pressure
b_j	j-th flowrate coefficient in Dynamic IPR model
B_l	formation factor of producing liquid
c_t	Total compressibility
d_c	Distance between pipe centers in annular spaces
D	Diameter
D^*	Dimensionless diameter
D_{ann}^*	Annulus dimensionless diameter

D_{eq}	Equivalent diameter
D_{EP}	Equi-peripheral diameter
D_h	Hydraulic diameter
D_i	Inner pipe OD
D_o	Outer pipe ID
e	Level of eccentricity
f	Fanning friction factor
$f(\cdot)$	Generalized function of pressure
g	Gravitational acceleration
h	Height of producing formation
h_b	Height of Couette viscometer bob
h_r	Reservoir thickness
i	Imaginary number
j	Summation index of Dynamic IPR model, or rheological dataset
k	Permeability
K	Consistency index
K_θ	Spring torsion coefficient
$m(\cdot)$	Real-gas pseudopressure function
M	Torque
n	Exponent of rheological model. Also timestep
N	Number of terms in Dynamic IPR model
N_e	Number of experimental datapoints for rheological models

N_{gv}	Dimensionless gas velocity number
N_{lv}	Dimensionless liquid velocity number
P	Pressure
P_e	Reservoir pressure
P_{wf}	Wellbore bottomhole flowing pressure
Q	Flowrate in standard conditions
r	Radial distance from center of wellbore
r_e	Radius of reservoir outer boundary
r_w	Wellbore radius
Re	Reynolds number
R_i	Couette viscometer bob radius
R_o	Couette viscometer rotor radius
S	Skin number
S_h	Skin of horizontal well
t	Time
tol	Tolerance
t_0	Time of initial contact of the drill bit with producing layer
t_e	End-of-transition time
T	Temperature
T_{res}	Reservoir temperature
u_{sg}	Gas superficial velocity
u_{sl}	Liquid superficial velocity

y_b	Half-length of reservoir width
Z	Real-gas compressibility factor

Subscripts and Superscripts

300	Shear stress or shear rate measured at 300 rpm
600	Shear stress or shear rate measured at 300 rpm
(1)	Dynamic IPR coefficients evaluated for unit-length
(a)	apparent viscosity
(h)	Dynamic IPR coefficients evaluated at length equal to “h”
exp	Experimental datapoint
F	Frictional
G	Gravitational
m	Mixture
max	Maximum
min	Minimum
mod	Model datapoint
mud	Drilling fluid
TP	Two-phase

Greek letters

α	Coefficient of the analytical solution
$\dot{\gamma}$	Shear rate

Δs	Drilled length
$\bar{\varepsilon}_{r,a}$	Mean absolute relative error
ε	Error
θ	Deflection angle during Couette viscometer test
μ	Dynamic viscosity
μ_N	Viscosity of Newtonian model
μ_p	Viscosity of Bingham plastic model
ρ_G	Density of gas
ρ_L	Density of liquid
σ	Liquid-gas surface tension
τ	Shear stress
τ_0	Yield stress of Bingham plastic model
τ_S	Yield stress of Herschel-Bulkley model
ϕ	Porosity
ω	Frequency of sinusoidal bottomhole pressure, or angular speed
Ω	Angular velocity of Couette viscometer rotor

TABLE OF CONTENTS

	Page
ABSTRACT	ii
DEDICATION.....	iv
ACKNOWLEDGEMENTS	v
CONTRIBUTORS AND FUNDING SOURCES.....	vi
NOMENCLATURE	vii
TABLE OF CONTENTS.....	xiv
LIST OF FIGURES	xvi
LIST OF TABLES.....	xix
1. INTRODUCTION AND PREVIOUS WORK.....	1
1.1. Motivation	1
1.2. Basic Well Control.....	3
1.3. Drilling Fluid Characterization.....	5
1.3.1. Viscosity	8
1.3.2. Gel-Strength	14
1.3.3. Literature gap	15
1.4. Wellbore Flow Dynamics.....	16
1.4.1. Upward Gas-Liquid Flow	18
1.4.2. The Upward, Gas-Liquid, Slugless Flow Domain in Pipes	21
1.4.3. Literature Gap	23
1.5. Formation Influx Modeling	24
1.5.1. Conventional IPR Models.....	25
1.5.2. The Dynamic IPR	28
1.5.3. Reservoir Characterization While Drilling	33
1.5.4. Literature Gap	34
1.6. Work Objective.....	34
1.6.1. Tasks.....	35
2. METHODOLOGY	37

2.1. Viscosity Measurements.....	37
2.1.1. Rotational Coaxial-Cylinder Viscometers	38
2.1.2. The Viscometer Chandler 7600.....	44
2.1.3. Test Matrix.....	52
2.1.4. Experimental procedure.....	54
2.2. Gas-Liquid Flow Loop	55
2.2.1. Flow Loop Description.....	57
2.2.2. Test Matrix.....	59
2.2.3. Experimental Procedure.....	61
2.3. Formation-Wellbore Coupling Model.....	62
2.3.1. Dynamic IPR as Formation-Fluid Influx Model	64
2.3.2. The Dynamic Influx Model.....	76
2.3.3. Applicability of the DIM	76
3. RESULTS AND DISCUSSIONS.....	78
3.1. Drilling Fluid Rheology	78
3.1.1. Modeling Drilling Fluid Rheology in HPHT	82
3.1.2. The Rheological Behavior of Contaminated Drilling Fluids in HPHT	90
3.1.3. The Impact of Proper Rheological Modeling in HPHT Drilling	101
3.2. Slugless Domain in Annular Spaces	105
3.2.1. Proof of Concept.....	105
3.2.2. Annulus Flow Loop	106
3.2.3. The Impact of the Annular Flow Regime Domain in Calculating BHP.....	124
3.3. Simulation of Formation-Fluid Influx During Drilling.....	125
3.3.1. Case 1: Real-Time Influx Estimation with DIM.....	126
3.3.2. Case 2: DIM While Drilling Horizontal Wells Underbalanced	129
4. CONCLUSIONS AND FUTURE WORK.....	132
REFERENCES	136
Appendix A	146
Appendix B.....	154
Appendix C.....	186

LIST OF FIGURES

	Page
Figure 1.1 Notable HPHT wells drilled since the year 2000. Reprinted from Shadravan and Amani (2012).....	3
Figure 1.2 Conceptual illustration of different upward, steady-state, gas-liquid flow patterns. Reprinted from Shoham (2006).....	20
Figure 1.3 Flow patterns in (a) concentric and (b) eccentric annular spaces. Reprinted from Caetano, Shoham, and Brill (1992a).	20
Figure 2.1 Schematic drawing of a rotational coaxial-cylinder viscometer.....	39
Figure 2.2 Flow chart explaining how to obtain the Herschel-Bulkley parameter using least-square method and brute-force computations.	43
Figure 2.3 Schematic drawing of original Chandler 7600 design.	45
Figure 2.4 Detailed drawing of the test vessel, modified after Ametek (2016).	46
Figure 2.6 Schematic drawing of HPHT viscometer after modifications.....	48
Figure 2.5 Modified Ametek Chandler 7600 partially assembled.....	49
Figure 2.7 Bubble point of butane around common room temperatures in the lab.....	52
Figure 2.8 Oil-Air flow loop schematics.....	58
Figure 2.9 Test matrix for air-oil flow loop showing the targeted experimental points..	60
Figure 2.10 Production as calculated from DIPR validated against conventional IPR solutions.	64
Figure 2.11 Comparison of pressure profiles inside gas-reservoir due to sinusoidal bottomhole pressure with oscillatory frequency of 0.05 Hz at (a) $t = 10$ s and (b) $t = 23$ s.....	67
Figure 2.12 Pressure profiles from Figure 2.11 zoomed in to show the existence of the u-shaped pressure component.....	68
Figure 2.13 Validation of the DIPR with skin effect against conventional IPR solutions.	72

Figure 2.14 Ratios of DIPR coefficients evaluated at different formation thicknesses in relation to the one-meter reference coefficients.	75
Figure 3.1 Curve-fit of different models for typical experimental rheology data (sample OBM1_s1).	82
Figure 3.2 Relative number of model regressions with mean absolute relative error within 5, 10, and 20% divided into (a) low- and (b) high- shear zones.	83
Figure 3.3 Heat map of average $\epsilon r, a$ at low shear rates, and different pressures and temperatures.	85
Figure 3.4 Heat map of average $\epsilon r, a$ at high shear rates, and different pressures and temperatures.	86
Figure 3.5 Drilling fluid failure example.	87
Figure 3.6 Relative number of model regressions for gas-cut muds with mean absolute relative error within 5, 10, and 20% divided into (a) low- and (b) high- shear zones.	89
Figure 3.7 Shear stresses of uncontaminated and gas-cut samples of the same drilling fluid (SBM_s1 and SBM_s1_gas).	94
Figure 3.8 Shear stresses of uncontaminated and gas-cut samples of the same drilling fluid (OBM2_s1 and OBM2_s1_gas).	95
Figure 3.9 Average relative reduction of the Herschel-Bulkley characteristic viscosity as a function of pressure for temperatures varying from 310 to 422 K (100 to 300 °F). The vertical bars indicate the 95 % confidence interval from the measurement uncertainty.	96
Figure 3.10 Phase diagram of butane.	96
Figure 3.11 Shear stresses of uncontaminated and gas-cut synthetic oil (samples bfSBM and bfSBM_gas).	98
Figure 3.12 Shear stresses of uncontaminated and diesel-contaminated SBM samples (SBM_s1 and SBM_contam).	100
Figure 3.13 Comparison between holdup calculated with the Schlegel, Hibiki, and Ishii (2010) model versus the measured holdup.	106
Figure 3.14 Comparison between data generated for this work and the work of Caetano, Shoham, and Brill (1992b). Vertical bars represent 15 % error,	

horizontal bars represent the 95% confidence interval of measurement uncertainty.	108
Figure 3.15 Eccentric 77.3-by-33.4 annulus showing a close-up of typical cap-bubble flow structure.	112
Figure 3.16 Flow regimes observed with the 77.3-by-42.2 mm annulus in concentric (a, b, and c), and eccentric (d, e, and f) configurations.	113
Figure 3.17 Concentric 77.3-by-33.4 showing cap-bubble-to-churn transition.	114
Figure 3.18 Flow regime maps for each annular dimension in concentric and eccentric configurations.	118
Figure 3.19 Comparison between calculated pressure gradient from different flow models and measured values.	123
Figure 3.20 Comparison between conventional transient IPR and DIPR to predict liquid production during underbalanced drilling.	127
Figure 3.21 Comparison between measured gas production during underbalanced drilling estimated with a transient IPR for horizontal wells and the DIPR....	131

LIST OF TABLES

	Page
Table 1.1 HPHT tiers and their limits.	11
Table 1.2 List of parameters of variables in Eqs. 1.14 through 1.19.	30
Table 2.1 Test matrix. Solid green squares indicate where data was collected. Hashed squares designate no data collected.	53
Table 2.2 Properties of soybean oil at different temperatures.	56
Table 2.3 Formation and formation-fluid parameters for examples in this work.	62
Table 2.4 Viscosity and pseudopressure function values for formation-fluid used in examples.	63
Table 2.5 Dynamic Influx Model equations.	76
Table 3.1 Torsion spring coefficients.	79
Table 3.2 Summary of rheological models and calculation methodologies to obtain model parameters.	81
Table 3.3 Summary of contamination level of each drilling fluid sample tested.	91
Table 3.4 List of shear stress test failures for different muds.	97
Table 3.5 Pressure difference between Herschel-Bulkley and other rheological models.	103
Table 3.6 Max pressure differences between Herschel-Bulkley and other rheological models for all pressure and temperature combinations.	104
Table 3.7 Characteristic diameters of annuli and their respective dimensionless numbers.	116
Table 3.8 Criteria for slug flow existence in annular spaces.	117
Table 3.9 Pressure gradient models used to predict experimental values.	120
Table B.1 Experimental shear-stress and gel-strength data.	170

Table B.2 Relative uncertainty of experimental measurements in relation to the mean value.	185
Table C.1 Experimental data for gas-liquid flow in pipe.	187
Table C.2 Experimental data for gas-liquid flow in concentric annulus.	188
Table C.3 Experimental data for gas-liquid flow in eccentric annulus.	189

1. INTRODUCTION AND PREVIOUS WORK

This work is divided in 4 chapters. This first chapter will give an overview of the problem we are proposing to solve. Initially, we will introduce the main concepts, fundamentals, and literature that are used as the basis of our work.

Chapter 2 will describe the experimental methods, where we will discuss the challenges faced while preparing for the tests, the limits of the used different equipment, and the assumptions we made. In this chapter we will also introduce the foundation of any model we derive.

Chapter 3 will show and discuss the results of the experiments. Qualitative and quantitative descriptions of the data generated will be presented. Mathematical models will be compared to experimental data for validation. Where no field or experimental data is available, mathematical models will be compared to existing simulators for benchmark.

Chapter 4 is the conclusion, where we will present the most remarkable achievements from this research.

1.1. Motivation

Petroleum engineering is roughly divided in three main branches: drilling, production, and reservoir. However, after taking a kick, that is, after formation-gas enters the wellbore, operations are no longer restricted to the drilling discipline, but instead they become an interdisciplinary challenge.

First, we must estimate the intensity of the kick, which requires knowledge on the formation properties such as permeability, porosity, and pore pressure, a job generally carried out by a reservoir engineer. Then, we need to assess how that influx will migrate up towards the surface, which is a two-phase flow problem, generally left in charge of the production engineer. Finally, the driller must kill the well using the resources at hand, that is, rig components (valves, pumps) and drilling materials, like muds.

These tasks do not happen isolated from each other, though. They are, in fact, a connected system where wellbore flow, bottomhole pressure and formation influx feed each other dynamically, and the driller is in charge of controlling it. This challenging scenario has become even more relevant as new drilling technologies are used and high-pressure and/or high-temperature reservoirs are explored. Figure 1.1 from Shadravan and Amani (2012) show the expanding number of HPHT wells and plays being explored around the world.

Some of the assumptions taken in developing classic well control are no longer valid in these new, challenging scenarios, which leaves us with the task of filling in the knowledge gaps where necessary. In the following paragraphs we will explore the scientific developments of each one of the events described above, showing what has been accomplished already and where they need improvement.

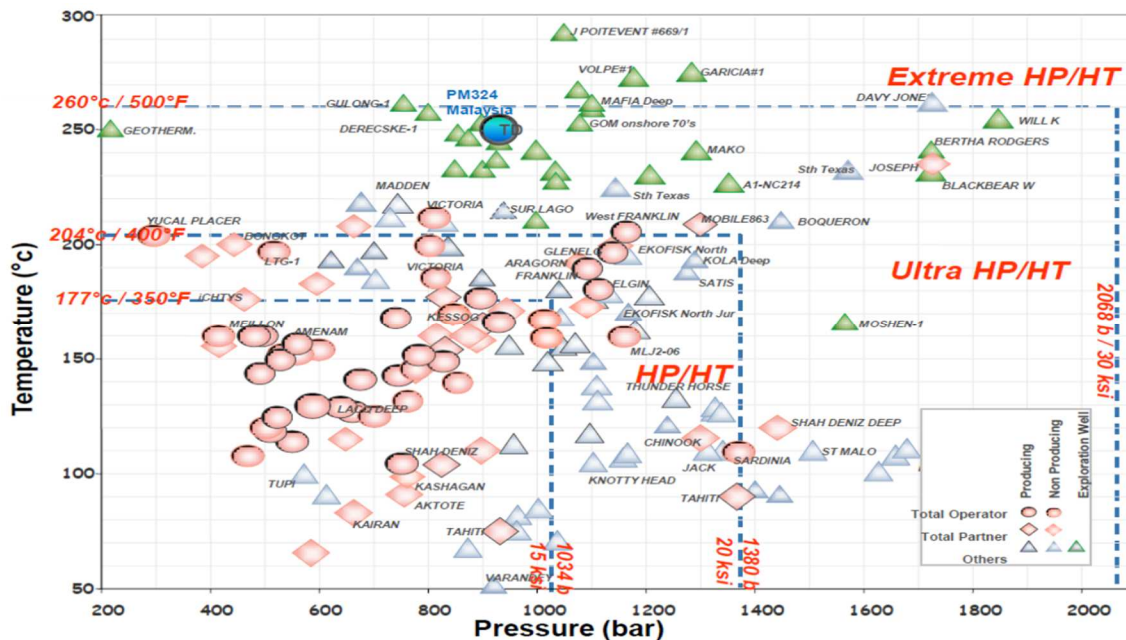


Figure 1.1 Notable HPHT wells drilled since the year 2000. Reprinted from Shadravan and Amani (2012).

1.2. Basic Well Control

Well control is an essential part of the rotary drilling process. It allows to safely detect and circulate kick out of the well and away from personnel and equipment. Failure to detect formation influx or malfunctioning of the well control system may lead to uncontrolled flow of formation fluids into the well, that is, a blowout. Well control theory aims to safely manage formation pressure by keeping formation fluids out of the wellbore. A kick is defined as formation fluid influx that causes a well-control emergency. Three factors are conventionally listed as prerequisites for a kick to occur: (i) pore pressure must be greater than wellbore pressure, (ii) permeability of the formation must be sufficiently high to allow for a significant influx, and (iii) formation-fluid viscosity must be low enough that it can flow out of the formation (Bourgoyne,

Millheim, and Chenevert 1985, Watson, Brittenham, and Moore 2003, Mitchell and Miska 2010).

A kick happens due to failure in keeping wellbore pressure higher than formation pressure, failure to keep the hole full while tripping, surge and swabbing, lost circulation, or mud cut by formation gas, oil, or water (Grace et al. 2003). The primary goal of well control is to avoid kicks in the first place, which in general means keeping the wellbore pressure above pore pressures and below fracture pressures of the formations being drilled (Watson, Brittenham, and Moore 2003, Rehm et al. 2013). Proper control of the bottomhole pressure (BHP) is, thus, fundamental to drilling operations, and can be achieved by either direct pressure measurement while drilling, or by estimating with wellbore flow models. Direct measurement can be problematic and susceptible to failure (Watson, Brittenham, and Moore 2003); therefore, a reliable hydraulic model of the wellbore flow is necessary (Mitchell and Miska 2010).

The pressure at the bottom of the well depends only on the annular hydrostatic pressure, frictional pressure losses in the annulus, and surface back pressure (API 2017). Since the back pressure is measured directly at the surface, a reliable hydraulic model depends on properly calculating hydrostatic pressure, that is, fluid density, and frictional pressure losses, which depends on flow rate and fluid viscosity (Economides et al. 2011).

As more unconventional reservoirs are explored and new drilling technologies become available, well control faces new challenges. Drilling methods like underbalanced drilling (UBD) and managed pressure drilling (MPD) as well as high-

pressure/high-temperature (HPHT) wells require a more fundamental understanding of drilling fluid properties and wellbore-formation behavior (Watson, Brittenham, and Moore 2003, Rehm et al. 2013). For instance, Bland et al. (2006) describe a gas influx in HPHT where formation-gas stays in solution until very close to surface. As gas starts coming out of solution, mud is pushed out of the hole, and pressure inside the wellbore decreases. As the pressure decreases, gas will start coming out of solution at deeper depths, creating a dangerous chain reaction which may lead to a blowout.

Furthermore, studies have shown that only 20 to 25% percent of kick happen during drilling, with another 25% taking place while making connections. This means that at least 50% of kicks occur while tripping in or out of the hole (Watson, Brittenham, and Moore 2003, Brakel et al. 2015), which suggests that pressure fluctuations due to surge and swab effects are more important to kick monitoring than regular mud circulation.

Therefore, understanding, simulating, and preventing kicks require a complete understanding of how drilling fluids, wellbore, and formations interact with each other. In the next sections, we will look at each one of these well control components, exploring the current applied technologies and research being developed.

1.3. Drilling Fluid Characterization

The first step towards a comprehensive description of the flow dynamics inside the wellbore is fluid characterization. Conventionally, liquid drilling- and formation-fluids are considered incompressible (Mitchell and Miska 2010); however, studies as early as Sorelle et al. (1982) have modeled mud density dependency on both pressure

and temperature. In that work, the authors developed an empirical model for drilling fluid density based on the compressibility and relative weight content of water, oil, and solids in the mud. While the compressibility of the solids is considered negligible, the authors determined the compressibility of oil by measuring the density of diesel at temperatures ranging from 311 K (100 °F) to 450 K (350 °F), and pressures varying from 0.101 MPa (14.7 psia) to 86.1 MPa (12,500 psia). The compressibility of water was determined by curve fitting tables of physical constants.

Subsequent work from Peters, Chenevert, and Zhang (1990) used a previously introduced mechanistic model based on a compositional material-balance equation. Like the early study from Sorelle et al. (1982) though, the model relies on experimental measurements of base-fluid compressibility and was validated for the same range of temperatures, with pressures up to 103.5 MPa (15,000 psia). The relative error between model and measured data was consistently below 1%. Zamora, Broussard, and Stephens (2000) generalize the Peters, Chenevert, and Zhang (1990) by introducing a multi-parameter equation the authors claim fits most base-fluids compressibility behavior. Later, Zamora et al. (2013) used that empirical equation to fit experimental data from multiple mineral, synthetic, and diesel oils. The data was collected for temperatures up to 589 K (600 °F) and pressures as high as 206.8 MPa (30,000 psia). Errors between the empirical model and measured data were below 0.7%. Currently, recommendations from API (2017) are based on these works.

During well-control scenarios, however, the density of the fluid column will be altered by the presence of formation-fluid (oil, water, or gas). Once inside the wellbore,

the formation-fluid can either flow as a separate phase, as a solute in the drilling fluid, or a combination of both. Assessing the change in bottomhole pressure (BHP) requires understanding how the formation-fluid behaves when in contact with the drilling fluid, especially if the formation fluid is a gas (Watson, Brittenham, and Moore 2003). The density of gas is orders of magnitude below the density of the drilling fluid, which causes the BHP to decrease significantly, and is the reason why gas influxes are considered the worst-case scenario in well control. Once a kick is detected, it is necessary to estimate the size of the influx. For that reason, gas solubility in drilling fluids has been studied extensively over the years. The classic work of Thomas, Lea, and Turek (1984) show the problems associated with the presence of gas in the mud by studying the solubility of methane in diesel for temperatures ranging from 311 K (100 °F) to 589 K (600 °F) and pressures reaching up to 51.2 MPa (8,000 psia). The authors use the Redlich-Kwong equation-of-state to predict saturation pressure of a gas-condensate migrating up the wellbore. O'Bryan et al. (1988) expand those finds by introducing a model for the solubility of gas in oil-based muds based on experimental solubility measurements of methane, ethane, natural gas, and carbon dioxide in diesel, mineral oils, drilling fluid emulsifiers, and OBMs. The model is validated on a low to moderate pressure range – up to 51.2 MPa (8,000 psia) – and temperatures of up to 422 K (300 °F). O'Bryan and Bourgoyne (1990) then calibrated the Peng-Robinson equation-of-state from PVT data collected at 311 K (100 °F) and up to 35.0 MPa (5,070 psia) to determine formation volume factor of gas-cut OBM. Berthezene et al. (1999), Bureau et al. (2002), Silva et al. (2004), Ribeiro et al. (2006), and Monteiro, Ribeiro, and Lomba

(2008) further explored the solubility of methane in different base-fluids. It was only with the work of An, Lee, and Choe (2015) that a model for density of gas-cut OBM in HPHT was introduced. Finally, the work of Torsvik, Skogestad, and Linga (2017) explored density changes in OBMs and their base-fluids for pressures up to 100 MPa (14.5×10^3 psia) and 473 K (392 °F). The authors have also successfully used the Peng-Robinson, and Soave-Redlich-Kwong equations of state to predict drilling fluid density at HPHT conditions, including those of gas-contaminated muds.

1.3.1. Viscosity

The frictional pressure losses inside the wellbore are the most difficult to estimate. To determine friction losses, it is necessary to establish appropriate mathematical models describing the forces present during fluid flow (Mitchell and Miska 2010). In the classical theory of hydrodynamics, the shear stress (τ) induced due to fluid flow, while independent of the strain rate itself ($\dot{\gamma}$), is directly proportional to the rate of strain by a constant value μ , called viscosity (Ferry 1970). These fluids are known as Newtonian fluids and they are defined by the stress-strain relationship shown in Eq. 1.1

$$\tau = \mu_N \dot{\gamma}, \quad (1.1)$$

where the subscript N stands for Newtonian.

The Newtonian fluid corresponds to the simplest model relating shear stresses and shear rates. Many fluids follow that model for very small strain rates; however, it is also common for other fluids, such as drilling muds, to deviate from the Newtonian fluid

model. The different relations between shear stress and shear rate are described by constitutive equations, or rheological equations of state (Ferry 1970).

When it comes to drilling fluids, Caenn, Darley, and Gray (2017) lists four constitutive equations of interest: the Newtonian, Bingham plastic, Power Law, and Power Law with yield stress. According to the authors, most drilling fluids do not conform to any one of the models, but their behavior can be predicted accurately enough for practical purposes.

Adding complexity to the Newtonian model, the Bingham plastic rheological relationship introduces a yield stress (τ_0), which can be defined as the shear stress necessary to initiate fluid flow. The Bingham plastic model is represented by Eq. 1.2,

$$\tau = \mu_p \dot{\gamma} + \tau_0, \quad (1.2)$$

where μ_p is the plastic viscosity of the fluid.

The Power Law model describes the fluid as a linear relationship between shear stress and shear rate in a log-log plane. Its mathematical formulation is shown in Eq. 1.3,

$$\tau = K_{PL} (\dot{\gamma})^{n_{PL}}, \quad (1.3)$$

where K_{PL} is the consistency index, which is numerically equal to shear stress value when shear rate is one. The exponent n is dimensionless.

Finally, the Power Law with yield stress, also known as Yield-Power-Law, YPL, or Herschel-Bulkley model, is given by Eq. 1.4,

$$\tau = \tau_S + K_{HB} (\dot{\gamma})^{n_{HB}}, \quad (1.4)$$

where τ_S and K_{HB} are the yield stress and consistency index of the Herschel-Bulkely model. They have similar physical meaning as τ_0 and K_{PL} , respectively, but are

represented by different mathematical symbols to allow for easy comparison between model parameters.

Several more complex rheological models exist in the literature; some derived focused on drilling fluids, some borrowed from other research fields. Bui and Tutuncu (2016) present an extensive review of the most relevant models used in the drilling industry, and introduce their own empirical model by fitting experimental data to cubic splines. Bailey and Peden (2000) suggest the Sisko model should be used by default in any hydraulic calculations of drilling fluids, since sufficient experimental data have demonstrated it is the most accurate constitutive relationship. The Sisko model is given by Eq. 1.5,

$$\tau = a\dot{\gamma} + b(\dot{\gamma})^c, \quad (1.5)$$

where a , b , and c are model parameters.

1.3.1.1. Drilling Fluid Viscosity as a function of Pressure and Temperature

The Bingham plastic and Power Law are the most popular viscosity models used in the Oil and Gas (O&G) Industry. Advanced models are generally ignored because they add an extra layer of complexity to hydraulic calculation of frictional pressure drop (Bailey and Peden 2000). Compiling to the problem, very limited work has been done on the effects of pressure and temperature on the rheology of drilling fluids. A few empirically determined functions of pressure and temperature exist, but they each apply to different viscosity models, making it very hard to set a standard method to determine viscosity as a function of pressure and temperature. In fact, the API (2017) recommends only that rheological properties at high-pressures and high-temperatures should be

obtained experimentally. This is, however, impractical, since HPHT rheometers are not readily available.

Shadravan and Amani (2012) present a historical background of what the term HPHT encapsulates, and propose a subdivision of the terms into three different ranges for both pressure and temperature that tries to consolidate the distinct definitions used by different operators and service companies in the O&G industry. The proposed limits are presented in Table 1.1. In this work, we will use these thresholds, but we also use HPHT as a generalizing term, referring to all tiers. It is also important to notice that low temperatures should also be considered outside the normal range of temperature. According to Zamora, Roy, and Slater (2013), Arctic and deepwater wells can cool drilling fluids to temperatures below 277.5 K (40 °F), but drilling fluid rheology in those conditions are not well studied – most rheological characterization is performed at temperatures above 293 K , i.e. 68 °F (Davison et al. 1999).

Tier / Common name	Pressure, MPa (psia)	Temperature, K (°F)
<i>No tier / Normal</i>	$p < 68.9$ (10k)	$T < 422$ (300)
<i>Tier I / High</i>	68.9 to 138 (10k-20k)	422 to 478 (300-400)
<i>Tier II / Ultra High</i>	138 to 207 (20k-30k)	478 to 533 400-500)
<i>Tier III / Extreme</i>	$p > 207$ (30k)	$T > 533$ (500)

Table 1.1 HPHT tiers and their limits.

One of the earliest relationships between drilling fluid viscosity and temperature was derived by Stiff (1970). Later, McMordie, Bennett, and Bland (1975) used the Hershel-Bulkley model and concluded that the logarithm of the shear stress is proportional to the pressure and inversely proportional to the temperature. Politte (1985)

provides an accurate model to compute the viscosity of diesel at temperatures varying from 298 K (77 °F) to 422 K (300 °F) and pressures in the range of 6.89 MPa (1,000 psia) to 103 MPa (15,000 psia). The author then uses the Bingham model to characterize OBMs and observes that a mud's plastic viscosity ratio between two sets of pressure and temperature is equal to the viscosity ratio of that mud's base-oil at the same pressure temperature sets. The author also found the yield point was very susceptible to experimental error, but weakly dependent on pressure. Using the Arrhenius equation as a the basis for their viscosity-pressure-temperature (μPT) models, Houwen and Geehan (1986) were able to improve the yield point modeling for the Herschel-Bulkley and Casson constitutive relations. Davison et al. (1999) also use Herschel-Bulkley and Casson to fit their μPT model to experimental data obtained at low temperature (277 K, or 40 °F); however, the authors do not make their model available. Lee, Shadravan, and Young (2012) are among the first to extend an Arrhenius equation-based μPT model to extreme HPHT conditions, reaching pressures as high as 241 MPa (35,000 psia) and temperatures of 560 K (550 °F). Gokdemir, Erkeköl, and Dogan (2017) created their own empirical μPT model based on Power Law and Herschel-Bulkley constitutive equations and validate it for pressures up to 82.7 MPa (12,000 psia), but only at temperatures ranging from 298 to 348 K (77 to 167 °F). All the μPT models discussed above apply primarily to high strain rates (greater than 100 RPM). Rommetveit and Bjorkevoll (1997) define a general model that can be used at low and high strain rates, but the authors do not show the accuracy of their claim, nor give detailed mathematical formulation of their model.

Among the experimental work published, Herzhaft et al. (2003) explore the effects of lower temperatures, from 273 to 353 K (32 to 176 °F), in drilling fluid rheology by measuring shear stress and complex relaxation modulus, which is out of the scope of this work. Amani (2012), Amani and Al-Jubouri (2012), and Amani, Al-Jubouri, and Shadravan (2012) published several experimental measurements of apparent viscosity, plastic viscosity, and yield point for both oil- and water-based muds at temperatures up to 561 K (550 °F) and pressures up to 241 MPa (35,000 psia). The apparent viscosity (μ_a) is a term commonly used to rheological characterization of drilling fluids and it represents the ratio between shear stress and shear rate. Since its definition is derived from the Newtonian constitutive relation, but is applied to non-Newtonian fluids, this viscosity measurement is qualified as apparent. While not relevant to this work, apparent viscosity helps retrieving shear stresses values.

To our knowledge, Torsvik, Myrseth, and Linga (2015) were the first to study the effects of formation-gas contamination on mud rheology. The authors dissolved methane at a 5.0% ratio by weight in an OBM and tested its viscosity at 373 K (212 °F) for pressures varying from 40 MPa (5,800 psia) to 64 MPa (9,300 psia). The authors noticed a significant reduction of viscosity for shear rates between 100 to 2000 s⁻¹ (58.8 to 1,176 RPM). Torsvik, Skogestad, and Linga (2017) later extended that work and analyzed the change in viscosity for gas-cut OBMs at 1.15% and 5.81% methane by weight, arriving to similar conclusions.

1.3.2. Gel-Strength

Thixotropy can be described as slow changes in fluid viscosity while rest. Thixotropic effects result from physicochemical restructuring of the fluid after it was destroyed by deformation, e.g. shearing (Malkin and Isayev 2012). Drilling fluids are, in general, thixotropic materials, and gel-strength is the parameter used to quantify it. Gel-strength is the initial shear stress necessary to initiate flow of a drilling fluid after a period of rest. Because of thixotropy, the gel-strength increases at a diminishing rate as the rest time increases until a maximum value is reached. This maximum value corresponds to the yield stress (Caenn, Darley, and Gray 2017).

A very limited amount of work has been done to fundamentally, or even empirically, characterize gel-strength behavior of drilling fluids. Garrison (1939) established a time-dependent relationship for gel-strength, validating their model against only one set of experiments. The Garrison model was later tested against other drilling muds by Weintritt and Hughes (1965), which confirmed the validity of the model for a two-hour period, but that had a significant deviation thereafter.

The O&G Industry lacks fundamental research on gel strength of drilling fluids. An enormous gap exists between the work of Annis (1967), who experimentally showed the effects of temperature on gel-strength for temperatures up to 422 (300 °F), and the studies by Amani (2012), Amani and Al-Jubouri (2012), and Amani, Al-Jubouri, and Shadravan (2012), who determined gel-strength in HPHT conditions in a series of tests. Most advances in this field come from other industries. Galdino et al. (2019) highlight important studies about thixotropy and develop a well control model that includes

thixotropic effects. The authors conclude that pressure increase during shut-in increases non-linearly due to thixotropy alone, and that the gel structure actually helps towards reducing the risk of a kick.

Surge and swab pressures also depend on gel strength and/or yield point stress. The pressure necessary to initiate the flow of the thixotropic drilling fluid is an inherent component of the pressure changes in the wellbore during pipe trips (Watson, Brittenham, and Moore 2003). The work of Samuel et al. (2003) shows steady-state and dynamic models of surge/swab compared to actual downhole-pressure data, and Crespo et al. (2012) develop a simplified, empirical model for surge/swab pressures based on measured rheological data, including yield-stress.

1.3.3. Literature gap

The first step towards describing flow in the wellbore is determining the hydraulics parameters of the fluid, namely density and viscosity. As described above, drilling fluids have been the topic of study for almost a century; a substantial effort has been put towards determining drilling fluid density, and the current models seem to predict measured values reasonably well.

The viscosity of drilling fluids, however, is less well understood, and no universally-accepted rheological model exists. This makes deriving pressure-temperature models for viscosity especially challenging since it has to done on a case-by-case level. Furthermore, gel-strength studies have been largely neglected, and very little is known about how this property changes with pressure and temperature.

1.4. Wellbore Flow Dynamics

During drilling operations, the driller is ultimately concerned with keeping the bottomhole pressure between pore and fracture pressures. Determining BHP is not straightforward since it depends on several variables: well geometry, pump rates, surface pressure, and fluid properties to name a few. From our current perspective, though, we are only interested in the flow downstream the bit nozzles, that is, once the drilling fluid is in the annulus moving up towards the surface. For simplicity, we are also considering a uniform annular space, with no changes in geometry. After computing the hydraulic parameters of the fluids flowing in the wellbore, we can determine the flow characteristics such as pressure gradient, frictional losses, and flow velocity. The upward single-phase flow of liquid is relatively simple and has been described and modeled for years (Economides et al. 2011).

With the influx of formation-fluid, however, the wellbore flow becomes more complex. First, the presence of formation-fluid implies the inclusion of another phase in the flow. This new phase may be a gas (natural gas, H_2S) or a liquid (brine, formation-oil), and it may or may not be miscible with the drilling fluid. While liquid influxes are not desirable, gas influxes are more concerning due to the difference between densities of the phases. Second, the influx of the new phase and its migration up the wellbore is a fully transient event, requiring detailed mathematical modeling. It is important to notice that during a well control event, the two-phase flow only takes place in one part of the wellbore. This region is bounded by single-phase, liquid flow regions, and its boundaries are not fixed. A detailed explanation of the issue is given by Galdino et al. (2019) who

also provide a thorough list of models developed throughout the years. In the next paragraphs we briefly describe a few of the most notable models, focusing on the issues faced by their authors and the assumptions they made.

Leblanc and Lewis (1968) introduced the first gas-kick model. Their model does not take in consideration the friction losses, slip velocity between gas and liquid, nor gas solubility in the drilling fluid. Simulation results with this model do not agree with field data observations, but they qualitatively capture the actual behavior. A later model by Hoberock and Stanbery (1981a) and Hoberock and Stanbery (1981b) describe the gas-kick ignoring heat transfer effects, but considering the dynamics of the fluid flow system, and the two-phase flow effects of the gas migration, that is, void fraction and two-phase friction losses. The authors used the Griffith (1964) correlation to estimate the bubble distribution along a column, and the Beggs and Brill (1973) method to calculate friction losses in this column. In this model, the BHP depends on the choke position adjustments and pump rate changes.

Nickens (1987) derived a new model where mud density is a function of pressure and temperature; however, the viscosity is considered constant. Gas slip velocity and two-phase flow friction are computed empirically. Santos (1991) created a gas-kick simulator for horizontal wells. The Bingham plastic viscosity model is used and assumed to be constant. In the region where two-phase flow takes place, the Beggs and Brill correlations is used to compute friction losses. Choe (2001) uses the Power Law constitutive relation and Beggs and Brill (1973) method to compute the two-phase flow friction losses. Unlike the previous simulators, the author uses the Hasan and Kabir

(1988) model to calculate gas distribution. Choe (2001) compares simulations from his model to those from Nickens (1987) and Santos (1991) and concludes that the models agree with each other, but do not have an exact match due to the different two-phase correlations.

1.4.1. Upward Gas-Liquid Flow

Estimating the pressure gradient of a gas-liquid flow in the wellbore requires not only an appropriate characterization of the fluids' physical properties, but also an understanding of how the flow itself takes place. The flow can take different configurations, or patterns, depending on several variables, such as gas rate, liquid rate, pressure, pipe size etc. These patterns give a qualitative description of the flow, and serve as basis for mathematical models, such as the previously mentioned Beggs and Brill (1973) model. Shoham (2006) presents an in-depth description of several models commonly used in the O&G industry.

Four kinds of upward, steady-state, gas-liquid flow patterns are commonly described: bubble, slug, churn, and annular (Shoham 2006, Economides et al. 2011). Below we give a brief description of each flow regime (Waltrich et al. 2019), and Figure 1.2 from Shoham (2006) show conceptual illustrations of these flows:

1. Bubble flow is characterized by gas phase (bubbles) dispersed in a continuous liquid phase. The bubbles can be small, approximately of the same size, evenly distributed, and migrating at the same velocity as the liquid phase. This is called dispersed bubble flow. The bubbles can also vary in size with some smaller bubbles moving upwards in a zigzag

motion and larger bubbles (called cap bubbles) following a straight path up. This last type of bubble flow is called cap bubble flow.

2. Slug flow develops as the gas phase flow rates increases. The small bubbles start to grow and coalesce, forming large, bullet-shaped, gas pockets, which are commonly referred to as Taylor bubbles. As the Taylor bubbles ascend, a thin film of liquid moves downwards around it until it reaches the bubble tail, where it finds a liquid slug occupying most of the volume of the pipe, with the exception of a few smaller gas bubbles.
3. Churn flow is a result of an increase in the gas rate, which causes the liquid slugs to break and move downward. The falling liquid is then pushed back up by a subsequent gas structure. This flow regime is characterized by a constant oscillatory motion of the liquid phase.
4. Annular flow occurs once the gas velocity is high enough to carry the liquid upwards on a thin film around the pipe walls. The gas flows in the center of this film, also carrying entrained liquid droplets.

The same flow patterns occur in annular spaces, as illustrated by Caetano, Shoham, and Brill (1992a) and reproduced here in Figure 1.3.

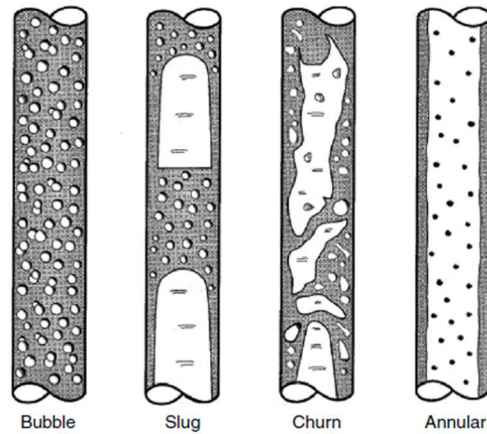


Figure 1.2 Conceptual illustration of different upward, steady-state, gas-liquid flow patterns. Reprinted from Shoham (2006).

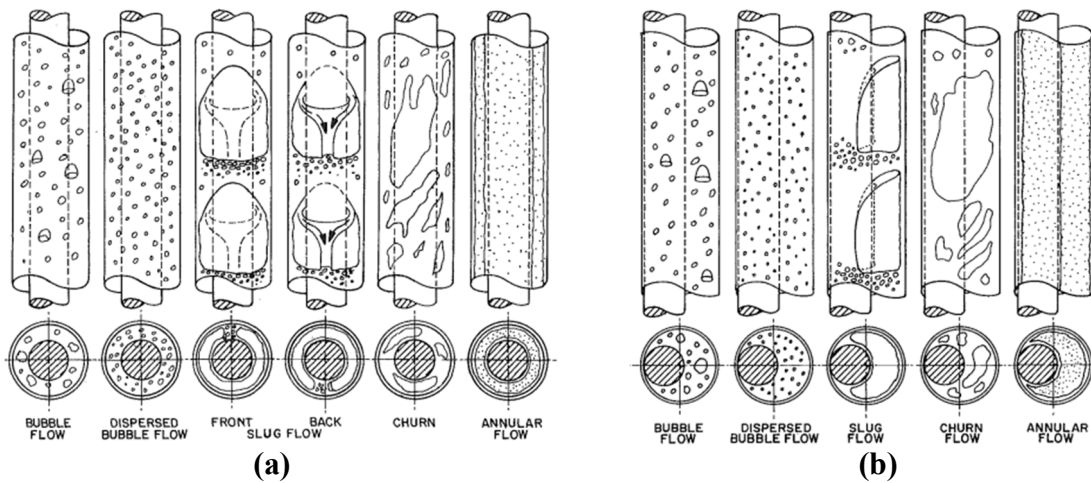


Figure 1.3 Flow patterns in (a) concentric and (b) eccentric annular spaces. Reprinted from Caetano, Shoham, and Brill (1992a).

The description of these flow regimes is based on visual observations made mostly through clear pipes in laboratory settings. As indicated by Pagan et al. (2016), the majority of the works describing these flow patterns use air and water as the gas and liquid phases, and the experiments are run in relatively small-diameter pipes, with ID below or equal to 0.10 m (4 in).

1.4.2. The Upward, Gas-Liquid, Slugless Flow Domain in Pipes

Kataoka and Ishii (1987) noticed that cap bubbles and slug bubbles dominate the flow behavior at high gas rates flowing through a stagnant column of liquid. They then concluded that the rise velocity of these large bubbles is the driving factor determining void fraction (α) and gas drift velocity (v_{gj}), one of the model's parameters. In fact, it was observed that, as the gas rate increases, v_{gj} becomes a strong function of the pipe diameter up to a point, which corresponds to the largest stable cap bubble. This theoretical largest cap bubble size is then used as the theoretical minimum above which a slugless domain is established. This criteria was later modified by Hibiki and Ishii (2003) to be written in terms of a dimensionless diameter (D^*) and it is presented in Eq. 1.6,

$$D^* = \frac{D}{\sqrt{\sigma/g (\rho_L - \rho_G)}} \geq 40, \quad (1.6)$$

where D is ID of the pipe, σ is the liquid-gas surface tension, g is the gravitational acceleration, ρ is the density of the fluid, and the subscripts L and G stand for liquid and gas, respectively. In this work, we will refer to D^* as the slugless diameter.

Using this criteria, Waltrich et al. (2019) presented a significant amount of experimental data from upward, gas-liquid flows in the slugless domain. The authors compared measured pressure gradient with those calculated from commonly used two-phase models and concluded that the current models can predict pressure gradient within 10% of measured values for bubble flow. However, discrepancies between calculated and measured values for other flow patterns were higher than 100% in some cases.

Capovilla et al. (2019) later used the model proposed by Schlegel, Hibiki, and Ishii (2010) on a similar dataset and concluded that it is more reliable than the previously analyzed O&G industry standards, predicting flow parameters within 25% of measured values for at least 79% of the cases evaluated.

1.4.2.1. Available Experimental Data for Slugless Domain in Pipes

Air and water are generally used as gas and liquid phases in two-phase flow experiments for several reasons: they are inexpensive, easily available, non-toxic, and relatively safe to handle. However, when it comes to establishing vertical, gas-liquid flow in the slugless domain, using air and water can be challenging. If we use Eq. 1.6 we estimate a minimum slugless-diameter of 0.108 m (4.25 in). This is unpractically large to handle in a spatially-restricted laboratory environment – for our calculations we considered 305 K (89.3 °F) as room temperature, 71.2×10^{-3} N/m as surface tension between air and water, 999 kg/m³ as the density of water, and 1.95 kg/m³ as the density of air at injection pressure of 170.3 kPa (10.0 psig). Furthermore, as the pipe diameters increase, the pumps and compressors necessary to reach the desired flowrates increase too, and so does cost. Using a different combination of fluids may be a solution to budget and space limitations; however, certain liquids and gases can be toxic, flammable, and/or expensive.

It is, thus, very difficult to setup experimental facilities for vertical, two-phase flow in slugless-diameter pipes, which makes data availability somewhat limited. A thorough list of experimental works in slugless-diameter pipes is presented by Pagan et al. (2016), Waltrich et al. (2019), and Capovilla et al. (2019). Among the combined 17

studies listed, only three were not done with air and water. Out of these three, two of them used water as the liquid phase and nitrogen or steam as the gas phase. Only one of the works used naphtha as the liquid phase in combination with air as the gas phase.

When it comes to vertical, gas-liquid flow in annular spaces, the existing literature is even more limited. Furthermore, there is no equivalent clear definition of slugless-diameter pipes for annular spaces. Wang et al. (2017) and Guo et al. (2017) provide different definitions for slugless domain in annuli. Zhao and Hibiki (2019) developed a tentative equation to classify slugless domain in annuli based on the work of Hibiki and Ishii (2003). The authors expression is given in Eq. 1.7,

$$D_{EP}^* = \frac{D_{EP}}{\sqrt{\sigma/g(\rho_L - \rho_G)}} \geq 40, \quad (1.7)$$

where D_{EP}^* is the dimensionless diameter for the Zhao and Hibiki (2019) model, and D_{EP} is the equi-peripheral diameter, defined in Eq. 1.8,

$$D_{EP} = D_o + D_i, \quad (1.8)$$

where D_i is the inner radius of the outer pipe, and D_o is the outer radius of the inner pipe. The D_{EP} represents a measure of the wetted perimeter in the annulus.

Using this criterion, Zhao and Hibiki (2019) analyze a list of 10 experimental datasets, and conclude only three fit the slugless domain in annuli definition.

1.4.3. Literature Gap

Formation-fluid migration up the annulus during drilling operations is a fully transient event. Creating and tuning models capable of accurately describing such events (i.e., well control emergencies) requires extensive experimental support.

A significant number of experimental works have been developed for gas-liquid flows in small-scale, small-diameter pipes. As the pipe diameters increase, however, it has been noted that the flow patterns change after certain fluid and geometrical parameters no longer allow for the existence of large bubbles inside the pipe. These conditions, which set the threshold for slugless-diameter pipes, make experimental work harder to plan and deploy due to dimension, material, and safety reasons, greatly reducing the amount of work available. Studies about slugless flow domain in annuli are even more rare, with the slugless-annulus concept being only loosely defined in the literature.

1.5. Formation Influx Modeling

Classical well-control literature uses conventional Influx Performance Relationship (IPR) models to estimate the size of the influx into the wellbore, as in Thomas, Lea, and Turek (1984), Nickens (1987), Billingham, Thompson, and White (1993), and Ilin et al. (2019). Modern studies, on the other hand, – especially those applied to MPD methods – rely on numerical simulations of complex, dynamic models such as those described in Ambrus et al. (2016) and Skogestad et al. (2019). Therefore, coupling formation- and wellbore-model generally comes at a price: it implies a tradeoff between computationally-expensive and inaccurate (or improperly-used) methods. Either way, studies are generally focused on building wellbore flow models, while only marginally accounting for formation-wellbore interaction. Sophisticated, first-principles based wellbore flow models also exist as we discussed before; however, not taking in consideration the fully-transient characteristic of well control can jeopardize the benefits

of the wellbore model by incorrectly evaluating the size of the influx. A possible solution for this problem is introduced here, as it provides reliable and accurate results while also being simple enough to be used in real-time applications.

1.5.1. Conventional IPR Models

Influx performance relationship (IPR) is a well-established concept in the oil and gas industry. In production operations, it estimates the production, that is, the formation-fluid flowrate, (Q) based on the reservoir- and wellbore-pressures (P_e and P_{wf} , respectively), and it has a general form given by Eq. 1.9,

$$Q = \text{PI} \times f(P_e, P_{wf}), \quad (1.9)$$

where PI is the productivity index, and $f(\cdot)$ is a generic function that will form $P_e - P_{wf}$ for single-phase liquid reservoirs, and $m(P_e) - m(P_{wf})$ for single-phase gas reservoirs, with $m(\cdot)$ being the real-gas pseudopressure function (Dake 1983). In that regard, there exists several IPR models, each one derived for different kinds of formation-fluids, reservoir drive mechanisms, wellbore geometry, etc.

The one thing in common with all Conventional IPR models, however, is the fact that wellbore-pressure is held constant, while reservoir-pressure is either constant (steady-state), monotonic (pseudosteady-state). The commonly called Transient IPR differs from the other ones in that its PI is time-dependent as it describes the reservoir behavior when wellbore pressure changes instantly from a constant value to another constant value. Eqs. 1.10, 1.11, and 1.12 are the mathematical expressions of the steady-state, pseudosteady-state, and transient IPRs for single-phase liquid reservoirs, respectively,

$$PI_{SS} = \frac{Q_{SS}}{P(r) - P_{wf}} = \frac{2\pi kh}{\mu \left[\ln \left(\frac{r}{r_w} \right) \right]}, \quad (1.10)$$

$$PI_{PSS} = \frac{Q_{PSS}}{P(r) - P_{wf}} = \frac{2\pi kh}{\mu \left[\ln \left(\frac{r}{r_w} \right) - \frac{r^2}{2r_e^2} \right]}, \quad (1.11)$$

$$PI_t(t) = \frac{Q(t)}{P_e - P_{wf}} = \frac{4\pi kh}{\mu \left[\ln \left(\frac{2.246 kt}{\phi \mu c_t r_w^2} \right) \right]}, \quad (1.12)$$

where the subscripts SS, PSS, and t stand for steady-state, pseudosteady-state, and transient, respectively, r_e is the reservoir outer boundary radius, r_w is the wellbore radius, k is the reservoir permeability, h is the height of the producing zone, ϕ is the reservoir porosity, μ is the fluid viscosity, c_t is the total compressibility, and t is time.

The conventional Transient IPR as presented in Eq. 1.12, or some variation of it, is usually utilized to estimate the volume of the influx from the formation into the wellbore (Thomas, Lea, and Turek 1984). While this equation is easy to use and does deliver accurate results, it is important to note that the transient aspect of this formulation is only valid until the pressure disturbance reaches the reservoir boundaries at time t_e . After this, the reservoir drive mechanism will determine the new PI. This time limit for the validity of Eq. 1.12 is given by Eq. 1.13,

$$t_e \cong \frac{1}{10} \frac{\phi \mu c_t \pi r_e^2}{k}, \quad (1.13)$$

In a typical drilling operation, it is easy to understand that if the wellbore pressure is lower than the formation pressure, the fluids in the formation pores will move from the formation towards the wellbore, as any form of Conventional IPRs would predict. This influx, though, will cause a change in wellbore flow with the introduction

of a new fluid-phase. This change in wellbore fluid flow can be significant, leading to changes in the entire pressure profile of the wellbore, including at the interface of the formation which originally caused the influx. While being submitted to a new pressure profile (i.e, new P_{wf}), this formation will behave differently than before, and influx from it may stop completely or it may increase substantially. Independently of what happens, however, it will cause the wellbore pressure profile to change once more, which, in turn, will affect the behavior of that same formation.

This interaction between wellbore and formation takes place dynamically and they do not operate separately. For that reason, Conventional IPRs are not appropriate tools to deal with well control scenarios. Well control is, by definition, a transient process, and, thus, all aspects contributing to it need to be viewed as such. Building an advanced, fully transient wellbore flow model is pointless if it not coupled with an equally good formation model. One solution to this problem is to use state-of-the-art reservoir simulators to compute the formation-fluid influx; however, these are computationally-expensive tools, which makes them impractical due to being time-consuming, and because they need extensive knowledge of formation-fluid and petrophysics properties. This problem was described by Skogestad et al. (2019) for example. In that work, the authors opted for a third alternative, that is, to develop and/or use formation-specific simulators. These are less computationally-expensive than general simulators, but they have limited application and require just as much knowledge of the formation as in the previous case.

1.5.2. The Dynamic IPR

As an alternative solution to the problems listed in the previous paragraphs, we propose the use of the Dynamic IPR (DIPR). The DIPR was introduced by Garcia et al. (2014). Just like the Conventional IPR models, the DIPR is based on the solution of the radial hydraulic diffusivity equation of a homogeneous, isotropic, circular-shaped, single-phase fluid reservoir with a vertical, finite-diameter well in its center, and is given by Eq. 1.14,

$$\frac{\partial^2}{\partial r^2} f(P) + \frac{1}{r} \frac{\partial}{\partial r} f(P) = \frac{\phi \mu c_t}{k} \frac{\partial}{\partial t} f(P), \quad (1.14)$$

where r is the radius from the center of the well, and $f(P)$ is a generic, continuous, and differentiable function of pressure (see Table 1.2).

Also like the Conventional IPR models, Eq. 1.14 is solved for the initial condition shown in Eq. 1.15,

$$f(P(r, t = 0)) = f(P(r, 0)) = 0, \text{ for } r_w \leq r \leq r_e. \quad (1.15)$$

The outer boundary condition in the solution of the DIPR is the same as that of the Steady-State IPR, which implies a constant reservoir pressure, and is shown in Eq. 1.16,

$$f(P(r = r_e, t)) = f(P(r_e, t)) = 0, \text{ for } t > 0. \quad (1.16)$$

The constant reservoir pressure assumption is valid in the context of the DIPR because this model is only valid for a short period of time relatively to the life of the well. The DIPR was originally conceived to be used as a reservoir-wellbore coupling for dying, and unstable wells. As it is the case here, the DIPR will only be used while well-

control events take place, which is timewise negligible relatively to the formation potential deliverability. Since it is unlikely that the pressure at the outer boundary of the reservoir will change in that time frame, we consider Eq. 1.16 to be valid.

Unlike any other Conventional IPR, though, the DIPR has a unique inner boundary condition, which is responsible for making it able to handle dynamic events. Here, the bottomhole pressure is not held constant, but instead it takes the form of a sinusoidal wave, as shown in Eq. 1.17,

$$f(P(r = r_w, t)) = f(P(r_w, t)) = \overline{f(P_{wf})} - A_{wf} \sin(\omega t), \text{ for } t > 0, \quad (1.17)$$

where $\overline{f(P_{wf})}$ is the average value of the sinusoidal oscillation (Table 1.2), A_{wf} is the sine amplitude, and ω is the sine frequency.

Sousa, Garcia, and Waltrich (2017b) give the solution of the generalized radial diffusivity equation (1.14), with Eq. 1.15 as initial condition, and Eqs. 1.16 and 1.17 as boundary conditions. The solution is presented in its generic form as Eq. 1.18,

$$f(P(r, t)) = F(r, \omega) \cos(\omega t) + G(r, \omega) \sin(\omega t), \quad (1.18)$$

where $F(\cdot)$ and $G(\cdot)$ are calculated in terms of Kelvin functions. The derivation of these functions is out of the scope of this work. For further information on these functions, we refer to (Barron and Barron 2012).

Sousa, Garcia, and Waltrich (2017b) also showed that evaluating Eq. 1.18 at $r = r_w$ together with Darcy's Law, it is possible to determine the fluid flow from the formation, which is given by Eq. 1.19,

$$Q(t) = \alpha r_w \sqrt{\omega \frac{\phi \mu c_t}{k}} \left[\cos(\omega t) \frac{\partial}{\partial r} F(r_w, r_e, \omega) + \sin(\omega t) \frac{\partial}{\partial r} G(r_w, r_e, \omega) \right], \quad (1.19)$$

where α is a coefficient determined from reservoir and fluid properties (Table 1.2).

Parameter	Single-phase liquid	Single-phase gas
$f(P(r, t))$	$P_e - P(r, t)$	$m(P_e) - m(P(r, t))$
$\overline{f(P_{wf})}$	$P_e - P_{wf}$	$m(P_e) - m(P_{wf})$
α	$\frac{2\pi kh}{\mu B_l}$	$\frac{T_{SC}}{T_{res}} \frac{\pi kh}{P_{SC}}$

Table 1.2 List of parameters of variables in Eqs. 1.14 through 1.19.

With Eq. 1.19 we are able to compute the flowrate of any influx if the bottomhole pressure is submitted to a sinusoidal pressure function of fixed frequency. This solution by itself is not very useful, but it can be generalized to any continuous and well-behaved bottomhole pressure.

1.5.2.1. The Generalized Dynamic IPR

Bottomhole pressure and formation-fluid flowrates are real, tangibly measurable parameters that take place simultaneously, and are intrinsically linked to each other. Even if measuring these parameters is not always straightforward, we can be sure that since they originate from the flow of a fluid continuum, they happen continuously (i.e., no jumps or discontinuities), and are integrable in relation to time.

In that regard, bottomhole pressure and formation-fluid flowrates are considered well-behaved functions of time. It is based on this property that we are able to generalize the solutions given by Eqs. 1.18 and 1.19 for any shape of $f(P(r_w, t))$ and $Q(t)$. For that

we utilize the Fourier Transform (FT), a mathematical tool that decomposes real, well-behaved functions of time into an infinite sum of complex, sinusoidal functions over the entire domain of oscillation frequencies (O'Neil 2007). By applying the FT to those equations, Garcia, Sousa, and Waltrich (2016) have shown that it is possible to obtain a frequency-domain productivity index, $PI(\omega)$, as given in Eq. 1.20,

$$PI(\omega) = \frac{Q(\omega)}{f(P(r_w, \omega))}, \quad (1.20)$$

which is fully defined by its absolute value $|PI(\omega)|$, Eq. 1.21,

$$|PI(\omega)| = \alpha \frac{r_w}{A_{wf}} \sqrt{\omega \frac{\phi \mu c_t}{k} \left[\left(\frac{\partial}{\partial r_w} F(r_w, \omega) \right)^2 + \left(\frac{\partial}{\partial r_w} G(r_w, \omega) \right)^2 \right]^{0.5}}, \quad (1.21)$$

and its phase angle $\varphi(PI(\omega))$, Eq. 1.22,

$$\varphi(PI(\omega)) = \tan^{-1} \left(\frac{\frac{\partial}{\partial r_w} F(r_w, \omega)}{\frac{\partial}{\partial r_w} G(r_w, \omega)} \right). \quad (1.22)$$

Eqs. 1.21 and 1.22 are derived from first principles and allow for the theoretical calculation of the complex productivity index at any given frequency (ω). It is important to notice that, for a given reservoir (formation) and formation-fluid, Eqs. 1.21 and 1.22 are only dependent on ω , which makes $PI(\omega)$ completely defined in the frequency domain. Thus, these equations are known as the frequency response of the wellbore-formation system we wish to describe.

The frequency response, however, does not provide a straightforward relation between $P(r_w, t)$ and $Q(t)$. The actual time-domain relationship between the fully transient bottomhole pressure and formation-fluid flow functions requires a time-

dependent relationship that does not depend on a fixed frequency value, as in Eqs. 1.18 and 1.19. Garcia, Sousa, and Waltrich (2016), and Sousa, Garcia, and Waltrich (2017c) have shown that this time response can be obtained by first approximating the complex productivity index by Eq. 1.23

$$PI(\omega) = \frac{Q(\omega)}{f(P(r_w, \omega))} \cong \frac{\sum_{j=0}^N a_j (i\omega)^j}{\sum_{j=0}^N b_j (i\omega)^j} = DIPR(\omega), \quad (1.23)$$

where $DIPR(\omega)$ is the generalized Dynamic IPR in the frequency domain, j is the index of the summation series, N is the number of coefficients in the sum (also known as the order), a_j and b_j are the coefficients of the sum, and i is the imaginary number.

If we rewrite the approximation presented in Eq. 1.26 as Eq. 1.24,

$$\sum_{j=0}^N a_j (i\omega)^j f(P(r_w, \omega)) \cong \sum_{j=0}^N b_j (i\omega)^j Q(\omega), \quad (1.24)$$

and we apply the reverse Fourier Transform and the Fourier Transform time-derivative properties, we obtain Eq. 1.25,

$$\sum_{j=0}^N a_j \frac{\partial^j}{\partial t^j} f(P(r_w, t)) \cong \sum_{j=0}^N b_j \frac{\partial^j}{\partial t^j} Q(t), \quad (1.25)$$

where $\partial^j / \partial t^j$ is the j -th time derivative.

Eq. 1.25 is the generalized Dynamic IPR in the time domain and is an approximation of the complex PI in the frequency domain (Eq. 1.23). Using Eq. 1.25 to couple bottomhole pressure and formation-fluid flow allows for easy and stable computational implementation. Besides, it is an approximation to the exact solution of any given input function, whether it is pressure or flowrate, being, thus, more reliable

than Conventional IPRs. In fact, it is easy to prove that the Conventional IPRs are particular cases of the DIPR, since, in those cases, the time derivatives of pressure and flowrate are zero, reducing Eq. 1.25 to the form shown in Eq. 1.26,

$$PI = \frac{Q(t)}{f(P(r_w, t))} \cong \frac{a_0}{b_0}, \quad (1.26)$$

which is just another way of writing Eq. 1.9.

1.5.2.2. Applicability of the Dynamic IPR

The main advantage of the DIPR over conventional IPRs and reservoir simulators is its power to capture the formation response to wellbore changes at different time-scales with virtually no computational effort. Therefore, as the name suggests, the Dynamic IPR was conceived to be used in non-steady-state, i.e., fully transient, scenarios. In that regard, the works of Garcia, Sousa, and Waltrich (2016), Sousa, Garcia, and Waltrich (2017c), Sousa, Garcia, and Waltrich (2017a), and Sousa, Garcia, and Waltrich (2017b) have done extensive work to validate the use of the DIPR under different circumstances.

1.5.3. Reservoir Characterization While Drilling

During underbalanced drilling, the use of real-time data and comprehensive formation-wellbore models gives the driller the opportunity to evaluate different formations while drilling. The idea behind reservoir characterization while drilling (RCWD) is analogous to well tests, but is more complex since bottomhole pressure, flowrates, and depth are time-dependent (Suryanarayana et al. 2007).

Shayegi et al. (2012) give an extensive review of how RCWD models have developed and compare the performance of the three current RCWD analysis methods,

namely Rate-Integral Productivity Index, Pressure-Transient Analysis, and Increasing-Boundary Analytical Model. The authors concluded that the different methods provide similar PIs. Shayegi et al. (2012) also determined that RCWD can be used to assess formation-pressure variations, which allows locating productive intervals in a lateral well and measuring their relative magnitudes.

1.5.4. Literature Gap

As new drilling technologies emerge and evolve, some degree of automation and real-time data analysis inherently becomes part of daily operations. Building a reliable and safe system requires a thorough understanding of all the parts, from the properties of the fluids involved, to how they flow in the wellbore, to how that same wellbore and fluids interact with the open formations being drilled.

As mentioned before, this integration between fluid flow and formation dynamics is generally either neglected by ignoring the transient nature of one of them, or made impractical by implementing complex and computationally-expensive methods that cannot be used in real-time applications. Therefore, there is a need for a model capable of coupling both sides that is simple enough to be used in real-time operations, but also accurate enough that it gives reliable results, comparable to reservoir simulators.

1.6. Work Objective

The purpose of this work is to create resources that allow for a fundamental and comprehensive understanding of well control emergencies, while being flexible, reliable, and user-friendly tools for simulations. This study will be developed from a series of

experiments and mathematical models describing many neglected aspects of well control and our goals are:

- Propose a methodology to test uncontaminated and gas-cut drilling fluids in HPHT conditions.
- Propose a unified viscosity model applicable to uncontaminated and gas-contaminated drilling fluids in HPHT.
- Define slugless domain in annular spaces and describe observed flow regimes.
- Generate experimental data in the slugless flow domain in annuli.
- Develop a coupled wellbore-formation tool to be used in kick simulation and well control monitoring.

1.6.1. Tasks

1. Characterize mud viscosity under HPHT conditions.
 - a. Study how gas contamination affects mud and base-fluid performances.
 - b. A series of modifications will be required to properly test the drilling fluids. The modifications will allow:
 - i. minimized contamination by foreign agents,
 - ii. Intentional, controlled contamination.
2. Describe the slugless flow domain for upward, gas-liquid flow in annuli.
 - a. Build small-scale analogs of immiscible gas-liquid flow and measure pressure gradient, and void fraction.

- b. Create/improve flow regime map for slugless flow domain in annular spaces.
- 3. Couple formation and wellbore models for real-time simulation and data analysis.
 - a. Describe fully transient, dynamic behavior of formation pressure and formation-fluid flow.
 - b. Model dynamic formation-wellbore interactions as a tool for formation-fluid influx monitoring.
 - c. Model formation-wellbore dynamics in horizontal wells.

2. METHODOLOGY

The work proposed here will be conducted on three fronts. First, we focus on mud rheology by modifying the HPHT-capable viscometer, obtaining mud samples, and testing them using standardized and new tests. We will test the mud, its base fluid (i.e., brine for WBM, and diesel for OBM), and mud contaminated with gas.

The second research effort will be concentrated on the characterization of upward gas-liquid flow in large pipes. We will build a small-scale, large-pipe analog flow loop. This flow loop will circulate common, soybean kitchen oil as the liquid phase, and air as the gas-phase.

Finally, a numerical model for coupling wellbore and formation simulation will be developed based on first-principles, and implemented on simple dynamic, fully-transient simulations. The model will then be benchmarked against O&G standard simulators.

2.1. Viscosity Measurements

The API (2017) describes two pieces of equipment usually used for measuring mud viscosity. First, the API Standard describes the orifice-viscometer Marsh funnel. This experimental setup consists of measuring how long it takes for a certain volume of test fluid to pass through a standard-size hole. This test cannot describe proper behavior of non-Newtonian fluids, and is, therefore, mostly used as a check to detect undesirable fluid consistency (Bourgoyne, Millheim, and Chenevert 1985).

The second type of equipment commonly utilized to measure viscosity is the rotational coaxial-cylinder viscometer, thoroughly explained in the paragraphs below.

2.1.1. Rotational Coaxial-Cylinder Viscometers

The use of rotational instruments is fundamental in understanding the rheological properties of different materials. The advantages of using such test method is twofold: first, it is able to impose onto a sample a given set of kinematic and dynamic flow characteristics which create a homogenous regime of deformation inside that sample. Second, this flow regime can be kept for as long as it is necessary (Malkin and Isayev 2012).

Several kinds of rotational tests, as well as geometries exist. It is not on the scope of this work to discuss each kind, so we will focus on the rotational coaxial-cylinders viscometers, also called Couette viscometers. They consist of two coaxial cylinders aligned along a vertical axis. The first cylinder, called bob, is internal and has an outer radius R_i . The second cylinder is larger and it houses the first. It is called rotor and has an inner radius R_o . Between the two cylinders rests the fluid to be tested which covers the bob with a height h_b . For our specific case, we assume the rotor rotates at a constant angular speed ω .

The movement of the rotor induces a shear stress (τ) in the fluid which acts upon the surface of the bob, causing an angular deflection of magnitude θ . The deflection of the bob is limited by a torsion spring of coefficient K_θ that is connected to the bob through a shaft, which generates a torque M . A representation of the Couette viscometer

is show in Figure 2.1 where the main parts of the equipment are identified and the variables describing the problem are indicated.

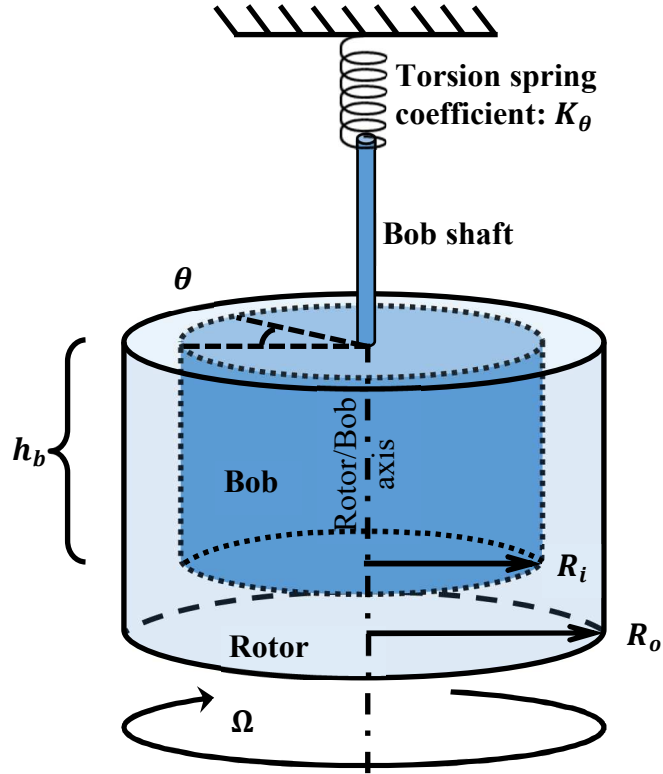


Figure 2.1 Schematic drawing of a rotational coaxial-cylinder viscometer.

Malkin and Isayev (2012) show that the shear rate ($\dot{\gamma}$) at the surface of the bob in a Couette-type viscometer can be expressed as Eq. 2.1,

$$\dot{\gamma} = \frac{2\Omega}{1 - \left(\frac{R_i}{R_o}\right)^2}, \quad (2.1)$$

where Ω is in radians per second.

Similarly, the shear stress at the surface of the bob can be written as a function of the torque M as Eq. 2.2,

$$\tau = \frac{M}{2\pi h_b R_i^2}, \quad (2.2)$$

Furthermore, the torque acting on the bob during experiments can be calculated with Eq. 2.3,

$$M = K_\theta \theta. \quad (2.3)$$

The coefficient of the spring is determined experimentally using a Newtonian, standard calibration fluid. Using Eqs. 1.1, 2.1, 2.2, and 2.3 we estimate K_θ with Eq. 2.4,

$$K_\theta = \frac{4\pi h_b \mu_N \Omega}{\theta \left(\frac{1}{R_i^2} - \frac{1}{R_o^2} \right)}, \quad (2.4)$$

where μ_N is the known viscosity of the Newtonian fluid used for calibration.

Once K_θ is known, we can use it to fit the experimental data to all sorts of different flow models. For instance, if we assume Bingham plastic flow model (Eq. 1.2), Caenn, Darley, and Gray (2017) show that torque and angular velocity are related by Eq. 2.5,

$$\Omega = \frac{\left(\frac{1}{R_i^2} - \frac{1}{R_o^2} \right)}{4\pi h_b \mu_p} M - \tau_0 \frac{\ln(R_o/R_i)}{\mu_p}. \quad (2.5)$$

The plastic viscosity (μ_p) and yield point (τ_0) are then determined by fitting a straight line to the experimental data. API (2017) suggests using this method at rotational velocities equivalent to 300 and 600 RPM.

If we assume the test fluid follows a power law model (Eq. 1.3), we compute the exponent n_{PL} and the consistency index K_{PL} by fitting the experimental data to the line in Eq. 2.6 (Caenn, Darley, and Gray 2017),

$$\log(\tau) = \log(K_{PL}) + n_{PL} \log(\dot{\gamma}). \quad (2.6)$$

As an alternative, we can also follow the guidelines from API (2017) where n is calculated by Eq. 2.7,

$$n_{PL} = \frac{\log(\theta_{600}/\theta_{300})}{\log(2)}, \quad (2.7)$$

and K_{PL} by Eq. 2.8,

$$K_{PL} = \frac{\tau_{300}}{511^n}, \quad (2.8)$$

where the subscripts 300 and 600 correspond to the angular velocity in RPMs in which the deflection angle (θ) or shear stress (τ) was measured.

The YPL (Herschel-Bulkley) model is determined by rewriting equation 1.4 as Eq. 2.9,

$$\ln(\tau - \tau_s) = \ln(K_{HB}) + n_{HB} \ln(\dot{\gamma}), \quad (2.9)$$

and using the least square method to fit the experimental data to this equation. Similarly, the Sisko model is computed by rewriting Eq. 1.5 as,

$$\ln(\tau - a\dot{\gamma}) = \ln(b) + c \ln(\dot{\gamma}). \quad (2.10)$$

To apply the least square method with Eqs. 2.9 and 2.10, however, it is necessary that the parameters τ_s and a are known beforehand. Since this is not the case, we then use an iterative method to find the best fit for both models by searching for the best

possible approximation for τ_s and a . The best approximation of these parameters is calculated by minimizing the mean absolute relative error ($\bar{\varepsilon}_{r,a}$), as defined by Eq. 2.11,

$$\bar{\varepsilon}_{r,a} = \frac{1}{N_e} \sum_{j=1}^{N_e} \frac{|\tau_j^{\text{mod}} - \tau_j^{\text{exp}}|}{\tau_j^{\text{exp}}}, \quad (2.11)$$

where N_e is the total number of experimental points, and τ_j^{mod} and τ_j^{exp} are, respectively, the model-calculated and experimental shear-stresses obtained at $\dot{\gamma}_j$, that is, the j^{th} shear-rate in the dataset.

With Eq. 2.11 we are able to find the best possible approximation for τ_s and a by pure brute-force computation. Since logarithms can only be calculated for positive numbers, we start our search with the highest possible values for τ_s and a , which are determined by Eqs. 2.12 and 2.13, respectively,

$$\ln(\tau - \tau_s) \Rightarrow \tau - \tau_s > 0 \Rightarrow \tau_s < \tau \Rightarrow \tau_s < \min_j \{\tau_j^{\text{exp}}\}, \text{ and} \quad (2.12)$$

$$\ln(\tau - a\dot{\gamma}) \Rightarrow \tau - a\dot{\gamma} > 0 \Rightarrow a < \tau/\dot{\gamma} \Rightarrow a < \min_j \{\tau_j^{\text{exp}}/\dot{\gamma}_j\}. \quad (2.13)$$

The flow chart shown in Figure 2.2 below summarizes how the least-square method and brute-force computation are used to determine the Herschel-Bulkley parameters.

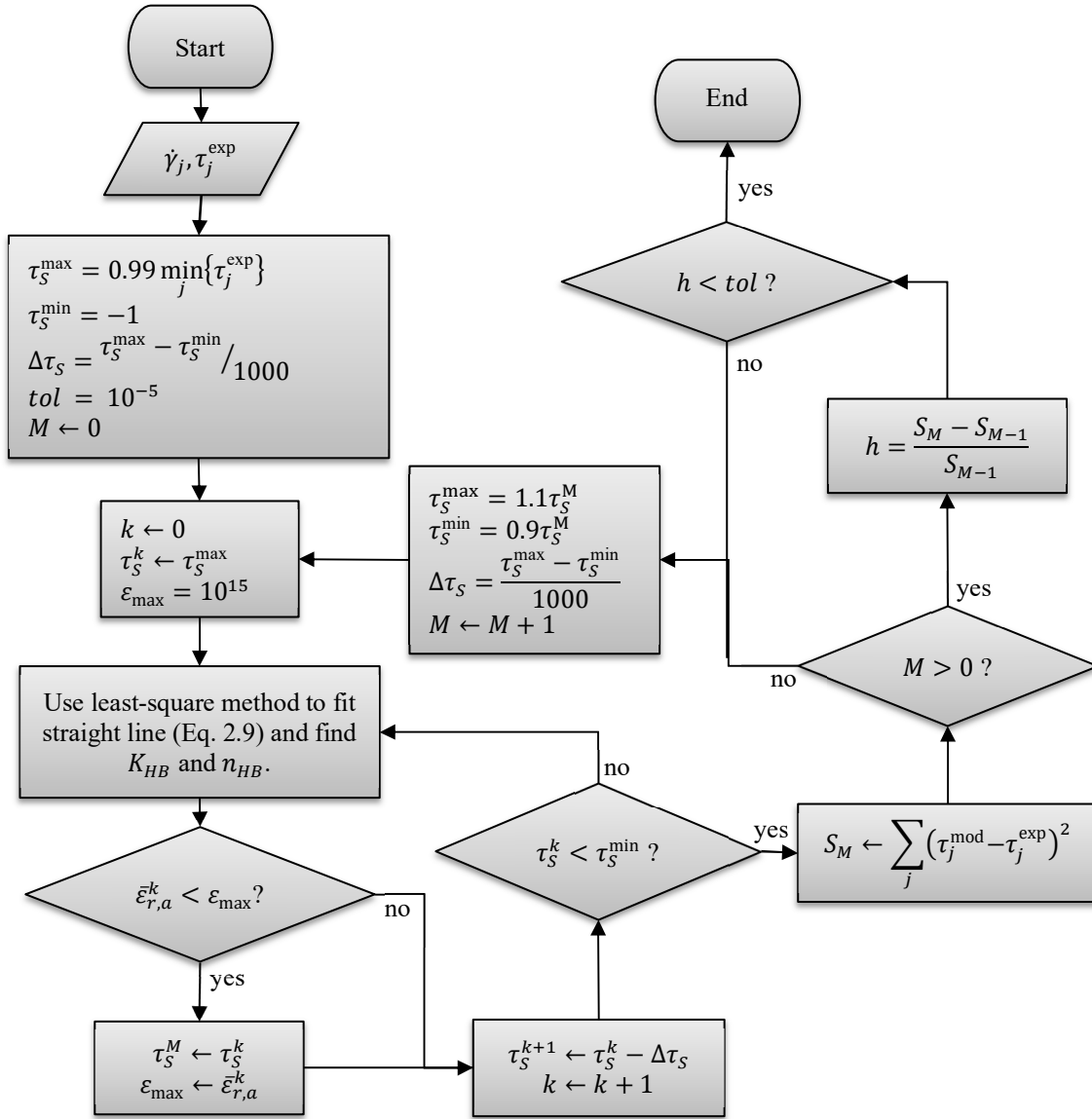


Figure 2.2 Flow chart explaining how to obtain the Herschel-Bulkley parameter using least-square method and brute-force computations.

The variables defined in the flow chart are only pertinent to the numerical method described in it, and have no physical meaning or particular significance to this study. Furthermore, it is important to observe that the same method can be applied to the Sisko model by replacing τ_S with a .

More sophisticated methods like the one introduced by Mullineux (2008) to compute the non-linear parameters of such models exist; however, given the simplicity of the calculations involved, we concluded that even the average personal computers available today can handle the computations described in Figure 2.2, for the entire dataset, in just a few minutes.

2.1.2. The Viscometer Chandler 7600

The Ametek Chandler 7600 is a high pressure/high temperature rotational coaxial-cylinder viscometer. A precision torsion spring and high-resolution encoder measure the torque created between a rotating sleeve, the rotor, and a stationary bob. The equipment can reach a maximum pressure of 275.89 MPa (40,000 psig) and a maximum temperature of 589 K (600 °F) (Ametek 2016).

The original viscometer Chandler 7600 controls pressure through a computer software operating a series of solenoid valves. These solenoid valves, in turn, control a pneumatic, pressure relief valve (APCV) and a high-pressure, pneumatic pump, which are used in tandem to reach the set-pressure value. Detailing how the pump and pressure relief valve work is beyond the scope of this work, but Figure 2.3 shows a schematic drawing of the original design of the Chandler 7600 with the parts that are relevant to this study.

The test vessel is detailed in Figure 2.4. It consists of a 3-part assembly, where the bottom part holds the test-fluid, the middle part serves as casing to the mechanical components of the viscometer, and the top part houses the torque measurement setup.

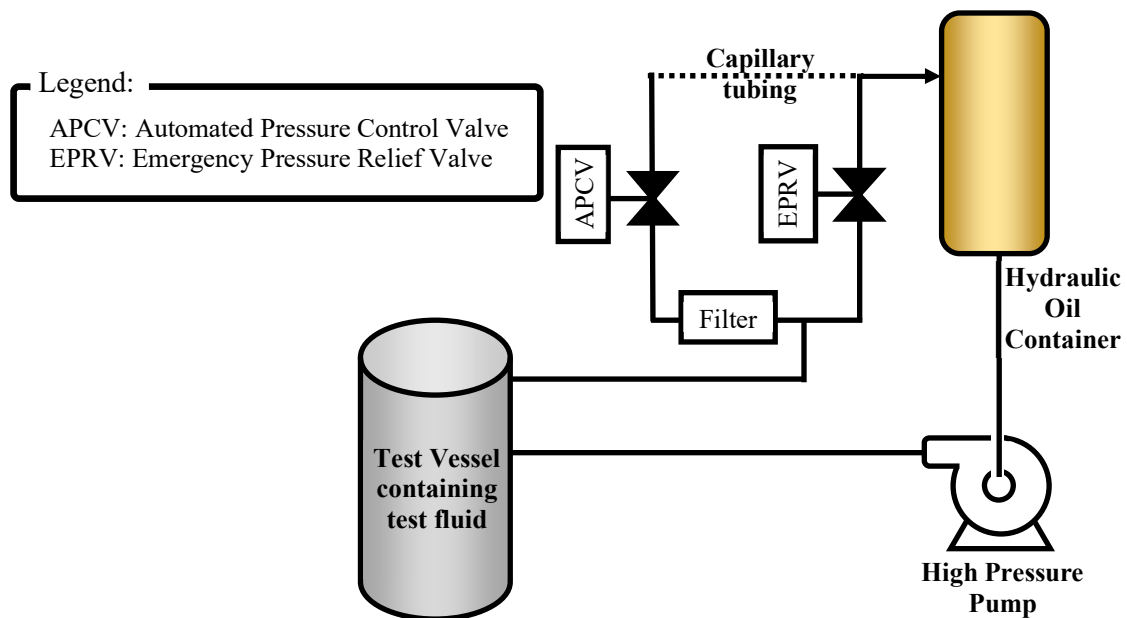


Figure 2.3 Schematic drawing of original Chandler 7600 design.

This design, while functional, allows for a series of operational problems, most of which are caused by the same factor. As mentioned above, pressurization takes place by injecting hydraulic fluid into the test vessel, making it get in direct contact with the test fluid. The mixing of hydraulic and test fluids is minimized by the presence of mechanical barriers limiting the contact between them and by the assumption that the density of the test fluid is greater than that of the hydraulic fluid. Experience, however, established that while the fluids do not completely mix together, they do contaminate each other. Signs of contamination are seen in the filter, constantly retaining solids from drilling fluids being tested, and by eventual clogging of the capillary tubing.

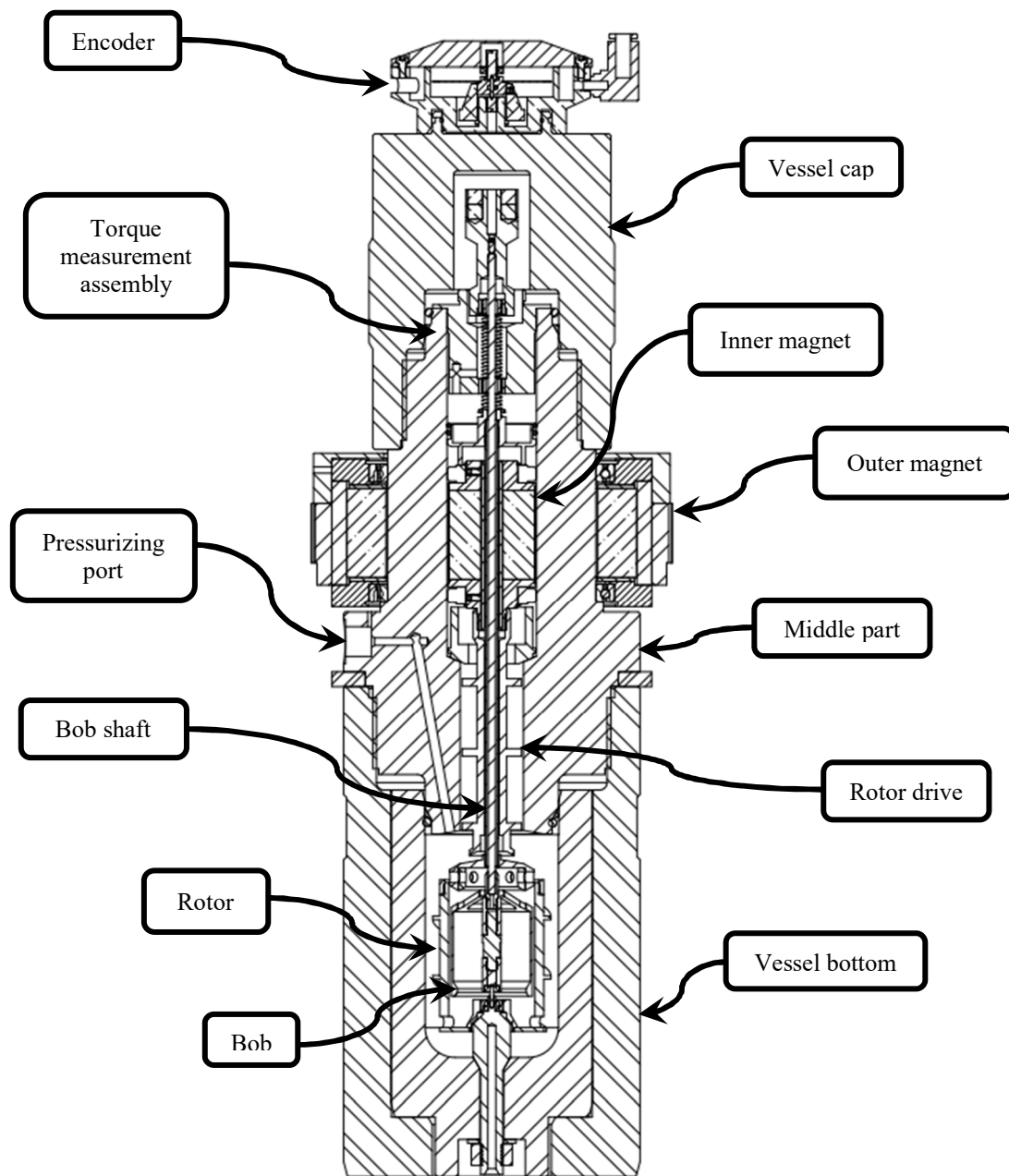


Figure 2.4 Detailed drawing of the test vessel, modified after Ametek (2016).

The contamination is minimized when testing WBM due to the immiscibility of the hydraulic fluid in water; however, it is commonly noticed with OBMs, since the

base-fluid of the mud and the hydraulic fluid are miscible. This problem is aggravated when testing base-fluids of OBMs, and NADF. These fluids are generally lighter than the hydraulic fluid, which despite the mechanical barriers, brings the heavier hydraulic fluid to the bottom of the test vessel. This, associated with the miscibility problem, causes a complete failure of the experiments since the fluid being tested becomes a mixture of hydraulic and mud base-fluid.

Since more reliable tests were needed, we redesigned the experimental setup to minimize, and even eliminate some of these operational issues. These modifications are discussed below.

2.1.2.1. Modifications

As discussed above, the main issue facing the viscosity tests originates from unwanted mixing of hydraulic and test fluids inside the test vessel after pressurization. To avoid that, we modified the viscometer Chandler 7600 by introducing an intermediary pressure vessel, whose function is to (i) isolate hydraulic fluid from test fluid through the presence of a physical barrier (a moving piston), (ii) transfer pressure from the pump to the testing vessel, and (iii) store pressurization fluid.

The pressurization fluid can be the test fluid itself, or another fluid used to pressurize the test fluid. A more comprehensive discussion about the nature and necessity of the pressurization fluid is found in section 2.1.2.2.

Isolating the hydraulic fluid from the test fluid had an additional benefit of freeing one port on the test vessel, which is now connected to a gas-liquid separator. The separator was put in place due to the presence of gas, which now can be used as a mud

contaminant. The injection of the gas is made through a third and final port on the test vessel which is channeled to the bottom of the test chamber. This port was underutilized in the original design of the viscometer. The whole setup is still operated the same way, that is, by a computer software. Figure 2.5 shows a schematic drawing of the viscometer after modifications.

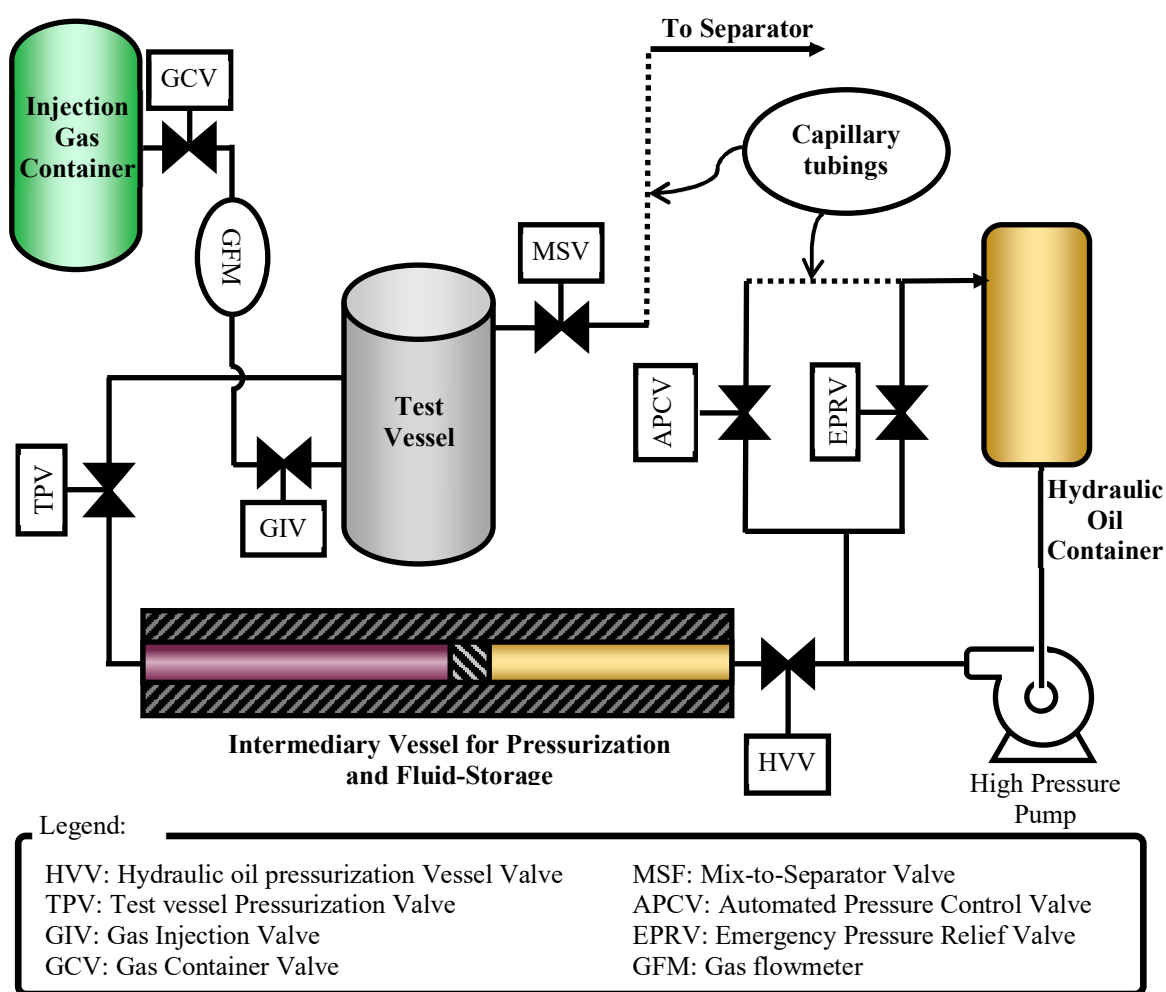


Figure 2.5 Schematic drawing of HPHT viscometer after modifications.

As part of the modifications implemented, we fabricated our own torsion springs to be used with the viscometer, steering away from the limited options given by the manufacturer. This makes the analysis of the data somewhat more convoluted, but simultaneously allows for a greater versatility of test fluids.

For the intermediary pressure vessel, we acquired the Autoclave Engineer model number OP0200SL60. This is a two-liter vessel providing a large amount of reserve volume for the pressuring fluid; however, for economic and practical reasons, we would recommend a smaller version, such as the one- or the half-liter vessels. From our experience, we also recommend using a non-magnetic alloy for the vessel, as that would allow for tracking the position of the piston inside. The intermediary vessel used in this work weighs approximately 400 lb and it can be seen in the bottom right corner of Figure 2.6.

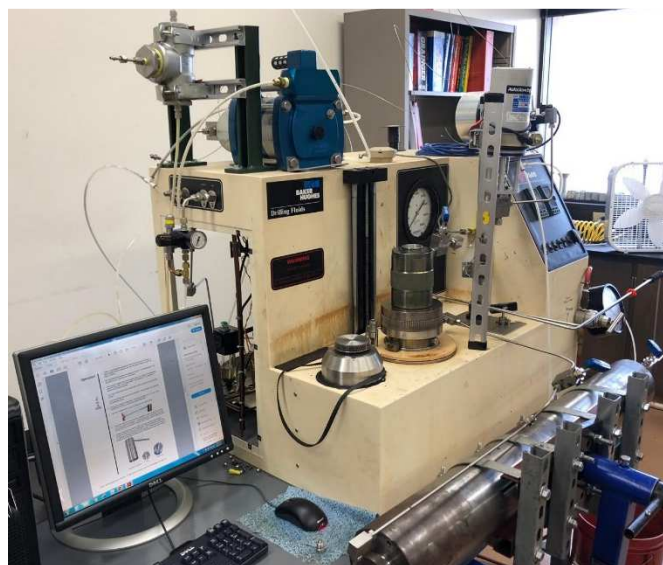


Figure 2.6 Modified Ametek Chandler 7600 partially assembled.

The mass flow rate is measured by a Micro Motion LF3M Coriolis (GFM in Figure 2.5). This flow meter measures flows varying from 0.103 to 3.640 kg/h (0.227 to 8.026 lb/h) at pressures up to 3.55 MPa (500 psig) with a 0.5 % accuracy.

We have also upgraded the original high-pressure pump and APCV with more reliable models. The new pump is an Autoclave Engineers model ASL400-02BCP, whereas the new APCV is an Autoclave Engineers model 60VM4072-C1S. The pump can be seen on top of the Chandler 7600 in Figure 2.6, standing to the side of the separator.

2.1.2.2. Pressurization fluid

Initially, the intermediary vessel was meant to be used as a barrier between hydraulic fluid and test fluid only. One side of this vessel would contain hydraulic fluid, which would push a piston and pressurized the test fluid on the other side of vessel. The test fluid on its turn would fill out the entire test vessel and, therefore, we could guarantee all experiments would be run on a uniform fluid, without contamination.

The preliminary tests carried out using the intermediary vessel showed a few problems, though. One of the early problems was not due to faulty conceptual design, but to lack of material. Real, field mud samples are only available in limited amounts (approximately 1 L); thus, waste had to be minimized, making the job of filling the entire test vessel and part of the intermediary vessel with test fluid impossible.

The conceptual method, though, worked well for testing diesel (base-fluid of OBM), since there was enough material available to carry the test. However, when, testing viscosity of brines (base-fluids of WBM), the method failed completely. The

calcium chloride (25% wt.) brine used was extremely corrosive to the magnets and the aluminum brackets holding the torsion spring in place. After one failed experiment, some of the parts of the viscometer had to be replaced.

From those experiences, we determined that the test fluid should only be present inside the bottom part of the test vessel (Figure 2.4), as it was originally designed. The only scenario where test fluid can be used to fill out the test vessel completely is if using low-density, non-corrosive fluids, like diesel, or synthetic oils. For any other test fluid, we must select a pressurization fluid that is low-density, non-corrosive, low-viscosity, and that has limited or no miscibility with the test fluid itself. Therefore, if testing WBM we would use diesel as the pressurization fluid. If the test subject is a NADF, we use tap water.

2.1.2.3. Gas Injection

The gas utilized as mud contaminant in our tests was butane. This choice is justified due to the butane's relatively low bubble point (Figure 2.7), which allows for safer injection and handling.

The butane is injected once the test vessel is completely full with test and pressurization fluids, and temperature has stabilized at 283 K (50 °F). Before actual injection, valve TPV is closed, and the air in line between GCV and GIV is removed with a vacuum pump; the line is subsequently filled up with butane. Once the pressure in the line is stabilized, the rotor is turned on to help dispersing butane in the test-fluid, and then an ice-pack is placed on the tubing between GIV and the test vessel. After that, GIV is carefully opened and gas-injection is registered by the low-flow Coriolis meter

(GFM). The ice-pack helps liquifying butane during injection. The injection pressure of butane varies between 170 and 205 kPa (10 and 15 psig), depending on the room temperature. Once GFM stops registering flow, GIV is closed. The amount of mass injected is calculated by integrating the mass flow rate data from GFM.

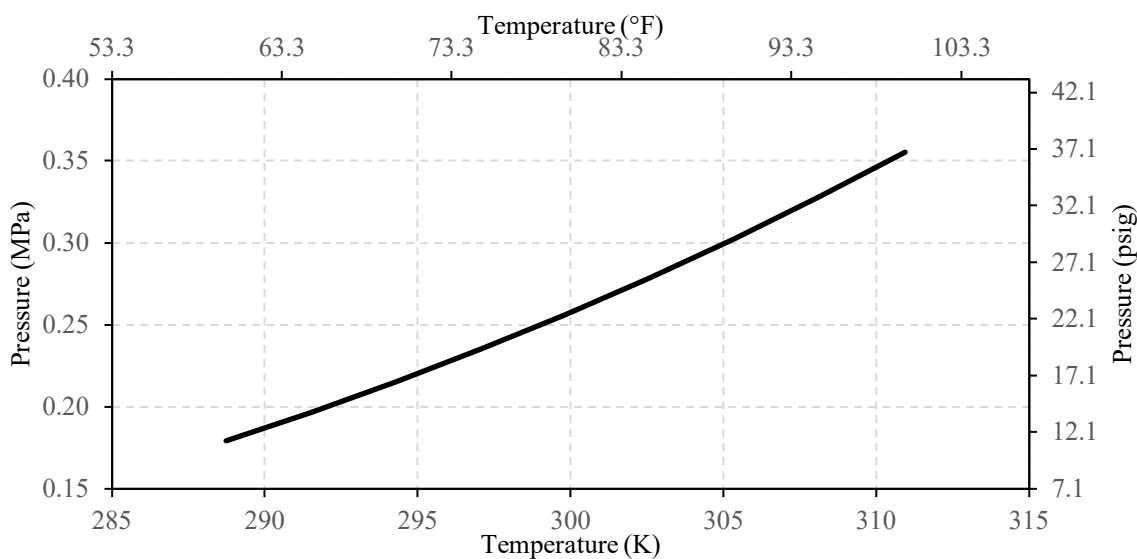


Figure 2.7 Bubble point of butane around common room temperatures in the lab.

Since the test vessel temperature is kept below the bubble point of butane, TPV is opened after the rotor has churned the gas-liquid mixture for at least 10 minutes. With TPV open, the test vessel can be pressurized; however, the first test is carried out at atmospheric pressure and 283 K (50 °F).

2.1.3. Test Matrix

We were able to test three different muds and their respective base-fluids. The mud samples available are simply referred to by their types, and they are will be called SBM, OBM1 (both used in undisclosed locations), and OBM2 (used in the Haynesville).

The test matrix used in this work was based on the work of Lee, Shadravan, and Young (2012) and is shown schematically in Table 2.1. At each combination of pressure and temperature, bob deflection is measured for the following rotational velocities 600, 300, 200, 100, 6, and 3 RPM. Furthermore, gel-strength tests were also measure for rest times of 10 seconds and 10 minutes. These tests follow the guidelines from API (2019), and API (2014).

Pressure, MPa (× 10 ³ psig)	Temperature, K (°F)										
	283 (50)	311 ^a (100)	366 ^a (200)	394 (250)	422 (300)	450 (350)	478 (400)				
12.1 (1.75)											
34.6 (5.00)											
69.1 (10.0)											
104 (15.0)											
138 (20.0)											
172 (25.0)											
207 (30.0)											
241 (35.0)											

a: Base-fluids test temperatures.

Table 2.1 Test matrix. Solid green squares indicate where data was collected. Hashed squares designate no data collected.

Due to operational limitations, the low-temperature tests were done at 283 K (50 °F). Also, malfunctioning of the heating units limited the high-temperature range to 478 K (400 °F) or 366 K (200 °F), depending on the mud sample.

HPHT viscometers are extremely sensitive and fragile pieces of equipment. Failure of parts, leaks, and malfunctioning are very common, and the machines require constant care and maintenance. For more information about the challenges involving HPHT rheology tests, we refer to the work of Zamora, Roy, and Slater (2013).

2.1.4. Experimental procedure

After the implementation of all modifications, the experimental procedure was modified from the original method indicated in Ametek (2016). Describing how to assemble the fluid-storage/pressurization and test vessel, tubing lines, and valves is important; however, it is not essential to how data is collected, and, thus, will not be explained here. The most important steps are listed below:

1. Fill the test vessel with 195 mL of test fluid.
2. Fill the fluid-storage side of the intermediary vessel with at least 350 mL of pressurization fluid. The position of the piston inside may need to be adjusted.
3. Fill the other side of the intermediary vessel with hydraulic fluid. This side must be completely full.
4. Reconnect intermediary vessel to the pressurization lines; make sure HVV, TPV and MSV are open, and GIV is closed.
5. Switch the pump on manually and wait until pressurization fluid reaches the separator.
6. Once pressurization fluid is detected at the separator, close MSV and turn off the pump.

7. If injecting gas, follow the steps below. If not, skip to 8.
 - 7.1. Turn on the chiller and wait until the sample temperature is at least 283 K.
 - 7.2. Use the computer software to set the system pressure to 0 psig.
Opening valve EPRV helps assuring the system is completely depressurized; however, this must be done with caution.
 - 7.3. Close TPV.
 - 7.4. Make sure GCV and GIV are closed, then empty the gas line using a vacuum pump.
 - 7.5. Once line pressure reaches 0 Pa, turn off the vacuum pump and open GCV.
 - 7.6. Place an ice-pack on the injection line between GIV and the test vessel.
 - 7.7. Turn on the rotor between 50 and 250 RPM.
 - 7.8. Carefully open GIV.
 - 7.9. Wait until mass flow rate at GFM is zero, then close GIV.
 - 7.10. Wait for a minimum of 10 minutes and then open TPV
8. Run test from computer software.

2.2. Gas-Liquid Flow Loop

To simulate a field-scale gas-liquid flow in a lab requires building a small-scale equivalent system. In this work, we are concerned with characterizing the bubble-to-churn transition region seen in large pipes, where slug flow does not exist. For this, we

need to build a flow loop where the pipe diameter follows the restriction given in Eq. 1.6.

As previously explained in Section 1.4.2.1, using air and water for large-diameter, two-phase flow experiments can be challenging. Thus, we chose to use another pair of fluids. One possibility would be to use hydrocarbons like methane with water, but that raised safety concerns, so we decided to keep air as our gas-phase, but we adopted vegetable oil as our liquid-phase. Table 2.2 summarizes the properties of soybean oil at several temperatures given by Sahasrabudhe et al. (2017).

Temperature K (°F)	Density kg/m³ (ppg)	Viscosity Pa·s (cP)	Surface tension N/m
295.15 (71.6)	915.7 (7.642)	0.0571 (57.1)	-
296.15 (73.4)	-	-	0.0313
313.15 (104)	903.3 (7.538)	0.0313 (31.3)	0.0306
333.15 (140)	892.4 (7.447)	0.0179 (17.9)	0.0299
353.15 (176)	867.6 (7.240)	0.0114 (11.4)	0.0287

Table 2.2 Properties of soybean oil at different temperatures.

Under the same conditions described above, the soybean oil-air system requires a minimum pipe ID of 0.0715 m (2.82 in), according to the conditions given by Eq. 1.6. This ID is 0.0057 m (0.225 in) smaller than a standard schedule 40, 3 in, PVC pipe, whose diameter is 0.0773 m (3.042 in).

Therefore, using soybean oil, air, and a 3-in PVC pipe, allows us to scale down large diameter systems like deepwater risers, and large wellbores. This is significant because we are able to replicate conditions, flow patterns, and flow pattern transitions unique to the large-diameter systems. Very few experimental works have been published

on this subject, even though this is a crucial step towards understanding the nature of flow in larger pipes. These experiments will give us tools to generate better gas-liquid flow models to simulate not only production flows, but also possible drilling scenarios, as in underbalanced operations, or in a well-control emergency.

2.2.1. Flow Loop Description

The flow loop consists of a 2.0 m (6.5 ft) long, 3-in (0.0773 m ID), clear PVC pipe mounted vertically onto a solid base. Upstream of the clear pipe, which we will refer to from now on as the test section, we find a vortex meter measuring liquid flow, and upstream the flowmeter we have a pump, which circulates the soybean oil stored inside the air-oil separator. The separator is found downstream the test section where the air-oil mixture is separated by gravity with the air being released to the atmosphere and the oil being recirculated through the system.

Just at the bottom of the clear pipe we find a 3-in ball valve and right above it we have the air injection port. Air is injected through a whole on the side wall of the pipe and the flow is controlled by a solenoid valve. Upstream the solenoid valve, before the compressed air storage tank, we have a Coriolis flow meter. At the injection port we have a gauge pressure transducer. On the second half of the test section, the pressure gradient is measured by a differential pressure transducer, which is connect to taps 1.0 m apart in the vertical direction. Figure 2.8 below shows a schematic drawing of the flow loop.

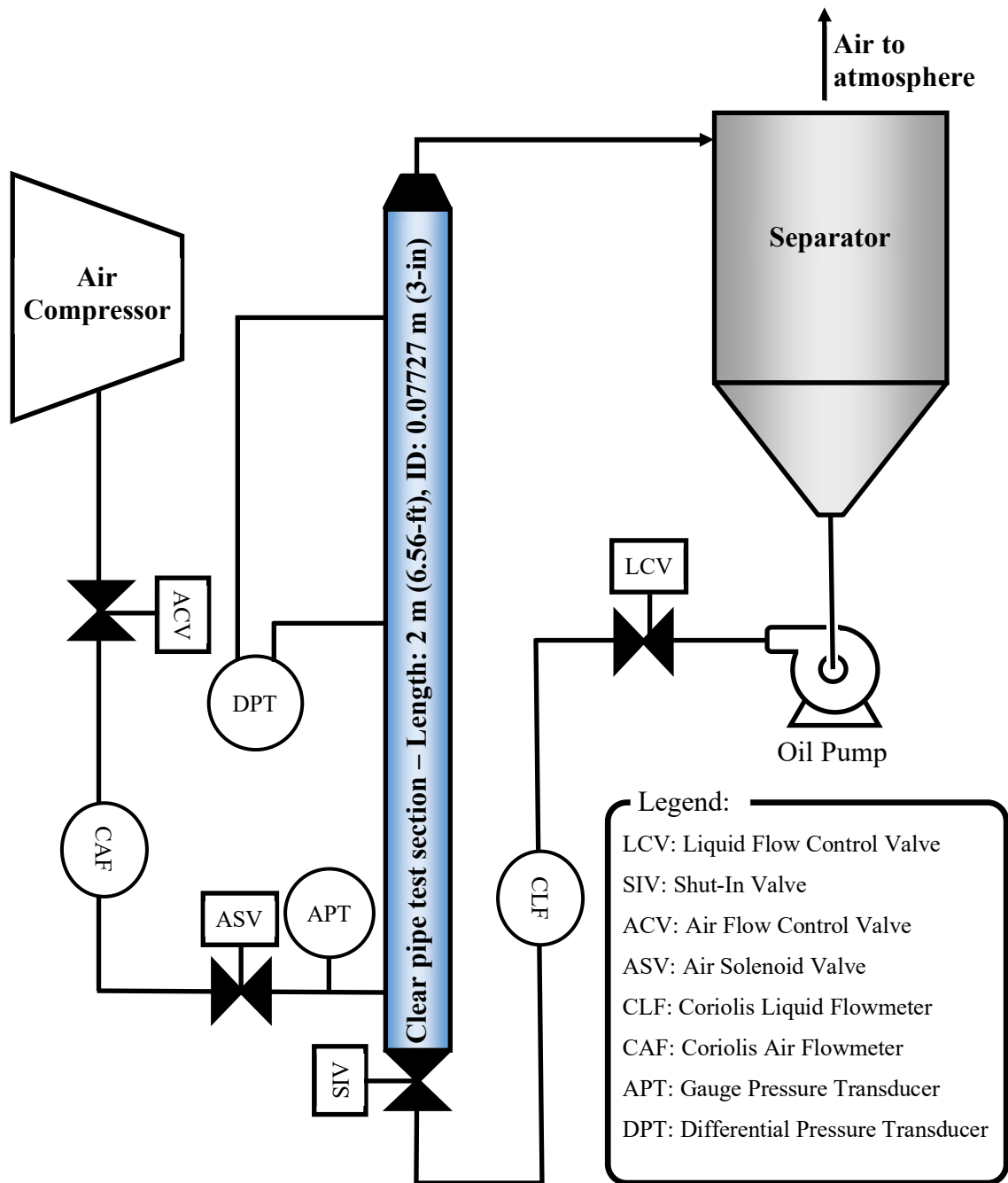


Figure 2.8 Oil-Air flow loop schematics.

The top-third of the test section can be separated from the rest by means of a pipe-union. The union creates an access point that allows for the insertion of smaller pipes inside the main 3-in pipe, creating an annular space.

2.2.2. Test Matrix

This experimental study has two main goals. First, we intend to find a definition of large annular spaces analogous to that of large-diameter pipes initially outlined in Kataoka and Ishii (1987). Second, once large annuli are defined, we will generate experimental data for large annular spaces. To achieve these objectives, we first need to prove that the small-scale flow loop built for this study actually behaves as a large-diameter pipe by comparing experimental results with large-diameter pipe model from Schlegel, Hibiki, and Ishii (2010).

Given the pump and air compressor limitations, this work is focused in the transition zone between bubble and churn flow regimes in vertical, upward, large-diameter pipes. The test matrix was designed based on work of Waltrich et al. (2019), where the bubble-to-churn boundary is defined as the lines $N_{lv}/N_{gv} = 1$, for $N_{lv} > 1$, and $N_{gv} = 1$, for $N_{lv} \leq 1$. These lines can be seen in Figure 2.9. The parameters N_{lv} and N_{gv} are the liquid and gas velocity numbers, respectively. Both numbers are related to the liquid- and gas- superficial velocities as shown in Eq 2.14,

$$N_{lv} = u_{sl} \sqrt[4]{\frac{\rho_L}{g \sigma}}, \quad (2.14)$$

and Eq. 2.15,

$$N_{gv} = u_{sg} \sqrt[4]{\frac{\rho_L}{g \sigma}}. \quad (2.15)$$

Using the data from the Table 2.2 and estimating an average test-temperature of 300 K (80 °F), we can plot the targeted experimental points against the expected flow regime map on a log-log scale of gas-, and liquid-superficial velocities (Figure 2.9).

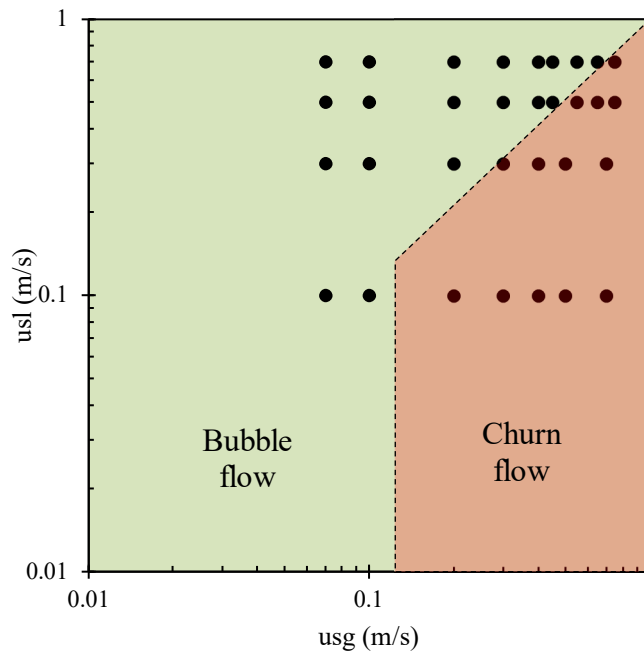


Figure 2.9 Test matrix for air-oil flow loop showing the targeted experimental points.

The same test-matrix will be used for the large-diameter pipe and the large annuli experiments. The large-diameter pipe experiments will serve as proof -of-concept to the large annulus tests. Since we are interested in determining the boundaries between large and small diameters, a series of different inner pipes will be used in the large annuli experiments. The OD of these pipes are 60.3, 48.3, 42.2, 33.4, and 26.7 mm (2.38, 1.90,

1.66, 1.32, and 1.05 inches). The large annuli tests will be performed in concentric and fully eccentric configurations.

2.2.3. Experimental Procedure

Once the electrical connections are secure, two different tests are performed: pressure gradient measurement, and average liquid holdup. The following steps summarize the experimental procedure for the former:

1. Turn on the pump and adjust liquid flow rate (reading from CLF) to desired value by either changing pump speed, positioning LCV, or a combination of both.
2. Set ACV to 10 psig and open ASV. Air will start to be injected.
3. Regulate ACV until desired air flow rate is reached on CAF.
4. Wait one minute for steady-state to be established.
5. Record pressure drop from DPT.

For the liquid holdup, the following procedure is repeated at least five times and the results averaged:

1. Wait until steady-state flow is established according to the previous instructions.
2. Turn off the pump, close SIV, and close ASV simultaneously.
3. Wait for two minutes and record the pressure reading from APT and the temperature of the oil inside the pipe.

4. Calculate the volume of oil above APT based on the measured pressure, temperature, pipe ID (and pipe OD if it is the case), and interpolating values from Table 2.2.

2.3. Formation-Wellbore Coupling Model

Before exploring how the concept of DIPR can be applied to drilling, it is necessary to understand its implications in production and what that teaches us regarding formation-wellbore interactions. The numerical routines used to simulate the examples listed here and in the rest of this work are given in Appendix A.

Using the gas well described in Tables 2.3 and 2.4, we can calculate the deliverability of the reservoir at any point in time for a fixed bottomhole pressure, in this case, $P_{wf} = 27.58$ MPa (4,000 psia). Figure 2.10 shows the DIPR response (red curve) validated against the result from Example 4-9 in Economides et al. (2011) (black curve).

Parameter	Value	Unit
h	23.77 (78)	m (ft)
P_e	31.81 (4,613)	MPa (psi)
\overline{P}_{wf}	27.58 (4,000)	MPa (psi)
A_{wf}	0.5171 (75)	MPa (psi)
r_w	0.200 (7-7/8)	m (in)
r_e	454.0 (1490)	m (ft)
c_t	1.566×10^{-8} (1.08×10^{-4})	Pa^{-1} (psi^{-1})
T	355.4 (180.0)	K ($^{\circ}\text{F}$)
ϕ	0.14	-
k	1.68×10^{-16} (0.17)	m^2 (mD)
μ (at P_e)	23.5×10^{-6} (0.0235)	$\text{Pa} \cdot \text{s}$ (cP)

Table 2.3 Formation and formation-fluid parameters for examples in this work.

Pressure MPa (psia)	Viscosity Pa·s (cP)	$m(P)$ Pa/s (psi ² /cP)
26.20 (3800)	21.1×10 ⁻⁶ (0.0211)	4.472×10 ¹⁹ (9.408×10 ⁸)
26.89 (3900)	21.4×10 ⁻⁶ (0.0214)	4.660×10 ¹⁹ (9.802×10 ⁸)
27.58 (4000)	21.7×10 ⁻⁶ (0.0217)	4.849×10 ¹⁹ (1.020×10 ⁹)
28.27 (4100)	22.0×10 ⁻⁶ (0.0220)	5.034×10 ¹⁹ (1.059×10 ⁹)
28.96 (4200)	22.3×10 ⁻⁶ (0.0223)	5.224×10 ¹⁹ (1.099×10 ⁹)
29.65 (4300)	22.3×10 ⁻⁶ (0.0223)	5.415×10 ¹⁹ (1.139×10 ⁹)
30.34 (4400)	22.6×10 ⁻⁶ (0.0226)	5.609×10 ¹⁹ (1.180×10 ⁹)
31.03 (4500)	23.2×10 ⁻⁶ (0.0232)	5.800×10 ¹⁹ (1.220×10 ⁹)
31.72 (4600)	23.5×10 ⁻⁶ (0.0235)	5.990×10 ¹⁹ (1.260×10 ⁹)
32.40 (4700)	23.8×10 ⁻⁶ (0.0238)	6.185×10 ¹⁹ (1.301×10 ⁹)
33.10 (4800)	24.1×10 ⁻⁶ (0.0241)	6.380×10 ¹⁹ (1.342×10 ⁹)

Table 2.4 Viscosity and pseudopressure function values for formation-fluid used in examples.

The differences between the productivity values from the DIPR and the conventional transient IPR (Eq. 1.12) are negligible, averaging at 0.08% and being no larger than 1.78%. At the end of transition flow time (vertical grey line, calculated with Eq. 1.13), this relative difference is only of 0.029%. It is also important to notice that after the end of transient flow, the conventional transient IPR keeps decreasing in value indefinitely, while the Dynamic IPR converges towards the steady-state production rate (blue line).

The case study and validation example presented in Figure 2.10 allows us to adopt the DIPR as an accurate and efficient formation-fluid flow model. However, before it can be used in drilling models to predict, monitor, and estimate sizes of kicks and lost circulation, we must understand how fluid flow during drilling differs from that of an ordinary production operation.

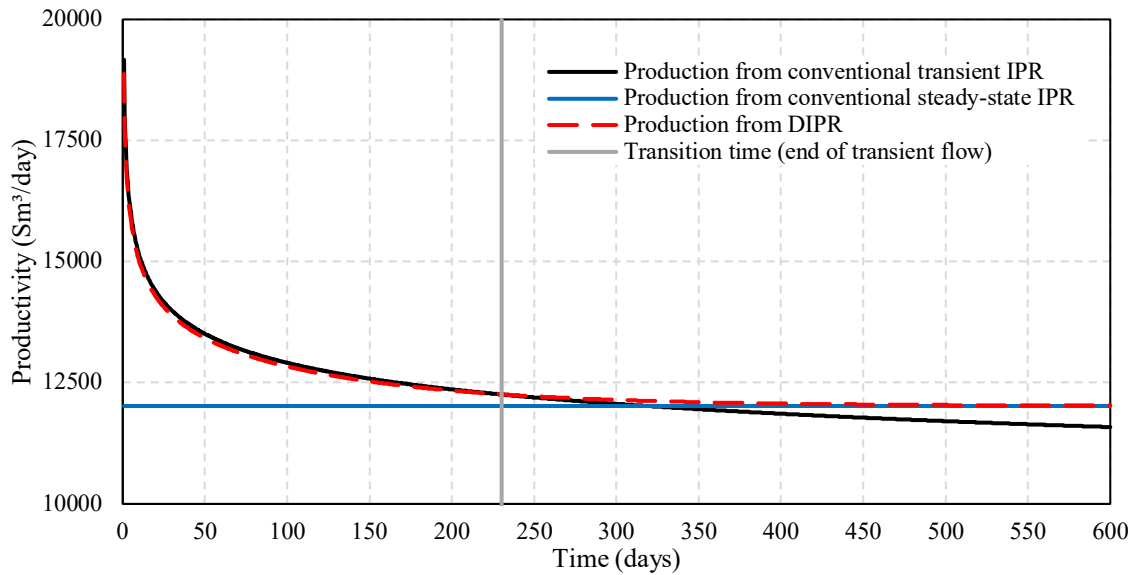


Figure 2.10 Production as calculated from DIPR validated against conventional IPR solutions.

We should also note that the DIPR can either be used to calculate current flowrate from bottomhole-pressure history, or current BHP from flowrate history; however, we are primarily interested in the former rather than the latter due to the nature of drilling and well control. In the next sections it is assumed that the bottomhole pressure is known, and it is used as an input parameter of the DIPR to obtain flowrate.

2.3.1. Dynamic IPR as Formation-Fluid Influx Model

Drilling and production operations are not so different insofar as fluid flow through the annular space in the wellbore is concerned. The differentiation between those two areas takes place mainly on how the wellbore flow and fluids interact with the formations. During production, the fluids flowing up the wellbore are the same as those coming out of the formation, i.e., the reservoir. Even if the fluid goes through phase changes while flowing, at reservoir depth, the fluid at the wellbore interface is the same

inside the hole and inside the formation. This is particularly important for the DIPR model because it can account for reservoir fluids being produced, or injected back in the reservoir (Garcia, Sousa, and Waltrich 2016).

During drilling, however, this does not hold true. The fluid flowing in the wellbore is some sort of drilling fluid, fabricated at the surface, and pumped downhole. This drilling fluid will likely differ in many ways from the fluids inside any formation, but that is not necessarily true. This will make the interaction between drilling fluid and formation fluid to vary, which, in turn, will affect how kicks and lost circulation will take place. For example, drilling overbalanced through an underpressurized aquifer with an oil-base mud is very different than doing the same with clear brine; however, in underbalanced drilling, the results would be similar (at least in regards to the fluid dynamics and flow through porous media, every other variable being considered constant, independent of drilling fluid in use). So, while drilling, formation-fluid and wellbore may interact in three different ways:

1. flow takes place from the formation into the wellbore (kick),
2. drilling fluid flows into the formation (lost circulation), or
3. no fluid is lost to formation (overbalanced drilling with mud cake).

The DIPR most obvious use would be during kick, when formation-fluids are entering the wellbore, but no wellbore fluid is injected into the formation. However, the DIPR as introduced before must be modified to properly model the other two situations. In the next sections, we will discuss these modifications.

2.3.1.1. Drilling with Clear Fluids

The main consequence of the analytical solution given by Eq. 1.18 is the existence of a u-shaped wave that propagates into the reservoir when the bottomhole pressure is not held constant. During production, depending on fluid and reservoir properties, this u-shaped pressure wave inside the reservoir can be so significant that its contribution to the reservoir pressure profile surpasses the main driving mechanism, i.e., the drawdown. The same holds true with the DIPR, which could be interpreted as a superposition of several Eq. 1.19 evaluated at different frequencies. Garcia, Sousa, and Waltrich (2016) and Sousa, Garcia, and Waltrich (2017c) showed that the existence of the u-shaped curve may reverse the direction of the fluid flow, meaning fluids can be injected back into the reservoir from the wellbore, even if the actual bottomhole pressure is never greater than the reservoir pressure.

Figure 2.11 shows the pressure profile inside a reservoir submitted to a sinusoidal bottomhole flowing pressure. The reservoir, fluid, and BHP are defined by the parameters in Tables 2.3 and 2.4, where $P_{wf} = \overline{P_{wf}} + A_{wf} \sin(2\pi ft)$, and the frequency of oscillation (f) is 0.05 Hz, that is, a 20-second period. If applied to a fully-transient bottomhole pressure, the steady-state expression (Eq. 1.10) may coincide with the analytical solution (Eq. 1.18) at some instances, as shown in Figure 2.11a, but it is more likely it will differ from the actual mathematical solution at other times, as shown in Figure 2.11b, for example.

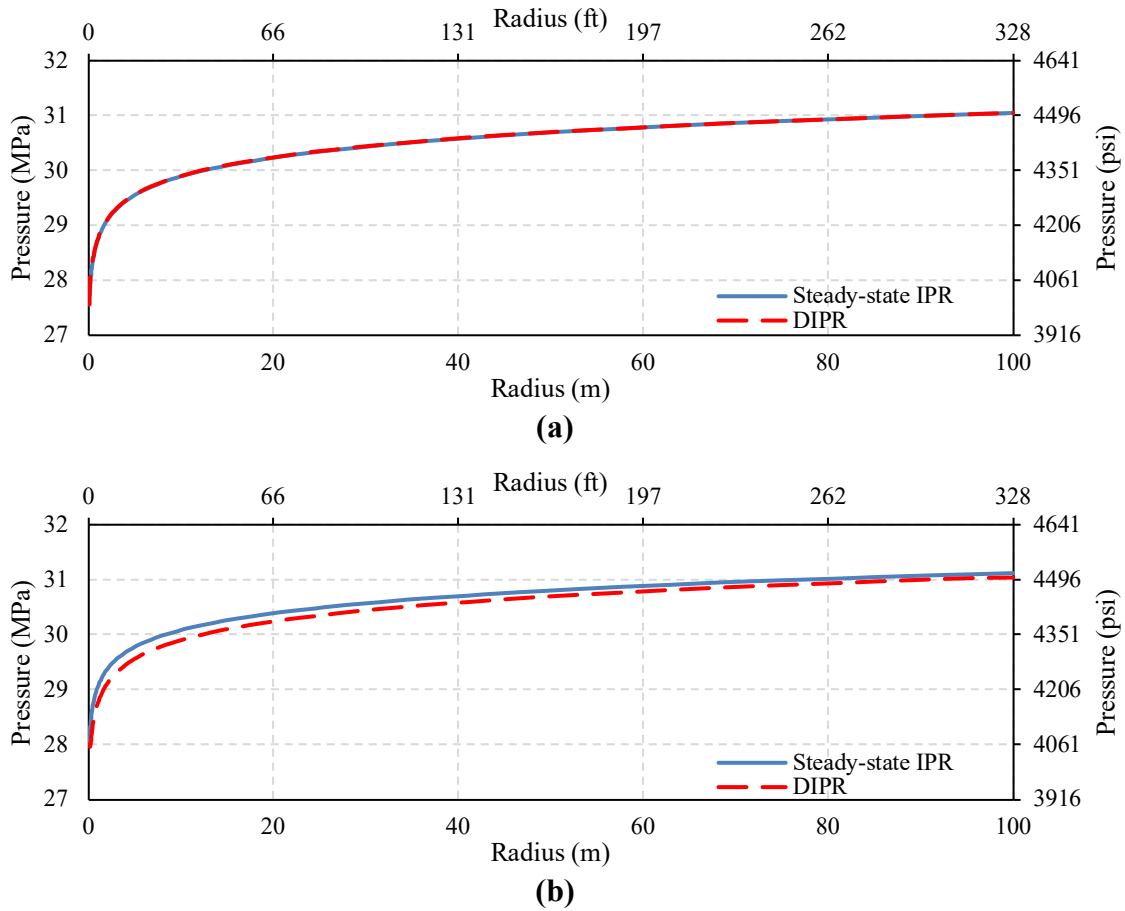


Figure 2.11 Comparison of pressure profiles inside gas-reservoir due to sinusoidal bottomhole pressure with oscillatory frequency of 0.05 Hz at (a) $t = 10$ s and (b) $t = 23$ s.

In fact, if we replot the graphs from Figure 2.11 and zoom into the first meter of the pressure profile, we can see the u-shaped component in both plots (Figure 2.12). The differences between analytical and steady-state solutions are of 135 kPa (20 psi) at $t = 10$ seconds (Figure 2.12a) and 394 kPa (57 psi) at $t = 23$ seconds (Figure 2.12b). These values while relatively low are still important in that they will fundamentally change the flow behavior of the formation-fluid. Furthermore, the differences between solutions can be amplified by changes in formation and fluid properties.

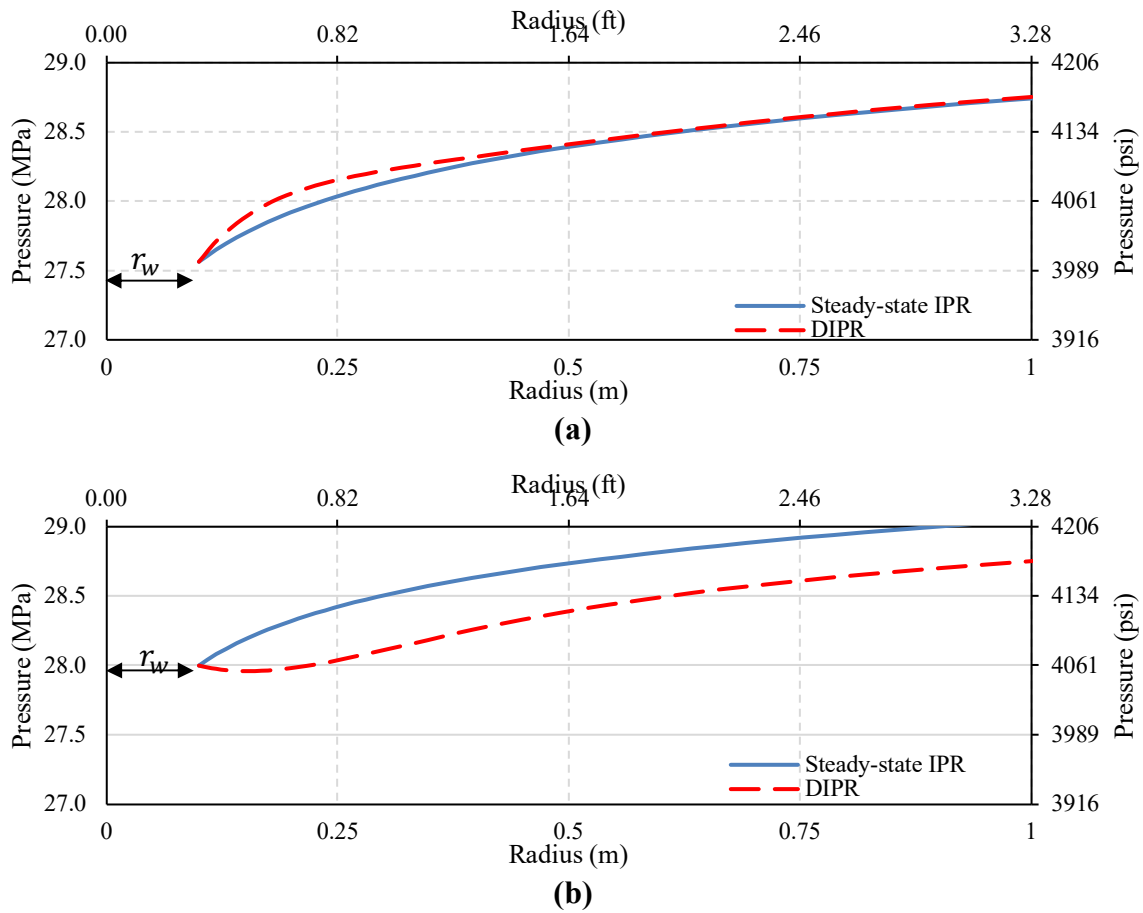


Figure 2.12 Pressure profiles from Figure 2.11 zoomed in to show the existence of the u-shaped pressure component.

The same phenomenon should be expected while drilling through any formation containing fluids. When drilling underbalanced, just like during production, the bottomhole pressure is, by definition, lower than reservoir pressure. Formation fluid is expected to flow into the wellbore, but, as a consequence of the u-shaped pressure wave, it is possible that drilling fluid is injected into the formation. Furthermore, the amount of fluid leaving the formation may surpass that expected by conventional steady-state analysis because of the u-shaped pressure wave.

Similarly, while drilling overbalanced, and if no mud cake is formed, drilling fluids tend to be injected into the formation causing lost circulation. Sometimes, this is intentional as during mud cap drilling. By analogy from what was discussed above, and considering the symmetry of the problem, it is expected that some formation fluids enter the wellbore as dynamic effects become significant (e.g., stopping circulation).

As mentioned before, the DIPR was derived to describe dynamic reservoir behavior during production, such as liquid-loading, slugging, ramp-ups, etc. Any injection cycle captured by the DIPR assumes that the fluid being injected is the reservoir fluid itself. In drilling though, this assumption is not valid.

The injection of drilling fluid is not properly described by the Dynamic IPR at all times; however, the DIPR can be modified to accommodate for such injections if we assume the following:

1. The drilling-fluid penetration distance is negligible in relation to the formation outer boundary radius.
2. The penetrated zone is concentric to the reservoir and drilling fluid is uniformly distributed in that zone.

The first assumption is justified by the fact that injection of clear drilling fluids will only occur as a worst-case scenario. Clear fluids like fresh water, brine, or diesel are generally used in completion (which is outside the scope of this work), or during underbalanced drilling, which favors flow from the formation rather than into it. If drilling overbalanced with clear fluids, this assumption may not hold true, depending on the level of overbalance.

The second assumption is a simplification that is not valid unless the previous assumption holds true. A piston-like injection of drilling fluid into a gas formation (our main concern in this work) is unlikely as the mobility ratio is much greater than one (Dake 1983). However, if the damaged zone is short enough, we can average its effect on the formation deliverability analogously to a skin factor, which is accounted for by the third assumption.

The last assumption is a consequence of the first two. Since the penetrated distance ($\Delta r_p = r_p - r_w$) is negligible in relation to the total length of the formation, we approximate the radial derivative of the pressure as the ratio between the pressure drop in the penetrated zone ($\Delta P_p = P(r_p, t) - P_{wf}(t)$) and the length of that zone, as shown in Eq. 2.16,

$$\frac{\partial}{\partial r} P(r, t) \cong \frac{\Delta P_p}{\Delta r_p}. \quad (2.16)$$

Using Darcy's law for radial flow (Dake 1983), we compute the injection rate at time $t = t_n$ as Eq. 2.17,

$$Q(t_n) = Q_n = \frac{kA}{\mu_{DF}} \frac{\partial}{\partial r} P(r, t) \cong \frac{2\pi r_w k h \Delta P_p}{\mu_{DF} \Delta r_p}, \quad (2.17)$$

where μ_{DF} is the viscosity of the drilling fluid, A is the area through which the fluid flows. If Q_n is positive, Eq. 2.17 is only valid while there is a penetrated zone, that is, $\Delta r_p > 0$.

The drilling fluid injected into or produced out of the formation at each timestep will occupy the pore volume $\Delta P V_n$ given by Eq. 2.18,

$$\Delta PV_n = \phi \pi \left(\left(r_p^{(n)} \right)^2 - \left(r_p^{(n-1)} \right)^2 \right) h (1 - S_{wc} - S_{fr}), \quad (2.18)$$

where $r_p^{(n)}$ and $r_p^{(n-1)}$ are the penetrated radii at times $t = t_n$ and $t = t_{n-1}$, respectively, S_{wc} is the irreducible water saturation, and S_{fr} is the formation fluid residual saturation.

The incremental volume of fluid injected into or expelled from the formation pores can also be computed as $\Delta PV_n = -Q_n \Delta t_n$, with $\Delta t_n = t_n - t_{n-1}$. We can thus prove that the penetration radius at t_n is given by Eq. 2.19,

$$r_p^{(n)} = \sqrt{\left(r_p^{(n-1)} \right)^2 - \frac{Q_n \Delta t_n}{\pi \phi h (1 - S_{wc} - S_{fr})}}, \quad (2.19)$$

where Q_n is the flowrate given by the DIPR, and the penetration radius is restricted by the condition $r_p \geq r_w$. Note that Q_n is negative during injection, implying that ΔPV_n is positive.

Once the drilling fluid penetration radius is known, we can estimate its effect on the formation deliverability by using Hawkins' formula (Dake 1983), Eq. 2.20,

$$S_n = \left(\frac{k}{k_p} - 1 \right) \ln \frac{r_p^{(n)}}{r_w}, \quad (2.20)$$

where S_n is the skin effect at time t_n , and k_p is the permeability of the invaded zone.

If k_p is known, the skin at each timestep can be calculated using Eqs. 2.19 and 2.20. Assuming S_n can be calculated, a new Dynamic IPR must be derived for the next timestep taking in consideration the invaded zone by using an equivalent wellbore radius given by Eq. 2.21,

$$r_w^{(n+1)} = r_w e^{-S_n}. \quad (2.21)$$

This new r_w , redefined at each timestep is derived from the definition of the effective wellbore radius due to the presence of skin and is given in Dake (1983). With Eq. 2.21, we incorporate damage to the Dynamic IPR by modeling positive skin as an analogous reduction in wellbore radius by a factor equal to e^{-S} . This change is, then, incorporated to the $DIPR_{n+1}$, that is the DIPR at $t = t_{n+1}$.

2.3.1.1.1. Validation of the DIPR with Formation Damage

Figure 2.13 reproduces the reservoir response under the same conditions used to generate Figure 2.10, but taking into account a skin value of 7. The DIPR corrected for skin effects (dashed red curve) once again performs well, following the conventional transient IPR solution (black curve) to the transition time (grey line) and staying within a 0.2 % relative difference. After transition time ($t = t_e$), the DIPR slowly approaches the conventional steady-state solution (blue line), but with a maximum relative difference of 1.2 %, which happens at transition time.

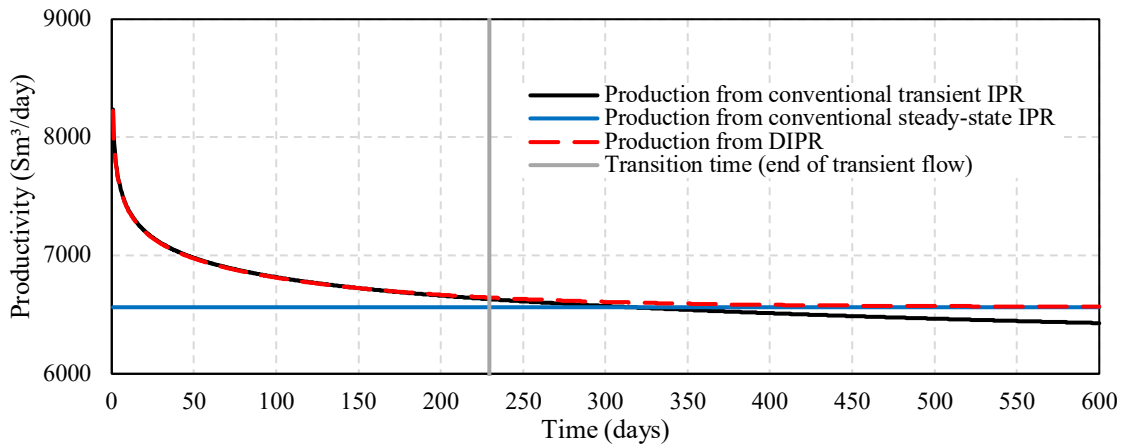


Figure 2.13 Validation of the DIPR with skin effect against conventional IPR solutions.

It is also important to note that a basic assumption of the Dynamic IPR is that the reservoir is filled with either gas, oil, or some combination of both. Therefore, even when drilling fluid is injected into the formation, the DIPR coefficients must be calculated using formation-fluid properties. However, the injection and production of fluids changes the interface across which the flow takes place. The procedure described above, thus, intends to overcome this problem and allows for the estimation of an invaded zone radius, which may be useful in designing wellbore completion. It also sets the base for the model described in the next section.

2.3.1.2. **Drilling Overbalanced with Mud Cake**

The goal of the mud cake during drilling is to isolate drilling fluids from the different formations, avoiding damage to the reservoirs, contamination of fresh-water aquifers, and losses. In terms of fluid flow and wellbore-formation interactions, the ideal mud cake acts as a check valve between the formation and the wellbore, allowing flow out of the later, but not into it, that is. $Q(t) \geq 0$ at all times. This also means that while overbalanced, the wellbore pressure is not transmitted to the formation, and, thus, $f(P_e, P_{wf}) \leq 0$ at all times. Therefore, under these circumstances the DIPR is valid only when the bottomhole pressure falls below the formation pressure, which may happen in several occasions: (i) when drilling zones with narrow margins between pore- and fracture- pressures, (ii) when pumps are shut down, and, most commonly, (iii) when tripping pipe in and, especially, out of the hole.

In reality, however, the mud cake behavior is more complex than what was described above; however, incorporating the physical properties, efficiency, and time-

dependency of the mud cake into a drilling model goes beyond the scope of this work. Nonetheless, if a mud cake model delivers an accurate estimation of filtrate penetration, Eqs. 2.20 and 2.21 are still valid, allowing for a better use of the DIPR.

2.3.1.3. Effects of Producing-Layer Length on the DIPR

The main disadvantage of the DIPR in relation to other inflow relationships is that its coefficients (Eq. 1.25) are obtained through curve fitting, making it hard to give them proper physical meaning. This does not mean, however, that these coefficients are mere curve fitting parameters. As we demonstrated with Eq. 1.26, the ratio between coefficients a_0 and b_0 is directly related to the conventional definition of productivity index. Since there exist no mathematical expression defining the a_j and b_j coefficients in Eq. 1.25, we will evaluate the effect of the producing formation length through a sensitivity analysis.

With the parameters given in Tables 2.3 and 2.4, we computed the DIPR coefficients for different formation layer thicknesses (h), varying from 1 cm to 100 m. Using the one-meter layer DIPR coefficients $a_j^{(1)}$ and $b_j^{(1)}$ as references, we obtain Figure 2.14. As it can be seen in Figure 2.14, the a_j coefficients are directly proportional to the reference value, while the b_j 's remain constant for all DIPR models evaluated at different formation thicknesses. This observation is actually in agreement with Eq. 1.19, which is the basis of the DIPR. In that equation, we can see that the flow rate is directly proportional to the formation thickness and the oscillating formation-pressure. Since the a_j coefficients are factors multiplying the dynamic pressure response, it follows that they are proportional to the reservoir height.

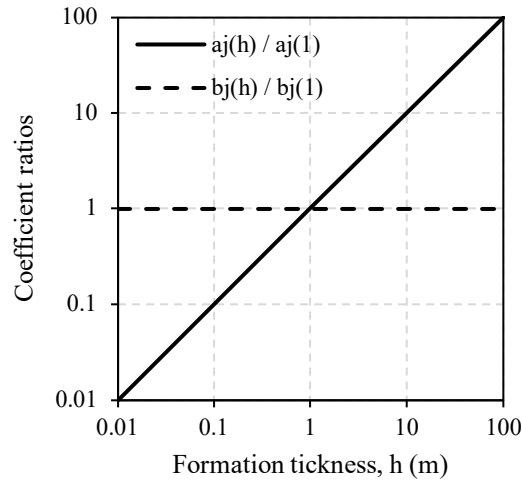


Figure 2.14 Ratios of DIPR coefficients evaluated at different formation thicknesses in relation to the one-meter reference coefficients.

Furthermore, the formation pressure changes are independent of the reservoir thickness, as it can be seen in Eq. 1.18. This is in agreement with the fact that the b_j coefficients (which can be seen as flow-rate modulators) remain constant for all the different DIPR computed.

Since during drilling the length of the producing layer depends on the rate-of-penetration (ROP), we must redefine Eq. 1.25 as Eq. 2.22,

$$\left(\int_{t_0}^t \text{ROP} \, dt \right) \sum_{j=0}^N \left[a_j^{(1)} \frac{\partial^j}{\partial t^j} f(P(r_w e^{-s}, t)) \right] \cong \sum_{j=0}^N \left[b_j^{(1)} \frac{\partial^j}{\partial t^j} Q(t) \right], \quad (2.22)$$

where t_0 is the time the bit first touches the producing layer, and $a_j^{(1)}$ and $b_j^{(1)}$ are the DIPR coefficients for the unit-length reservoir, as defined before.

2.3.2. The Dynamic Influx Model

The different uses of the DIPR as model for influx of formation-fluids into the wellbore is summarized in one new comprehensive tool called Dynamic Influx Model (DIM), which is summarized in Table 2.5 below.

Is mud cake formed?	Pressure conditions	Model
Yes	$P_{wf} \leq P_e$	Eq. 2.22
	$P_{wf} > P_e$	N/A
No	Any	Eq. 2.22, and Eqs.2.19-2.21

Table 2.5 Dynamic Influx Model equations.

In the next section, a series of examples demonstrating the importance of using the DIPR to describe wellbore-formation interaction is presented. We will show potential serious consequences of not taking into account the dynamics of the wellbore and the formation through simple, idealized, but relevant drilling scenarios.

2.3.3. Applicability of the DIM

The DIM can be applied to several drilling operations as it is explained in the following paragraphs. An actual example will be carried out in Chapter 3.

2.3.3.1. Underbalanced Drilling (UBD)

When drilling underbalanced, the drilled formations are constantly flowing due to the pressure difference between wellbore and formation pressure (Sun 2016), making UBD the closest analog to production operations among other drilling techniques. Since

the DIPR model was initially conceived as a tool for production analysis and simulation, UBD becomes the most obvious case for the application of DIM.

Even though UBD is a well-established practice and has been safely deployed in many instances, it is worth looking at the formation-wellbore interaction through the DIPR perspective.

2.3.3.2. Managed Pressure Drilling (MPD)

As explained in Section 2.3.1.2, conventional underbalanced drilling does not require a dedicated wellbore-formation coupling tool as most interactions between the two fluid domains are dampened by the existence of mud cake. However, in a few circumstances, bottomhole pressure will fall below formation pressure.

This can be a significant problem when using MPD to drill narrow windows between pore- and fracture-pressures, as even small bottomhole pressure oscillations may cause kicks as BHP fall below formation pressure. Under those circumstances, having an accurate influx model like DIM can lead to safer drilling operations as it allows for the optimization of drilling program and well control equipment.

2.3.3.3. Pipe tripping

Among all incidents that may cause formation influx, pipe tripping is by far the most common cause of kicks, as we discussed in Section 1.2. If coupled with a swab model, the DIM can accurately deliver the influx size such a transient BHP could cause.

3. RESULTS AND DISCUSSIONS

The next paragraphs are dedicated to presented the experimental and theoretical results gathered during the development of this work. As in the previous chapters, this part is separated into three different sections, each one focusing in one of the major subjects of the dissertation.

Due to the large amount of data generated, here we present and discuss in detail reoccurring base cases, as well as any exceptions. All experimental data are reported as Appendices, which are properly referenced in the next sections.

Before we proceed, however, we must introduce the idea of measurement uncertainty.

The measurement uncertainty of a variable x_i , assuming a Gaussian distribution is given by Eq. 3.1,

$$u_i = u(x_i) = 1.96 \sigma(x_i), \quad (3.1)$$

where $\sigma(x_i)$ is standard deviation when measuring x_i , and u_i is the uncertainty of that measurement.

3.1. Drilling Fluid Rheology

While running rheological experiments, we used four different sets of torsion springs. The manufacturer of the viscometer used in this study provides two kinds of spring with different coefficients (K_θ). While running the first set of experiments, we were in possession of the manufacturer's largest-coefficient spring (called S-OEM here). Nonetheless, we observed high deflection angles while using S-OEM (up to 306°),

which cautioned us into limiting the shear rates used in these initial experiments to avoid breaking the spring.

To avoid this problem, we were compelled to design and fabricate our own set of springs, with each spring coefficient being properly measured using calibration fluids. The spring coefficients are described in Table 3.1.

Spring Name	K_θ , N-m / rad
S-20	1.961×10^{-3}
S-OEM	8.668×10^{-3}
S-500-1	25.24×10^{-3}
S-500-2	24.73×10^{-3}

Table 3.1 Torsion spring coefficients.

The springs S-500 were designed to limit the deflection angle to a maximum of 180° in the worst case scenario within the test matrix (Table 2.1), that is, low temperature, high-pressure, and high shear rate. The spring S-20, on the other hand, was designed to measure deflections in very low-viscosity fluids, like brines, diesel, and synthetic oils.

Due to the physical limits of S-OEM, some experiments could not run the entire shear rate sweep of a typical drilling fluid rheology test (as described in Section 2.1.3). Thus, the unusual shear-rates of 425.6 and 255.3 s^{-1} (which correspond respectively to 250 and 150 RPM) were included to maximize the data available for modeling the drilling fluid rheology.

We fitted the collected data to the models introduced in Section 1.3.1 and we evaluate the fit-quality by looking at the mean absolute relative error. When computing

the Bingham Plastic model parameters, however, we used two different methods. The first method corresponds to what has been described in Section 1.3.1, and fits all the available data to the same straight line given by Eq. 1.2. This method is simply referred to as the Bingham Plastic model. The second method, which we will call the Bingham plastic according to API, or BPAPI for short) follows the general guidelines of the API (2017) recommendations. The plastic viscosity of the BPAPI model is called PV and it corresponds to the slope of the line fitted through the shear-stresses obtained at 1021.4 and 510.7 s^{-1} (300 and 600 RPM). The yield stress, called yield point, or YP , is obtained as the extrapolation of that line to $\dot{\gamma} = 0 s^{-1}$. Mathematically, the plastic viscosity and yield point for the BPAPI model are given by Eqs. 3.2 and 3.3, respectively,

$$PV = \frac{\tau_{600} - \tau_{300}}{1021.4 - 510.7}, \text{ and} \quad (3.2)$$

$$YP = 2 \cdot \tau_{300} - \tau_{600}. \quad (3.3)$$

where τ_{300} and τ_{600} are the shear-stresses at 510.7 s^{-1} (300 RPM) and 1021.4 s^{-1} (600 RPM) respectively.

We are now in possession of six different models to characterize drilling fluid rheology in HPHT conditions. The models are summarized in Table 3.2 while Figure 3.1 shows an example of the model regressions applied to the drilling fluid sample OBM1_s1 at 310.9 K (100 °F) and 13.9 MPa (2,000 psig).

Model	Equations	Methodology
Bingham Plastic (BP)	1.2 for all $\dot{\gamma}$	Use least square method (LSM) to fit experimental data.
API recommendations for Bingham Plastic (BPAPI)	3.2 and 3.3	Apply API equations. If data not available, model cannot be calculated.
Power Law (PL)	1.3 and 2.6	Use LSM.
API recommendations for Power Law (PLAPI)	2.7 and 2.8	Apply API equations. If data not available, model cannot be calculated.
Herschel-Bulkley (HB)	2.9	Flow chart from Figure 2.2
Sisko	2.10	Flow chart from Figure 2.2

Table 3.2 Summary of rheological models and calculation methodologies to obtain model parameters.

Even with a limited amount of drilling fluid samples (three muds and their corresponding base-fluids), we were able to run 394 tests. This database serves as the basis of a performance analysis of the rheological models in Table 3.2. Out of the 394 tests, 182 tests were run with uncontaminated drilling fluid, 171 were mixed with butane, and 41 were contaminated with diesel. The butane is used as an analogue to gas-influxes, and the diesel as representative of a liquid-influx.

All the collected data is listed in Appendix B in a series of tables showing measured shear-stresses, measurement uncertainties, the calculated parameters for each of the models listed in Table 3.2, and their mean absolute relative errors ($\bar{\epsilon}_{r,a}$).

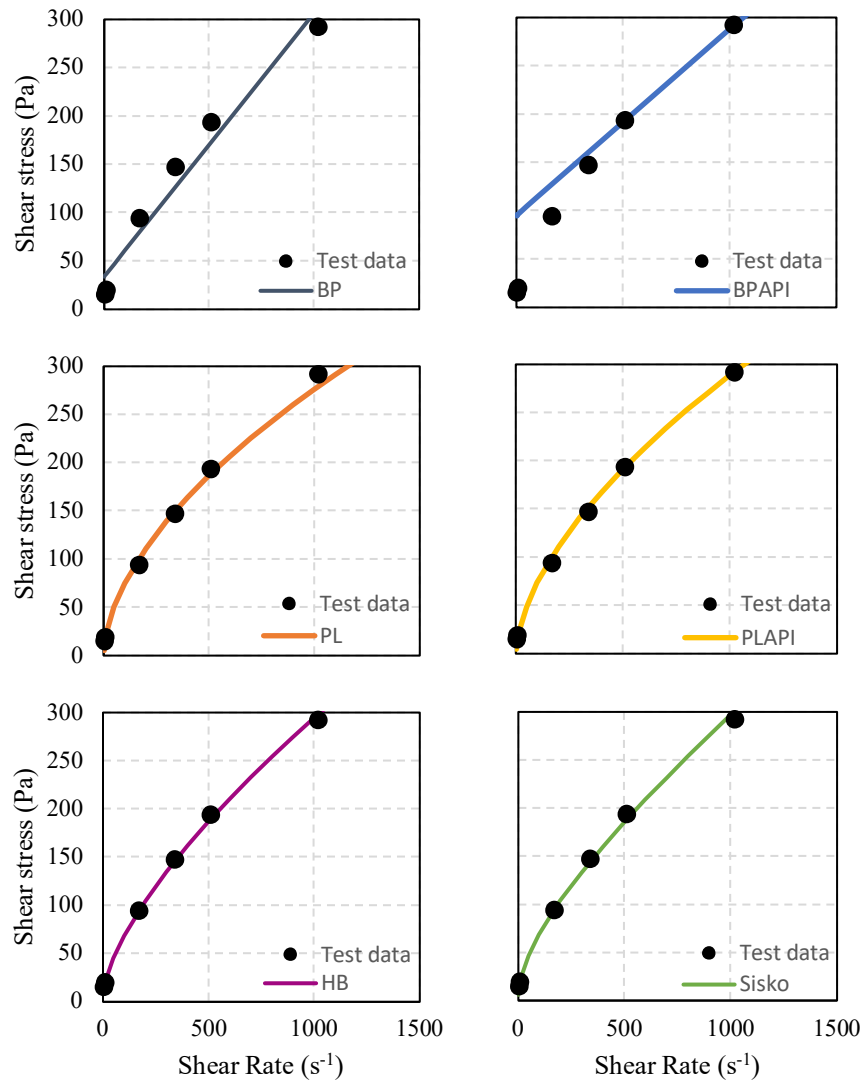


Figure 3.1 Curve-fit of different models for typical experimental rheology data (sample OBM1_s1).

In the next paragraphs we will show the most relevant cases observed in our analysis, and the practical impacts of these findings.

3.1.1. Modeling Drilling Fluid Rheology in HPHT

The first step towards characterizing the rheological behavior of drilling fluids is to understand the effects of pressure, temperature, and shear-rate. As indicated in Section

2.1.3, the experimental procedure executed for this work is comprised of shear stress measurements through pressure-, temperature-, and shear-rate sweeps. Figure 3.2 below shows the performance of each one of the models from Table 3.2 by looking at the mean absolute relative error ($\bar{\epsilon}_{r,a}$), as defined by Eq. 2.11, while splitting the data in two parts: a low-shear zone limited by shear rates below 10.2 s^{-1} (6 RPM), and a high-shear zone, with shear rates above 170.2 s^{-1} (100 RPM).

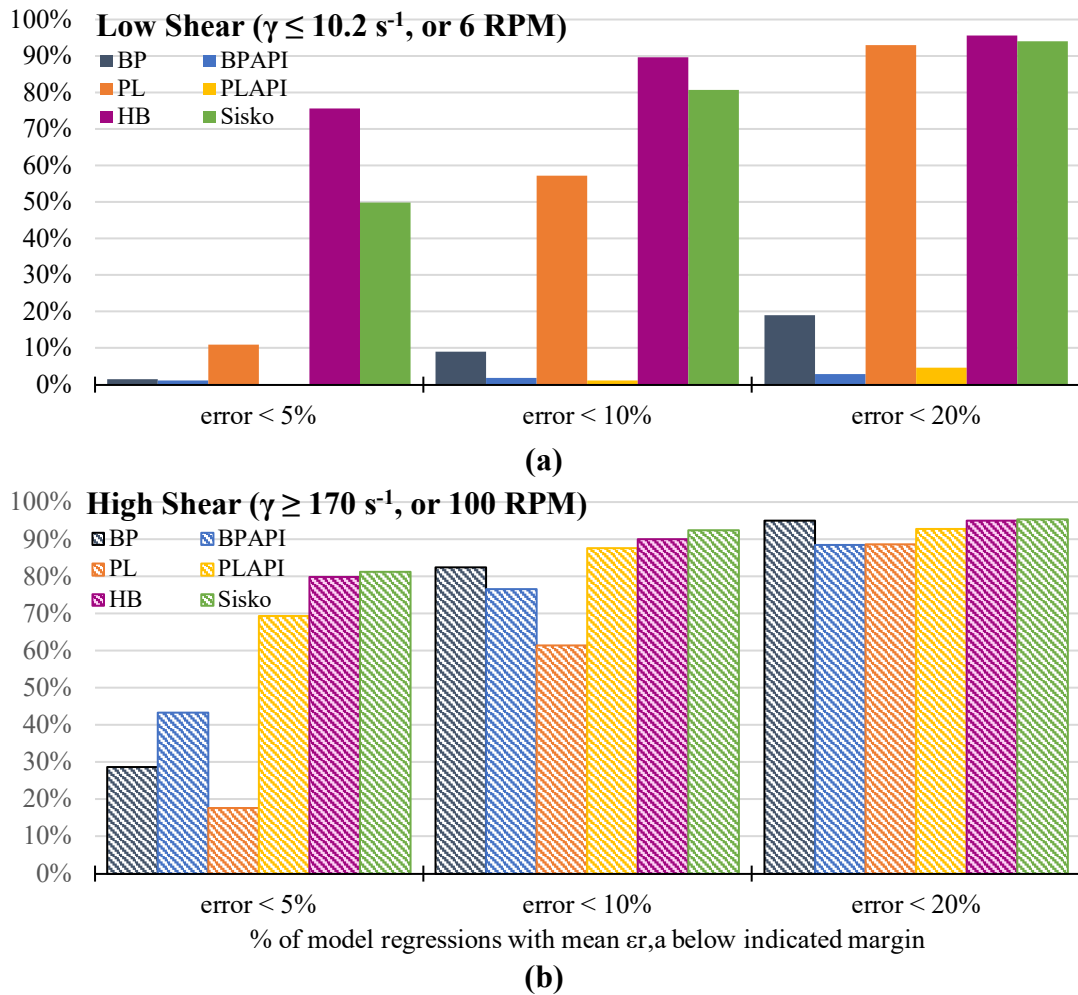


Figure 3.2 Relative number of model regressions with mean absolute relative error within 5, 10, and 20% divided into (a) low- and (b) high- shear zones.

Since BPAPI and PLAPI do not account for the low shear-rate readings, the models do not perform well in the low-shear zone, as it can be seen from Figure 3.2a. This does not, however, hold true in the high-shear zone, where both models are able to fit at least 75% of the experimental data within a 10 % error margin. The BP model also performs poorly in the low-shear zone, despite including the entire dataset in its regression. Its performance in the high-shear zone, on the other hand, is considerably better, especially in the 20 % error margin, where BP can satisfactorily fit more than 95 % of all experiments. The PL model has a consistent performance in both the low- and high-shear zones, where it performs poorly in the narrow error margin of 5 %, but has acceptable performance at the larger error margin of 20 %. In fact, inside the 20% error mark in the high-shear zone, all models perform similarly; however, HB and Sisko perform consistently better at both shear zones, and at all error margins. Within the 5% error margin, HB and Sisko are superior to any other model by at least a factor of 4.54 in the low shear zone and 1.16 in the high-shear zone. The Sisko model performs slightly better in the high-shear zone when compared to HB, but HB performance in the low-shear, 5 % error margin surpasses the Sisko by a factor of 1.52. Given how easy it is to compute the parameters of BPAPI and PLAPI, these models become very practical, and, therefore, popular, even if they are not the most appropriate models to represent HPHT rheology data. Overall, the HB model performs better, and is able to fit the experimental data within 5 % error for at least 76 and 80 % of all low- and high-shear tests, respectively. In an effort to further understand how the models perform in the wide variety of conditions encountered in HPHT, we plotted in Figures 3.3 and 3.4

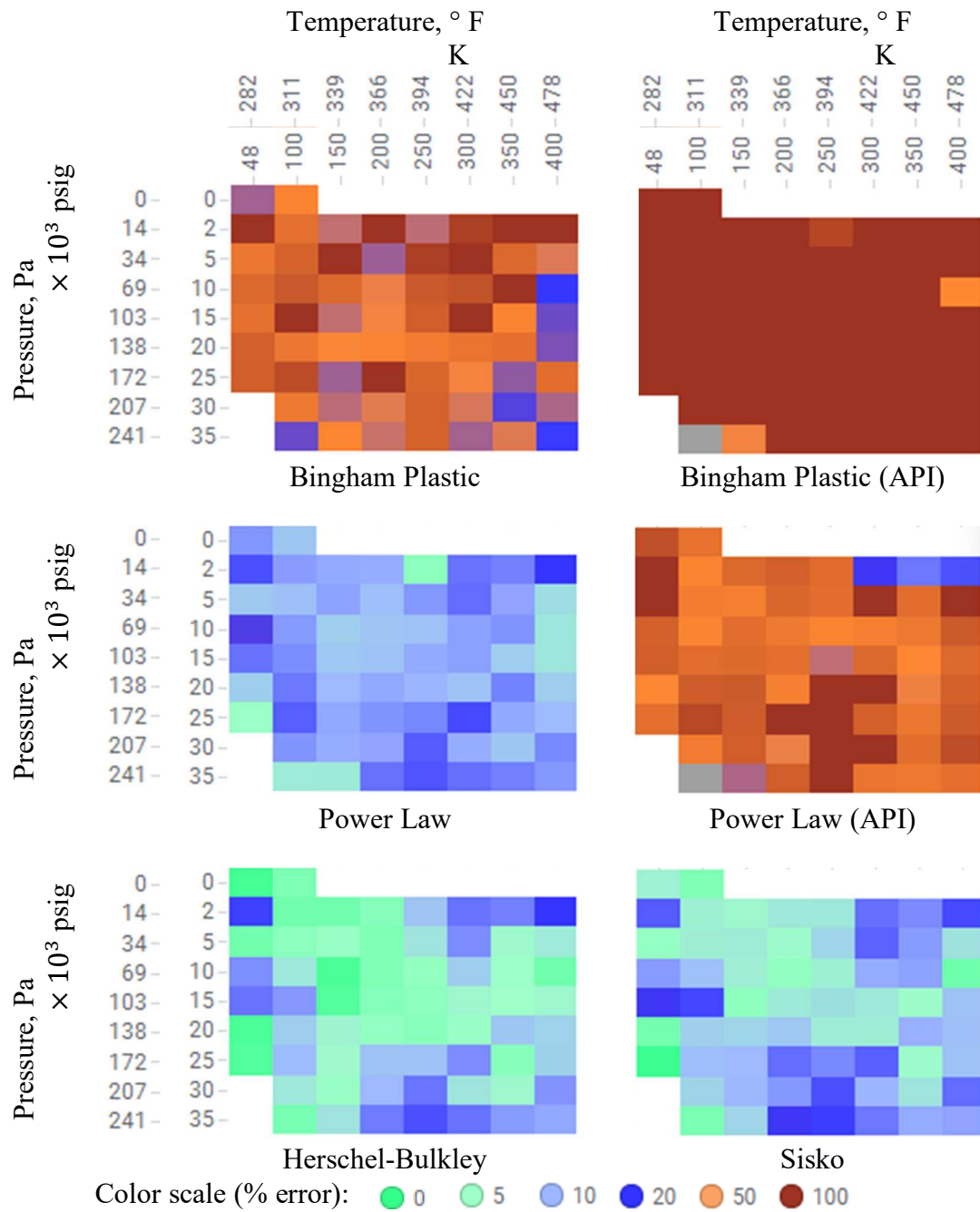


Figure 3.3 Heat map of average $\bar{\epsilon}_{r,a}$ at low shear rates, and different pressures and temperatures.

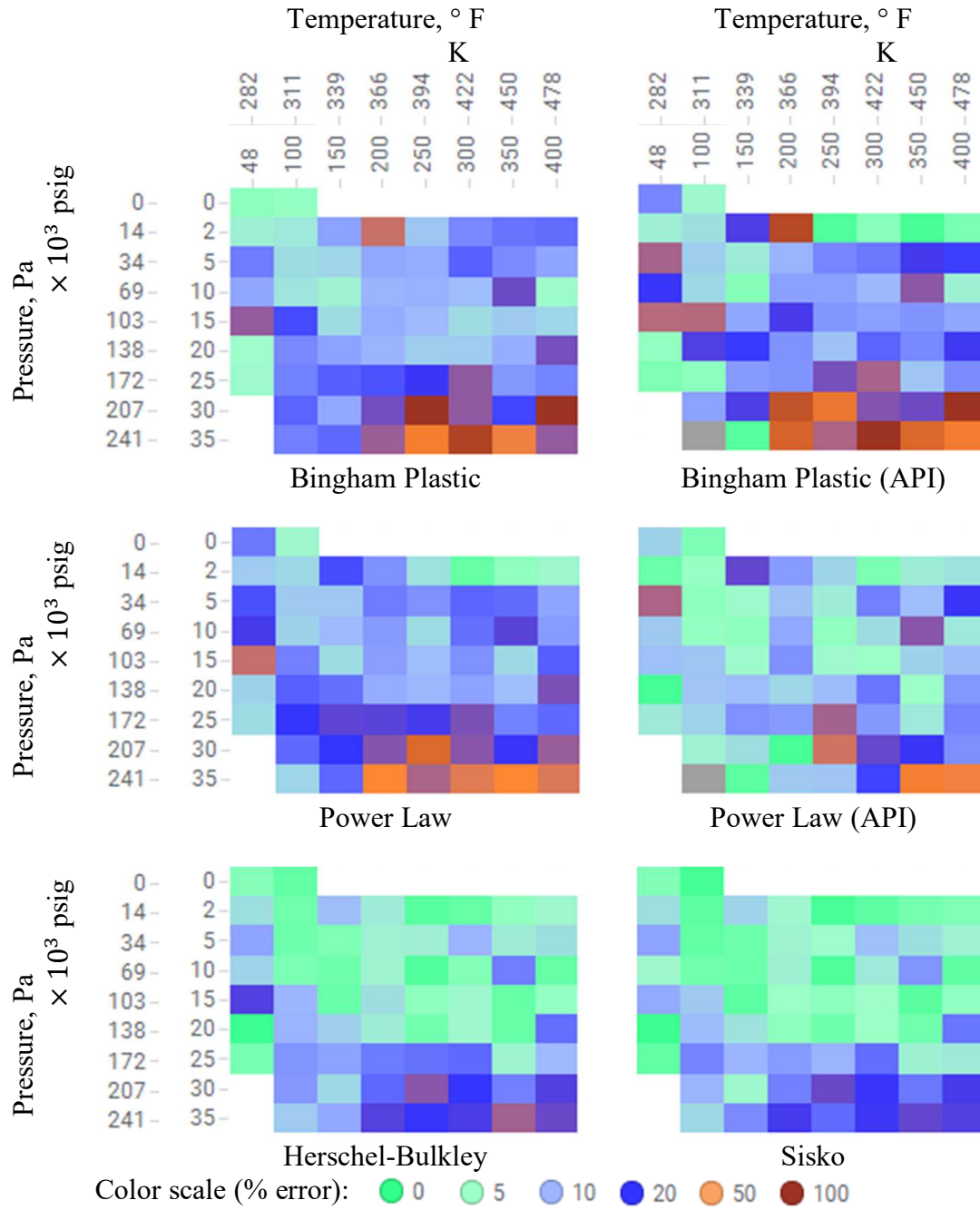


Figure 3.4 Heat map of average $\bar{\epsilon}_{r,a}$ at high shear rates, and different pressures and temperatures.

The heat maps show us that, despite the overall poor fit-quality of the BP, BPAPI, and PLAPI models, they actually perform well in the high-shear zone at low-to-intermediate pressures (up to 69MPa, or 10,000 psi) and temperatures below 394 K (250 °F), as seen in Figure 3.4. Since rheological tests are regularly run at standard conditions, it is only understandable why the BPAPI and PLAPI models are so commonly used. The performance of BPAPI, however, rapidly decline as pressure and temperature increase, with the model providing very poor fits above 172 MPa (25,000 psig). The PL model has a moderate performance, but the heat maps from both Figures 3.3 and 3.4 clearly show the superior fit-quality provided by the HB and Sisko models. For these models, moderate-to-poor performance is only noticed at extreme high pressures (above 207 MPA, or 30,000 psig). This, however, is due in part to drilling fluids failure during tests in these extreme conditions. Failures are indicated by an unexpected change in drilling fluid behavior, and it is exemplified in Figure 3.5 below, which plots the shear stresses obtained from sample SBM_s1 at 477.6 K (400 °F).

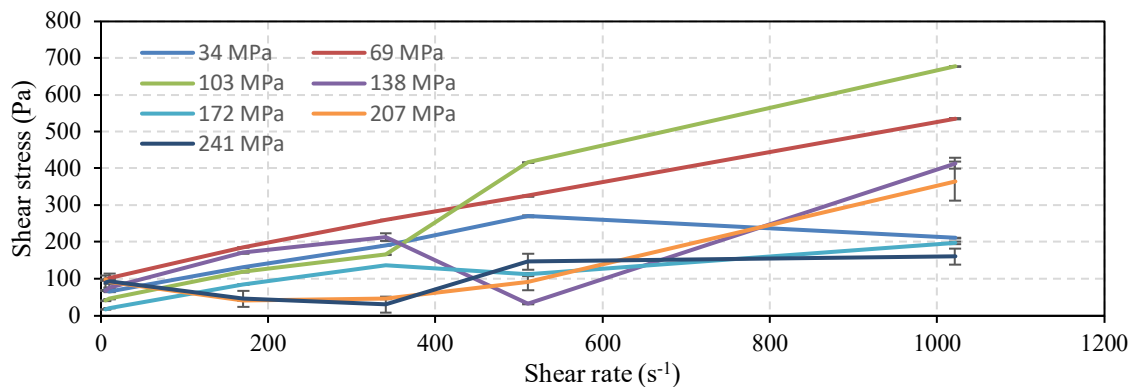


Figure 3.5 Drilling fluid failure example.

In Figure 3.5 the first sign of failure starts at the lowest pressure (34 MPa, or 5,000 psig), where shear-stress reading falls drastically at 1021.4 s^{-1} . In fact, the only test at 477.6 K that generates data corresponding to a typical behavior of drilling fluids takes place at 69 MPa (10,000 psig). At higher pressures the rheological behavior of the drilling fluid has a different nature. It was noticed that, during failure, the shear stress drops to a minimum at an intermediate shear rate between 170.2 and 510.7 s^{-1} (100 and 300 RPM). After that minimum, shear stresses increase again, resulting in a concave curve.

Given the performance of all tests, we estimate that the HB model is the most suitable to fit experimental data from HPHT tests. While its use is not as straightforward as the BPAPI or PLAPI, it is relatively easy to implement a routine to calculate its parameters using the flow chart from Figure 2.2. The Sisko model also provides a good fit to HPHT rheology data, but this model has the disadvantage that its parameters lack physical meaning. For these reasons, we recommend HB as the most appropriate rheological model to characterize HPHT drilling fluids.

3.1.1.1. Modeling Rheology of Contaminated Drilling Fluids in HPHT

The discussion introduced in Section 3.1.1 only concerns the 238 uncontaminated samples. In this section, we present a similar analysis, but looking at the 250 contaminated drilling fluid samples. Figure 3.6 shows the mean absolute relative error distribution for all six models in the low- and high-shear zones.

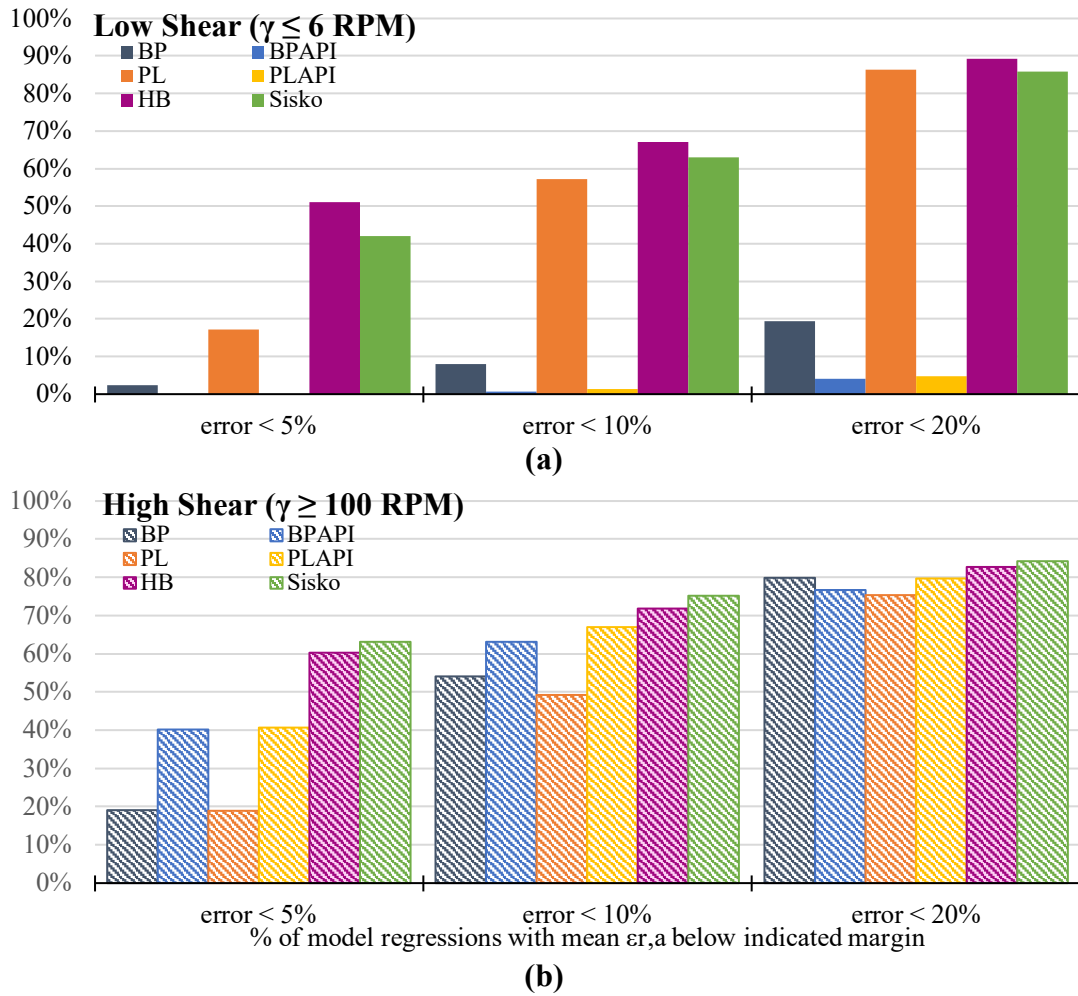


Figure 3.6 Relative number of model regressions for gas-cut muds with mean absolute relative error within 5, 10, and 20% divided into (a) low- and (b) high-shear zones.

The performance of the models is similar to what was observed in Section 3.1.1. Most models perform well in the high-shear zone, but only the HB and Sisko models deliver acceptable fits in the lower-shear range. In the contaminated fluid cases, however, HB is the only model able to fit at least 50% of all tests within any desired performance mark; hence strengthening the case for HB as the universal rheological model for HPHT drilling fluids.

3.1.2. The Rheological Behavior of Contaminated Drilling Fluids in HPHT

The impact of formation-fluid in the rheology of drilling fluids was evaluated by injecting butane following the procedure described in Section 2.1.4. Due to an operational mistake, one of the SBM samples was contaminated with diesel fuel. This kind of contamination was not in the original scope of this work, but given our limited access to drilling fluids and a general interest in understanding every possible aspect of drilling fluid behavior, we carried out the rheological test of that mud nonetheless. Furthermore, a failure in the data acquisition system during the first injection resulted in an unknown amount of butane being injected into an OBM1 mud sample. Table 3.3 summarizes the contamination levels used in this study.

As it is described in Section 2.1.4, the butane contamination takes place by forcing liquified butane into the unpressurized test vessel where the drilling fluid sample is confined. Thus, injection is limited by solubility of liquid butane in the drilling fluid being tested, which itself is a function of pressure and temperature. Since the butane source is at relatively low pressure – 207 kPa (15 psig) – the amount of butane we were able to inject varied between 0.23 and 0.99 % by weight. These numbers are not very different from the contamination levels used in Torsvik, Myrseth, and Linga (2015), and Torsvik, Skogestad, and Linga (2017), which vary from 0.35 to 5.81 %.

Fluid	Contaminant	Sample name	Mass of contaminant, g	Level of contamination by mass, %
OBM1	Butane	OBM1_gas	N/A ^(a)	N/A ^(a)
OBM2	Butane	OBM2_gas	1.19	0.32
SBM	Butane	SBM_s2_gas	3.75	0.99
SBM	Diesel	SBM_contam	-	12.7 ^(b)
Base fluid of OBM1	Butane	bfOBM1_gas	0.69	0.26
Base fluid of OBM2	Butane	bfOBM2_gas	0.61	0.23
Base fluid of SBM	Butane	bfSBM_gas	2.35	0.94

a: Data acquisition system failure

b: Estimated value based on retort test results

Table 3.3 Summary of contamination level of each drilling fluid sample tested.

Even with low levels of contamination, the presence of butane impacted the rheological properties of the muds. The SBM and OBM2 were the most affected by the presence of gas. Figure 3.7 shows a side-by-side comparison of the shear stress measurements done under the same conditions between an uncontaminated SBM sample (SBM_s1), and a contaminated (or gas-cut) mud (sample SBM_s1_gas). The general trend observed in Figure 3.7 shows a consistent reduction of shear stress measurements. In order to compare how shear stresses are affected by butane as a mud-contaminant, we need to define performance parameters. Since the plastic viscosity and yield stress are easily calculated with the BPAPI model, these numbers are generally used to compare rheological behavior of different drilling fluids. As we established before, though, the

BPAPI is not a good model for HPHT rheological characterization, and, thus, a new set of parameters must be defined.

Here, we will introduce a new concept, analogous to the Bingham plastic viscosity, but derived for the Herschel-Bulkley model. This new parameter, which we will call the Herschel-Bulkley characteristic viscosity (μ_{HB}) is defined as the slope of the shear stress curve against shear-rate evaluated at the mid-point between the two highest shear rates, that is, at 766 s^{-1} (450 RPM). The Herschel-Bulkley characteristic viscosity is given by Eq. 3.4

$$\mu_{HB} = \left. \frac{\partial \tau}{\partial \dot{\gamma}} \right|_{\dot{\gamma}=766} = n_{HB} K_{HB} (766)^{n_{HB}-1}. \quad (3.4)$$

This parameter expresses how the fluid shear stress change as a function of shear rate. While its value is only valid for where it is evaluated (766 s^{-1}), it is used as a representative value for the entire high-shear zone. The Herschel-Bulkley model, unlike the Power Law or Sisko models, also has the advantage of providing us a yield stress (τ_S), which can itself be used as a parameter to compare rheological behavior of muds.

Using τ_S and μ_{HB} as comparison parameters, we notice an average reduction of 14 % in the characteristic viscosity between samples SBM_s1 and SBM_s1_gas (Figure 3.7). This reduction is consistent across most pressures and temperatures and no clear trend was noticed, except at 478 K (400 °F). At this temperature, μ_{HB} could not be computed for most of the contaminated mud tests due to fluid failure for pressures greater than 103.5 MPa (15,000 psig).

Yield stress is also reduced on the gas-cut mud, but by the more significant factor of 30 %. As it was the case before, the yield stress reduction at 478 K is more significant than in the other temperatures by at least 2.5 times, averaging a yield stress reduction of 76%. Due to limited number of samples available, a thorough statistical analysis could not be carried here. These results, thus, are only individual observations and cannot be considered as the expected behavior of gas-cut drilling fluids. In fact, a reduction in shear stress was already expected since the viscosity of butane is several orders of magnitude smaller than that of the mud itself.

The OBM2 sample, however, did not always behave as expected. Figure 3.8 shows that up to the temperature of 422 K (300 °F), the gas-cut mud sample presented an average reduction in μ_{HB} of 41 %, but in this case, there is a trend implying that this reduction becomes more significant as pressure increases. As it can be seen in Figure 3.9, the trend indicates that no significant reduction happens up to 69 MPa (10,000 psig), but it increases beyond that up to 207 MPa (30,000 psig), where it seems to approach 100 %. Contrary to what happened with the SBM samples, the yield stress behavior is not clear. Up to 422 K, the τ_s of the contaminated mud reaches several times its original value at lower pressures. This is reversed as the pressure increases, as between 104 and 138 MPa (15,000 and 20,000 psig) the yield stress values of the gas-cut mud fall below that of the uncontaminated sample. This change is too small to be noticed in Figure 3.8, but the differences in yield stress are up to 10 times greater than the uncertainty of the measurements, which allows us to conclude that the presence of butane alters the behavior of OBM2 at low shear rates by a statistically meaningful amount .

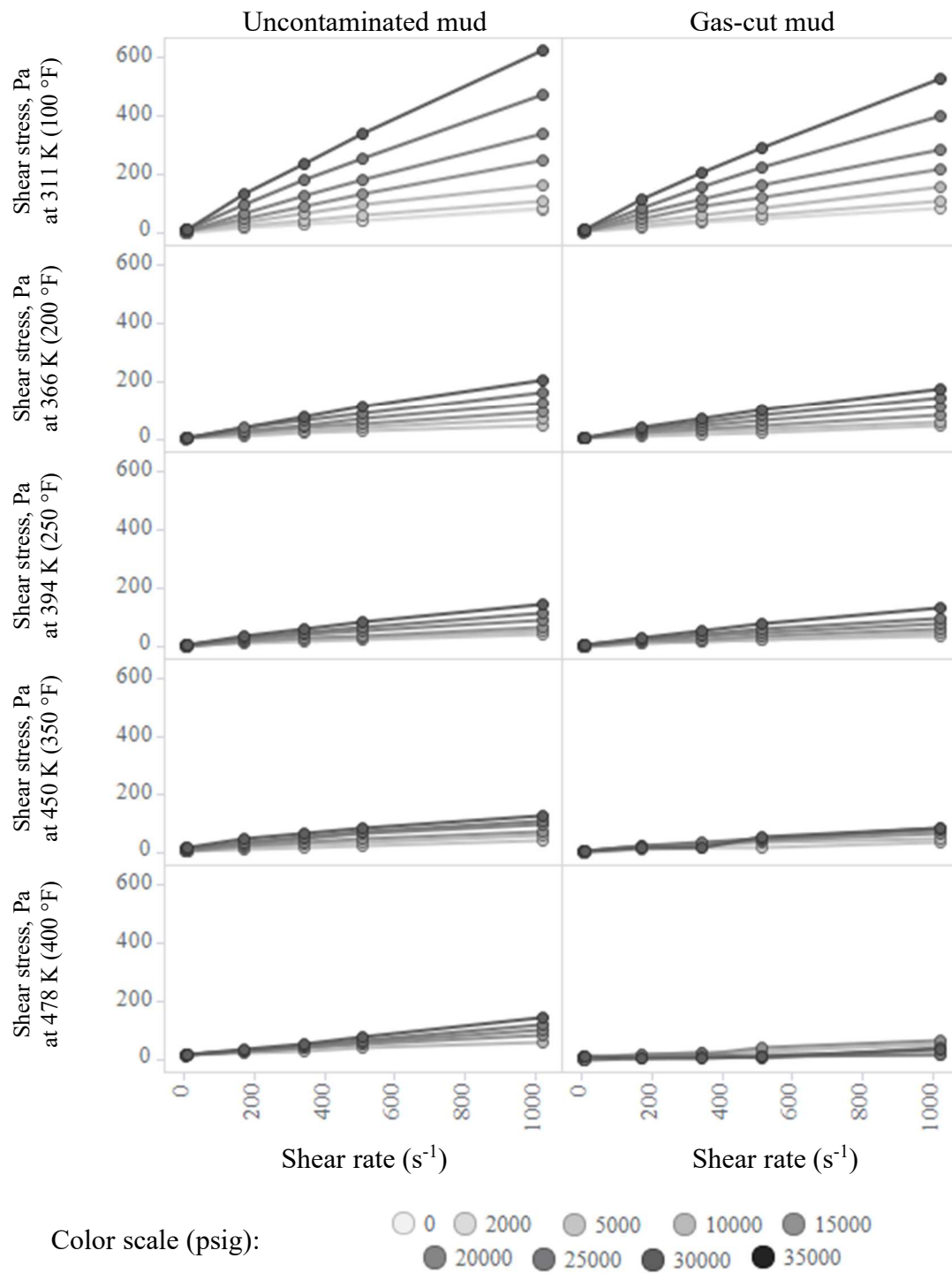


Figure 3.7 Shear stresses of uncontaminated and gas-cut samples of the same drilling fluid (SBM_s1 and SBM_s1_gas).

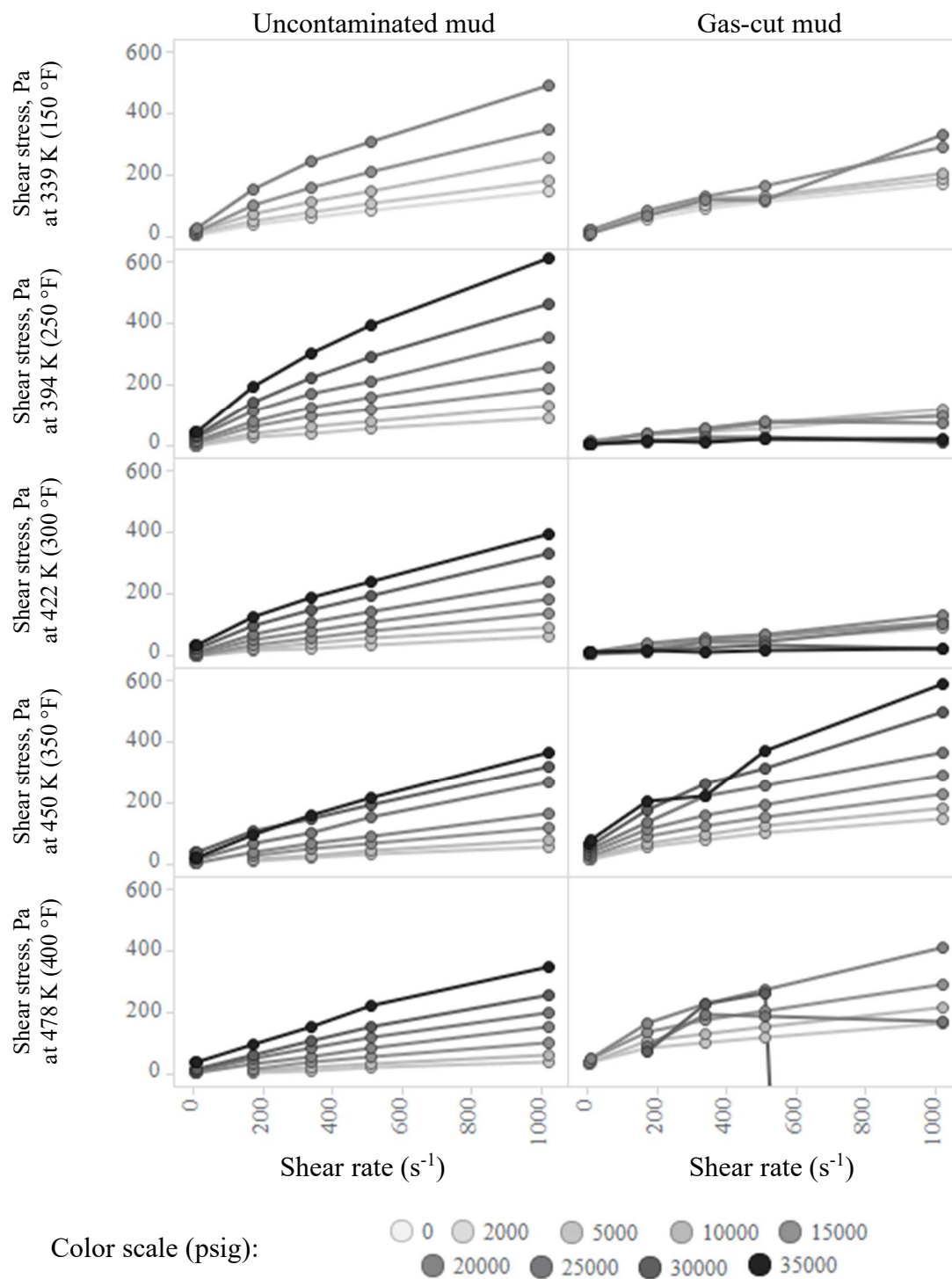


Figure 3.8 Shear stresses of uncontaminated and gas-cut samples of the same drilling fluid (OBM2_s1 and OBM2_s1_gas).

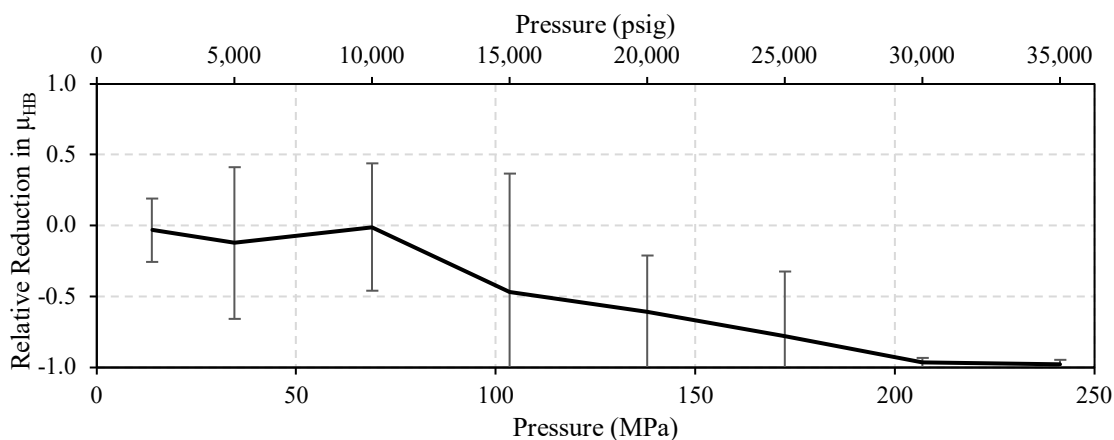


Figure 3.9 Average relative reduction of the Herschel-Bulkley characteristic viscosity as a function of pressure for temperatures varying from 310 to 422 K (100 to 300 °F). The vertical bars indicate the 95 % confidence interval from the measurement uncertainty.

The most striking feature in Figure 3.8 though are the plots of shear stresses at 450 and 478 K (350 and 400 °F). At these temperatures, we see a substantial increase in both the characteristic viscosities and the yield stresses, negating all observations and trends noticed before. This counterintuitive behavior may be partially explained by the phase-behavior of butane, plotted in Figure 3.10.

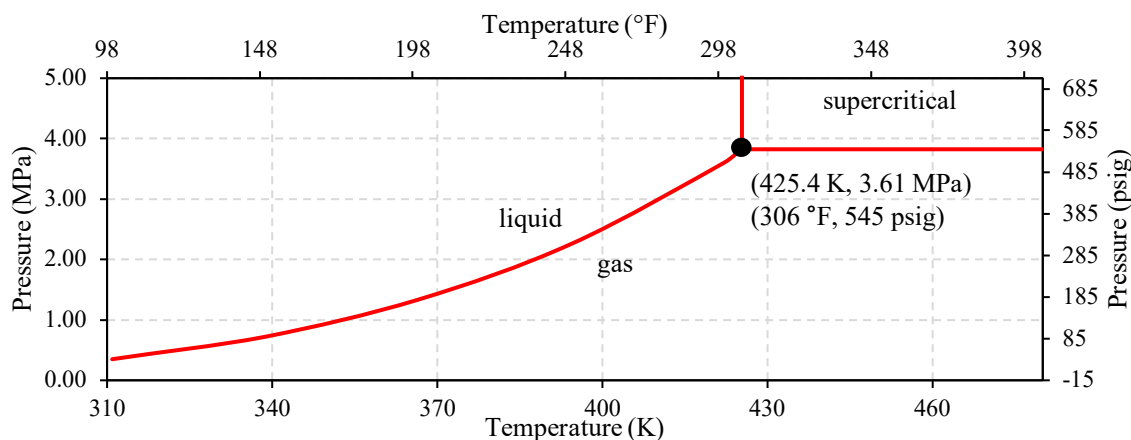


Figure 3.10 Phase diagram of butane.

As indicated by the curve, butane is in its supercritical state above 3.6 MPa and 425 K. Thus, at all test conditions, butane is in its liquid state, except when we reach these temperatures. This could also help explain why we see early failures at those same temperatures with the SBM sample.

In fact, the most important difference between contaminated and uncontaminated muds is that fluid failure tends to occur sooner in the presence of butane. With OBM1_s1, the only observed failure happens at 311 K (100 °F) and 172 MPa (25,000 psig). Once butane is injected, failure also at 339 K (150 °F) and 207 MPa (30,000 psig). Table 3.4 summarizes all observed failures and show how the injection of butane interfered with the expected behavior of the mud.

Mud	Uncontaminated	Contaminated
OBM1	311 K, 172 MPa	311 K, 172 MPa 339 K, 207 MPa
OBM2	311 K, 138 MPa	311 K, 103 MPa 339 K, 138 MPa 366 K, 138 MPa 394 K, 138 MPa 422 K, 172 MPa 450 K, 241 MPa 478 K, 172 MPa
SBM	-	450 K, 207 MPa 478 K, 34.6 MPa

Table 3.4 List of shear stress test failures for different muds.

The effects of butane in the different mud samples, however, is not reflected on the behavior of their respective base-fluids. Figure 3.11 shows an example of that by comparing the shear stresses from the uncontaminated and contaminated base-fluid of the synthetic-based mud (i.e., samples bfSBM and bfSBM_gas, respectively).

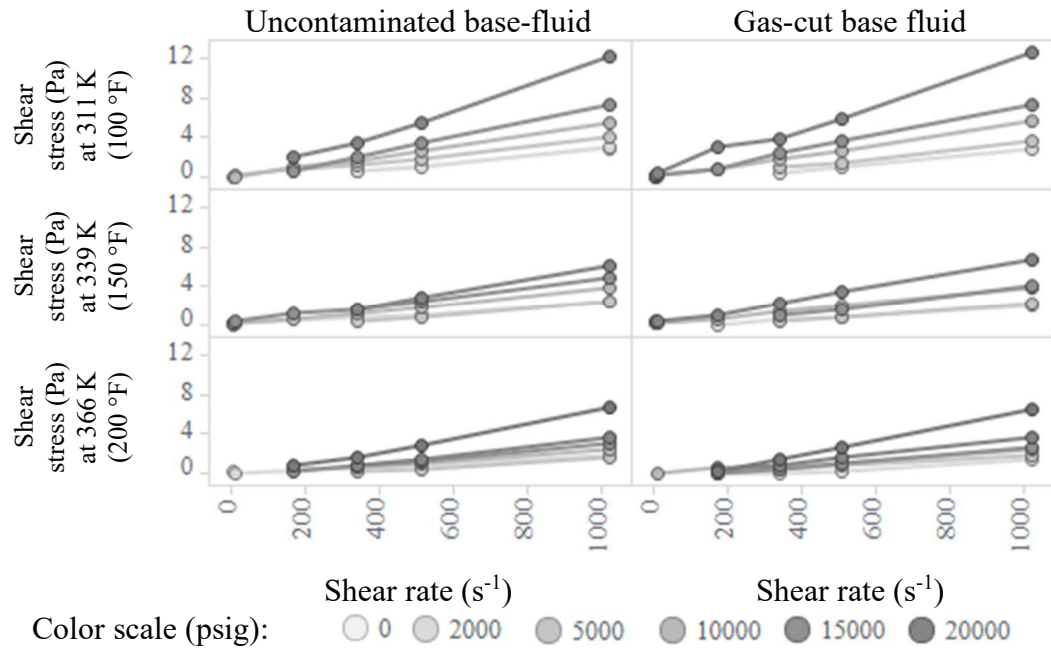


Figure 3.11 Shear stresses of uncontaminated and gas-cut synthetic oil (samples bfSBM and bfSBM_gas).

In the range of temperatures tested, the presence of butane had no significant effect on the characteristic viscosity of the base-fluids. Due to erratic measurements in the low-shear zone, an analysis on how butane impacts the yield stresses of base-fluids could not be done (all measurements uncertainties are given in Appendix B).

3.1.2.1. Diesel Contamination

As mentioned before, the contamination by diesel was due to an operational error. We used diesel as pressurizing agent instead of water when running the first set of tests with the SBM. The mistake, however, gave us the opportunity to look at two different issues and quantify them in a meaningful way.

The first, and more obvious, problem we were able to assess is the effect of diesel as a contaminant. If we think of diesel fuel as an analogue of liquid hydrocarbon influxes from formations, we can see that its presence has a great impact in the plastic viscosity. At lower temperatures, the absolute change in the shear stress slope is greater, as it can be seen in Figure 3.12, but at higher temperatures, the relative drop is even more significant, with μ_{HB} being reduced by more than 60% at 450 K (350 °F) and 207 MPa (30,000 psig). It is also important to mention that the introduction of diesel in the mud seems to have caused sagging, or facilitated separation of the liquid and solid phases. This was noticed after running a retort test (API 2019). We collected a 10 mL sample from the top of the test vessel and after submitting it to the retort equipment, the mass of solids had dropped by nearly 50.3 % from the same sample before test started. The maximal reduction in solid contents from the other uncontaminated tests was less than 12 %. The level of contamination by diesel was deduced by the volume of liquid recovered from the retort test. We saw an increase of 28 % in the recovered liquid content, which corresponds to the introduction of 12.7 % of diesel by weight.

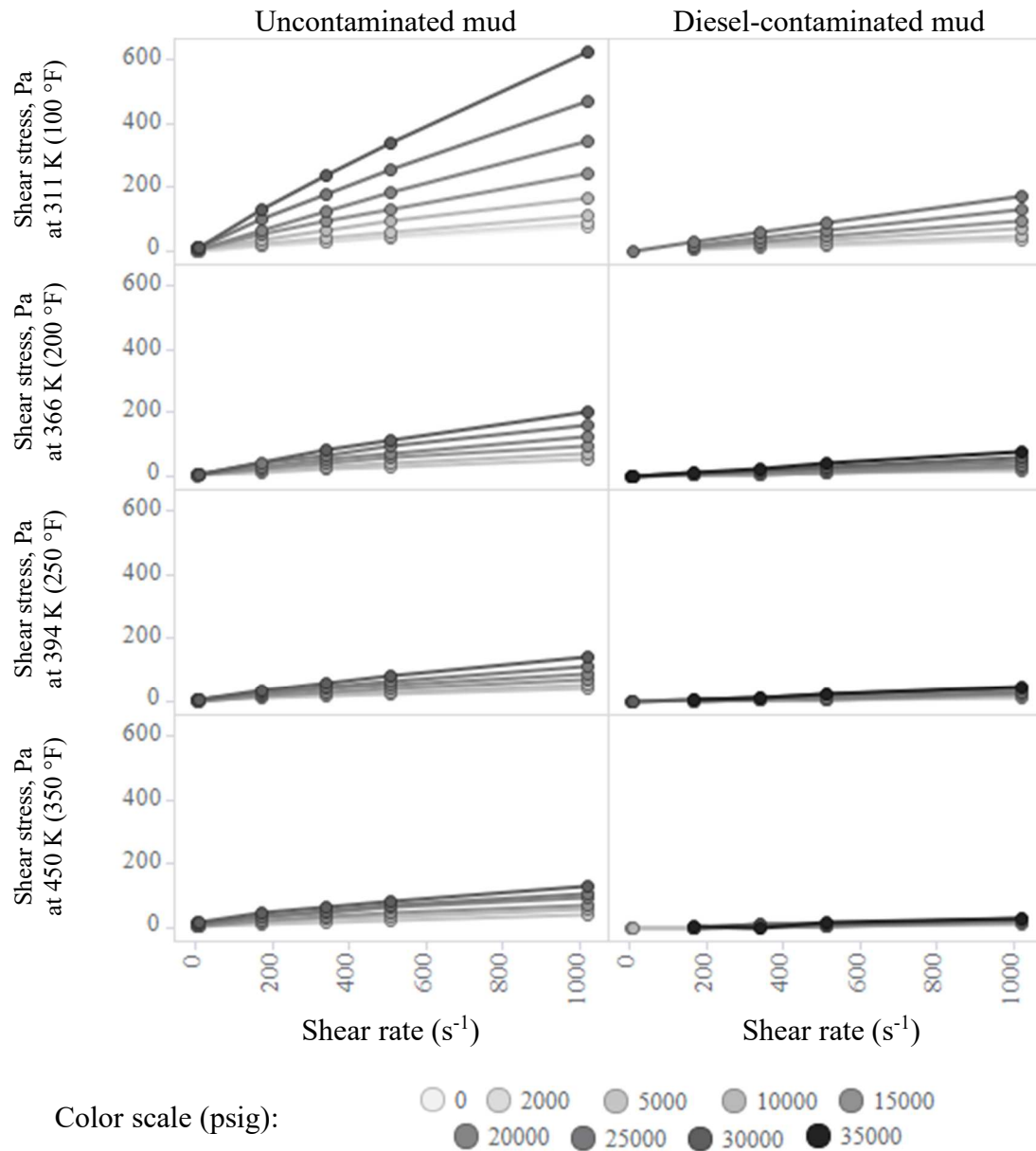


Figure 3.12 Shear stresses of uncontaminated and diesel-contaminated SBM samples (SBM_s1 and SBM_contam).

This brings us to our second problem. As explained in Section 2.1.2.1, one of the modifications in the test procedure introduced by this work concerns the use of different pressurizing fluids depending on what type of drilling fluid will be analyzed. In the

original equipment setup, the pressurizing fluid is the hydraulic oil used by the high-pressure pump, and it gets in direct contact with the test sample, similar to what happened with the diesel contamination incident. However, by using water as the pressurizing fluid and physically isolating it from the hydraulic oil, we minimized the contamination of the sample. Running retort tests on samples after the viscosity tests, we saw a max contamination of 2.1 % of water by weight. The sample size we dispose is statistically insignificant; however, given the differences in shear stress measurements and the retort analysis, we can conclude that our physical modifications to the viscometer has reduced the contamination of the test sample by the pressurizing fluid.

3.1.3. The Impact of Proper Rheological Modeling in HPHT Drilling

Next, we present a brief study showing the impact of proper rheological modeling in the bottomhole pressure and drilling safety. We will estimate the frictional pressure loss in the horizontal section of a typical well in the Haynesville Shale Play based on the information below, provided in Billa et al. (2011):

1. TVD: 14,500 ft (4,420 m),
2. MD: 18,500 (5,639 m),
3. Pore pressure: 16.5 ppg (1,981 kg/m³),
4. Temperature: 360 °F (455 K), and
5. Horizontal section hole size: 6.5 in (0.1651 m).

Additional information necessary to run a reasonable scenario is taken from Schumacker and Vogelsberg (2019). Even though these authors are concerned with slim-hole well-design in the Permian Basin, their discussion includes the selection of mud-

motors and drill pipes in similar hole sizes (6.25 to 6.75 in). From this discussion, we respectively infer the following additional information:

1. Circulation rate: 375 gpm (0.0236 m³/s), and
2. Drill string OD: 4.5 in (0.1143 m).

We calculate the frictional pressure drop in the horizontal section by first estimating the Reynolds number of the liquid flow with Eq. 3.5 (Economides et al. 2011),

$$Re = \frac{\rho_{\text{mud}} u_{\text{mud}} D_h}{\mu_{\text{mud}}^{(a)}}, \quad (3.5)$$

where ρ_{mud} is the density of the mud, u_{mud} is the velocity of the flow in the annular region, $\mu_{\text{mud}}^{(a)}$ is the apparent viscosity of the mud at the current velocity, and D_h is the hydraulic diameter, defined as Eq. 3.6,

$$D_h = D_o - D_i. \quad (3.6)$$

The apparent viscosity is calculated with Eq. 3.7,

$$\mu_{\text{mud}}^{(a)} = \frac{\tau(\dot{\gamma})}{\dot{\gamma}}, \quad (3.7)$$

where $\tau(\dot{\gamma})$ is the shear stress as calculated by the chosen rheological model, and the shear rate is calculated with Eq. 3.8 (Caenn, Darley, and Gray 2017),

$$\dot{\gamma} = 2.4 \frac{u_{\text{mud}}}{D_h}, \quad (3.8)$$

where u_{mud} is in ft/min, D_h is in inches, and $\dot{\gamma}$ is in s⁻¹.

Once Reynolds is properly calculated, we compute the frictional pressure gradient with Eq. 3.9 (Economides et al. 2011),

$$\left(\frac{\Delta p}{\Delta L}\right)_F = \frac{2f\rho_{\text{mud}}u_{\text{mud}}^2}{D_h}, \quad (3.9)$$

where f is the Fanning friction factor calculated with the Colebrook-White equation found in Economides et al. (2011).

With the information given above, we calculate the pressure in the horizontal section to be 12,430 psig, or 85.8 MPa, with a total length of 4,000 ft, or 102 m. We then use the rheological models for drilling fluids OBM2 and SBM at 450 K (350 °F) and pressures of 68.9 and 103.4 MPa (10,000 and 15,000 psig) to quantify the error between all rheological models in relation to HB. We did not compute the difference between the Sisko and HB models since they deliver very similar results, as discussed in the previous paragraphs of this Section.

Table 3.5 summarizes the results of this simulation, where the sign (-) designates an underestimation and (+) an overestimation. As it can be noticed, the pressure differences are small and negligible; however, this is due to coincidental circumstances, where all models give similar data-fits in the operating range inferred from the works of Billa et al. (2011) and Schumacker and Vogelsberg (2019).

Pressure	Pressure Difference by Model, kPa (psig)			
	BP	BPAPI	PL	PLAPI
68.9 MPa (10,000 psig)	+14.5 (+2.1)	+14.5 (+2.1)	+39.3 (+5.7)	+78.6 (+11.4)
103.4 MPa (15,000 psig)	-114 (-16.5)	-114 (-16.5)	0.0	+15.8 (+2.5)

Table 3.5 Pressure difference between Herschel-Bulkley and other rheological models.

If we keep the well geometry as is, but change the bottomhole pressure and temperature, the maximum error grows significantly. Table 3.6 shows the max errors seen with each model and indicates at which conditions those errors happen.

Mud	Model	Max difference, MPa (psig)	Pressure, MPa (psig)	Temperature, K (°F)
OBM2	BP	-1.7 (-255)	241 (35,000)	394 (250)
	BPAPI	-0.76 (-111)	138 (20,000)	339 (150)
	PL	-0.21 (-30.0)	104 (15,000)	311 (100)
	PLAPI	+1.2 (+167)	241 (35,000)	477 (400)
SBM	BP	-0.76 (-110)	207 (30,000)	311 (100)
	BPAPI	-0.38 (-55.7)	207 (30,000)	311 (100)
	PL	-0.22 (-31.4)	172 (25,000)	311 (100)
	PLAPI	+0.15 (+21.8)	172 (25,000)	450 (350)

Table 3.6 Max pressure differences between Herschel-Bulkley and other rheological models for all pressure and temperature combinations.

Some of the errors shown in Table 3.6 are important and may cause well control problems, especially if drilling in a narrow window between pore- and fracture-pressures. Small changes in well geometry and pumps rates, may also aggravate the problem. For instance, in the original simulation scenario, from the 272 simulations, 16 resulted in errors larger than 689.4 kPa (100 psi), and 49 had errors greater than 344.7 kPa (50 psi). Just by slowing down the pumps to 200 gpm and changing the drillstring to 4-in pipes instead of 4.5-in, those errors mounted to 20 and 68, respectively.

3.2. Slugless Domain in Annular Spaces

The first step towards defining the slugless annular space is to validate the experimental setup. A series of experiments using the pipe flow loop described in Section 2.2.1 serves as proof-of-concept that the slugless flow domain in pipes (Section 1.4.2) can be achieved in reduced, lab-scale tests. Once we demonstrate the flow loop can be used as an analogue to represent flow conditions in the field, we proceed with our goal to define and characterize slugless flow domain in annular spaces.

In the next paragraphs, we will detail the experimental results in the validation and investigation procedures. The acquired data is listed in Appendix C.

3.2.1. Proof of Concept

Capovilla et al. (2019) compared different models for slugless flow domain in pipes against experimental data and concluded that the drift-flux model of Schlegel, Hibiki, and Ishii (2010) delivers the most accurate results. Using this model as a benchmark, we compared the liquid holdup measurements obtained from the pipe flow loop tests with the model predictions and the results are plotted in Figure 3.13.

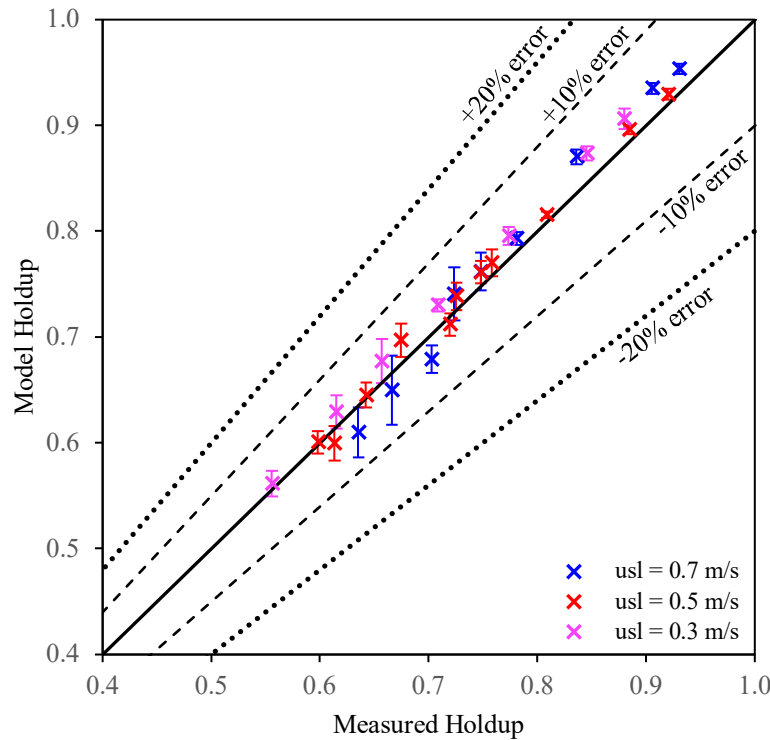


Figure 3.13 Comparison between holdup calculated with the Schlegel, Hibiki, and Ishii (2010) model versus the measured holdup.

The model and experimental setup show a remarkable agreement with 100 % of the data falling within the ± 10 % error band. Given the high level of agreement between experimental data and model, we considered the lab-scale flow loop flowing soybean oil and air as representative of field dimensions for superficial liquid velocities greater between 0.3 and 0.7 m/s (1.0 and 2.3 ft/sec), allowing us to proceed with our investigation of slugless flow domain in annular spaces.

3.2.2. Annulus Flow Loop

The original test matrix for this series of experiments is defined in Section 2.2.2. The experimental program is comprised of five different annular geometries, which will

be referred to as 77.3-by-XX.X, where 77.3 is the inner diameter of the outer pipe, and XX.X is the outer diameter of the inner pipe, both in millimeters. Each unique geometry was then tested in concentric and eccentric forms, resulting in 10 datasets. These datasets map only a small area of flow regimes, but of particular interest for drilling operations. A series of issues were faced during the execution of the experimental program, which are detailed below.

By introducing the different inner pipes to create the annular space, we significantly reduce the flow area and, therefore, increase the superficial velocities of the fluids at a rate proportional to the square of the equivalent radius. This made it hard to establish a steady liquid flow rate for the lower superficial velocities. The centrifugal pump use did not perform well at low frequencies, causing a high variability in measurement, some as high as 70 %. For this reason, we decided to not use the data acquired at lower liquid velocities (0.1 and 0.3 m/s), and, thus, we will focus our work on the higher liquid superficial velocities, that is, 0.5 and 0.7 m/s. We also faced a problem with the differential pressure transducer used to measure the total pressure gradient in the test section. The pressure-drop between the intakes of the transducer exceeded the equipment capability for all tests with the 60.3 mm inner pipe, rendering the acquired data not particularly relevant to this work.

Nevertheless, we were still able to run and record data for 80 distinct tests, 20 per each of the four different annular spaces. Each annular space provides two datasets: one for concentric, and the other for fully eccentric pipes.

The dataset generated in this experimental work is validated against the data provided in Caetano, Shoham, and Brill (1992b). One of the cases presented in this work has a very similar geometry to one of our setups: it consists of a 77.3 mm outer diameter and a 42.2 mm inner diameter annular space in concentric configuration running air and kerosene through a 13.7 m flow loop. We decided to use this example as a benchmark because Kerosene has a similar surface tension to soybean oil, and also because the flow is developed in a much longer test section. The holdup measurements are compared in Figure 3.14 below.

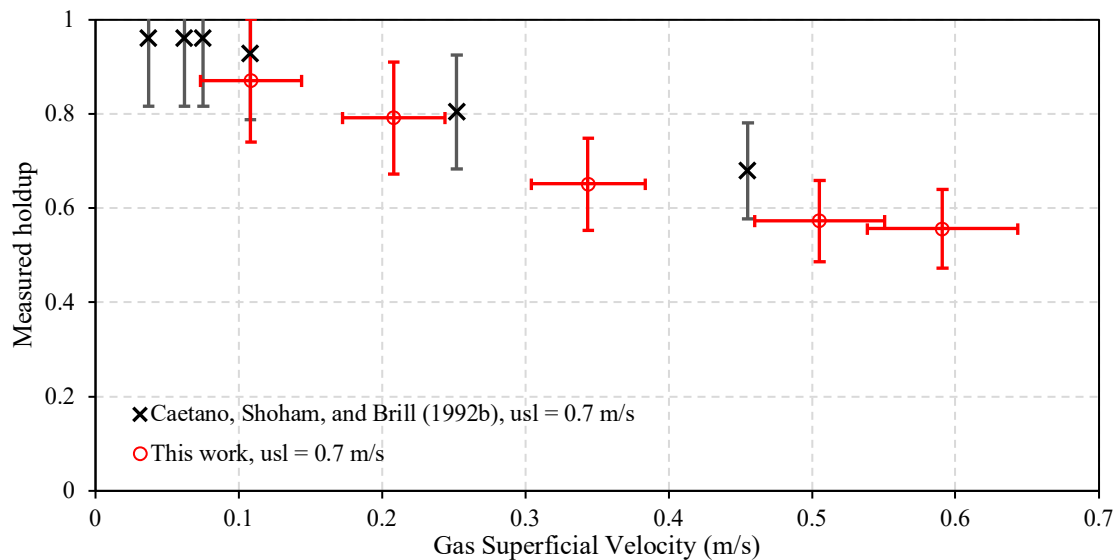


Figure 3.14 Comparison between data generated for this work and the work of Caetano, Shoham, and Brill (1992b). Vertical bars represent 15 % error, horizontal bars represent the 95% confidence interval of measurement uncertainty.

As it can be seen in the plot above, the holdup measurements agree well within a 15 % error margin (vertical bars). The horizontal bars are the air velocity measurement

uncertainty, assuming a 95 % confidence interval. While this is not a definite proof that our pipe length (2 m) is representative of the fully-developed flow, it indicates that our findings can replicate the results of a much longer test section within an uncertainty margin of 15 %.

With that in mind, we start our exploration of the slugless domain in upward, two-phase flow in annular spaces by analyzing the observed flow patterns. Even though we considered the acquired data from the low liquid velocities (0.1 and 0.3 m/s) or 77.3- by-60.3 annular space as unreliable, the visual observations are still valid, and will be used in our flow regime descriptions.

3.2.2.1. Observed Flow Regimes and Their Characteristics

The dimensions of the inner pipes used in this work were carefully chosen to provide a wide understanding on how flow regimes at low gas-superficial velocities change depending on the geometry of the annular space.

1. Cap-bubble. Large bubbles migrate upwards at higher velocity than smaller bubbles. These large bubbles are the result of smaller ones coalescing. As the bubble grows, it moves upwards faster, but its growth is limited by either the stability of the bubble, or the annular space dimension. In a concentric configuration, the cap bubbles are even distributed in the annular space; however, in eccentric form, the cap-bubbles tend to occupy the large gap between pipes, whereas a larger amount of smaller bubbles will concentrate in the small channel formed around the contact between pipes. In Figure 3.15 we can see on the right

side of the picture a large and elongated bubble that collapses before it can wrap itself around the inner pipe. On the left side of Figure 3.15 we see small, round bubbles concentrated around the region where both pipes touch. Figure 3.16a and d show a cap-bubble flow in the same annular space (77.3-by-42.2) in its concentric and eccentric configurations respectively.

2. Slug. In an annular space, defining slug flow can be challenging due to the lack of symmetry. Caetano, Shoham, and Brill (1992a) give a clear description of what slug flow is in both concentric and eccentric configurations, which is exemplified by Figure 1.3. Here we provide an example of slug flow in concentric annular spaces by showing the “front” side Taylor in Figure 3.16b-1. At the bottom part of Figure 3.16b-2, we see the back side of the Taylor bubble and the preferential channel through which the liquid flows downwards as the bubble migrates upwards.
3. Churn. An increasing gas flow rate will cause the formation of very large and elongated bubbles that migrate upwards in a chaotic motion. Liquid slugs are seen periodically (but not at a regular pace), but they are destroyed by large gas bubbles. Once these liquid slugs are destroyed, the fall back and accumulate, reinitiating the upwards motion, only to be broken one more time by the next ascending gas pocket. Figure 3.16c shows the collapsed liquid slug moving downwards in a concentric

annulus, whereas Figure 3.16f shows the large gas bubble breaking through the liquid slug in the same annular geometry, but in its eccentric form. In concentric configuration, the chaotic flow takes place evenly around the inner pipe, but in eccentric annulus, the gas concentrates where the gap is larger. The region close to where the pipes touch has a high liquid concentration.

4. Cap-bubble-to-slug transition. It is easier to identify slug flow – as described in Caetano, Shoham, and Brill (1992a) – in annular spaces where the gap between the outer and inner pipe is small. Once the gap starts to become significant, the Taylor bubble becomes unstable and collapses back to smaller cap-bubble. The cap bubbles then keep migrating upwards and coalesce along the way only to form another Taylor bubble, which will collapse again, repeating the cycle. An example of this behavior is seen in Figure 3.16e-1 where a small Taylor bubble is migrating up, but then suddenly collapses into smaller cap-bubbles as seen in Figure 3.16e-2.
5. Cap-bubble-to-churn transition. The transition between cap-bubble and churn happens in large annular spaces, as the maximum size of the bubbles is restricted by its stability. In these conditions, the cap-bubble flow regime (Figure 3.17a) is interrupted by periodic gas-pockets traveling at higher speeds (Figure 3.17b).

6. Slug-to-churn transition. As the gas flow rate increases, the gas concentration in the liquid slug between Taylor bubbles increases as well. This sometimes leads to the liquid slug being bridged by the gas bubble below resulting in a localized churn-like flow.

Classifying flow regimes is, ultimately, subjective as it gives margin to interpretation, but by giving detailed description of each flow pattern, we expect to have as little variation as possible. Thus, using the flow pattern description given above, we classified each one of the 170 tests to generate flow regime maps for each annular space in their concentric and eccentric configurations. The maps are plotted in Figure 3.18. In addition to classifying the flow regimes, we also established boundaries where transition between flow patterns take place. These are indicated by the transparent lines in the plots.



Figure 3.15 Eccentric 77.3-by-33.4 annulus showing a close-up of typical cap-bubble flow structure.

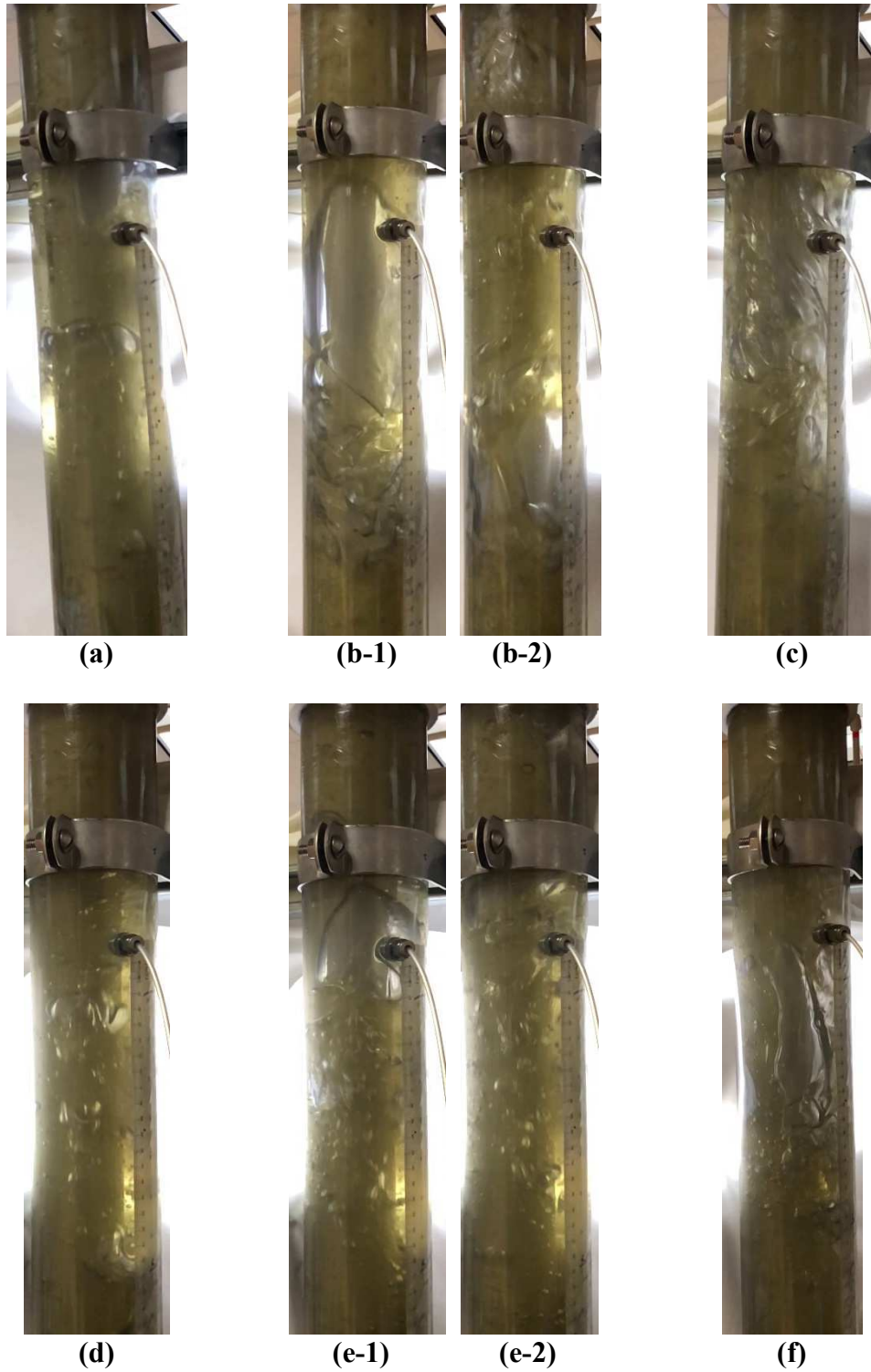


Figure 3.16 Flow regimes observed with the 77.3-by-42.2 mm annulus in concentric (a, b, and c), and eccentric (d, e, and f) configurations.

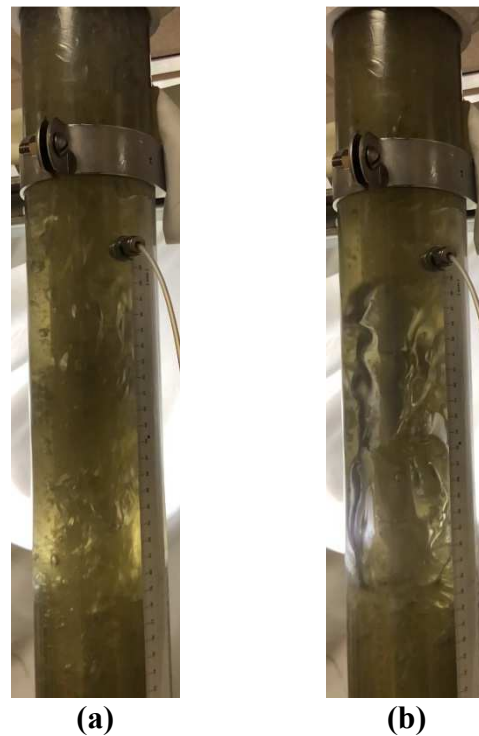


Figure 3.17 Concentric 77.3-by-33.4 showing cap-bubble-to-churn transition.

Figure 3.18 helps us understand the existence of slug flow in annular spaces. According to our interpretation of the observed flow regimes, no slug flow is seen in the 77.3-by-33.4 and 77.3-by-26.7 annuli in both concentric and eccentric configurations. On the opposite end, slug flow occurs in the 77.3-by-48.3 and 77.3-by-60.3 concentric and eccentric annuli. At the 77.3-by-42.2 annuli, however, a transitional behavior seems to take place as slug flow is seen in the concentric configuration, but not in the eccentric annulus. Some other observations are important in establishing a slugless domain, flow regime map in annular spaces.

First, we can see that the four flow regime maps in the slugless flow domain, that is, the 77.3-by-26.7 and 77.3-by-33.4 annuli in concentric and eccentric configurations, are virtually the same. For those four maps, the boundary between cap-bubble and churn is a nearly-vertical line located in the same place.

For the slug domain flow maps, we can see that as the annular space grows, the line separating the boundary between cap-bubble and slug moves closer to the line dividing slug and churn flows. In the eccentric case, this shift seems to happen more drastically, culminating in the 77.3-by-42.2 where a transitional flow state was observed and the two lines appear to be superimposed.

Since our goal is to define the boundary of the slugless flow domain in annular spaces with an expression analogous to Eq. 1.6, we computed the different dimensionless diameters (D^*) by replacing the pipe diameter in Eq. 1.6 with the characteristic diameters of annular spaces, namely the hydraulic, the equi-peripheral, and the equivalent diameters, expressed respectively by Eqs. 3.6 and 1.8, and the equation $D_{eq} = (D_o^2 - D_i^2)^{0.5}$, where D_{eq} represents the diameter of a circular area of equal size to the effective flow area in an annular space. Table 3.7 gives the results of the modified Eq. 1.6 for each annular geometry and different diameter definitions.

In the original work of Kataoka and Ishii (1987), the threshold for the slugless domain in pipes was given by $D^* > 30$. Later, Schlegel et al. (2009) noticed that for $D^* > 40$, the gas-liquid flow structures dramatically change, and established a criterion separating “large” from “medium”, or intermediate-size, pipes. Brooks et al. (2012) then argued that a critical diameter is not a fixed number, but it occurs over a large range of

pipe sizes as transitional flow characteristics change from small to large pipe diameters. In a later work, Shen et al. (2014) used $D^* > 40$ as the threshold for slugless flow domain, and $D^* < 18$ as the critical value for the existence of the slug flow domain. The author argued that values between 18 and 40 represent transition zones.

Annular dimension (mm)	D_h (mm)	D_{eq} (mm)	D_{EP} (mm)	$D_{\text{annulus}, h}^*$	$D_{\text{annulus}, eq}^*$	$D_{\text{annulus}, EP}^*$
77.3×26.7	50.6	72.5	103.9	26.9	38.6	55.3
77.3×33.4	43.9	69.7	110.7	23.3	37.0	58.8
77.3×42.2	35.1	64.7	119.4	18.7	34.4	63.5
77.3×48.3	29.0	60.3	125.5	15.4	32.1	66.7
77.3×60.3	16.9	48.3	137.6	9.0	25.7	73.2

Table 3.7 Characteristic diameters of annuli and their respective dimensionless numbers.

Using Shen et al. (2014) reasoning, the original observations from Kataoka and Ishii (1987), the numbers in Table 3.7, and the flow maps in Figure 3.18, we conclude that the hydraulic diameter is the most reliable parameter to determine the existence of slug flow in annular spaces. Thus, we express the dimensionless annulus diameter (D_{ann}^*) as Eq. 3.10,

$$D_{\text{ann}}^* = \frac{D_h}{\sqrt{\sigma/g(\rho_L - \rho_G)}}, \quad (3.10)$$

and we set the boundaries for the existence of slug flow in annular spaces with the definitions given in Table 3.8.

Slug flow existence in annuli	Criteria
Slug flow domain	$D_{\text{ann}}^* < 18$
Transition	$18 \leq D_{\text{ann}}^* \leq 30$
Slugless flow domain	$D_{\text{ann}}^* > 30$

Table 3.8 Criteria for slug flow existence in annular spaces.

The criterion for slugless flow domain given in Table 3.8 may seem to extrapolate the observations from our experiments. As we can see from Table 3.7, the largest D_{ann}^* we reached was 26.9; however, a couple of facts allowed us to establish that critical value of D_{ann}^* . First, as shown in Figure 3.18, we did not see slug flow in the 77.3-by-26.7 and 77.3-by-33.4 annuli, which correspond to dimensionless annulus diameters of 26.9 and 23.3, respectively.

The second fact which allowed us to set $D_{\text{ann}}^* > 30$ as the lower boundary for the slugless flow domain comes from the proof-of-concept set of experiments described in the previous Section. For those experiments, we used the same 77.3 mm pipe that served as the outer diameter of our annular spaces to flow the same fluids, under the same conditions, as those experiments in annular spaces. In that case, we also did not observe the existence of slug flow, and we calculated the dimensionless diameter as 40.9. If we then look at the 77.3 mm pipe as an extrapolation of our annular space where $D_i = 0$, we feel confident setting the criteria in Table 3.8, while keeping in line with the typical boundaries used in pipes.

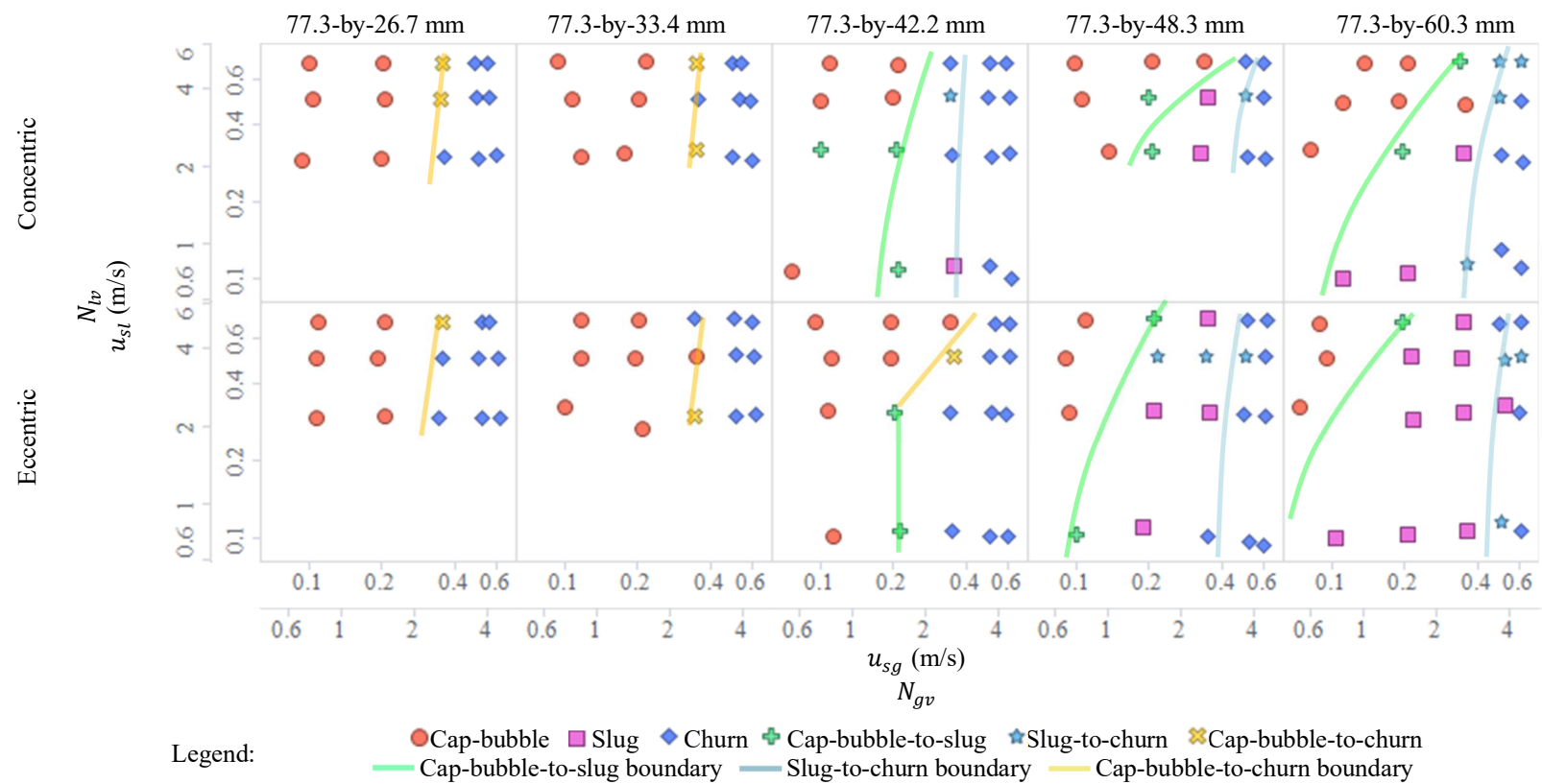


Figure 3.18 Flow regime maps for each annular dimension in concentric and eccentric configurations.

3.2.2.2. Pressure Gradient Models

Pressure gradient models are mathematical formulations based on the description of different flow regimes observed in pipes and annular spaces. As indicated in Section 1.4.1 and in the previous paragraphs, there exist many flow regimes and transitional states. However, all models ultimately have the same goal, that is, to predict liquid holdup and pressure gradient. The liquid holdup is a relative measure of the volume occupied by the liquid at a given section of the flow. The pressure gradient on the other hand is the total pressure drop by unit length and it is generally calculated as the sum of three components, gravitational, acceleration, and frictional (Shoham 2006).

Two-phase flow during well control events are fully transient phenomena. However, as indicated in Section 1.4, quantifying and modeling kick migration rely on the correct understanding of how the different steady-state flow patterns take place. With that in mind, we compared our experimental measurements with the predicted values from a series of upward, gas-liquid flow models.

Due to the limited length of the test-section used ($L/D = 26$), our holdup measurements are subject to large uncertainties. For that reason, we decided to focus our study on analyzing how the existing models can predict pressure gradient for the experiments in the following annular spaces: 77.3-by-26.7, 77.3-by-33.4, 77.3-by-42.2, and 77.3-by-48.3 mm. We compared our pressure gradient measurements in concentric and eccentric configurations with the models in Table 3.9.

Model Name	Model Acronym	Sources
Caetano	CSB	Caetano, Shoham, and Brill (1992a) Caetano, Shoham, and Brill (1992b)
Zhao and Hibiki	ZH	Zhao and Hibiki (2019)
Schlegel in Slug Flow Domain	SSD	Schlegel, Hibiki, and Ishii (2010)
Schlegel in Slugless Flow Domain	SSL	Schlegel, Hibiki, and Ishii (2010)

Table 3.9 Pressure gradient models used to predict experimental values.

With models ZH, SSD, and SSL we can estimate liquid holdup (H_l) with relative ease, which in turn allows for the calculation of the gravitational pressure gradient with Eq. 3.11,

$$\left(\frac{\Delta P}{\Delta L}\right)_{TP,G} = \rho_m g, \quad (3.11)$$

where g is the gravitational acceleration, and ρ_m is the density of the oil-air mixture given by Eq. 3.12,

$$\rho_m = H_l \rho_{oil} + (1 - H_l) \rho_{air}. \quad (3.12)$$

The two-phase, frictional pressure gradient for these models is calculated using Eq. 3.13,

$$\left(\frac{\Delta P}{\Delta L}\right)_{TP,F} = 2f_{CSB} \frac{\rho_m (u_{sg} + u_{sl})^2}{D_h}, \quad (3.13)$$

where f_{CSB} is the two-phase friction factor calculated according to Caetano, Shoham, and Brill (1992a).

The acceleration component is negligible for all flow regimes, except slug flow, as indicated by Caetano, Shoham, and Brill (1992b). In slug flow, the frictional pressure gradient is also different as Eq. 3.13 is multiplied by the ratio between the length of the liquid slug over the sum of the lengths of liquid slug itself and the Taylor bubble. Model SSD follows CSB when computing the frictional and acceleration pressure drop components.

Figure 3.19 show the results for each model separated by the annular sizes. In the figure, the blue points represent a superficial liquid velocity of 0.7 m/s, while the red ones correspond to $u_{sl} = 0.5$ m/s. The solid, round markers represent concentric tests, and the square, no-filling markers stand for eccentric annuli.

The CSB model performs particularly well for the annular configuration of 77.3-by-42.2 mm, which is most likely due to the fact that this is the exact same annulus dimension the original work from Caetano, Shoham, and Brill (1992b) used to validate its results. This model is capable of predicting pressure gradient for most cases within a 20 % error margin, especially if the calculated pressure drop is greater than 6 kPa/m. The only discrepancies noticed with this model concern the 77.3-by-48.3 annulus, where the model overshoots the pressure gradient by more than 20 % in a couple of cases. Overall, however, the model works well, especially considering it was not originally conceived to account for the slugless flow domain. The original work behind CSB distinguishes fully-develop from developing Taylor bubbles, which roughly correspond to our current concept about the existence of slug flow. However, the model still needs to be modified

to fully account for the effects of larger annular space where Taylor bubbles are not stable.

The ZH, on the other hand, was formulated with the slugless flow domain in mind. The model was fine-tuned to fit existing experimental data from concentric annuli. This explains the model's exceptional performance for concentric annular spaces, with all datapoints within a 10 % error margin, even for experiments outside the slugless flow domain. The same does not happen for the pressure gradient prediction in eccentric annuli though, with the model consistently overestimating the pressure gradient by 10 to 20 %, even in the slugless flow domain.

The SSD and SSL models are complimentary in that they respectively cover the slug and slugless flow domains in pipes. That explains why the SSD model underestimates the pressure gradient in the 77.3-by-26.7 and 77.3-by-33.4 annular spaces, but has better results, albeit not perfect, for the smaller annuli. Similar to CSB, from which the SSD borrows its acceleration pressure drop component in slug flow, the predictions in the 77.3-by-48.3 annulus are not ideal, but are still within a 20 % error band. The SSL model, however, has exceptional performance predicting pressure gradient in the slugless flow domain, with most datapoints falling within the 10 % error margin. The performance of the model for the eccentric case, however, is remarkable, even in the slug flow domain. This is probably due to the fact that SSL was originally conceived for pipes. As the eccentric annulus gets larger, the flow section becomes closer to that of a regular pipe. In the concentric annuli, that is not the case, so SSL underestimates the pressure gradient.

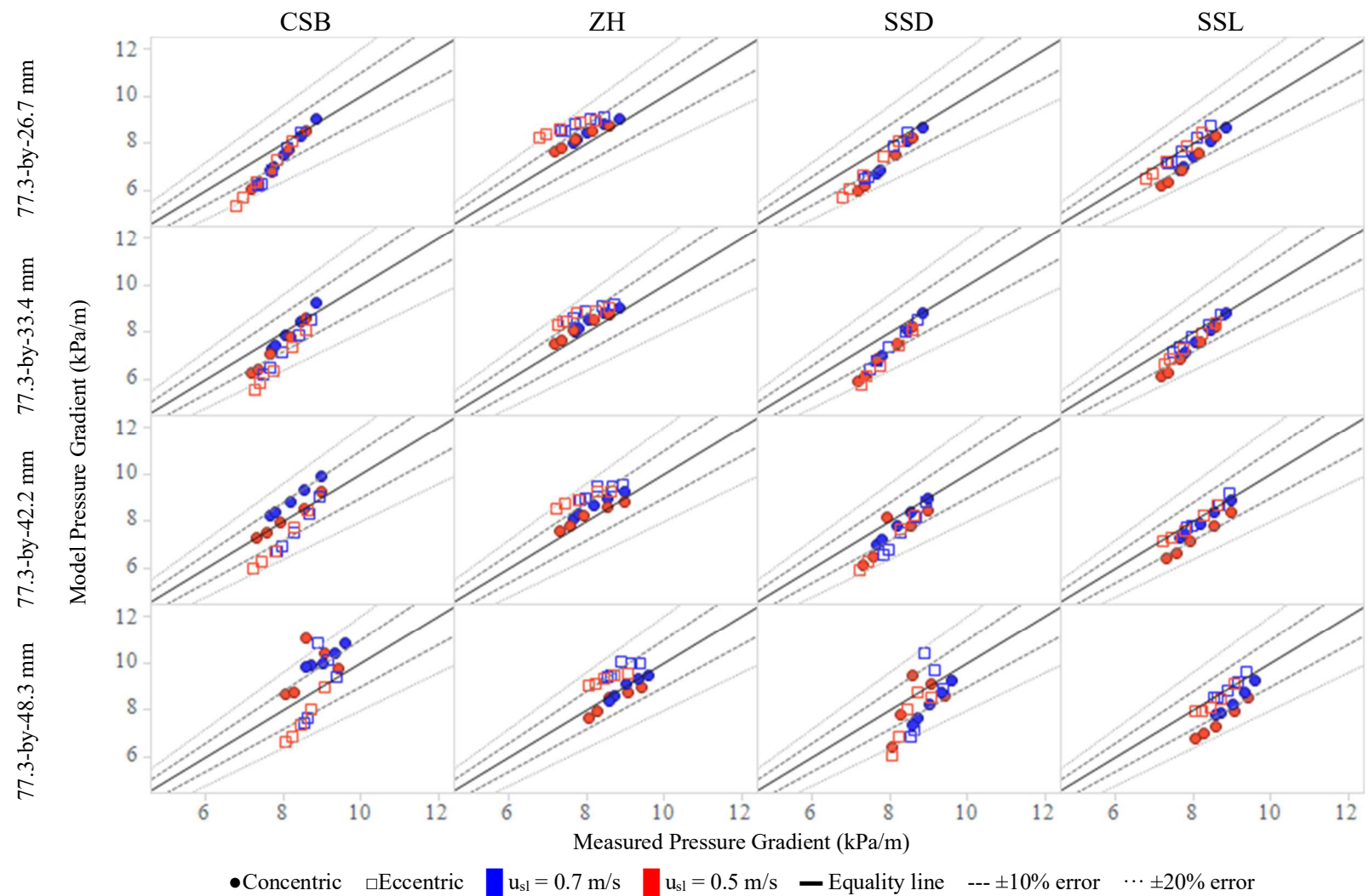


Figure 3.19 Comparison between calculated pressure gradient from different flow models and measured values.

With Figure 3.19 and the models listed in Table 3.9, we recommend the ZH model as the best pressure gradient prediction tool for upward, gas-liquid flow in concentric annular spaces. For fully-eccentric annuli, we recommend the SSL slugless flow domain pipe model. Using the concept of eccentricity defined by Eq. 3.14,

$$e = \frac{2d_c}{D_h}, \quad (3.14)$$

where d_c is the distance between pipe centers, we define the total pressure gradient in the slugless flow domain in annular spaces as Eq. 3.15,

$$\left(\frac{\Delta p}{\Delta L}\right)_{\text{ann, slugless}} = (1 - e) \left(\frac{\Delta p}{\Delta L}\right)_{ZH} + e \left(\frac{\Delta p}{\Delta L}\right)_{SSL}, \quad (3.15)$$

where the subscripts ZH and SSL indicate the total pressure gradients calculated with the Zhao and Hibiki (2019) and Schlegel, Hibiki, and Ishii (2010) models.

It is important to note that even though these models delivered great results outside the slugless flow domain, we can only recommend them if the slugless flow criteria in annuli is met (Table 3.8). In the slug flow domain, the CSB model is still preferable.

3.2.3. The Impact of the Annular Flow Regime Domain in Calculating BHP

As it was mentioned before, these flow models are not meant to model fully-transient events like the influx of a gas bubble in the well while drilling. They are instead used as references in the calculations determining the pressure losses and flow characteristics taking place in these transient problems. We can, however, use these models to approximate the wellbore flow during underbalanced drilling. In an effort to

quantify the importance of using the appropriate flow model, we will analyze the total pressure drop on a short pipe (1,000 m, or 3280 ft).

Using the experimental results as reference, we know that for an eccentric annuli with $D_h = 50.6$ mm, the fluid properties described in Table 2.2, $u_{sl} = 0.7$ m/s, and $u_{sg} = 0.35$ m/s, the total measured pressure drop is 7.71 kPa/m, which in a 1,000 m corresponds to 7.71 MPa, or 1,118 psi.

The appropriate model to estimate the case described above is the SSL. With this model, we calculate a pressure total pressure drop of 7.67 MPa, or 1112. That corresponds to a negligible difference of 40 kPa, or 6 psi. If we, however, use the ZH model, we obtain a total pressure drop of 8.80 MPa (1276 psi). This corresponds to a more significant difference of 1.09 MPa (158 psi), or 0.93 ppg.

The CSB model can estimate pressure gradient in both concentric and eccentric annular configurations. Nevertheless, if we try to use it in the slugless flow domain like in the example we are discussing, the total pressure-drop calculated with CSB is 6.90 MPa (1,001 psi). As with the ZH model, this difference between measured and estimated pressure gradients results in an absolute error of 0.81 MPa (117 psi), or 0.68 ppg.

3.3. Simulation of Formation-Fluid Influx During Drilling

In the following paragraphs we will show two examples of formation-influx estimation with DIM based on cases available in the literature. Both examples concern underbalanced drilling, with the first case being a simulated liquid-influx, and the second one providing actual field-data of gas-influx while drilling a horizontal well.

3.3.1. Case 1: Real-Time Influx Estimation with DIM

This first simulation is based on the synthetic case of UBD given by Example 1 in Vefring et al. (2006). The problem can be summarized as a horizontal well drilling through a producing formation at a constant ROP (0.005 m/s, 59 ft/hr). This formation is subdivided into 10 different zones of equal length (30 m, 98.4 ft), with each zone having its own permeability. For further assumptions and parameter values, we recommend consulting the original work.

Vefring et al. (2006) estimate influx with a modified version of the conventional transient IPR as seen in Eq. 3.16 below,

$$Q(t) = \frac{4\pi k \Delta s (P_e - P_{wf})}{\mu \left[\ln \left(\frac{2.246 kt}{\phi \mu c_t r_w^2} \right) + 2 S \right]}, \quad (3.16)$$

where Δs is the length of the formation being drilled.

The use of Eq. 3.16, which is just an adaptation of Eq. 1.12, to estimate influx from horizontal wells ignores most assumptions used in deriving the equation in the first place. While we do not agree with its use in such cases, it is not uncommon to utilize Eq. 3.16 for testing other models, such as those for wellbore-flow (Xu et al. 2018), early kick-detection (Sun et al. 2018), or choke-control in MPD (Gravdal et al. 2010). In all these works, the influx is not the object of analysis, but just a tool to test the proposed models.

The main goal of this example is, thus, not to show the accuracy of the DIM, but to benchmark it against the conventional transient IPR in a simplified case. With that in mind, we generated Figure 3.20, where the responses from a sinusoidal bottomhole

pressure for both the DIM and the conventional transient IPR are plotted. Additionally, we also provide a plot of the relative difference between the liquid rates obtained using both methods.

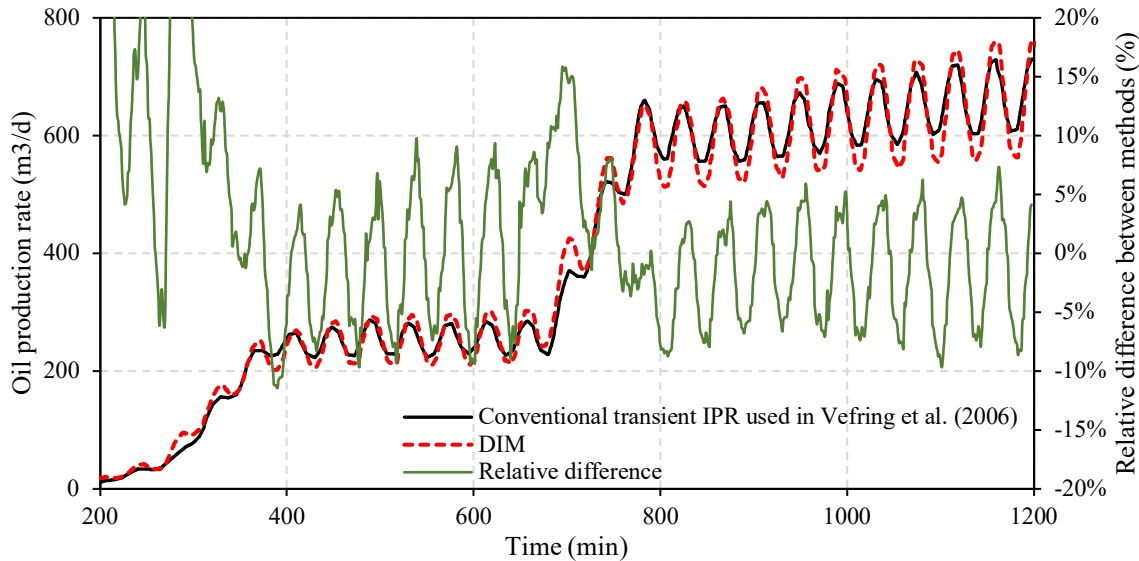


Figure 3.20 Comparison between conventional transient IPR and DIPR to predict liquid production during underbalanced drilling.

Drilling through the producing zones start around minute 170. During the first 20 minutes, the two methods deliver very different relative results (over 100 %); however, this is due to a discontinuity at the beginning of production, causing production spikes in the very early stages of production. Once the initial effects are no longer important, the relative difference between the methods rapidly decreases, falling within $\pm 10\%$ error after 200 minutes, and later staying within 5 % from each other after the 600th minute.

This example shows that the DIM can be used in lieu of the conventional transient IPR for simulating influx from reservoirs, but two additional observations must

be highlighted. First, in this example, the DIM requires only 10 equations, one for each zone. The flow-rate is then calculated based on the drilled length of each zone, such as indicated in Eq. 2.22. The conventional transient IPR, on the other hand, is valid only for a step-like change in bottomhole pressure; thus, to simulate a sinusoidal BHP, it is necessary to approximate the sine wave as a series of pressure step-functions for very small timesteps. Each one of these functions are then superimposed to generate a response such as the black curve seen in Figure 3.20. Furthermore, when doing these calculations and handling each one of these equations, one must also keep track of their time range validity. As explained in Section 1.5.1, the conventional transient IPR is only valid for the conditions given in Eq. 1.13. While this is not a concern in this specific example ($3.3 \text{ months} \leq t_e \leq 20.1 \text{ months}$), it can be important under other circumstances.

The second important aspect of this example that must be addressed concerns the accuracy of the DIM. As we have shown, both methods agree, with a maximum error of 10 % once the initial effects of production are no longer significant. Also as previously mentioned, this example is used to compare the DIM with what is common practice in the scientific publications. The proper oil flowrate, however, is actually delivered by the DIM. The Dynamic Influx Model is based on the analytical derivation of a reservoir under sinusoidal bottomhole pressure, which is the exact case being analyzed in this Case 1. Therefore, the DIM is not only more convenient to use in general, but in this specific example, it is the more appropriate model.

3.3.2. Case 2: DIM While Drilling Horizontal Wells Underbalanced

This case-study is based on a real UBD operation provided in Farshidi et al. (2008). Specifically, we used the first field-case introduced by the authors. That work directly provides many of the reservoir and fluid properties necessary to run our model (DIM), but some parameters had to be estimated either based on the simulated data presented in the same work, or by inferring values based on the best available information. This is particularly important for two reasons: first, for the assumptions used in calculating the pseudopressure function, and second, for estimating the skin factor associated with the horizontal well.

The pseudopressure function depends on two variables not provided by Farshidi et al. (2008), the compressibility (Z) factor of the formation-gas, and its viscosity as a function of pressure and temperature. We estimated the Z -factor based on the Sutton (1985) and Dranchuk and Abou-Kassem (1975) correlations. The viscosity as function of pressure and temperature, on the other hand, is computed based on a few pieces of information, the gas-viscosity at reservoir conditions, the reservoir pressure, and the charts from Carr, Kobayashi, and Burrows (1954). From this we also inferred a reservoir temperature of 367 K (200 °F).

As it was previously discussed, DIM is based on the Eq. 1.24, which was derived for a vertical well centered in a cylindrical, homogeneous reservoir. Therefore, DIM is not suitable to be used as a model for estimating influx from a horizontal well without modifications. The modification required to use DIM with horizontal wells is provided by Eq. 2.21, that is, by incorporating a skin effect to the original DIM. In that regard, we

used the Furui, Zhu, and Hill (2003) to estimate the skin factor associated with horizontal wells (S_h) and given by Eq. 3.17,

$$S_h = \frac{\pi y_b}{h_r} - 1.917 \quad (3.17)$$

where h_r is the reservoir thickness, and y_b is the half-length of the reservoir width. In our case, we assume a rectangular reservoir with a width of $2r_e$, making $y_b = r_e$.

Still based on the work of Furui, Zhu, and Hill (2003), we redefine the outer boundary of the reservoir in Eq. 1.19 by replacing r_e with h_r , and modify the flowrate equation to the form presented in Eq. 3.18,

$$Q(t) = \frac{T_{SC}}{T_{res}} \frac{\pi k \Delta s}{P_{SC}} \sqrt{\omega \frac{\phi \mu c_t}{k}} \left[\cos(\omega t) \frac{\partial}{\partial r} F(r_w e^{-s_h}, h_r, \omega) + \sin(\omega t) \frac{\partial}{\partial r} G(r_w e^{-s_h}, h_r, \omega) \right] r_w e^{-s_h}. \quad (3.18)$$

Using Eq. 3.18 instead of Eq. 1.19 to compute the coefficients in Eq. 2.22, we can use now use the DIM model as defined in Table 2.5. The result from our simulation is compared to the field and simulated data provided in Farshidi et al. (2008), and they are plotted in Figure 3.21.

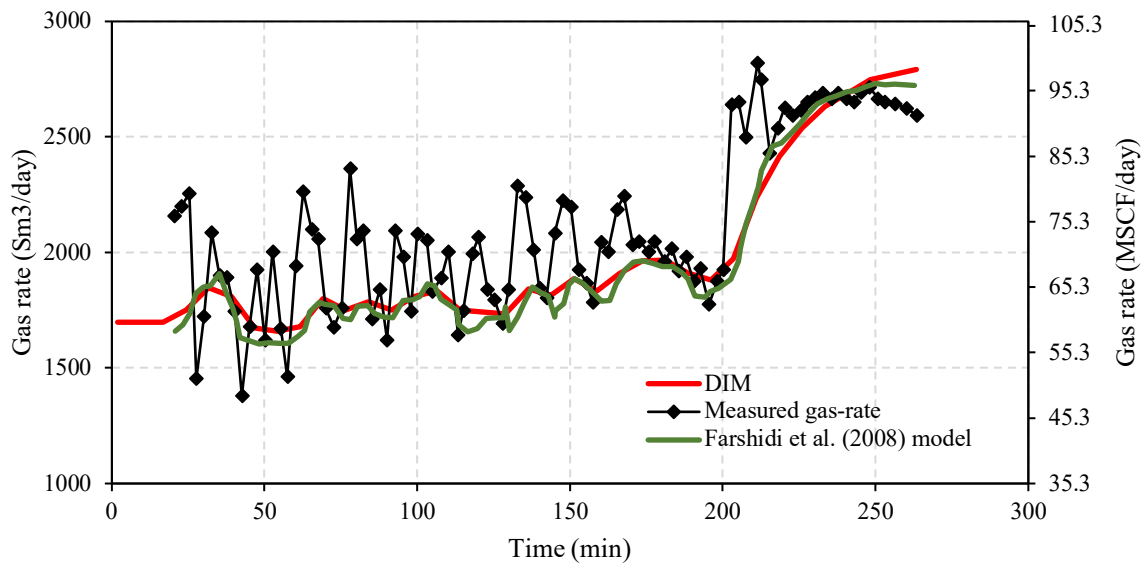


Figure 3.21 Comparison between measured gas production during underbalanced drilling estimated with a transient IPR for horizontal wells and the DIPR.

From the graph in Figure 3.21, we can see that DIM can track the gas production from the formation during underbalanced operations very reasonably, especially considering the approximations made due to incomplete information about reservoir and fluid properties. The DIM follows the model used in the original publication very closely, and both are able to track the behavior of the actual measurements. The only major difference between the DIM the modified transient IPR used in Farshidi et al. (2008) is at the end, where both methods seem to diverge from the measured curve. In that case, the DIM does not perform well, and predicts an increase in influx where there actually is an increase. We believe this is due to the fact that the reservoir temperature and gas PVT properties are only approximated, and that the BHP profile provided in the original work is probably a smoothed version of the actual field-measurements.

4. CONCLUSIONS AND FUTURE WORK

Drilling safely is paramount to guarantee the well-being of the persons involved in field operations, and to minimize environmental impacts. This work has attempted to bridge the knowledge gap in different areas of drilling, and provide tools for safer operations. The entire work has been divided in a three-pronged approach, with each front analyzing different issues related to well-control, identifying their weaknesses, and proposing solutions.

In that regard, the main conclusions of this work will follow the same reasoning. We start by the rheological characterization of drilling fluids:

1. We established a test methodology for rheology of drilling fluids in HPHT where contamination by pressurizing fluid is minimized.
2. We introduced a protocol to inject gas into drilling fluid samples and test the gas-contaminated mud in HPHT.
3. The Herschel-Bulkley model is the most suitable to characterize rheology in a large range of pressures and temperatures.
4. Inaccurate rheological modeling can lead to BHP errors greater than 0.1 ppg.
5. Muds contaminated with formation-fluid analogues (diesel and butane) exhibit close rheological behavior to the uncontaminated mud; however, their shear stress buildup tend to collapse at lower pressure and temperature conditions.

The next topic of study consists of identifying flow regimes in larger annular spaces. From that study we concluded:

1. As in upward pipe flow, annular spaces also have a minimum diameter after which the Taylor bubble is unstable and slug flow no longer takes place.
2. From our data, we determined that the dimensionless hydraulic diameter is the best indicative of the boundaries between slug and slugless flow domains.
3. From all the hydraulic models tested in this work, we determined that the Zhao and Hibiki (2019) is the best for concentric annuli in slugless flow domain.
4. Similarly, the Schlegel, Hibiki, and Ishii (2010) model for slugless flow domain in pipes is the best model to simulate slugless flow domain in fully-eccentric annuli.
5. We introduced a new model for slugless flow domain in pipes at any eccentricity level.
6. Differentiating the slug from the slugless flow domain is important, as inappropriate flow regimes may cause bottomhole pressure estimate errors close to 1.0 ppg even at short depths. This can prove to be a problem in the field as it may lead to significant influx volumes, or losses.

Finally, the last topic of our work regards the dynamic behavior and interactions between reservoir (or formations) and the flow in the wellbore during drilling. From that section we concluded:

1. We modified a reservoir production optimization tool called the Dynamic IPR to account for skin factor. It was validated against conventional IPRs for a simple drawdown case.
2. We introduced the Dynamic Influx Model as a tool to estimate formation-fluid influx during drilling. The DIM results were compared to existing literature, and it shows good agreement.
3. We introduced a new model for the DIPR (and DIM) for horizontal wells. The model gives good results when compared to real UBD data. We speculate that it could give better results if a one uses a higher sampling rate for the BHP.
4. The DIM is computationally easier to use than the conventional IPR models for vertical and horizontal wells. The DIM model only requires one equation to keep track of the producing reservoir, whereas conventional transient IPR require the discretization of the input (generally the BHP) into several step functions, each one generating a unique equation, which must be accounted for and superimposed onto each other.

The work developed here is very important to the future of drilling. We provided tools and experimental basis for safer and more efficient field operations; however, there

still is much to be explored. In the next paragraphs, we list some of the most important topics we believe must be investigated further:

1. Increase gas-contamination level of muds by injecting gas at higher pressure (currently Coriolis max pressure is 500 psig). Methane is preferable as injection-gas.
2. Run extensive gel-strength tests with buildup times varying from 10 seconds to at least one hour with several mud types. The goal here is to derive a model for gelling time and find a correlation between final gel-strength and yield stress in HPHT conditions.
3. Improve annulus flow loop by extending its length ($L/D > 100$), adding quick-closing valves at the bottom and top of test-section to measure holdup, upgrading pump, VSD, and air-oil separator. A system allowing to adjust the eccentricity of the pipe must also be part of the experimental setup.
4. Account for mud cake formation to enhance overbalanced drilling simulation with DIM. Understanding of cake buildup rate, filtrate flow, and pressure loss through mud cake is necessary.
5. Refine DIM horizontal well model by simulating more real data.
6. Derive a reservoir characterization while drilling tool.
7. Couple DIM with real-time kick-monitoring tools.
8. Build new kick simulator incorporating appropriate rheological, annulus flow, and formation-fluid influx models.

REFERENCES

- Amani, Mahmood. 2012. The rheological properties of oil-based mud under high pressure and high temperature conditions. *Advances in Petroleum Exploration and Development* **3** (2): 21-30.
- Amani, Mahmood, Mohammed Jumaah Al-Jubouri. 2012. An Experimental Investigation of the The Effects of Ultra High Pressures and Temperatures on the Rheological Properties of Water-Based Drilling Fluids. Proc., International Conference on Health, Safety and Environment in Oil and Gas Exploration and Production, Perth, Australia, 9. doi: 10.2118/157219-MS.
- Amani, Mahmood, Mohammed Al-Jubouri, Arash Shadravan. 2012. Comparative study of using oil-based mud versus water-based mud in HPHT fields. *Advances in Petroleum Exploration and Development* **4** (2): 18-27.
- Ambrus, Adrian, Ulf Jakob Flø Aarsnes, Ali Karimi Vajargah et al. 2016. Real-time estimation of reservoir influx rate and pore pressure using a simplified transient two-phase flow model. *Journal of Natural Gas Science and Engineering* **32**: 439-452. doi: <https://doi.org/10.1016/j.jngse.2016.04.036>.
- Instruction Manual Model 7600 HPHT Viscometer. 2016. Broken Arrow, OK: Ametek Chandler Engineering. <https://www.chandlereng.com/-/media/ametekchandlereng/files/pdfs/model%207600%20ultra%20hpht%20viscometer%20manual.pdf>.
- An, J., K. Lee, J. Choe. 2015. Well Control Simulation Model of Oil-Based Muds for HPHT Wells. Proc., SPE/IATMI Asia Pacific Oil & Gas Conference and Exhibition, Nusa Dua, Bali, Indonesia, 13. doi: 10.2118/176093-MS.
- Annis, Max R. 1967. High-Temperature Flow Properties of Water-Base Drilling Fluids. *Journal of Petroleum Technology* **19** (08): 1074-1080. doi: 10.2118/1698-PA.
- API Recommended Practice 13B-1: Field Testing Water-Based Drilling Fluids. 2014: American Petroleum Institute.
- API Recommended Practice 13D: Rheology and Hydraulics of Oil-well Drilling Fluids; Seventh Edition. 2017.
- API Recommended Practice 13B-2 (E1) (E2) (A1): Field Testing Oil-Based Drilling Fluids. 2019: American Petroleum Institute.

- Bailey, W. J., J. M. Peden. 2000. A Generalized and Consistent Pressure Drop and Flow Regime Transition Model for Drilling Hydraulics. *SPE Drilling & Completion* **15** (01): 44-56. doi: 10.2118/62167-PA.
- Barron, Randall F., Brian R. Barron. 2012. *Design for thermal stresses*. Hoboken, N.J. :, Wiley (Reprint).
- Beggs, D. H., J. P. Brill. 1973. A Study of Two-Phase Flow in Inclined Pipes. *Journal of Petroleum Technology* **25** (05): 607-617. doi: 10.2118/4007-PA.
- Berthezene, N., J. C. de Hemptinne, A. Audibert et al. 1999. Methane solubility in synthetic oil-based drilling muds. *Journal of Petroleum Science and Engineering* **23** (2): 71-81. doi: [https://doi.org/10.1016/S0920-4105\(99\)00008-X](https://doi.org/10.1016/S0920-4105(99)00008-X).
- Billa, Richard J., Jose Francisco Mota, Barry Schneider et al. 2011. Drilling Performance Improvement in the Haynesville Shale. Proc., SPE/IADC Drilling Conference and Exhibition, Amsterdam, The Netherlands, 6. doi: 10.2118/139842-MS.
- Billingham, John, Martin Thompson, D. B. White. 1993. Advanced Influx Analysis Gives More Information Following a Kick. Proc., SPE/IADC Drilling Conference, Amsterdam, Netherlands, 11. doi: 10.2118/25710-MS.
- Bland, Ronald G., Gregory Alan Mullen, Yohnny N. Gonzalez et al. 2006. HPHT Drilling Fluid Challenges. Proc., IADC/SPE Asia Pacific Drilling Technology Conference and Exhibition, Bangkok, Thailand, 11. doi: 10.2118/103731-MS.
- Bourgoyne, A. T., K. K. Millheim, M. E. Chenevert. 1985. *Applied Drilling Engineering*, 41-43. Richardson, UNITED STATES, Society of Petroleum Engineers (Reprint).
- Brakel, J. D., B. A. Tarr, W. Cox et al. 2015. SMART Kick Detection; First Step on the Well Control Automation Journey. Proc., SPE/IADC Drilling Conference and Exhibition, London, England, UK, 17. doi: 10.2118/173052-MS.
- Brooks, Caleb S., Sidharth S. Paranjape, Basar Ozar et al. 2012. Two-group drift-flux model for closure of the modified two-fluid model. *International Journal of Heat and Fluid Flow* **37**: 196-208. doi: <https://doi.org/10.1016/j.ijheatfluidflow.2012.04.002>.
- Bui, Binh Thanh, Azra Nur Tutuncu. 2016. A Generalized Rheological Model for Drilling Fluids With Cubic Splines. *SPE Drilling & Completion* **31** (01): 26-39. doi: 10.2118/169527-PA.

- Bureau, N., J. C. de Hemptinne, A. Audibert et al. 2002. Interactions Between Drilling Fluid and Reservoir Fluid. Proc., SPE Annual Technical Conference and Exhibition, San Antonio, Texas, 12. doi: 10.2118/77475-MS.
- Caenn, R., HCH Darley, G.R. Gray. 2017. *Composition and Properties of Drilling and Completion Fluids*, 159-191, 239, Elsevier Science (Reprint).
- Caetano, E. F., O. Shoham, J. P. Brill. 1992a. Upward Vertical Two-Phase Flow Through an Annulus—Part I: Single-Phase Friction Factor, Taylor Bubble Rise Velocity, and Flow Pattern Prediction. *Journal of Energy Resources Technology* **114** (1): 1-13. doi: 10.1115/1.2905917.
- Caetano, E. F., O. Shoham, J. P. Brill. 1992b. Upward Vertical Two-Phase Flow Through an Annulus—Part II: Modeling Bubble, Slug, and Annular flow.
- Capovilla, Matheus S., Renato P. Coutinho, Pedro Cavalcanti de Sousa et al. 2019. Experimental investigation of upward vertical two-phase high-velocity flows in large-diameter pipes. *Experimental Thermal and Fluid Science* **102**: 493-505. doi: <https://doi.org/10.1016/j.expthermflusci.2018.12.024>.
- Carr, Norman L., Riki Kobayashi, David B. Burrows. 1954. Viscosity of Hydrocarbon Gases Under Pressure. *Journal of Petroleum Technology* **6** (10): 47-55. doi: 10.2118/297-G.
- Choe, J. 2001. Advanced Two-Phase Well Control Analysis (November). *Journal of Canadian Petroleum Technology* **40** (11): 9. doi: 10.2118/01-11-01.
- Crespo, Freddy E., Ramadan Mohammed Ahmed, Arild Saasen et al. 2012. Surge-and-Swab Pressure Predictions for Yield-Power-Law Drilling Fluids. *SPE Drilling & Completion* **27** (04): 574-585. doi: 10.2118/138938-PA.
- Dake, Laurence P. 1983. *Fundamentals of Reservoir Engineering*, 1st edition, 125, 126, 141-145, 154-158, 248, 295-297, 389. Oxford, United Kingdom: Developments in Petroleum Science, Elsevier Science (Reprint) (repr. 2013).
- Davison, J. M., S. Clary, A. Saasen et al. 1999. Rheology of Various Drilling Fluid Systems Under Deepwater Drilling Conditions and the Importance of Accurate Predictions of Downhole Fluid Hydraulics. Proc., SPE Annual Technical Conference and Exhibition, Houston, Texas, 13. doi: 10.2118/56632-MS.
- Dranchuk, P. M., H. Abou-Kassem. 1975. Calculation of Z Factors For Natural Gases Using Equations of State. *Journal of Canadian Petroleum Technology* **14** (03): 4. doi: 10.2118/75-03-03.

- Economides, M.J., A.D. Hill, C. Ehlig-Economides et al. 2011. *Petroleum Production Systems*, 1st edition, 78, 87-91, 709, Pearson Education (Reprint).
- Farshidi, S, DF Yu, J Slade et al. 2008. Permeability estimation from inflow data during underbalanced drilling. *Journal of Canadian Petroleum Technology* **47** (6): 56-63.
- Ferry, John D. 1970. *Viscoelastic Properties of Polymers*, 1-2. USA, John Wiley & Sons (Reprint). <https://doi.org/10.1002/pol.1970.110080815>.
- Furui, Kenji, D. Zhu, A. D. Hill. 2003. A Rigorous Formation Damage Skin Factor and Reservoir Inflow Model for a Horizontal Well (includes associated papers 88817 and 88818). *SPE Production & Facilities* **18** (03): 151-157. doi: 10.2118/84964-PA.
- Galdino, Jonathan F., Gabriel M. Oliveira, Admilson T. Franco et al. 2019. Gas kick detection and pressure transmission in thixotropic, compressible drilling fluids. *Journal of Petroleum Science and Engineering* **180**: 138-149. doi: <https://doi.org/10.1016/j.petrol.2019.05.029>.
- Garcia, A. Posenato, P. Cavalcanti de Sousa, P. J. Waltrich. 2016. A Transient Coupled Wellbore-Reservoir Model Using a Dynamic IPR Function. Proc., SPE Annual Technical Conference and Exhibition, 26-28 September, Dubai, UAE. doi: 10.2118/181691-MS.
- Garcia, Artur P., Gilson M. Neto, Marcos B. Machado et al. 2014. Dynamic IPR - Modeling Reservoir Well Interactions to Improve Transient Simulations of Wells. Proc., SPE Latin America and Caribbean Petroleum Engineering Conference, 21-23 May, Maracaibo, Venezuela. doi: <https://doi.org/10.2118/169375-MS>.
- Garrison, Allen D. 1939. Surface Chemistry of Clays and Shales. *Transactions of the AIME* **132** (01): 191-204. doi: 10.2118/939191-G.
- Gokdemir, Muzaffer Gorkem, Selcuk Erkeköl, Huseyin Ali Dogan. Investigation of High Pressure Effect on Drilling Fluid Rheology. American Society of Mechanical Engineers Digital Collection.
- Grace, Robert D., Bob Cudd, Richard S. Carden et al. 2003. *Blowout and Well Control Handbook*, 40. Burlington, Gulf Professional Publishing (Reprint). <http://dx.doi.org/10.1016/B978-075067708-0/50002-5>.
- Gravdal, Jan Einar, Michael Nikolaou, Øyvind Breyholtz et al. 2010. Improved Kick Management During MPD by Real-Time Pore-Pressure Estimation. *SPE Drilling & Completion* **25** (04): 577-584. doi: 10.2118/124054-PA.

- Griffith, Peter. 1964. The prediction of low-quality boiling voids.
- Guo, Ruixuan, Yuanhang Chen, Renato Peixoto Coutinho et al. 2017. Numerical and Experimental Investigations of Gas Kick Migration During Casing While Drilling. Proc., SPE Health, Safety, Security, Environment, & Social Responsibility Conference - North America, New Orleans, Louisiana, USA, 14. doi: 10.2118/184416-MS.
- Hasan, A. Rashid, C. Shah Kabir. 1988. A Study of Multiphase Flow Behavior in Vertical Wells. *SPE Production Engineering* **3** (02): 263-272. doi: 10.2118/15138-PA.
- Herzhaft, Benjamin, Lionel Rousseau, Laurent Neau et al. 2003. Influence of Temperature and Clays/Emulsion Microstructure on Oil-Based Mud Low Shear Rate Rheology. *SPE Journal* **8** (03): 211-217. doi: 10.2118/86197-PA.
- Hibiki, Takashi, Mamoru Ishii. 2003. One-dimensional drift-flux model for two-phase flow in a large diameter pipe. *International Journal of Heat and Mass Transfer* **46** (10): 1773-1790.
- Hoberock, L. L., S. R. Stanbery. 1981a. Pressure Dynamics in Wells During Gas Kicks: Part 1 - Component Models and Results. *Journal of Petroleum Technology* **33** (08): 1357-1366. doi: 10.2118/9256-PA.
- Hoberock, L. L., S. R. Stanbery. 1981b. Pressure Dynamics in Wells During Gas Kicks: Part 2 - Component Models and Results. *Journal of Petroleum Technology* **33** (08): 1367-1378. doi: 10.2118/9822-PA.
- Houwen, O. H., T. Geehan. 1986. Rheology of Oil-Base Muds. Proc., SPE Annual Technical Conference and Exhibition, New Orleans, Louisiana, 12. doi: 10.2118/15416-MS.
- Ilin, Andrew, Sayamik Ameen Rostami, Kedar Deshpande et al. 2019. Real-Time Gas Influx Analysis and Control in Managed Pressure Drilling. Proc., SPE Annual Caspian Technical Conference, Baku, Azerbaijan, 12. doi: 10.2118/198361-MS.
- Kataoka, Isao, Mamoru Ishii. 1987. Drift flux model for large diameter pipe and new correlation for pool void fraction. *International Journal of Heat and Mass Transfer* **30** (9): 1927-1939.
- Leblanc, J. L., R. L. Lewis. 1968. A Mathematical Model of a Gas Kick. *Journal of Petroleum Technology* **20** (08): 888-898. doi: 10.2118/1860-PA.
- Lee, John, Arash Shadravan, Steven Young. 2012. Rheological Properties of Invert Emulsion Drilling Fluid under Extreme HPHT Conditions. Proc., IADC/SPE

- Drilling Conference and Exhibition, San Diego, California, USA, 9. doi: 10.2118/151413-MS.
- Malkin, Alexander Ya, Avraam I. Isayev. 2012. *Rheology - Concepts, Methods, and Applications (2nd Edition)*, 2nd edition. Toronto, ChemTec Publishing (Reprint).
- McMordie, W. C., Jr., R. B. Bennett, R. G. Bland. 1975. The Effect of Temperature and Pressure on the Viscosity of Oil-Base Muds. *Journal of Petroleum Technology* **27** (07): 884-886. doi: 10.2118/4974-PA.
- Mitchell, Robert F., Stefan Z. Miska. 2010. *Fundamentals of Drilling Engineering*, 179, 625-639. Richardson, UNITED STATES, Society of Petroleum Engineers (Reprint).
- Monteiro, Eduardo Nascimento, Paulo Roberto Ribeiro, Rosana Fatima Teixeira Lomba. 2008. Study of the PVT Properties of Gas - Synthetic Drilling Fluid Mixtures Applied to Well Control Operations. Proc., SPE Annual Technical Conference and Exhibition, Denver, Colorado, USA, 15. doi: 10.2118/116013-MS.
- Mullineux, Glen. 2008. Non-linear least squares fitting of coefficients in the Herschel–Bulkley model. *Applied Mathematical Modelling* **32** (12): 2538-2551. doi: <https://doi.org/10.1016/j.apm.2007.09.010>.
- Nickens, H. V. 1987. A Dynamic Computer Model of a Kicking Well. *SPE Drilling Engineering* **2** (02): 159-173. doi: 10.2118/14183-PA.
- O'Bryan, Patrick L., Adam T. Bourgoyne, Jr. 1990. Swelling of Oil-Based Drilling Fluids Resulting From Dissolved Gas. *SPE Drilling Engineering* **5** (02): 149-155. doi: 10.2118/16676-PA.
- O'Bryan, Patrick L., Adam T. Bourgoyne, Jr., Teresa G. Monger et al. 1988. An Experimental Study of Gas Solubility in Oil-Based Drilling Fluids. *SPE Drilling Engineering* **3** (01): 33-42. doi: 10.2118/15414-PA.
- O'Neil, P. 2007. *Advanced Engineering Mathematics*, Cengage Learning (Reprint).
- Pagan, E., W. C. Williams, S. Kam et al. 2016. Modeling vertical flows in churn and annular flow regimes in small- and large-diameter pipes. Proc., 10th North American Conference on Multiphase Technology, Banff, Canada, 16.
- Peters, Ekwere J., Martin E. Chenevert, Chunhal Zhang. 1990. A Model for Predicting the Density of Oil-Base Muds at High Pressures and Temperatures. *SPE Drilling Engineering* **5** (02): 141-148. doi: 10.2118/18036-PA.

- Politte, M. D. 1985. Invert Oil Mud Rheology as a Function of Temperature and Pressure. Proc., SPE/IADC Drilling Conference, New Orleans, Louisiana, 18. doi: 10.2118/13458-MS.
- Rehm, B., J. Schubert, A. Haghshenas et al. 2013. *Managed Pressure Drilling*, 23, Elsevier Science (Reprint).
- Ribeiro, Paulo R., Pedro A. Pessôa-Filho, Rosana F. T. Lomba et al. 2006. Measurement and modeling of methane dissolution in synthetic liquids applied to drilling fluid formulation for deep and ultradeep water wells. *Journal of Petroleum Science and Engineering* **51** (1): 37-44. doi: <https://doi.org/10.1016/j.petrol.2005.11.007>.
- Rommetveit, R., K. S. Bjorkevoll. 1997. Temperature and Pressure Effects on Drilling Fluid Rheology and ECD in Very Deep Wells. Proc., SPE/IADC Middle East Drilling Technology Conference, Bahrain, 9. doi: 10.2118/39282-MS.
- Sahasrabudhe, Shreya N., Veronica Rodriguez-Martinez, Meghan O'Meara et al. 2017. Density, viscosity, and surface tension of five vegetable oils at elevated temperatures: Measurement and modeling. *International Journal of Food Properties* **20** (sup2): 1965-1981. doi: 10.1080/10942912.2017.1360905.
- Samuel, G. Robello, Ashwin Sunthakar, Glen McColpin et al. 2003. Field Validation of Transient Swab-Surge Response With Real-Time Downhole Pressure Data. *SPE Drilling & Completion* **18** (04): 280-283. doi: 10.2118/85109-PA.
- Santos, O. L. A. 1991. Well-Control Operations in Horizontal Wells. *SPE Drilling Engineering* **6** (02): 111-117. doi: 10.2118/21105-PA.
- Schlegel, J. P., P. Sawant, S. Paranjape et al. 2009. Void fraction and flow regime in adiabatic upward two-phase flow in large diameter vertical pipes. *Nuclear Engineering and Design* **239** (12): 2864-2874. doi: <https://doi.org/10.1016/j.nucengdes.2009.08.004>.
- Schlegel, Joshua, Takashi Hibiki, Mamoru Ishii. 2010. Development of a comprehensive set of drift-flux constitutive models for pipes of various hydraulic diameters. *Progress in Nuclear Energy* **52** (7): 666-677.
- Schumacker, Eric, Philip Vogelsberg. 2019. Slimhole Unconventional Well-Design Optimization Enables Drilling Performance Improvement and Cost Reduction. *SPE Drilling & Completion* **34** (04): 426-440. doi: 10.2118/192953-PA.
- Shadravan, Arash, Mahmood Amani. 2012. HPHT 101: What Every Engineer or Geoscientist Should Know about High Pressure HighTemperature Wells. Proc., SPE Kuwait International Petroleum Conference and Exhibition, Kuwait City, Kuwait, 27. doi: 10.2118/163376-MS.

- Shayegi, Sara, C. Shah Kabir, Flemming If et al. 2012. Reservoir Characterization Begins at First Contact With the Drill Bit. *SPE Drilling & Completion* **27** (01): 11-21. doi: 10.2118/159247-PA.
- Shen, Xiuzhong, Joshua P Schlegel, Shaowen Chen et al. 2014. Flow characteristics and void fraction prediction in large diameter pipes. In *Frontiers and Progress in Multiphase Flow I*, 55-103. Springer.
- Shoham, Ovadia. 2006. *Mechanistic modeling of gas-liquid two-phase flow in pipes*. Ovadia Shoham, Society of Petroleum Engineers (Reprint).
- Silva, C. T., J. R. L. Mariolani, E. J. Bonet et al. 2004. Gas Solubility in Synthetic Fluids: A Well Control Issue. Proc., SPE Annual Technical Conference and Exhibition, Houston, Texas, 6. doi: 10.2118/91009-MS.
- Skogestad, Jan Ole, Knut S. Bjørkevoll, Johnny Frøyen et al. 2019. Well Control Incident in the North Sea as Interpreted with Advanced Gas Influx Modelling. Proc., SPE/IADC International Drilling Conference and Exhibition, The Hague, The Netherlands, 18. doi: 10.2118/194145-MS.
- Sorelle, Roland R., Ricardo A. Jardiolin, Peter Buckley et al. 1982. Mathematical Field Model Predicts Downhole Density Changes In Static Drilling Fluids. Proc., SPE Annual Technical Conference and Exhibition, New Orleans, Louisiana, 11. doi: 10.2118/11118-MS.
- Sousa, Pedro Cavalcanti de, Artur P. Garcia, Paulo J. Waltrich. 2017a. Analytical Development of a Dynamic IPR for Transient Two-Phase Flow in Reservoirs. Proc., SPE Annual Technical Conference and Exhibition, San Antonio, Texas, USA, 14. doi: 10.2118/187232-MS.
- Sousa, Pedro Cavalcanti de, Artur P. Garcia, Paulo J. Waltrich. 2017b. Investigation of Pressure Profiles of Reservoirs with Wells under Transient, Unstable Flow. Proc., SPE Annual Technical Conference and Exhibition, San Antonio, Texas, USA, 18. doi: 10.2118/187178-MS.
- Sousa, Pedro Cavalcanti de, Artur P. Garcia, Paulo J. Waltrich. 2017c. A Transient Inflow Performance Relationship (IPR) for the Early and Late Life of Gas Wells: The Dynamic Gas IPR. Proc., 36th International Conference on Ocean, Offshore and Arctic Engineering, Trondheim, Norway.
- Stiff, Henry A., Jr. 1970. Interpolating or Extrapolating Drilling Fluid Viscosities to Reference Temperatures. *Journal of Petroleum Technology* **22** (10): 1247-1248. doi: 10.2118/3154-PA.

- Sun, Baojiang. 2016. Multiphase Flow in Oil and Gas Well Drilling. In, 89. Singapore, John Wiley & Sons.
- Sun, Xiaohui, Baojiang Sun, Shuai Zhang et al. 2018. A new pattern recognition model for gas kick diagnosis in deepwater drilling. *Journal of Petroleum Science and Engineering* **167**: 418-425. doi: <https://doi.org/10.1016/j.petrol.2018.04.035>.
- Suryanarayana, P. V., Kennedy, Ravimadhav N. Vaidya et al. 2007. Use of a New Rate-Integral Productivity Index in Interpretation of Underbalanced Drilling Data for Reservoir Characterization. Proc., Production and Operations Symposium, Oklahoma City, Oklahoma, U.S.A., 7. doi: 10.2118/106756-MS.
- Sutton, R. P. 1985. Compressibility Factors for High-Molecular-Weight Reservoir Gases. Proc., SPE Annual Technical Conference and Exhibition, Las Vegas, Nevada, 16. doi: 10.2118/14265-MS.
- Thomas, David C., James F. Lea, Jr., E. A. Turek. 1984. Gas Solubility in Oil-Based Drilling Fluids: Effects on Kick Detection. *Journal of Petroleum Technology* **36** (06): 959-968. doi: 10.2118/11115-PA.
- Torsvik, A, V Myrseth, H Linga. 2015. Drilling Fluid Rheology at Challenging Drilling Conditions—An Experimental Study Using a 1000 Bar Pressure Cell. *Annual Trans. of the Nordic Rheology Society* **22**: 45-51.
- Torsvik, Anja, Jan Ole Skogestad, Harald Linga. 2017. An Experimental Study of Gas Influx in Oil-Based Drilling Fluids for Improved Modeling of High-Pressure, High-Temperature Wells. *SPE Drilling & Completion* **32** (04): 245-254. doi: 10.2118/178860-PA.
- Vefring, Erlend H., Gerhard H. Nygaard, Rolf J. Lorentzen et al. 2006. Reservoir Characterization During Underbalanced Drilling (UBD): Methodology and Active Tests. *SPE Journal* **11** (02): 181-192. doi: 10.2118/81634-PA.
- Waltrich, Paulo J., Matheus S. Capovilla, Woonchan Lee et al. 2019. Experimental Evaluation of Wellbore Flow Models Applied to Worst-Case-Discharge Calculations for Oil Wells. *SPE Drilling & Completion* **34** (03): 315-333. doi: 10.2118/184444-PA.
- Wang, Ning, Baojiang Sun, Peibin Gong et al. 2017. Improved Void Fraction Correlation for Two-Phase Flow in Large-Diameter Annuli. *Chemical Engineering & Technology* **40** (4): 745-754. doi: 10.1002/ceat.201600119.
- Watson, D., T. Brittenham, P.L. Moore. 2003. *Advanced Well Control*, vi, 134, 135, 149, 150, 216-220, Society of Petroleum Engineers (Reprint).

- Weintritt, D. J., R. G. Hughes. 1965. Factors Involved in High-Temperature Drilling Fluids. *Journal of Petroleum Technology* **17** (06): 707-716. doi: 10.2118/1043-PA.
- Xu, Zhengming, Xianzhi Song, Gensheng Li et al. 2018. Development of a transient non-isothermal two-phase flow model for gas kick simulation in HTHP deep well drilling. *Applied Thermal Engineering* **141**: 1055-1069. doi: <https://doi.org/10.1016/j.applthermaleng.2018.06.058>.
- Zamora, M., P. N. Broussard, M. P. Stephens. 2000. The Top 10 Mud-Related Concerns in Deepwater Drilling Operations. Proc., SPE International Petroleum Conference and Exhibition in Mexico, Villahermosa, Mexico, 9. doi: 10.2118/59019-MS.
- Zamora, Mario, Sanjit Roy, Kenneth Slater. 2013. Issues With the Density and Rheology of Drilling Fluids Exposed to Extreme Temperatures and Pressures. Proc., ASME 2013 32nd International Conference on Ocean, Offshore and Arctic Engineering, Vol. Volume 6: Polar and Arctic Sciences and Technology; Offshore Geotechnics; Petroleum Technology Symposium. doi: 10.1115/omae2013-11428.
- Zamora, Mario, Sanjit Roy, Kenneth S. Slater et al. 2013. Study on the Volumetric Behavior of Base Oils, Brines, and Drilling Fluids Under Extreme Temperatures and Pressures. *SPE Drilling & Completion* **28** (03): 278-288. doi: 10.2118/160029-PA.
- Zhao, Quanbin, Takashi Hibiki. 2019. One-dimensional drift-flux correlation for vertical upward two-phase flow in large size concentric and eccentric annuli. *International Journal of Multiphase Flow* **113**: 33-44.

APPENDIX A

The routines used to simulate the Dynamic IPR and Dynamic Influx Model were run in MATLAB. Below, we have transcripts of these routines.

This first routine is used to plot Figure 2.10. The functions DIPR_liquid, and DIPR_gas are given in the end.

```
%%Pseudopressure and pressure vectors below from Petroleum Production
%Systems book, 2nd Ed., Table 4-6
mVec = (6894.76^2)/(1e-3) * [8.917e5; 3.548e6; 7.931e6; 1.401e7;
2.174e7; 3.108e7; 4.202e7; 5.450e7; 6.849e7; 8.396e7; 1.1009e8;
1.192e8; 1.389e8; 1.598e8; 1.821e8; 2.056e8; 2.303e8; 2.562e8; 2.831e8;
3.111e8; 3.401e8; 3.700e8; 4.009e8; 4.326e8; 4.651e8; 4.984e8; 5.324e8;
5.670e8; 6.023e8; 6.381e8; 6.745e8; 7.114e8; 7.487e8; 7.864e8; 8.245e8;
8.630e8; 9.018e8; 9.408e8; 9.802e8; 1.020e9; 1.059e9; 1.099e9; 1.139e9;
1.180e9; 1.220e9; 1.260e9; 1.301e9; 1.342e9; 1.382e9; 1.423e9];
pVec = 6894.76 * [100; 200; 300; 400; 500; 600; 700; 800; 900; 1000;
1100; 1200; 1300; 1400; 1500; 1600; 1700; 1800; 1900; 2000; 2100; 2200;
2300; 2400; 2500; 2600; 2700; 2800; 2900; 3000; 3100; 3200; 3300; 3400;
3500; 3600; 3700; 3800; 3900; 4000; 4100; 4200; 4300; 4400; 4500; 4600;
4700; 4800; 4900; 5000];

rw = 0.0999744; %7" ID
re = sqrt(160*43560/pi) * 0.3048; %from example 4-6 of PPS book
k = 0.17 * 9.86923e-16;
h = 23.7744;
u = 23.5e-6; %viscosity of methane at Pwf and 100F %1cP = 1e-3 Pa.s
c = 1.08e-4 * 1.45038e-4; %ct = 5.0e-6 psi^-1
phi = 0.14;
T = (180-32) / 9 * 5 + 273.15;
Pe = 4613 * 6894.76; %1 psi = 6894.76 Pa
Pwf = 4000 * 6894.76;
f = 2e-8;
N = 1000;
tMAX = 600 * 24 * 60 * 60;
t = linspace(0,tMAX,N);
P = 6894.76 * 4000 * ones(1, N);
Gid = DIPR_gas( rw, re, k, h, u, c, phi, T, Pe, pVector, mVector, order
);
[Q_final, ~] = lsim(Gid, Pe - P, t);
```

This next routine is used in Section 3.3.1. The variables t_BHP , BHP , t_Q , and Q were obtained by extracting data from the plots given in Vefring et al. (2006).

```
Pe_zones = 1e5 * [230,260,220,220,240,280,230,230,250,220]; %bara
k_zones = 9.86923e-16 * [300,600,400,100,50,800,200,300,100,400]; %mD
twf = linspace(0, 1200*60, 1200*60 + 1);
Pwf = interp1(t_BHP, BHP, twf, 'linear', 'extrap');
S = 0;
rw = 0.067*exp(-S);
re = 1000;
h = 1;
u = 0.05; %lcP = 1e-3 Pa.s
c = 2.18e-9;
phi = 0.15;
order = 20;
Q_zones = zeros(size(twf,2),10);
for i = 1:10
    k = k_zones(i);
    Pe = Pe_zones(i);
    DIPR_current = DIPR_liquid( rw, re, k, h, u, c, phi, Pe, Pwf, twf,
order );
    twf_current = twf((i-1)*6000+1:72001) - (i-1)*6000;
    Pwf_current = Pwf((i-1)*6000+1:72001);
    [Q_current, ~] = lsim(DIPR_current, Pe - Pwf_current, twf_current);
    %time response
    h_at_twf = 30 * ones(size(twf_current,2),1);
    h_at_twf(1:6000) = twf_current(1:6000)' * 0.005;
    Q_zones((i-1)*6000+1:72001,i) = Q_current .* h_at_twf;
end
Q_final = zeros(size(twf,2),1);
for i = 1:10
    Q_final = Q_final + Q_zones(:,i);
end
```

This routine is used in Section 3.3.2. The variables t_BHP , BHP , t_Qcom , $Qcom$, t_Qmeas , $Qmeas$, k_zones , h_zones were obtained by extracting data from the figures given in Farshidi et al. (2008).

```
clear
timeDelay = 5 * 24 * 60 * 60;
pVector =
[1000000,1200000,1400000,1600000,1800000,2000000,2200000,2400000,260000
0,2800000,3000000,3200000,3400000,3600000,3800000,4000000,4200000,44000
00,4600000,4800000,5000000,5200000,5400000,5600000,5800000,6000000,6200
000,6400000,6600000,6800000,7000000];
mVector =
[7.84673648203965e+16,1.12999208018756e+17,1.53820866742719e+17,2.00931
```

```

504368805e+17,2.54328527521371e+17,3.14007587595853e+17,3.7996258358217
6e+17,4.52185666179681e+17,5.30667243193095e+17,6.15395986197310e+17,7.
06358838457107e+17,8.03541024086251e+17,9.06926058428743e+17,1.01649575
964353e+18,1.13223026147248e+18,1.25410802716979e+18,1.38210586457002e+
18,1.51619894227019e+18,1.65636080690058e+18,1.80256340145710e+18,1.954
77708466782e+18,2.11297065136461e+18,2.27711135383002e+18,2.44716492408
907e+18,2.62309559711420e+18,2.80486613491161e+18,2.99243785145632e+18,
3.18577063844265e+18,3.38482299181667e+18,3.58955203905674e+18,3.799913
56716794e+18];
zVector =
[0.990085103279642,0.988149926764654,0.986231429144463,0.98432992914926
6,0.982445745043548,0.980579194476322,0.978730594332653,0.9769002605845
07,0.975088508144525,0.973295650720390,0.971522000670076,0.969767868860
316,0.968033564526256,0.966319395133562,0.964625666242470,0.96295268137
6042,0.961300741888676,0.959670146838327,0.958061192862667,0.9564741740
57238,0.954909381854496,0.953367104909704,0.951847628984695,0.950351236
839293,0.948878208119878,0.947428819256537,0.946003343353534,0.94460205
0092871,0.943225205628036,0.941873072489240,0.940545909480067];
twf1 = linspace(0, 1199 + timeDelay, 1200 + timeDelay);
%Pwf1 = 3000 * 1000 + (BHP(1) - 3000*1000)/twf1(end) * twf1;
Pwf1 = BHP(1) * ones(1, size(twf1,2));
twf2 = linspace(1200 + timeDelay, 15800 + timeDelay, (15800-1200) + 1);
Pwf2 = interp1(t_BHP, BHP, twf2,'linear','extrap');
twf = [twf1, twf2];
Pwf = [Pwf1, Pwf2];

T = 200;
T = (T - 32) / 9 * 5 + 273.15;
Pe = 6000 * 1000;
hr = 6;
rw = 0.076;
re = 400/2; %Furui, corresponds to 1300 ft spacing between wells
u = 0.0137e-3; %lcP = 1e-3 Pa.s
c = 1.856e-7;
phi = 0.10;
Sz_zones = 1.1513 * 2 * hr ./ h_zones * log(hr / (2*pi*rw));
req_zones = rw.*exp(-Sz_zones);

S = 0;
Iani = 1;

S_Furui = pi*re/hr/Iani - 1.917 + S;

order = 15;
numZones = 13;
Q_zones = zeros(size(twf,2), numZones);
mPe = mInt( pVector, mVector, Pe );
mPwf = mInt( pVector, mVector, Pwf );
drawdown = mPe - mPwf;
Psc = 101324;
Tsc = 15.55 + 273.15; %60F
zwf = interp1(pVector, zVector, Pwf);
for i = 1:numZones

```



```

k = k_zones(i);
h = h_zones(i);
Sz = Sz_zones(i);
req = req_zones(i);
DIPR_current = DIPR_gas( rw*exp(-S_Furui), hr, k, h, u, c, phi, T,
Pe, pVector, mVector, order ); %Furui model
[Q_current, ~] = lsim(DIPR_current, drawdown, twf); %time response
Q_zones(:,i) = Q_current;
end

Q_final = zeros(size(twf,2),1);
for i = 1:10
    Q_final = Q_final + Q_zones(:,i);
end

```

The proper Dynamic IPR functions follow. They are divided by case. First we present the undersaturated oil reservoir DIPR. All auxiliary functions used in the body of the main function are given in the end.

```

function Gid = DIPR_liquid( rw, re, k, h, u, c, phi, Pe, Pwf, twf,
order )

A = (phi*u*c)/k;

%Productivity index
J = 2*pi*k*h/u/log(re/rw);

Freq = logspace(-12,2,2000);
Awf = 50 * 6894.76;
for i = 1:length(Freq)
    f = Freq(i);
    w = 2*pi*f;

    rhow = sqrt(A*w)*rw;
    rhoe = sqrt(A*w)*re;
    W = [0 -Awf 0 0]';

    %Boundary conditions
    M = [ber0(rhow) bei0(rhow) ker0(rhow) kei0(rhow);
        -bei0(rhow) ber0(rhow) -kei0(rhow) ker0(rhow);
        ber0(rhoe) bei0(rhoe) ker0(rhoe) kei0(rhoe);
        -bei0(rhoe) ber0(rhoe) -kei0(rhoe) ker0(rhoe)];

    X = lsqlin(M,W);

    absoluteValue(i) = (2*pi*k*h/u)*rw*sqrt(A*w)*sqrt(DF(rhow,X)^2
+ DG(rhow,X)^2)*86400/Awf;

```

```

        phaseAngle(i) = atan(DF(rhow,X)/DG(rhow,X));

        if ~isreal(DF(rhow,X)) || ~isreal(DG(rhow,X))
            pause
        end

    end

    Complex = absoluteValue.*exp(1i.*phaseAngle);
    W0 = (2*pi*Freq)';

    sys = frd(Complex, Freq, 'FrequencyUnit', 'Hz');
    Gid = tfest(sys, order, order);
end

```

Now we give the gas reservoir DIPR.

```

function [Gid] = DIPR_gas( rw, re, k, h, u, c, phi, T , Pe, pVector,
mVector, order )
%Computing DIPR
Psc = 101324;
Tsc = 15.55 + 273.15; %60F
A = (phi*u*c)/k;
Freq = logspace(-10,0,2000);
mPwf = mInt( pVector, mVector, Pe );
mAwf = mInt( pVector, mVector, Pe + 50 * 6894.76 );
mAwf = mAwf - mPwf;
absoluteValue = zeros(1,length(Freq));
phaseAngle = zeros(1,length(Freq));
for i = 1:length(Freq)
    f = Freq(i);
    w = 2*pi*f;

    rhow = sqrt(A*w)*rw;
    rhoe = sqrt(A*w)*re;
    W = [0 mAwf 0 0]';

    %B.C.
    M = [ber0(rhow) bei0(rhow) ker0(rhow) kei0(rhow);
        -bei0(rhow) ber0(rhow) -kei0(rhow) ker0(rhow);
        ber0(rhoe) bei0(rhoe) ker0(rhoe) kei0(rhoe);
        -bei0(rhoe) ber0(rhoe) -kei0(rhoe) ker0(rhoe)];
    X = lsqlin(M,W);

    absoluteValue(i) =
    pi*k*h*(Tsc/Psc)*(rw/T)*sqrt(A*w)*sqrt(DF(rhow,X)^2 +
    DG(rhow,X)^2)*86400/abs(mAwf);
    phaseAngle(i) = atan(DF(rhow,X)/DG(rhow,X));
end

Complex = absoluteValue .* exp(1i.*phaseAngle);

```

```

sys = frd(Complex, Freq, 'FrequencyUnit', 'Hz');
Gid = tfest(sys, order, order);
end

```

Finally, the auxiliary functions.

```

%***BESSEL FUNCTIONS*****
function y = ber0(x)
    y = real(besseli(0,x*1i^(-1/2)));
end

function y = bei0(x)
    y = -imag(besseli(0,x*1i^(-1/2)));
end

function y = ker0(x)
    y = real(besselk(0,x*1i^(-1/2)));
end

function y = kei0(x)
    y = -imag(besselk(0,x*1i^(-1/2)));
end

function y = ber1(x)
    y = real(besseli(1,x*1i^(-1/2))/1i);
end

function y = bei1(x)
    y = -imag(besseli(1,x*1i^(-1/2))/1i);
end

function y = ker1(x)
    y = real(1i*besselk(1,x*1i^(-1/2)));
end

function y = kei1(x)
    y = -imag(1i*besselk(1,x*1i^(-1/2)));
end

%***FIRST ORDER DERIVATIVES*****
function y = Dber0(x)
    y = (ber1(x)+bei1(x))/sqrt(2);
end

function y = Dbei0(x)
    y = (bei1(x)-ber1(x))/sqrt(2);
end

function y = Dker0(x)
    y = (ker1(x)+kei1(x))/sqrt(2);
end

```

```

end

function y = Dkei0(x)
    y = (kei1(x)-ker1(x))/sqrt(2);
end

%***SECOND ORDER DERIVATIVES*****
function y = D2ber0(x)
    y = -bei0(x)-(1/x)*Dber0(x);
end

function y = D2bei0(x)
    y = ber0(x)-(1/x)*Dbei0(x);
end

function y = D2kei0(x)
    y = ker0(x)-(1/x)*Dkei0(x);
end

function y = D2ker0(x)
    y = -kei0(x)-(1/x)*Dker0(x);
end

%***DIFFUSIVITY SOLUTION WITH BESSEL FUNCTIONS*****
function f = F(r,X)
    a = X(1); b = X(2); c = X(3); d = X(4);
    f = a*ber0(r) + b*bei0(r) + c*ker0(r) + d*kei0(r);
end

function g = G(r,X)
    a = X(1); b = X(2); c = X(3); d = X(4);
    g = b*ber0(r,X) - a*bei0(r) + d*ker0(r) - c*kei0(r);
end

function Df = DF(r,X)
    a = X(1); b = X(2); c = X(3); d = X(4);
    Df = a*Dber0(r) + b*Dbei0(r) + c*Dker0(r) + d*Dkei0(r);
end

function Dg = DG(r,X)
    a = X(1); b = X(2); c = X(3); d = X(4);
    Dg = b*Dber0(r) - a*Dbei0(r) + d*Dker0(r) - c*Dkei0(r);
end

function D2f = D2F(r,X)
    a = X(1); b = X(2); c = X(3); d = X(4);
    D2f = a*D2ber0(r) + b*D2bei0(r) + c*D2ker0(r) + d*D2kei0(r);
end

function D2g = D2G(r,X)
    a = X(1); b = X(2); c = X(3); d = X(4);

```

```

    D2g = b*D2ber0(r) - a*D2bei0(r) + d*D2ker0(r) - c*D2kei0(r);
end

function p = prt(r,t,A,w,X)
    rho = sqrt(A*w)*r;
    p = F(rho,X)*cos(w*t) + G(rho,X)*sin(w*t);
end

function Dp = Dprt(r,t,A,w,X)
    rho = sqrt(A*w)*r;
    Dp = sqrt(A*w)*(DF(rho,X)*cos(w*t) + DG(rho,X)*sin(w*t));
end

function D2p = D2prt(r,t,A,w,X)
    rho = sqrt(A*w)*r;
    D2p = D2F(rho,X)*cos(w*t) + D2G(rho,X)*sin(w*t);
end

%*****INTERPOLATIONS FOR mp*****
function mP = mInt(Pvec,mvec,P)
    mP = interp1(Pvec, mvec, P, 'spline');
end

function Pi = pInt(mvec,Pvec,m)
    Pi = interp1(mvec, Pvec, m, 'spline');
end

```

APPENDIX B

Here we present the treated data divided into two tables. Table B.1 lists the average shear stress for each test, while Table B.2 lists the relative uncertainty for each one of those measurements considering a 95 % confidence interval.

Sample	Temp. (° F)	Press. (psig)	Shear stresses (dyne / cm ²) at different angular velocities (RPM)								Gel-strength	
			600	300	250	200	150	100	6	3	10-sec	10-min
OBM1_s1	100	2000	2917.6	1931.7	-	1469.0	-	938.2	191.8	148.1	147.2	240.9
OBM1_s1	100	5000	3952.5	2396.1	-	1850.9	-	1190.2	216.8	164.6	149.4	290.0
OBM1_s1	100	10000	6348.1	3710.7	-	2815.8	-	1803.6	323.4	238.2	220.8	406.0
OBM1_s1	100	15000	-	5715.1	-	4221.1	-	2633.8	493.0	361.3	345.7	524.2
OBM1_s1	100	20000	-	-	7442.9	6296.8	-	3839.2	721.8	509.0	472.9	791.8
OBM1_s1	100	25000	-	-	12790.8	8386.4	-	5505.9	1238.0	908.3	785.2	1133.1
OBM1_s1	100	30000	-	-	6238.8	8807.5	-	6158.5	1494.9	1179.5	992.6	1394.1
OBM1_s1	100	35000	-	-	12426.8	12322.0	-	8159.8	1767.5	1470.8	1293.7	2123.5
OBM1_s1	150	5000	2209.6	1407.0	-	1055.9	-	689.2	169.5	142.3	131.6	247.6
OBM1_s1	150	10000	3300.3	1987.0	-	1486.0	-	994.8	232.0	190.5	165.1	713.8
OBM1_s1	150	15000	-	2736.9	-	2046.3	-	1355.3	293.1	234.7	238.7	363.6
OBM1_s1	150	20000	-	-	3318.6	2862.7	-	1829.0	386.8	305.6	254.3	539.8
OBM1_s1	150	25000	-	-	4740.8	4078.3	-	2504.5	535.8	421.6	439.0	1420.4
OBM1_s1	150	30000	-	-	6942.4	5922.1	-	3552.8	780.7	606.7	568.8	1929.4
OBM1_s1	150	35000	-	-	5834.7	7833.2	-	4994.6	1250.0	1002.4	970.3	1492.2
OBM1_s1	200	2000	1938.3	1333.4	-	1072.0	-	779.4	361.3	370.3	421.6	499.6
OBM1_s1	200	5000	2309.5	1602.0	-	1319.1	-	931.9	389.0	392.6	388.1	606.7
OBM1_s1	200	10000	3005.0	2047.2	-	1646.6	-	1185.8	457.7	451.5	510.8	633.5
OBM1_s1	200	15000	-	2592.3	-	2115.9	-	1474.8	548.3	525.5	579.9	1153.2
OBM1_s1	200	20000	-	-	2910.0	2543.3	-	1796.0	646.4	605.4	564.3	1481.1
OBM1_s1	200	25000	-	-	3647.8	3167.4	-	2188.2	751.2	688.3	597.8	1581.5
OBM1_s1	200	30000	-	-	4769.4	4144.8	-	2746.2	943.5	852.1	865.5	1521.2
OBM1_s1	200	35000	-	-	6400.8	5521.9	-	3668.8	1225.0	1090.3	1427.6	2371.1
OBM1_s2	100	2000	3210.6	2136.4	-	1702.4	-	1176.4	290.9	241.8	198.5	646.9
OBM1_s2	100	5000	4574.4	2839.5	-	2238.1	-	1548.9	363.1	296.2	232.0	553.2
OBM1_s2	100	10000	7212.3	4417.8	-	3459.6	-	2339.8	596.4	479.6	385.9	579.9

Sample	Temp. (° F)	Press. (psig)	Shear stresses (dyne / cm ²) at different angular velocities (RPM)								Gel-strength	
			600	300	250	200	150	100	6	3	10-sec	10-min
OBM1_s2	100	15000	-	6711.7	-	5175.8	-	3378.4	880.2	685.2	693.7	934.6
OBM1_s2	100	20000	-	-	8552.4	7478.6	-	4851.9	1347.3	1048.8	905.6	1269.2
OBM1_s2	100	25000	-	-	8991.8	10253.8	-	6039.9	1851.4	1550.2	1164.3	1974.0
OBM1_s2	100	30000	-	-	6039.4	6997.2	-	5147.7	1280.3	1136.7	974.7	1197.8
OBM1_s2	100	35000	-	-	9997.3	8494.4	-	6003.3	1672.5	1278.5	988.1	1362.9
OBM1_s2	150	2000	2380.0	1567.6	-	1267.0	-	885.5	282.4	259.2	191.8	724.9
OBM1_s2	150	5000	3007.2	1983.8	-	1605.1	-	1127.3	346.6	307.4	263.2	493.0
OBM1_s2	150	10000	4215.7	2707.4	-	2209.1	-	1519.4	440.3	377.0	296.7	544.3
OBM1_s2	150	15000	-	3667.9	-	2896.6	-	2010.2	578.6	484.0	392.6	1280.3
OBM1_s2	150	20000	-	-	4401.3	3747.3	-	2572.7	723.1	593.8	506.3	1010.4
OBM1_s2	150	25000	-	-	5986.8	5172.6	-	3381.5	945.8	764.2	680.3	1164.3
OBM1_s2	150	30000	-	-	9052.0	7619.1	-	4678.3	1327.6	1067.1	1101.9	1456.5
OBM1_s2	150	35000	-	-	7614.2	8747.3	-	6203.6	1883.5	1498.5	1536.8	3080.4
OBM1_s2	200	2000	1665.3	1107.2	-	870.4	-	619.7	227.5	228.4	316.7	356.9
OBM1_s2	200	5000	2018.7	1322.3	-	1036.8	-	718.2	244.0	237.8	225.3	379.2
OBM1_s2	200	10000	2718.2	1734.5	-	1396.3	-	927.5	309.6	293.5	419.3	791.9
OBM1_s2	200	15000	-	2363.0	-	1889.7	-	1317.8	461.3	434.5	381.4	1081.8
OBM1_s2	200	20000	-	-	2763.7	2407.7	-	1703.3	603.1	564.3	562.1	1017.1
OBM1_s2	200	25000	-	-	3618.4	3075.0	-	2148.0	759.7	701.3	869.9	1351.7
OBM1_s2	200	30000	-	-	4840.3	4313.0	-	2847.1	1014.5	923.0	1133.1	1764.4
OBM1_s2	200	35000	-	-	6870.5	5823.1	-	3922.2	1414.6	1238.8	1371.8	2872.9
OBM1_gas	100	2000	3633.6	2449.6	-	2020.9	-	1361.5	319.4	249.8	276.6	334.6
OBM1_gas	100	5000	5040.1	3235.2	-	2546.8	-	1740.3	400.2	323.0	285.5	678.1
OBM1_gas	100	10000	7575.8	4789.0	-	3772.7	-	2606.6	669.6	556.3	481.8	626.8
OBM1_gas	100	15000	-	6767.0	-	5326.1	-	3684.0	1088.5	906.0	698.2	1126.4
OBM1_gas	100	20000	-	-	8330.2	7341.2	-	5022.7	1511.4	1268.3	1048.4	1570.3

Sample	Temp. (° F)	Press. (psig)	Shear stresses (dyne / cm ²) at different angular velocities (RPM)							Gel-strength		
			600	300	250	200	150	100	6	3	10-sec	10-min
OBM1_gas	100	25000	-	-	3378.4	1473.9	-	1249.1	587.1	462.6	455.0	1026.1
OBM1_gas	100	30000	-	-	2251.5	1442.3	-	1879.0	431.4	559.0	528.6	818.6
OBM1_gas	100	35000	-	-	3082.2	4557.0	-	2734.7	1145.2	767.3	481.8	894.4
OBM1_gas	150	2000	2713.7	1821.5	-	1475.7	-	1014.0	334.1	303.4	336.8	452.8
OBM1_gas	150	5000	3274.4	2206.9	-	1759.9	-	1249.1	408.2	365.4	327.0	833.3
OBM1_gas	150	10000	4602.5	3069.2	-	2501.3	-	1779.5	620.5	566.1	590.6	1083.6
OBM1_gas	150	15000	-	4042.6	-	3268.2	-	2337.2	858.8	775.8	624.6	1153.2
OBM1_gas	150	20000	-	-	4807.3	4298.7	-	3045.6	1075.6	968.9	874.4	1168.8
OBM1_gas	150	25000	-	-	6316.9	5546.9	-	3939.1	1502.1	1320.0	1110.8	1719.8
OBM1_gas	150	30000	-	-	6997.2	4297.4	-	1986.5	484.9	377.4	633.5	756.2
OBM1_gas	150	35000	-	-	3147.7	2790.4	-	857.0	292.2	213.2	307.8	1017.1
OBM1_gas	200	2000	2090.5	1449.9	-	1204.0	-	887.8	426.0	435.4	417.1	477.3
OBM1_gas	200	5000	2466.1	1733.6	-	1405.7	-	1065.3	505.4	497.4	484.0	604.5
OBM1_gas	200	10000	3208.4	2231.4	-	1845.1	-	1379.8	631.7	619.2	508.6	885.5
OBM1_gas	200	15000	-	2812.7	-	2352.3	-	1754.5	809.2	803.9	751.7	1137.6
OBM1_gas	200	20000	-	-	3197.7	2888.1	-	2173.0	949.8	928.4	762.8	1467.7
OBM1_gas	200	25000	-	-	4090.8	3629.1	-	2659.7	1161.7	1063.1	921.2	1336.1
OBM1_gas	200	30000	-	-	5235.1	4231.3	-	3198.6	1679.6	1590.8	225.3	95.9
OBM1_gas	200	35000	-	-	2.7	21.0	-	91.0	155.2	160.6	24.5	2.2
SBM_contam	100	2000	352.0	185.6	-	115.5	-	45.5	-	-	-	20.1
SBM_contam	100	5000	502.3	231.1	-	150.3	-	67.8	-	-	-	15.6
SBM_contam	100	10000	723.1	341.7	-	245.4	-	111.1	-	-	-	31.2
SBM_contam	100	15000	979.2	484.5	-	315.8	-	144.1	-	-	-	26.8
SBM_contam	100	20000	1285.2	643.7	-	441.6	-	203.4	-	-	-	15.6
SBM_contam	100	25000	1740.7	873.9	-	574.6	-	280.2	6.2	-	-	35.7
SBM_contam	150	5000	249.4	114.7	-	83.4	-	29.9	-	-	4.5	17.8

Sample	Temp. (° F)	Press. (psig)	Shear stresses (dyne / cm ²) at different angular velocities (RPM)								Gel-strength	
			600	300	250	200	150	100	6	3	10-sec	10-min
SBM_contam	150	10000	368.0	177.6	-	122.7	-	53.1	-	-	-	29.0
SBM_contam	150	15000	488.5	236.4	-	167.7	-	66.9	-	-	4.5	35.7
SBM_contam	150	20000	680.3	353.3	-	232.4	-	125.4	26.8	15.6	22.3	37.9
SBM_contam	150	25000	861.9	438.5	-	305.1	-	159.3	29.0	25.9	35.7	42.4
SBM_contam	150	30000	1137.6	549.6	-	365.8	-	193.6	25.4	22.3	31.2	35.7
SBM_contam	150	35000	1325.8	660.2	-	425.1	-	209.2	11.2	4.0	-	35.7
SBM_contam	200	5000	204.8	108.9	-	87.9	-	42.8	18.3	12.9	11.2	13.4
SBM_contam	200	10000	232.9	120.9	-	80.7	-	38.4	3.6	1.8	13.4	13.4
SBM_contam	200	15000	292.6	134.3	-	76.7	-	38.4	-	-	6.7	11.2
SBM_contam	200	20000	378.7	179.3	-	116.0	-	55.3	-	-	4.5	22.3
SBM_contam	200	25000	486.3	240.9	-	152.1	-	81.2	0.9	-	-	29.0
SBM_contam	200	30000	608.9	309.6	-	196.3	-	105.7	8.5	3.1	0.0	24.5
SBM_contam	200	35000	796.3	392.6	-	229.7	-	137.0	22.3	17.4	13.4	40.1
SBM_contam	250	5000	148.1	50.9	-	67.8	-	13.4	-	-	0.0	2.2
SBM_contam	250	10000	186.9	64.7	-	35.2	-	14.3	-	-	0.0	2.2
SBM_contam	250	15000	208.8	81.6	-	72.3	-	15.6	-	-	-	0.0
SBM_contam	250	20000	268.6	139.2	-	88.8	-	38.4	3.6	1.3	17.8	2.2
SBM_contam	250	25000	322.1	142.8	-	119.1	-	41.5	-	-	-	2.2
SBM_contam	250	30000	410.4	211.0	-	107.1	-	66.5	5.4	3.6	17.8	4.5
SBM_contam	250	35000	465.7	219.9	-	143.6	-	61.6	-	-	-	2.2
SBM_contam	300	5000	113.3	44.2	-	10.7	-	4.5	-	-	-	0.0
SBM_contam	300	10000	157.5	82.5	-	39.7	-	17.0	5.8	4.0	6.7	2.2
SBM_contam	300	15000	197.2	79.9	-	49.5	-	15.6	-	-	0.0	0.0
SBM_contam	300	20000	225.3	99.5	-	61.6	-	20.5	-	-	0.0	0.0
SBM_contam	300	25000	272.1	123.6	-	92.8	-	32.1	-	-	-	0.0
SBM_contam	300	30000	335.5	173.5	-	65.6	-	55.8	8.0	8.0	13.4	4.5

Sample	Temp. (° F)	Press. (psig)	Shear stresses (dyne / cm ²) at different angular velocities (RPM)								Gel-strength	
			600	300	250	200	150	100	6	3	10-sec	10-min
SBM_contam	300	35000	356.9	168.2	-	120.0	-	40.1	-	-	-	2.2
SBM_contam	350	5000	150.8	43.3	-	34.8	-	12.0	7.6	8.0	4.5	0.0
SBM_contam	350	10000	135.6	67.4	-	5.8	-	10.3	3.1	2.7	0.0	0.0
SBM_contam	350	15000	156.1	82.5	-	38.4	-	13.8	-	-	0.0	0.0
SBM_contam	350	20000	227.5	82.5	-	43.3	-	22.8	-	-	-	-
SBM_contam	350	25000	243.1	113.8	-	135.2	-	21.9	-	-	-	2.2
SBM_contam	350	30000	267.7	137.4	-	114.7	-	27.7	-	-	-	0.0
SBM_contam	350	35000	309.2	156.1	-	16.1	-	40.1	-	-	2.2	0.0
SBM_sl_gas	47.5	0	1433.3	662.0	-	460.8	-	255.6	38.8	30.8	24.5	80.3
SBM_sl_gas	47.5	2000	1310.2	746.8	-	523.7	-	290.0	17.8	5.4	8.9	60.2
SBM_sl_gas	47.5	2000	1697.4	918.5	-	643.3	-	372.5	54.4	38.4	55.8	82.5
SBM_sl_gas	47.5	5000	2190.4	1244.6	-	892.2	-	532.2	123.6	106.2	66.9	98.1
SBM_sl_gas	47.5	10000	3175.0	1763.9	-	1280.3	-	718.7	109.7	82.1	60.2	145.0
SBM_sl_gas	47.5	15000	4786.8	2665.9	-	1883.0	-	1068.0	165.5	124.5	102.6	254.3
SBM_sl_gas	47.5	20000	6805.4	3783.9	-	2682.5	-	1544.0	240.0	177.1	167.3	354.7
SBM_sl_gas	47.5	25000	17465.6	9284.4	-	6882.1	-	4219.3	662.5	458.2	477.3	910.1
SBM_sl_gas	100	2000	850.3	482.7	-	357.8	-	209.7	38.4	31.7	31.2	142.8
SBM_sl_gas	100	5000	1074.7	583.5	-	440.8	-	252.9	40.6	29.4	33.5	84.8
SBM_sl_gas	100	10000	1544.9	873.5	-	629.9	-	368.0	60.7	46.4	46.8	89.2
SBM_sl_gas	100	15000	2152.9	1202.3	-	880.6	-	507.2	78.5	57.5	60.2	142.8
SBM_sl_gas	100	20000	2873.4	1622.9	-	1173.7	-	671.4	88.8	59.3	73.6	196.3
SBM_sl_gas	100	25000	4020.3	2235.5	-	1556.9	-	872.1	111.5	74.5	82.5	149.4
SBM_sl_gas	100	30000	5261.0	2918.9	-	2061.9	-	1160.3	150.3	99.0	124.9	171.8
SBM_sl_gas	150	2000	617.0	366.7	-	273.5	-	170.9	40.1	29.9	33.5	111.5
SBM_sl_gas	150	5000	737.4	428.3	-	318.1	-	193.6	36.6	25.0	33.5	162.8
SBM_sl_gas	150	10000	1036.8	581.7	-	432.3	-	259.2	45.1	34.4	37.9	185.1

Sample	Temp. (° F)	Press. (psig)	Shear stresses (dyne / cm ²) at different angular velocities (RPM)								Gel-strength	
			600	300	250	200	150	100	6	3	10-sec	10-min
SBM_sl_gas	150	15000	1397.2	778.9	-	582.2	-	349.3	65.1	52.2	62.5	225.3
SBM_sl_gas	150	20000	1813.4	1051.9	-	763.7	-	455.5	92.8	73.6	75.8	113.8
SBM_sl_gas	150	25000	2249.7	1296.8	-	941.3	-	554.1	95.5	70.5	73.2	115.5
SBM_sl_gas	150	30000	2907.7	1631.0	-	1155.0	-	674.1	109.7	78.1	84.8	142.8
SBM_sl_gas	200	5000	463.1	269.0	-	211.0	-	132.5	41.5	36.1	35.7	69.1
SBM_sl_gas	200	10000	621.0	377.0	-	286.4	-	179.8	46.8	37.0	44.6	75.8
SBM_sl_gas	200	15000	830.2	497.0	-	380.1	-	232.9	52.2	38.8	40.1	95.9
SBM_sl_gas	200	20000	1123.7	645.5	-	483.1	-	295.8	52.6	38.8	40.1	111.5
SBM_sl_gas	200	25000	1452.5	845.8	-	617.4	-	380.5	78.1	60.2	66.9	140.5
SBM_sl_gas	200	30000	1765.7	1017.6	-	718.7	-	419.3	56.7	39.3	37.9	140.5
SBM_sl_gas	200	35000	2012.8	1157.7	-	834.7	-	499.2	90.1	70.5	69.1	98.1
SBM_sl_gas	250	5000	385.4	235.5	-	178.0	-	108.4	29.4	25.9	31.2	37.9
SBM_sl_gas	250	10000	457.7	268.6	-	197.6	-	111.1	13.4	10.3	4.5	44.6
SBM_sl_gas	250	15000	595.6	353.8	-	267.2	-	153.9	21.4	16.5	20.1	69.1
SBM_sl_gas	250	20000	789.2	481.8	-	367.6	-	232.0	53.5	42.8	51.3	107.1
SBM_sl_gas	250	25000	994.8	582.6	-	430.0	-	264.1	44.2	34.4	31.2	127.1
SBM_sl_gas	250	30000	1309.8	766.0	-	549.6	-	329.2	57.5	41.9	46.8	153.9
SBM_sl_gas	250	35000	1487.3	908.7	-	662.5	-	413.1	92.8	71.8	73.6	147.2
SBM_sl_gas	300	5000	396.1	236.9	-	167.7	-	113.8	26.3	24.1	20.1	29.0
SBM_sl_gas	300	10000	542.5	346.2	-	258.3	-	162.4	45.9	43.7	44.6	51.3
SBM_sl_gas	300	15000	676.3	432.7	-	309.2	-	192.7	49.5	45.5	49.1	55.8
SBM_sl_gas	300	20000	816.4	514.4	-	367.1	-	222.2	55.3	49.5	33.5	64.7
SBM_sl_gas	300	25000	972.5	629.5	-	456.4	-	274.4	90.1	81.6	82.5	104.8
SBM_sl_gas	300	30000	1138.9	699.1	-	510.3	-	298.4	83.0	63.8	62.5	145.0
SBM_sl_gas	350	5000	344.4	207.9	-	158.4	-	103.9	21.4	20.1	20.1	33.5
SBM_sl_gas	350	10000	514.4	334.6	-	266.3	-	175.3	57.1	54.9	35.7	49.1

Sample	Temp. (° F)	Press. (psig)	Shear stresses (dyne / cm ²) at different angular velocities (RPM)								Gel-strength	
			600	300	250	200	150	100	6	3	10-sec	10-min
SBM_sl_gas	350	15000	652.2	430.0	-	317.6	-	207.4	61.1	57.5	37.9	71.4
SBM_sl_gas	350	20000	767.8	507.7	-	317.6	-	222.6	65.1	62.5	40.1	82.5
SBM_sl_gas	350	25000	826.2	510.8	-	372.9	-	236.0	87.0	79.0	60.2	91.5
SBM_sl_gas	350	30000	863.7	566.1	-	169.5	-	211.9	60.7	49.5	53.5	89.2
SBM_sl_gas	350	35000	1054.2	713.8	-	147.7	-	209.7	70.9	59.3	42.4	95.9
SBM_sl_gas	400	5000	211.0	270.3	-	190.9	-	130.7	65.1	68.7	40.1	62.5
SBM_sl_gas	400	10000	535.3	325.2	-	260.5	-	185.6	100.8	95.0	87.0	124.9
SBM_sl_gas	400	15000	678.1	416.2	-	166.4	-	118.7	45.5	40.6	22.3	133.8
SBM_sl_gas	400	20000	414.4	33.5	-	213.2	-	170.4	75.8	66.9	37.9	58.0
SBM_sl_gas	400	25000	198.1	112.0	-	136.1	-	84.3	20.1	17.4	51.3	49.1
SBM_sl_gas	400	30000	365.8	91.0	-	45.5	-	41.5	91.0	98.1	102.6	42.4
SBM_sl_gas	400	35000	161.0	146.8	-	30.3	-	45.5	92.8	88.8	6.7	64.7
SBM_sl	100	0	766.9	400.6	-	297.6	-	157.5	25.9	18.3	2.2	87.0
SBM_sl	100	2000	877.5	448.3	-	320.3	-	178.0	29.0	22.8	24.5	182.9
SBM_sl	100	5000	1106.8	591.1	-	401.1	-	221.7	31.2	22.3	22.3	98.1
SBM_sl	100	10000	1657.7	944.9	-	662.0	-	371.6	67.4	50.4	55.8	207.4
SBM_sl	100	15000	2465.6	1335.7	-	922.6	-	511.7	72.7	56.7	60.2	147.2
SBM_sl	100	20000	3418.5	1822.8	-	1260.7	-	679.9	82.1	57.1	55.8	198.5
SBM_sl	100	25000	4723.0	2543.7	-	1787.6	-	987.2	142.8	105.7	100.4	214.1
SBM_sl	100	30000	6239.3	3372.6	-	2387.6	-	1312.5	148.1	104.8	93.7	232.0
SBM_sl	150	2000	579.5	330.6	-	241.8	-	164.6	66.9	63.8	95.9	165.1
SBM_sl	150	5000	546.0	306.0	-	220.4	-	135.6	40.1	33.5	60.2	95.9
SBM_sl	150	10000	558.5	312.3	-	238.2	-	148.1	47.7	45.5	58.0	151.7
SBM_sl	150	15000	544.7	301.6	-	228.0	-	140.5	46.4	42.4	62.5	111.5
SBM_sl	150	20000	567.9	323.0	-	219.0	-	160.6	65.1	60.7	73.6	98.1
SBM_sl	150	25000	573.7	326.6	-	256.1	-	162.4	62.5	57.5	64.7	147.2

Sample	Temp. (° F)	Press. (psig)	Shear stresses (dyne / cm ²) at different angular velocities (RPM)								Gel-strength	
			600	300	250	200	150	100	6	3	10-sec	10-min
SBM_s1	150	30000	571.5	335.5	-	233.8	-	158.8	59.3	56.7	82.5	107.1
SBM_s1	200	5000	514.8	281.9	-	220.8	-	145.9	54.0	47.3	69.1	169.5
SBM_s1	200	10000	706.6	397.9	-	289.5	-	176.7	33.9	29.0	49.1	120.4
SBM_s1	200	15000	964.5	567.0	-	440.3	-	256.5	67.4	58.9	62.5	98.1
SBM_s1	200	20000	1266.1	737.0	-	513.9	-	316.7	74.5	61.1	64.7	131.6
SBM_s1	200	25000	1614.0	930.1	-	675.9	-	404.2	85.7	69.1	66.9	122.7
SBM_s1	200	30000	2032.9	1123.3	-	803.0	-	-	73.6	-	-	-
SBM_s1	250	5000	429.2	252.1	-	193.2	-	128.9	45.5	43.7	37.9	80.3
SBM_s1	250	10000	546.9	311.8	-	236.4	-	152.6	34.8	29.9	26.8	58.0
SBM_s1	250	15000	683.9	389.5	-	290.9	-	178.0	27.7	23.6	31.2	104.8
SBM_s1	250	20000	907.4	532.2	-	397.9	-	252.1	58.9	50.9	53.5	133.8
SBM_s1	250	25000	1156.8	664.3	-	488.9	-	307.8	70.5	58.0	55.8	187.4
SBM_s1	250	30000	1435.1	833.8	-	586.6	-	353.8	69.1	53.1	63.3	139.2
SBM_s1	350	5000	426.9	237.8	-	190.5	-	124.0	34.8	32.6	24.5	37.9
SBM_s1	350	10000	592.9	364.0	-	286.8	-	197.2	73.2	69.6	55.8	64.7
SBM_s1	350	15000	737.9	483.1	-	371.6	-	244.0	72.7	56.7	60.2	75.8
SBM_s1	350	20000	940.0	639.7	-	491.6	-	331.0	128.5	119.1	102.6	120.4
SBM_s1	350	25000	1082.3	731.2	-	555.4	-	368.9	120.9	111.1	104.8	138.3
SBM_s1	350	30000	1295.9	857.9	-	675.0	-	464.0	180.2	170.9	138.3	187.4
SBM_s1	400	10000	605.8	403.7	-	310.0	-	218.6	159.3	157.0	149.4	174.0
SBM_s1	400	15000	837.8	522.8	-	395.3	-	285.5	207.9	197.2	189.6	236.4
SBM_s1	400	20000	1039.0	596.0	-	428.3	-	300.2	195.8	167.7	191.8	205.2
SBM_s1	400	25000	1227.7	668.7	-	484.5	-	324.8	184.2	119.1	167.3	216.4
SBM_s1	400	30000	1470.4	777.6	-	571.5	-	371.2	199.4	171.8	167.3	196.3
SBM_s1	400	35000	1693.0	913.6	-	662.0	-	435.8	225.7	195.8	193.6	213.7
OBM2_s1	100	0	1734.2	1045.3	-	784.3	-	503.2	122.8	108.0	67.8	424.0

Sample	Temp. (° F)	Press. (psig)	Shear stresses (dyne / cm ²) at different angular velocities (RPM)								Gel-strength	
			600	300	250	200	150	100	6	3	10-sec	10-min
OBM2_s1	100	2000	2214.7	1279.6	-	947.3	-	583.6	110.2	88.7	67.8	275.4
OBM2_s1	100	5000	2840.2	1640.2	-	1171.6	-	741.0	131.1	90.1	83.1	332.2
OBM2_s1	100	10000	4044.6	2369.0	-	1830.0	-	1126.6	202.4	162.2	122.4	605.5
OBM2_s1	100	15000	5886.8	3416.0	-	2490.5	-	1648.5	283.3	219.0	133.3	579.2
OBM2_s1	100	20000	9431.4	1373.1	-	2170.1	-	2294.2	519.8	403.9	249.2	1169.4
OBM2_s1	150	2000	1464.5	836.7	-	640.0	-	404.4	76.1	67.8	54.6	515.9
OBM2_s1	150	5000	1817.3	1070.2	-	805.7	-	512.4	113.7	98.8	89.6	365.0
OBM2_s1	150	10000	2556.5	1499.5	-	1159.8	-	737.9	156.5	126.3	89.6	452.5
OBM2_s1	150	15000	3511.7	2136.9	-	1624.1	-	1009.4	175.7	141.2	89.6	454.6
OBM2_s1	150	20000	4942.1	3091.2	-	2456.4	-	1517.0	274.1	218.1	153.0	647.0
OBM2_s1	200	2000	996.7	580.6	-	385.1	-	257.1	14.4	7.9	-	378.1
OBM2_s1	200	5000	1256.8	769.0	-	570.1	-	367.7	66.0	53.8	39.3	275.4
OBM2_s1	200	10000	1719.8	1023.4	-	796.1	-	479.6	79.1	61.6	54.6	-
OBM2_s1	200	15000	2260.1	1375.8	-	1033.9	-	633.4	109.7	84.8	65.6	491.8
OBM2_s1	200	20000	2817.1	1704.5	-	1293.6	-	810.1	114.1	79.1	43.7	410.9
OBM2_s1	200	25000	4033.7	2393.5	-	-	-	1243.7	208.1	163.5	107.1	432.8
OBM2_s1	250	5000	918.0	545.1	-	385.1	-	257.9	26.2	8.3	39.3	163.9
OBM2_s1	250	10000	1321.1	785.6	-	634.3	-	412.2	50.7	39.3	21.9	137.7
OBM2_s1	250	15000	1887.2	1193.0	-	953.5	-	608.5	109.3	101.0	48.1	279.8
OBM2_s1	250	20000	2574.5	1574.2	-	1254.2	-	796.9	167.9	159.1	65.6	242.6
OBM2_s1	250	25000	3523.5	2125.5	-	1690.5	-	1148.9	288.1	294.6	128.5	342.7
OBM2_s1	250	30000	4629.1	2900.1	-	2227.8	-	1433.9	327.0	334.4	139.9	470.0
OBM2_s1	250	35000	6103.7	3937.5	-	3009.9	-	1922.2	437.2	440.2	177.1	443.7
OBM2_s1	300	5000	617.3	352.4	-	249.6	-	143.4	0.9	-	10.9	45.9
OBM2_s1	300	10000	936.4	547.8	-	399.6	-	245.2	28.4	13.1	21.9	63.4
OBM2_s1	300	15000	1358.7	783.4	-	574.0	-	345.8	16.6	-	6.6	74.3

Sample	Temp. (° F)	Press. (psig)	Shear stresses (dyne / cm ²) at different angular velocities (RPM)								Gel-strength	
			600	300	250	200	150	100	6	3	10-sec	10-min
OBM2_s1	300	20000	1821.2	1067.6	-	794.8	-	489.2	53.8	41.5	2.2	65.6
OBM2_s1	300	25000	2427.1	1427.3	-	1089.0	-	690.7	121.1	116.7	15.3	174.9
OBM2_s1	300	30000	3302.8	1969.0	-	1473.2	-	977.5	240.0	243.9	104.9	266.7
OBM2_s1	300	35000	3934.0	2385.2	-	1882.9	-	1268.6	353.2	346.7	120.2	382.5
OBM2_s1	350	5000	550.0	326.1	-	230.4	-	99.7	-	-	-	26.2
OBM2_s1	350	10000	816.6	456.8	-	279.3	-	166.6	-	-	-	8.7
OBM2_s1	350	15000	1188.6	678.9	-	487.4	-	273.7	-	-	-	17.5
OBM2_s1	350	20000	1645.9	939.0	-	705.6	-	426.7	37.2	40.7	-	19.7
OBM2_s1	350	25000	2676.3	1525.3	-	1046.1	-	694.7	199.3	198.9	115.8	146.4
OBM2_s1	350	30000	3183.0	1966.4	-	1501.2	-	1068.0	386.0	393.0	174.9	257.9
OBM2_s1	350	35000	3675.7	2195.9	-	1622.3	-	971.8	221.2	210.7	6.6	118.0
OBM2_s1	400	5000	405.7	205.5	-	125.0	-	43.3	-	-	-	0.0
OBM2_s1	400	10000	640.9	344.9	-	230.4	-	117.6	-	-	-	-
OBM2_s1	400	15000	1046.6	553.0	-	391.7	-	186.7	-	-	-	0.0
OBM2_s1	400	20000	1534.9	870.0	-	596.7	-	350.6	66.4	68.6	45.9	2.2
OBM2_s1	400	25000	2028.4	1188.2	-	855.1	-	507.5	137.7	132.5	69.9	6.6
OBM2_s1	400	30000	2551.7	1521.8	-	1057.5	-	623.8	149.9	156.1	0.0	2.2
OBM2_s1	400	35000	3478.5	2257.1	-	1566.8	-	978.8	383.0	383.4	146.4	98.4
OBM2_gas	100	2000	2277.2	1420.3	-	1073.7	-	733.1	191.0	176.6	133.3	397.8
OBM2_gas	100	5000	3401.6	2217.3	-	1772.7	-	1139.7	274.1	252.7	157.4	629.5
OBM2_gas	100	10000	5701.0	3658.6	-	2815.8	-	1817.3	398.7	355.9	338.8	1484.2
OBM2_gas	100	15000	-41744.3	3446.6	-	4014.5	-	2959.2	898.4	787.3	520.2	1228.4
OBM2_gas	100	20000	1335.1	775.1	-	655.3	-	598.5	428.0	543.8	301.6	760.7
OBM2_gas	150	2000	1694.9	1150.6	-	900.1	-	570.1	181.9	162.6	159.6	400.0
OBM2_gas	150	5000	1863.6	1275.2	-	1021.7	-	721.3	199.3	167.4	126.8	465.6
OBM2_gas	150	10000	2069.1	1340.3	-	1255.1	-	725.7	243.5	205.5	218.6	443.7

Sample	Temp. (° F)	Press. (psig)	Shear stresses (dyne / cm ²) at different angular velocities (RPM)								Gel-strength	
			600	300	250	200	150	100	6	3	10-sec	10-min
OBM2_gas	150	15000	2896.2	1671.7	-	1305.8	-	872.1	244.4	199.3	231.7	526.8
OBM2_gas	150	20000	3335.6	1174.2	-	1205.7	-	709.5	91.8	58.1	37.2	146.4
OBM2_gas	200	2000	1223.2	744.1	-	576.6	-	383.0	99.2	84.8	72.1	194.5
OBM2_gas	200	5000	1507.8	894.4	-	680.7	-	445.0	112.4	95.7	72.1	273.2
OBM2_gas	200	10000	1919.6	1099.9	-	846.3	-	557.4	115.8	90.5	59.0	247.0
OBM2_gas	200	15000	1997.0	1347.8	-	901.4	-	663.6	199.3	147.3	118.0	299.5
OBM2_gas	200	20000	1475.4	1098.6	-	866.5	-	607.7	171.8	148.2	142.1	273.2
OBM2_gas	200	25000	220.3	223.0	-	278.0	-	207.2	12.7	5.7	28.4	146.4
OBM2_gas	250	5000	1020.3	587.1	-	453.8	-	322.2	92.2	74.8	54.6	284.2
OBM2_gas	250	10000	1223.6	738.4	-	588.0	-	406.1	152.6	123.3	107.1	253.6
OBM2_gas	250	15000	988.0	729.2	-	505.4	-	378.1	117.2	94.9	118.0	255.7
OBM2_gas	250	20000	757.2	786.0	-	544.3	-	403.1	130.3	104.0	72.1	161.8
OBM2_gas	250	25000	142.1	288.5	-	291.6	-	116.3	43.7	47.7	37.2	48.1
OBM2_gas	250	30000	155.6	214.2	-	184.5	-	143.4	46.8	57.3	26.2	91.8
OBM2_gas	250	35000	216.0	221.6	-	140.3	-	193.7	30.2	33.2	45.9	80.9
OBM2_gas	300	5000	903.6	531.2	-	400.4	-	247.9	72.6	61.6	80.0	270.2
OBM2_gas	300	10000	1111.3	668.0	-	531.6	-	315.6	108.9	100.5	137.7	316.9
OBM2_gas	300	15000	1109.1	631.3	-	525.9	-	207.7	51.6	43.7	52.5	192.4
OBM2_gas	300	20000	1318.9	713.5	-	560.4	-	392.6	138.6	122.8	135.5	367.2
OBM2_gas	300	25000	1019.0	444.2	-	429.3	-	124.6	39.8	56.8	-	133.3
OBM2_gas	300	30000	255.7	337.9	-	-	-	187.1	108.4	129.8	24.0	69.9
OBM2_gas	300	35000	208.5	184.5	-	87.9	-	184.0	93.6	120.7	148.6	266.7
OBM2_gas	350	5000	1461.4	1009.0	-	814.9	-	589.7	187.1	159.1	100.5	255.7
OBM2_gas	350	10000	1820.8	1233.7	-	981.0	-	713.5	217.7	184.9	115.8	365.0
OBM2_gas	350	15000	2293.4	1564.2	-	1257.7	-	906.2	302.5	258.8	163.9	373.8
OBM2_gas	350	20000	2910.6	1951.9	-	1571.6	-	1134.4	394.3	337.5	223.0	474.3

Sample	Temp. (° F)	Press. (psig)	Shear stresses (dyne / cm ²) at different angular velocities (RPM)								Gel-strength	
			600	300	250	200	150	100	6	3	10-sec	10-min
OBM2_gas	350	25000	3674.4	2574.9	-	2238.7	-	1395.0	504.0	429.7	299.5	684.2
OBM2_gas	350	30000	4955.7	3120.0	-	2631.7	-	1765.7	655.7	557.4	417.5	749.7
OBM2_gas	350	35000	5884.7	3709.3	-	2237.4	-	2065.2	781.6	671.5	526.8	894.0
OBM2_gas	400	5000	1638.5	1180.3	-	1000.7	-	831.5	415.3	345.8	148.6	395.6
OBM2_gas	400	10000	2170.1	1558.9	-	1318.0	-	1060.1	416.2	345.4	131.1	347.5
OBM2_gas	400	15000	2923.3	2052.9	-	1755.6	-	1350.4	515.9	422.3	148.6	203.3
OBM2_gas	400	20000	4138.2	2724.0	-	2269.8	-	1664.3	512.4	402.6	155.2	159.6
OBM2_gas	400	25000	1696.6	1869.3	-	1929.6	-	916.3	-	-	-	338.8
OBM2_gas	400	30000	-112159.5	2623.4	-	2264.9	-	753.7	-	-	306.0	144.3
bf_OBM1	100	0	23.6	8.8	-	4.3	-	-	-	-	0.2	-
bf_OBM1	100	2000	30.4	12.9	-	8.0	-	2.7	-	-	2.8	-
bf_OBM1	100	5000	38.8	18.8	-	12.8	-	6.2	2.0	2.4	3.8	4.0
bf_OBM1	100	10000	54.2	24.9	-	16.2	-	6.7	-	-	2.4	0.0
bf_OBM1	100	15000	83.1	40.9	-	27.4	-	14.4	3.3	3.1	3.3	4.9
bf_OBM1	100	20000	116.7	54.5	-	33.9	-	11.1	-	-	-	0.0
bf_OBM1	150	2000	23.7	11.8	-	8.3	-	-	2.1	2.0	3.8	4.3
bf_OBM1	150	5000	25.1	10.8	-	6.7	-	5.2	-	-	1.7	-
bf_OBM1	150	10000	30.7	11.4	-	5.8	-	-	-	-	0.5	-
bf_OBM1	150	15000	45.3	19.2	-	11.5	-	7.0	-	-	2.4	-
bf_OBM1	150	20000	64.4	30.8	-	20.8	-	10.4	1.6	2.0	4.0	4.5
bf_OBM1	200	2000	15.6	6.3	-	4.2	-	-	-	0.1	1.7	0.0
bf_OBM1	200	5000	15.6	4.9	-	2.2	-	-	-	-	-	0.0
bf_OBM1	200	10000	27.1	13.2	-	9.5	-	5.5	2.6	3.0	4.0	4.7
bf_OBM1	200	15000	29.3	12.0	-	7.0	-	1.6	-	-	0.5	0.9
bf_OBM1	200	20000	37.6	15.5	-	8.4	-	2.3	-	-	-	0.0
bf_OBM1	200	25000	57.4	29.6	-	18.4	-	5.6	3.4	2.4	4.5	6.4

Sample	Temp. (° F)	Press. (psig)	Shear stresses (dyne / cm ²) at different angular velocities (RPM)								Gel-strength	
			600	300	250	200	150	100	6	3	10-sec	10-min
bf_OBM1_gas	100	2000	33.1	15.8	-	10.8	-	5.6	1.0	1.0	6.4	1.4
bf_OBM1_gas	100	5000	35.9	14.7	-	8.5	-	1.8	-	-	0.2	0.7
bf_OBM1_gas	100	10000	53.6	24.1	-	14.8	-	3.4	-	-	1.6	1.9
bf_OBM1_gas	100	15000	72.7	31.3	-	19.3	-	4.5	-	-	0.0	0.0
bf_OBM1_gas	100	20000	117.5	58.3	-	37.0	-	14.5	-	-	2.8	-
bf_OBM1_gas	150	2000	17.2	5.4	-	2.2	-	-	-	-	-	0.0
bf_OBM1_gas	150	5000	24.8	11.0	-	6.8	-	2.1	0.1	-	4.7	0.0
bf_OBM1_gas	150	10000	34.6	15.6	-	10.3	-	-	0.4	-	1.4	2.9
bf_OBM1_gas	150	15000	40.2	15.7	-	8.1	-	-	-	-	0.2	0.0
bf_OBM1_gas	150	20000	59.2	26.2	-	16.3	-	6.3	-	-	1.0	-
bf_OBM1_gas	200	2000	12.5	3.4	-	0.8	-	-	-	-	-	-
bf_OBM1_gas	200	5000	18.4	8.0	-	4.0	-	1.1	-	-	-	0.2
bf_OBM1_gas	200	10000	21.1	8.0	-	4.5	-	-	-	-	0.0	0.3
bf_OBM1_gas	200	15000	32.3	15.0	-	10.0	-	7.7	1.1	0.8	2.1	1.0
bf_OBM1_gas	200	20000	40.4	18.7	-	12.8	-	-	0.8	0.8	4.2	2.6
bf_OBM1_gas	200	25000	48.7	22.0	-	11.5	-	-	-	-	-	0.0
bf_OBM2	100	0	28.7	11.4	-	6.5	-	-	-	-	1.4	-
bf_OBM2	100	2000	29.7	10.5	-	5.2	-	-	-	-	-	-
bf_OBM2	100	5000	40.3	19.2	-	12.8	-	8.3	1.6	1.0	6.8	2.4
bf_OBM2	100	10000	55.2	26.2	-	16.7	-	10.4	0.5	-	0.2	0.5
bf_OBM2	100	15000	74.1	33.7	-	20.9	-	6.4	-	-	0.2	0.0
bf_OBM2	100	20000	121.8	55.4	-	33.8	-	19.5	-	-	0.2	0.0
bf_OBM2	150	2000	23.6	11.1	-	7.6	-	-	1.1	1.0	4.0	1.6
bf_OBM2	150	5000	24.2	9.0	-	4.6	-	-	-	-	-	-
bf_OBM2	150	10000	38.1	18.3	-	12.5	-	7.1	1.9	1.5	6.8	4.7
bf_OBM2	150	15000	49.5	24.0	-	16.9	-	11.5	3.2	2.6	6.1	5.2

Sample	Temp. (° F)	Press. (psig)	Shear stresses (dyne / cm ²) at different angular velocities (RPM)								Gel-strength	
			600	300	250	200	150	100	6	3	10-sec	10-min
bf_OBM2	150	20000	61.7	29.1	-	16.0	-	-	-	-	0.0	-
bf_OBM2	200	2000	18.7	8.5	-	5.7	-	-	1.0	1.1	3.8	3.6
bf_OBM2	200	5000	16.2	4.9	-	1.9	-	-	-	-	-	0.0
bf_OBM2	200	10000	25.2	10.8	-	6.8	-	4.2	-	-	2.4	0.0
bf_OBM2	200	15000	30.5	11.9	-	7.4	-	1.1	-	-	1.6	0.9
bf_OBM2	200	20000	37.2	15.1	-	8.2	-	-	-	-	-	0.2
bf_OBM2	200	25000	66.6	27.7	-	15.9	-	8.8	-	-	-	-
bf_OBM2_gas	100	2000	29.1	10.7	-	4.5	-	-	-	-	-	0.0
bf_OBM2_gas	100	5000	37.0	15.0	-	9.3	-	-	-	-	1.2	-
bf_OBM2_gas	100	10000	56.0	26.7	-	18.5	-	8.9	1.3	1.0	3.8	4.5
bf_OBM2_gas	100	15000	73.6	37.1	-	23.7	-	8.9	1.2	1.0	5.0	-
bf_OBM2_gas	100	20000	126.1	58.8	-	38.0	-	30.1	3.3	2.3	6.9	4.5
bf_OBM2_gas	150	2000	20.2	7.5	-	5.3	-	0.1	-	-	-	-
bf_OBM2_gas	150	5000	23.3	8.6	-	4.7	-	-	-	-	-	0.0
bf_OBM2_gas	150	10000	38.4	19.4	-	13.7	-	5.9	2.9	2.7	4.9	5.2
bf_OBM2_gas	150	15000	40.8	15.9	-	9.5	-	-	-	-	-	0.0
bf_OBM2_gas	150	20000	66.6	35.0	-	23.3	-	9.9	4.1	4.2	9.0	2.6
bf_OBM2_gas	200	2000	13.4	3.0	-	0.9	-	0.2	-	-	0.9	-
bf_OBM2_gas	200	5000	18.5	7.6	-	4.2	-	4.3	-	-	1.6	1.7
bf_OBM2_gas	200	10000	24.3	10.5	-	6.6	-	5.6	0.3	-	4.0	0.0
bf_OBM2_gas	200	15000	27.4	9.6	-	4.8	-	0.9	-	-	0.9	0.0
bf_OBM2_gas	200	20000	36.6	16.4	-	8.7	-	4.3	-	-	1.7	-
bf_OBM2_gas	200	25000	65.6	26.2	-	14.4	-	2.0	-	-	0.3	-
bf_OBM3	100	0	26.3	8.2	-	3.6	-	-	-	-	-	0.0
bf_OBM3	100	2000	36.4	18.1	-	12.1	-	8.6	1.5	1.6	4.9	1.4
bf_OBM3	100	5000	39.3	14.8	-	8.6	-	3.4	-	-	-	0.0

Sample	Temp. (° F)	Press. (psig)	Shear stresses (dyne / cm ²) at different angular velocities (RPM)								Gel-strength	
			600	300	250	200	150	100	6	3	10-sec	10-min
bf_OBM3	100	10000	64.4	29.3	-	19.7	-	9.1	0.4	0.6	2.4	3.1
bf_OBM3	100	15000	95.0	45.2	-	29.5	-	16.6	2.4	2.4	5.0	4.7
bf_OBM3	100	20000	131.4	63.1	-	42.1	-	20.3	3.9	2.3	2.4	5.2
bf_OBM3	150	2000	24.8	12.6	-	8.7	-	7.3	3.5	3.2	7.5	5.0
bf_OBM3	150	5000	29.6	14.0	-	9.3	-	-	0.7	1.0	2.3	3.8
bf_OBM3	150	10000	34.0	12.2	-	5.8	-	-	-	-	-	-
bf_OBM3	150	15000	48.9	19.6	-	11.6	-	3.6	-	-	0.3	0.0
bf_OBM3	150	20000	69.5	31.1	-	20.2	-	5.8	-	-	4.2	3.3
bf_OBM3	200	2000	12.2	3.2	-	0.6	-	0.3	-	-	-	0.0
bf_OBM3	200	5000	17.0	6.0	-	1.7	-	2.1	-	-	-	0.0
bf_OBM3	200	10000	25.9	11.5	-	7.4	-	0.7	-	-	1.4	1.0
bf_OBM3	200	15000	32.3	13.3	-	7.8	-	3.2	-	-	0.9	0.3
bf_OBM3	200	20000	39.0	14.9	-	8.0	-	1.9	-	-	0.3	0.0
bf_OBM3	200	25000	58.2	28.5	-	18.4	-	9.8	5.8	6.0	4.2	6.4
bf_OBM3_gas	100	2000	30.6	10.5	-	4.7	-	-	-	-	-	0.0
bf_OBM3_gas	100	5000	44.9	21.3	-	14.6	-	-	2.7	2.6	9.0	5.2
bf_OBM3_gas	100	10000	58.1	23.2	-	13.2	-	5.8	-	-	-	0.0
bf_OBM3_gas	100	15000	85.0	37.4	-	22.0	-	6.0	-	-	-	0.0
bf_OBM3_gas	100	20000	141.1	68.5	-	42.9	-	18.9	-	-	1.0	0.9
bf_OBM3_gas	150	2000	22.7	8.8	-	5.0	-	0.7	-	-	-	-
bf_OBM3_gas	150	5000	22.6	6.7	-	1.7	-	-	-	-	-	0.0
bf_OBM3_gas	150	10000	33.8	12.6	-	6.1	-	-	-	-	-	0.0
bf_OBM3_gas	150	15000	47.6	17.8	-	9.5	-	2.9	-	-	0.7	0.0
bf_OBM3_gas	150	20000	69.3	31.1	-	21.1	-	-	2.0	1.2	4.7	0.0
bf_OBM3_gas	200	2000	11.3	1.6	-	-	-	-	-	-	-	0.0
bf_OBM3_gas	200	5000	22.0	11.2	-	7.8	-	6.0	3.1	2.8	4.0	4.0

Sample	Temp. (° F)	Press. (psig)	Shear stresses (dyne / cm ²) at different angular velocities (RPM)								Gel-strength	
			600	300	250	200	150	100	6	3	10-sec	10-min
bf_OBM3_gas	200	10000	25.9	11.1	-	6.9	-	3.8	-	-	1.2	1.2
bf_OBM3_gas	200	15000	36.4	16.5	-	11.5	-	5.4	1.9	2.1	2.3	3.5
bf_OBM3_gas	200	20000	44.2	20.8	-	13.3	-	8.6	0.9	0.4	6.2	3.5
bf_OBM3_gas	200	25000	67.8	36.5	-	23.7	-	15.9	4.4	3.8	8.7	8.0

Table B.1 Experimental shear-stress and gel-strength data.

Sample	Temp. (°F)	Press. (psig)	Shear stress uncertainty (%) at different angular velocities (RPM)							
			600	300	250	200	150	100	6	3
OBM1_sl	100	2000	0.9	1.5	-	1.2	-	0.7	6.2	4.5
OBM1_sl	100	5000	0.1	0.7	-	3.5	-	1.2	4.1	5.1
OBM1_sl	100	10000	0.2	0.6	-	4.7	-	1.0	5.3	4.0
OBM1_sl	100	15000	-	0.5	-	5.0	-	0.7	2.9	2.8
OBM1_sl	100	20000	-	-	0.4	3.3	-	0.7	2.0	2.9
OBM1_sl	100	25000	-	-	0.6	4.4	-	4.1	2.4	1.2
OBM1_sl	100	30000	-	-	41.4	5.1	-	8.1	4.1	1.2
OBM1_sl	100	35000	-	-	4.4	4.8	-	1.9	2.0	5.5
OBM1_sl	150	5000	0.2	2.3	-	20.4	-	1.0	2.6	6.3
OBM1_sl	150	10000	0.4	0.2	-	13.3	-	0.8	5.2	5.8
OBM1_sl	150	15000	-	1.3	-	4.5	-	0.7	2.5	4.6
OBM1_sl	150	20000	-	-	2.2	9.9	-	1.0	3.1	3.0
OBM1_sl	150	25000	-	-	1.9	4.4	-	0.7	2.7	2.2
OBM1_sl	150	30000	-	-	3.3	3.9	-	0.5	1.9	1.6
OBM1_sl	150	35000	-	-	26.3	2.6	-	1.0	5.1	1.8
OBM1_sl	200	2000	0.6	1.4	-	2.7	-	0.8	0.9	1.2
OBM1_sl	200	5000	0.2	1.5	-	10.7	-	0.8	1.5	1.4
OBM1_sl	200	10000	0.2	0.7	-	5.9	-	0.7	2.0	2.3

Sample	Temp. (°F)	Press. (psig)	Shear stress uncertainty (%) at different angular velocities (RPM)							
			600	300	250	200	150	100	6	3
OBM1_s1	200	15000	-	0.8	-	8.6	-	0.6	1.7	1.7
OBM1_s1	200	20000	-	-	1.3	4.8	-	0.7	0.9	1.3
OBM1_s1	200	25000	-	-	1.4	6.0	-	0.7	1.0	1.2
OBM1_s1	200	30000	-	-	2.3	4.7	-	0.2	0.9	0.5
OBM1_s1	200	35000	-	-	2.3	3.0	-	3.9	0.8	0.3
OBM1_s2	100	2000	1.3	1.1	-	0.6	-	0.6	2.3	2.7
OBM1_s2	100	5000	0.1	0.8	-	0.7	-	0.8	3.1	3.5
OBM1_s2	100	10000	0.2	0.3	-	6.2	-	0.7	1.8	2.7
OBM1_s2	100	15000	-	0.1	-	4.3	-	0.6	0.9	1.7
OBM1_s2	100	20000	-	-	0.1	0.7	-	0.4	0.8	1.2
OBM1_s2	100	25000	-	-	5.9	0.4	-	3.7	1.1	1.3
OBM1_s2	100	30000	-	-	59.0	12.6	-	8.0	9.0	6.5
OBM1_s2	100	35000	-	-	29.7	26.7	-	22.0	6.2	6.9
OBM1_s2	150	2000	0.5	1.2	-	1.6	-	0.3	3.2	2.2
OBM1_s2	150	5000	0.2	1.7	-	7.8	-	1.0	2.6	2.5
OBM1_s2	150	10000	0.1	1.1	-	6.7	-	1.1	1.1	2.2
OBM1_s2	150	15000	-	0.5	-	7.0	-	0.7	1.6	2.1
OBM1_s2	150	20000	-	-	1.4	6.3	-	0.6	1.1	1.6
OBM1_s2	150	25000	-	-	1.2	4.2	-	0.8	1.2	1.1
OBM1_s2	150	30000	-	-	0.4	1.5	-	3.0	0.9	1.1
OBM1_s2	150	35000	-	-	7.3	5.8	-	1.2	0.8	0.6
OBM1_s2	200	2000	0.4	1.1	-	9.1	-	1.0	1.9	3.7
OBM1_s2	200	5000	0.3	3.2	-	29.9	-	1.4	1.0	2.1
OBM1_s2	200	10000	0.2	2.1	-	19.4	-	1.3	0.6	2.3
OBM1_s2	200	15000	-	0.6	-	8.5	-	0.6	1.2	2.2
OBM1_s2	200	20000	-	-	1.3	10.7	-	0.7	0.6	1.2

Sample	Temp. (°F)	Press. (psig)	Shear stress uncertainty (%) at different angular velocities (RPM)							
			600	300	250	200	150	100	6	3
OBM1_s2	200	25000	-	-	0.6	4.5	-	0.3	1.0	0.8
OBM1_s2	200	30000	-	-	2.3	6.2	-	0.6	0.2	0.7
OBM1_s2	200	35000	-	-	4.2	2.5	-	3.7	5.8	2.6
OBM1_gas	100	2000	0.8	1.5	-	5.5	-	1.1	3.8	4.5
OBM1_gas	100	5000	1.3	0.8	-	3.6	-	0.9	5.2	3.5
OBM1_gas	100	10000	1.5	0.7	-	2.5	-	0.6	3.4	3.5
OBM1_gas	100	15000	-	1.0	-	2.8	-	0.5	1.8	1.3
OBM1_gas	100	20000	-	-	0.2	1.1	-	0.5	2.7	1.9
OBM1_gas	100	25000	-	-	170.9	178.5	-	30.9	9.7	8.5
OBM1_gas	100	30000	-	-	195.7	224.5	-	82.7	10.3	36.3
OBM1_gas	100	35000	-	-	46.6	65.9	-	53.1	17.4	12.5
OBM1_gas	150	2000	0.5	1.7	-	9.5	-	1.2	4.0	3.9
OBM1_gas	150	5000	0.1	1.3	-	7.1	-	0.6	3.2	4.1
OBM1_gas	150	10000	0.2	0.8	-	9.2	-	0.6	3.4	2.7
OBM1_gas	150	15000	-	0.8	-	2.7	-	0.7	2.7	2.2
OBM1_gas	150	20000	-	-	1.1	2.0	-	0.6	2.6	2.2
OBM1_gas	150	25000	-	-	1.2	4.2	-	0.2	1.0	0.7
OBM1_gas	150	30000	-	-	85.6	21.9	-	16.4	8.9	2.8
OBM1_gas	150	35000	-	-	86.4	116.6	-	81.6	14.6	15.1
OBM1_gas	200	2000	0.3	2.7	-	25.7	-	1.5	3.5	1.9
OBM1_gas	200	5000	0.3	2.4	-	19.6	-	1.5	2.6	3.3
OBM1_gas	200	10000	0.8	1.6	-	10.1	-	0.6	3.0	2.9
OBM1_gas	200	15000	-	0.7	-	11.7	-	0.7	1.2	1.4
OBM1_gas	200	20000	-	-	1.9	5.0	-	0.4	1.8	1.7
OBM1_gas	200	25000	-	-	2.1	5.1	-	1.5	2.0	1.0
OBM1_gas	200	30000	-	-	4.5	7.4	-	2.1	1.0	1.4

Sample	Temp. (°F)	Press. (psig)	Shear stress uncertainty (%) at different angular velocities (RPM)							
			600	300	250	200	150	100	6	3
OBM1_gas	200	35000	-	-	2601.6	4471.2	-	444.5	61.3	20.5
SBM_contam	100	2000	2.4	12.4	-	99.3	-	30.8	-	-
SBM_contam	100	5000	0.7	11.2	-	106.9	-	19.7	-	-
SBM_contam	100	10000	1.0	6.2	-	56.6	-	10.9	-	-
SBM_contam	100	15000	0.3	2.1	-	36.0	-	9.0	-	-
SBM_contam	100	20000	0.4	2.7	-	11.0	-	6.5	-	-
SBM_contam	100	25000	0.3	2.6	-	6.1	-	3.4	31.3	-
SBM_contam	150	5000	0.8	28.6	-	68.2	-	30.3	-	-
SBM_contam	150	10000	1.2	17.3	-	84.7	-	12.2	-	-
SBM_contam	150	15000	0.0	12.9	-	35.0	-	12.2	-	-
SBM_contam	150	20000	0.5	6.0	-	51.2	-	6.2	0.0	28.0
SBM_contam	150	25000	0.5	3.9	-	13.1	-	3.7	15.1	9.3
SBM_contam	150	30000	2.4	3.4	-	20.4	-	4.9	9.4	13.9
SBM_contam	150	35000	2.4	4.8	-	6.7	-	4.5	27.7	48.7
SBM_contam	200	5000	5.3	15.7	-	159.4	-	16.8	10.7	28.3
SBM_contam	200	10000	2.1	24.0	-	86.6	-	16.9	67.1	205.0
SBM_contam	200	15000	0.7	21.9	-	64.8	-	16.9	-	-
SBM_contam	200	20000	0.5	11.6	-	71.4	-	11.7	-	-
SBM_contam	200	25000	1.1	6.4	-	53.5	-	11.2	268.4	-
SBM_contam	200	30000	0.5	7.6	-	64.5	-	6.9	23.1	76.7
SBM_contam	200	35000	2.4	5.2	-	34.3	-	9.7	0.0	11.2
SBM_contam	250	5000	49.2	62.1	-	228.1	-	76.6	-	-
SBM_contam	250	10000	19.5	26.2	-	208.9	-	82.7	-	-
SBM_contam	250	15000	1.9	43.8	-	84.5	-	28.0	-	-
SBM_contam	250	20000	1.9	21.8	-	120.9	-	5.1	67.1	178.9
SBM_contam	250	25000	2.1	11.7	-	72.6	-	19.1	-	-

Sample	Temp. (°F)	Press. (psig)	Shear stress uncertainty (%) at different angular velocities (RPM)							
			600	300	250	200	150	100	6	3
SBM_contam	250	30000	1.1	12.2	-	128.1	-	10.8	44.7	67.1
SBM_contam	250	35000	0.8	12.9	-	35.6	-	11.9	-	-
SBM_contam	300	5000	5.7	79.9	-	784.6	-	98.0	-	-
SBM_contam	300	10000	3.7	22.2	-	152.9	-	23.1	41.3	91.1
SBM_contam	300	15000	16.6	35.8	-	302.1	-	34.3	-	-
SBM_contam	300	20000	1.9	30.1	-	171.8	-	17.8	-	-
SBM_contam	300	25000	2.5	28.3	-	129.5	-	15.5	-	-
SBM_contam	300	30000	2.2	15.9	-	152.9	-	5.5	29.8	29.8
SBM_contam	300	35000	2.6	21.4	-	86.8	-	13.3	-	-
SBM_contam	350	5000	30.3	46.6	-	411.0	-	32.5	31.6	29.8
SBM_contam	350	10000	10.0	39.3	-	2838.0	-	71.3	76.7	73.0
SBM_contam	350	15000	2.8	30.2	-	365.8	-	56.6	-	-
SBM_contam	350	20000	32.9	33.7	-	480.0	-	28.5	-	-
SBM_contam	350	25000	7.4	15.8	-	225.3	-	32.9	-	-
SBM_contam	350	30000	0.0	4.8	-	269.7	-	18.0	-	-
SBM_contam	350	35000	0.8	2.8	-	1078.7	-	20.4	-	-
SBM_sl_gas	47.5	0	11.8	5.0	-	0.8	-	0.9	6.2	6.4
SBM_sl_gas	47.5	2000	1.0	1.9	-	5.7	-	4.3	30.0	196.7
SBM_sl_gas	47.5	2000	1.7	3.8	-	2.2	-	1.9	14.6	24.7
SBM_sl_gas	47.5	5000	1.1	0.8	-	3.6	-	0.9	8.1	9.9
SBM_sl_gas	47.5	10000	0.3	1.4	-	2.1	-	1.5	12.4	18.2
SBM_sl_gas	47.5	15000	0.4	0.5	-	1.3	-	1.5	8.2	10.4
SBM_sl_gas	47.5	20000	0.5	0.5	-	1.1	-	0.9	6.1	8.3
SBM_sl_gas	47.5	25000	10.9	0.6	-	1.7	-	2.3	1.8	3.2
SBM_sl_gas	100	2000	0.4	5.7	-	8.0	-	1.5	12.5	11.5
SBM_sl_gas	100	5000	0.6	5.2	-	1.5	-	4.0	11.8	12.4

Sample	Temp. (°F)	Press. (psig)	Shear stress uncertainty (%) at different angular velocities (RPM)							
			600	300	250	200	150	100	6	3
SBM_sl_gas	100	10000	0.4	2.8	-	3.9	-	1.2	7.9	16.9
SBM_sl_gas	100	15000	0.7	1.2	-	1.7	-	1.2	4.7	17.3
SBM_sl_gas	100	20000	1.2	0.5	-	0.8	-	0.9	2.2	8.4
SBM_sl_gas	100	25000	0.5	0.4	-	1.5	-	0.7	0.0	7.9
SBM_sl_gas	100	30000	0.3	0.8	-	4.1	-	3.2	6.4	8.6
SBM_sl_gas	150	2000	1.1	4.7	-	1.8	-	1.4	7.7	22.2
SBM_sl_gas	150	5000	0.3	5.3	-	1.2	-	1.9	20.0	33.7
SBM_sl_gas	150	10000	0.4	1.0	-	1.1	-	0.8	10.6	11.4
SBM_sl_gas	150	15000	0.8	0.8	-	2.5	-	1.9	3.0	4.6
SBM_sl_gas	150	20000	1.0	1.2	-	2.9	-	0.8	2.6	4.2
SBM_sl_gas	150	25000	1.3	2.8	-	1.2	-	0.9	3.2	6.8
SBM_sl_gas	150	30000	1.0	1.4	-	0.6	-	0.5	1.8	5.6
SBM_sl_gas	200	5000	0.8	2.7	-	1.1	-	1.8	5.8	5.4
SBM_sl_gas	200	10000	0.8	1.2	-	0.8	-	1.3	0.0	6.5
SBM_sl_gas	200	15000	0.6	0.7	-	0.6	-	1.0	7.5	6.2
SBM_sl_gas	200	20000	0.5	0.4	-	0.5	-	1.3	4.5	10.1
SBM_sl_gas	200	25000	0.6	1.0	-	1.1	-	0.6	0.0	5.1
SBM_sl_gas	200	30000	1.4	0.5	-	1.2	-	1.0	4.2	6.1
SBM_sl_gas	200	35000	1.7	1.3	-	0.8	-	1.1	2.7	3.4
SBM_sl_gas	250	5000	0.9	6.2	-	1.1	-	4.6	12.4	9.3
SBM_sl_gas	250	10000	0.8	5.2	-	2.0	-	3.3	0.0	23.3
SBM_sl_gas	250	15000	0.5	1.7	-	1.4	-	2.8	11.2	14.5
SBM_sl_gas	250	20000	0.5	1.7	-	0.5	-	2.7	0.0	4.6
SBM_sl_gas	250	25000	0.7	1.0	-	1.1	-	0.9	4.4	7.0
SBM_sl_gas	250	30000	3.4	0.5	-	0.7	-	2.0	3.4	8.7
SBM_sl_gas	250	35000	1.7	1.9	-	0.8	-	1.6	2.6	2.7

Sample	Temp. (°F)	Press. (psig)	Shear stress uncertainty (%) at different angular velocities (RPM)							
			600	300	250	200	150	100	6	3
SBM_sl_gas	300	5000	1.3	2.7	-	1.2	-	0.0	7.4	8.1
SBM_sl_gas	300	10000	1.3	2.1	-	0.8	-	4.0	5.2	5.5
SBM_sl_gas	300	15000	0.5	1.6	-	1.3	-	3.8	3.9	5.3
SBM_sl_gas	300	20000	0.5	0.8	-	0.7	-	3.6	3.5	7.4
SBM_sl_gas	300	25000	0.6	1.0	-	0.9	-	1.1	2.7	2.9
SBM_sl_gas	300	30000	2.1	1.4	-	0.4	-	0.7	2.4	3.8
SBM_sl_gas	350	5000	1.9	5.8	-	0.0	-	2.3	11.2	0.0
SBM_sl_gas	350	10000	1.3	3.3	-	0.9	-	1.4	4.2	4.4
SBM_sl_gas	350	15000	0.9	2.3	-	0.8	-	1.5	3.9	3.4
SBM_sl_gas	350	20000	1.6	1.0	-	10.3	-	0.9	5.6	0.0
SBM_sl_gas	350	25000	9.6	31.4	-	6.3	-	3.3	3.6	3.0
SBM_sl_gas	350	30000	24.8	4.3	-	22.3	-	0.0	6.0	7.4
SBM_sl_gas	350	35000	7.7	0.8	-	24.9	-	1.5	2.8	4.0
SBM_sl_gas	400	5000	3.1	7.2	-	1.3	-	1.8	5.6	2.8
SBM_sl_gas	400	10000	2.8	3.2	-	1.4	-	1.1	1.9	2.5
SBM_sl_gas	400	15000	1.0	0.6	-	4.8	-	1.6	5.3	9.0
SBM_sl_gas	400	20000	34.8	48.0	-	50.4	-	6.4	0.0	0.0
SBM_sl_gas	400	25000	19.5	46.1	-	9.1	-	2.3	0.0	11.2
SBM_sl_gas	400	30000	146.5	231.5	-	14.6	-	5.8	45.2	8.9
SBM_sl_gas	400	35000	270.9	136.9	-	120.4	-	5.3	2.6	2.2
SBM_sl	100	0	0.5	11.3	-	17.4	-	11.9	70.3	49.0
SBM_sl	100	2000	0.6	9.2	-	11.1	-	4.4	21.3	16.1
SBM_sl	100	5000	1.0	6.6	-	5.0	-	3.6	26.2	31.0
SBM_sl	100	10000	1.0	1.6	-	5.1	-	4.6	16.2	19.0
SBM_sl	100	15000	0.1	3.4	-	9.7	-	3.3	13.2	16.0
SBM_sl	100	20000	0.1	2.7	-	3.9	-	2.0	13.8	15.9

Sample	Temp. (°F)	Press. (psig)	Shear stress uncertainty (%) at different angular velocities (RPM)							
			600	300	250	200	150	100	6	3
SBM_sl	100	25000	0.2	3.0	-	2.7	-	0.7	7.2	9.5
SBM_sl	100	30000	0.4	0.7	-	5.8	-	1.6	13.9	20.2
SBM_sl	150	2000	0.8	10.7	-	28.9	-	3.5	4.6	9.2
SBM_sl	150	5000	1.4	7.4	-	47.2	-	2.7	0.0	13.1
SBM_sl	150	10000	0.7	10.2	-	30.9	-	3.4	5.0	5.3
SBM_sl	150	15000	0.7	8.2	-	14.9	-	4.4	4.2	10.3
SBM_sl	150	20000	0.9	10.0	-	47.7	-	5.8	5.6	6.0
SBM_sl	150	25000	1.0	8.3	-	46.8	-	2.9	0.0	6.4
SBM_sl	150	30000	0.8	12.9	-	25.3	-	1.2	4.0	6.9
SBM_sl	200	5000	0.9	8.8	-	4.2	-	1.6	8.9	16.5
SBM_sl	200	10000	1.2	6.7	-	5.4	-	1.1	5.8	15.1
SBM_sl	200	15000	1.7	5.1	-	11.2	-	2.4	5.4	15.4
SBM_sl	200	20000	0.9	2.8	-	16.2	-	1.0	7.9	14.8
SBM_sl	200	25000	1.4	3.2	-	2.7	-	0.9	4.6	4.5
SBM_sl	200	30000	1.0	3.8	-	4.0	-	-	4.2	-
SBM_sl	250	5000	0.9	7.3	-	2.0	-	1.5	5.3	5.5
SBM_sl	250	10000	0.9	6.5	-	2.3	-	1.6	6.9	8.0
SBM_sl	250	15000	0.4	5.6	-	2.3	-	1.1	14.1	10.1
SBM_sl	250	20000	0.4	3.5	-	0.6	-	0.0	4.1	3.8
SBM_sl	250	25000	0.7	3.0	-	2.2	-	0.0	3.4	5.3
SBM_sl	250	30000	1.0	1.7	-	0.7	-	1.4	3.5	4.5
SBM_sl	350	5000	0.9	10.4	-	6.4	-	1.9	6.9	7.4
SBM_sl	350	10000	1.0	7.9	-	1.7	-	1.2	2.7	5.3
SBM_sl	350	15000	0.6	3.4	-	0.6	-	1.0	3.3	4.2
SBM_sl	350	20000	0.3	3.6	-	1.2	-	0.7	3.0	2.0
SBM_sl	350	25000	1.4	3.4	-	0.6	-	0.6	3.0	3.3

Sample	Temp. (°F)	Press. (psig)	Shear stress uncertainty (%) at different angular velocities (RPM)							
			600	300	250	200	150	100	6	3
SBM_s1	350	30000	1.0	4.7	-	2.8	-	0.9	2.0	1.4
SBM_s1	400	10000	0.8	6.3	-	10.7	-	0.0	1.5	1.5
SBM_s1	400	15000	0.9	5.4	-	3.1	-	1.1	0.9	4.3
SBM_s1	400	20000	0.5	5.3	-	3.5	-	0.8	1.9	7.9
SBM_s1	400	25000	0.8	5.0	-	2.0	-	0.7	1.3	3.3
SBM_s1	400	30000	1.0	2.2	-	4.8	-	1.8	1.2	1.8
SBM_s1	400	35000	1.3	1.8	-	0.7	-	0.9	1.1	1.6
OBM2_s1	100	0	0.2	3.4	-	2.2	-	0.7	6.7	9.1
OBM2_s1	100	2000	0.7	1.5	-	0.9	-	1.4	10.5	14.3
OBM2_s1	100	5000	0.5	3.3	-	18.4	-	2.8	20.3	57.2
OBM2_s1	100	10000	1.0	2.9	-	24.8	-	2.9	8.4	7.8
OBM2_s1	100	15000	1.2	2.2	-	19.6	-	5.7	4.1	5.4
OBM2_s1	100	20000	1.5	100.8	-	114.6	-	2.3	4.3	3.5
OBM2_s1	150	2000	0.3	5.6	-	2.9	-	3.0	6.2	4.5
OBM2_s1	150	5000	0.2	1.9	-	1.0	-	0.7	4.6	1.9
OBM2_s1	150	10000	0.5	1.0	-	1.0	-	0.3	5.7	4.4
OBM2_s1	150	15000	1.2	0.7	-	0.5	-	1.4	6.1	4.6
OBM2_s1	150	20000	2.3	1.7	-	6.9	-	1.4	3.6	2.6
OBM2_s1	200	2000	0.8	15.2	-	117.3	-	15.5	53.9	112.9
OBM2_s1	200	5000	0.8	7.5	-	2.3	-	12.1	18.0	20.8
OBM2_s1	200	10000	0.8	7.1	-	7.7	-	10.1	7.1	13.4
OBM2_s1	200	15000	1.0	2.8	-	27.2	-	1.0	5.1	7.5
OBM2_s1	200	20000	0.4	3.6	-	1.6	-	1.2	5.6	5.9
OBM2_s1	200	25000	5.6	8.9	-	-	-	5.7	8.9	9.7
OBM2_s1	250	5000	2.0	11.2	-	10.8	-	4.1	11.5	23.1
OBM2_s1	250	10000	1.6	4.2	-	1.9	-	2.2	7.1	15.4

Sample	Temp. (°F)	Press. (psig)	Shear stress uncertainty (%) at different angular velocities (RPM)							
			600	300	250	200	150	100	6	3
OBM2_sl	250	15000	2.0	1.8	-	9.2	-	4.3	13.9	15.7
OBM2_sl	250	20000	1.8	1.6	-	1.3	-	1.5	7.9	10.0
OBM2_sl	250	25000	2.9	3.3	-	5.5	-	2.0	9.7	6.3
OBM2_sl	250	30000	1.6	2.5	-	5.1	-	0.6	8.2	5.1
OBM2_sl	250	35000	2.8	0.7	-	0.7	-	0.6	7.0	5.4
OBM2_sl	300	5000	2.4	5.6	-	2.2	-	1.6	268.4	-
OBM2_sl	300	10000	2.1	2.3	-	0.5	-	0.8	10.7	0.0
OBM2_sl	300	15000	0.4	3.6	-	4.3	-	2.8	39.1	-
OBM2_sl	300	20000	0.4	0.5	-	0.5	-	1.1	20.8	29.2
OBM2_sl	300	25000	1.6	1.7	-	1.4	-	0.6	8.1	7.6
OBM2_sl	300	30000	0.5	1.5	-	15.0	-	5.2	10.5	16.7
OBM2_sl	300	35000	1.4	1.6	-	46.2	-	6.3	6.7	7.1
OBM2_sl	350	5000	1.3	11.9	-	124.9	-	17.9	-	-
OBM2_sl	350	10000	1.9	9.8	-	68.0	-	29.2	-	-
OBM2_sl	350	15000	1.2	11.5	-	43.7	-	9.0	-	-
OBM2_sl	350	20000	1.1	9.7	-	4.0	-	2.3	28.2	16.0
OBM2_sl	350	25000	29.0	18.8	-	11.4	-	7.1	8.5	7.1
OBM2_sl	350	30000	1.1	8.3	-	262.0	-	15.3	13.1	14.3
OBM2_sl	350	35000	2.5	1.6	-	9.8	-	3.2	7.7	8.5
OBM2_sl	400	5000	2.9	5.7	-	7.4	-	8.3	-	-
OBM2_sl	400	10000	2.8	6.5	-	5.5	-	11.1	-	-
OBM2_sl	400	15000	2.3	3.6	-	4.0	-	7.7	-	-
OBM2_sl	400	20000	2.4	3.6	-	4.5	-	2.7	3.5	3.4
OBM2_sl	400	25000	0.8	2.2	-	1.0	-	2.1	0.0	3.7
OBM2_sl	400	30000	0.4	1.5	-	3.3	-	1.3	4.3	8.6
OBM2_sl	400	35000	6.5	7.5	-	1.5	-	1.3	3.7	2.9

Sample	Temp. (°F)	Press. (psig)	Shear stress uncertainty (%) at different angular velocities (RPM)							
			600	300	250	200	150	100	6	3
OBM2_gas	100	2000	0.2	1.8	-	8.4	-	6.4	6.8	8.1
OBM2_gas	100	5000	0.2	1.1	-	9.6	-	3.1	8.7	7.4
OBM2_gas	100	10000	0.5	1.1	-	9.7	-	3.4	5.0	6.2
OBM2_gas	100	15000	-6.3	156.5	-	25.4	-	4.6	5.9	2.1
OBM2_gas	100	20000	30.4	91.6	-	332.4	-	30.8	4.8	8.9
OBM2_gas	150	2000	12.0	21.4	-	42.0	-	21.8	29.5	33.7
OBM2_gas	150	5000	4.7	17.4	-	38.1	-	24.7	3.5	7.4
OBM2_gas	150	10000	43.9	14.1	-	36.0	-	5.3	1.6	4.9
OBM2_gas	150	15000	30.9	15.5	-	15.9	-	3.9	1.5	3.8
OBM2_gas	150	20000	139.0	61.0	-	46.5	-	13.6	14.4	13.4
OBM2_gas	200	2000	1.7	4.3	-	1.9	-	2.2	4.9	8.3
OBM2_gas	200	5000	1.2	5.2	-	2.1	-	1.6	4.3	3.7
OBM2_gas	200	10000	1.0	5.2	-	1.4	-	2.8	2.6	2.6
OBM2_gas	200	15000	36.0	18.1	-	7.3	-	6.6	3.5	1.6
OBM2_gas	200	20000	88.5	6.2	-	17.4	-	21.7	3.8	3.2
OBM2_gas	200	25000	42.8	10.1	-	155.1	-	19.0	44.1	181.6
OBM2_gas	250	5000	0.7	8.5	-	6.6	-	2.2	3.9	2.6
OBM2_gas	250	10000	1.6	8.2	-	11.4	-	1.4	1.3	1.9
OBM2_gas	250	15000	101.7	20.8	-	31.8	-	11.7	5.5	2.5
OBM2_gas	250	20000	42.9	27.0	-	34.7	-	5.7	4.4	3.7
OBM2_gas	250	25000	75.7	52.1	-	124.9	-	12.1	9.8	19.5
OBM2_gas	250	30000	12.1	31.5	-	245.5	-	20.3	19.0	14.4
OBM2_gas	250	35000	141.3	45.4	-	273.5	-	28.2	43.1	39.1
OBM2_gas	300	5000	1.8	3.5	-	4.7	-	2.6	6.7	3.8
OBM2_gas	300	10000	8.2	12.5	-	8.4	-	14.3	3.3	4.3
OBM2_gas	300	15000	18.9	40.2	-	22.6	-	13.5	4.5	0.0

Sample	Temp. (°F)	Press. (psig)	Shear stress uncertainty (%) at different angular velocities (RPM)							
			600	300	250	200	150	100	6	3
OBM2_gas	300	20000	22.5	40.8	-	38.0	-	16.4	1.7	1.6
OBM2_gas	300	25000	131.9	36.0	-	143.1	-	30.7	46.6	16.0
OBM2_gas	300	30000	157.1	139.9	-	-	-	37.7	8.2	17.2
OBM2_gas	300	35000	164.2	68.8	-	2731.2	-	9.2	40.6	13.1
OBM2_gas	350	5000	0.3	3.6	-	0.7	-	0.9	3.1	5.2
OBM2_gas	350	10000	0.3	3.7	-	11.1	-	1.3	3.3	2.6
OBM2_gas	350	15000	0.2	1.6	-	1.3	-	0.4	1.9	1.9
OBM2_gas	350	20000	0.4	0.7	-	0.7	-	1.0	1.8	1.1
OBM2_gas	350	25000	1.1	15.6	-	11.4	-	0.8	1.7	1.1
OBM2_gas	350	30000	2.9	5.3	-	28.3	-	2.0	1.5	2.7
OBM2_gas	350	35000	2.5	5.1	-	103.2	-	1.2	2.0	1.7
OBM2_gas	400	5000	0.7	2.8	-	3.9	-	0.6	7.1	3.8
OBM2_gas	400	10000	0.3	1.2	-	2.1	-	0.9	0.9	4.1
OBM2_gas	400	15000	0.9	1.0	-	9.1	-	0.6	0.6	3.0
OBM2_gas	400	20000	2.0	3.1	-	3.2	-	2.6	5.5	1.6
OBM2_gas	400	25000	151.3	56.5	-	61.6	-	52.0	-	-
OBM2_gas	400	30000	-51.5	55.0	-	171.7	-	80.1	-	-
bf_OBM1	100	0	1.9	9.0	-	38.1	-	-	-	-
bf_OBM1	100	2000	0.5	2.4	-	10.9	-	736.4	-	-
bf_OBM1	100	5000	1.3	2.1	-	5.5	-	316.2	168.4	86.0
bf_OBM1	100	10000	0.7	3.0	-	6.9	-	184.6	-	-
bf_OBM1	100	15000	0.8	4.0	-	3.8	-	80.7	47.4	61.3
bf_OBM1	100	20000	1.1	2.6	-	11.3	-	117.0	-	-
bf_OBM1	150	2000	0.8	1.3	-	12.1	-	-	113.2	124.5
bf_OBM1	150	5000	1.0	4.1	-	11.7	-	296.1	-	-
bf_OBM1	150	10000	1.8	6.2	-	14.7	-	-	-	-

Sample	Temp. (°F)	Press. (psig)	Shear stress uncertainty (%) at different angular velocities (RPM)							
			600	300	250	200	150	100	6	3
bf_OBM1	150	15000	0.3	1.8	-	8.2	-	200.4	-	-
bf_OBM1	150	20000	0.5	0.9	-	4.6	-	143.3	181.7	111.1
bf_OBM1	200	2000	1.8	2.9	-	30.0	-	-	-	3186.9
bf_OBM1	200	5000	2.8	3.8	-	43.4	-	-	-	-
bf_OBM1	200	10000	0.7	1.8	-	12.1	-	324.1	127.1	73.6
bf_OBM1	200	15000	1.4	3.7	-	13.5	-	962.9	-	-
bf_OBM1	200	20000	1.7	5.5	-	9.3	-	492.7	-	-
bf_OBM1	200	25000	1.5	8.8	-	18.5	-	211.4	199.6	192.7
bf_OBM1_gas	100	2000	1.0	1.2	-	7.5	-	221.2	402.7	297.6
bf_OBM1_gas	100	5000	1.6	2.3	-	9.6	-	1007.6	-	-
bf_OBM1_gas	100	10000	0.5	2.1	-	2.0	-	574.0	-	-
bf_OBM1_gas	100	15000	0.4	1.8	-	1.9	-	414.7	-	-
bf_OBM1_gas	100	20000	0.9	4.0	-	4.6	-	75.8	-	-
bf_OBM1_gas	150	2000	0.9	3.4	-	44.8	-	-	-	-
bf_OBM1_gas	150	5000	1.1	2.8	-	17.1	-	584.1	3989.8	-
bf_OBM1_gas	150	10000	0.9	4.1	-	5.4	-	-	400.4	-
bf_OBM1_gas	150	15000	0.9	1.2	-	17.9	-	-	-	-
bf_OBM1_gas	150	20000	0.3	2.7	-	7.9	-	207.7	-	-
bf_OBM1_gas	200	2000	2.4	5.5	-	120.4	-	-	-	-
bf_OBM1_gas	200	5000	2.4	4.6	-	19.3	-	1005.6	-	-
bf_OBM1_gas	200	10000	1.3	7.0	-	33.3	-	-	-	-
bf_OBM1_gas	200	15000	0.6	1.0	-	10.3	-	180.4	65.1	294.8
bf_OBM1_gas	200	20000	0.9	0.8	-	5.2	-	-	385.4	296.5
bf_OBM1_gas	200	25000	5.1	7.9	-	9.9	-	-	-	-
bf_OBM2	100	0	0.6	7.6	-	16.0	-	-	-	-
bf_OBM2	100	2000	0.6	4.4	-	10.7	-	-	-	-

Sample	Temp. (°F)	Press. (psig)	Shear stress uncertainty (%) at different angular velocities (RPM)							
			600	300	250	200	150	100	6	3
bf_OBM2	100	5000	1.0	4.9	-	7.2	-	280.8	72.9	239.4
bf_OBM2	100	10000	0.5	3.0	-	5.1	-	82.3	691.9	-
bf_OBM2	100	15000	0.4	4.0	-	4.2	-	302.8	-	-
bf_OBM2	100	20000	2.6	1.1	-	3.3	-	272.1	-	-
bf_OBM2	150	2000	2.1	8.5	-	10.0	-	-	329.8	290.3
bf_OBM2	150	5000	2.1	14.3	-	20.6	-	-	-	-
bf_OBM2	150	10000	0.8	9.1	-	6.9	-	304.7	33.3	186.3
bf_OBM2	150	15000	0.6	4.1	-	3.7	-	218.5	131.1	109.3
bf_OBM2	150	20000	1.4	13.0	-	5.7	-	-	-	-
bf_OBM2	200	2000	2.2	13.1	-	13.2	-	-	361.1	168.8
bf_OBM2	200	5000	1.1	32.5	-	29.8	-	-	-	-
bf_OBM2	200	10000	2.9	10.3	-	13.8	-	394.1	-	-
bf_OBM2	200	15000	0.8	8.5	-	14.8	-	1330.4	-	-
bf_OBM2	200	20000	1.0	9.7	-	18.9	-	-	-	-
bf_OBM2	200	25000	7.2	5.5	-	7.5	-	719.8	-	-
bf_OBM2_gas	100	2000	0.8	10.6	-	9.8	-	-	-	-
bf_OBM2_gas	100	5000	1.0	10.8	-	11.2	-	-	-	-
bf_OBM2_gas	100	10000	0.3	4.0	-	4.8	-	190.6	308.7	324.5
bf_OBM2_gas	100	15000	1.7	3.5	-	5.3	-	239.5	374.4	332.3
bf_OBM2_gas	100	20000	4.0	2.4	-	2.3	-	159.5	127.3	177.8
bf_OBM2_gas	150	2000	0.9	24.7	-	13.8	-	11774.5	-	-
bf_OBM2_gas	150	5000	2.2	13.3	-	25.7	-	-	-	-
bf_OBM2_gas	150	10000	2.8	6.3	-	14.9	-	287.0	117.7	95.0
bf_OBM2_gas	150	15000	1.1	11.6	-	14.9	-	-	-	-
bf_OBM2_gas	150	20000	1.9	6.6	-	4.6	-	408.9	83.9	98.7
bf_OBM2_gas	200	2000	1.1	20.5	-	49.1	-	14700.7	-	-

Sample	Temp. (°F)	Press. (psig)	Shear stress uncertainty (%) at different angular velocities (RPM)							
			600	300	250	200	150	100	6	3
bf_OBM2_gas	200	5000	4.2	13.2	-	15.3	-	437.5	-	-
bf_OBM2_gas	200	10000	2.9	5.8	-	23.1	-	150.7	851.5	-
bf_OBM2_gas	200	15000	1.0	6.4	-	32.5	-	1085.1	-	-
bf_OBM2_gas	200	20000	0.4	13.3	-	27.9	-	349.0	-	-
bf_OBM2_gas	200	25000	1.1	2.8	-	9.7	-	2535.2	-	-
bf_OBM3	100	0	1.2	15.9	-	48.7	-	-	-	-
bf_OBM3	100	2000	4.2	1.7	-	21.2	-	52.6	167.0	110.0
bf_OBM3	100	5000	3.0	4.7	-	28.6	-	343.6	-	-
bf_OBM3	100	10000	1.9	3.8	-	6.8	-	177.6	460.5	573.6
bf_OBM3	100	15000	1.4	4.1	-	2.4	-	119.7	63.4	122.4
bf_OBM3	100	20000	1.3	4.4	-	5.0	-	37.1	146.0	114.1
bf_OBM3	150	2000	1.0	7.5	-	13.6	-	177.4	98.5	68.5
bf_OBM3	150	5000	2.5	9.8	-	15.2	-	-	600.8	269.7
bf_OBM3	150	10000	0.7	8.0	-	17.9	-	-	-	-
bf_OBM3	150	15000	1.6	7.3	-	15.9	-	392.4	-	-
bf_OBM3	150	20000	1.2	7.0	-	2.5	-	263.1	-	-
bf_OBM3	200	2000	5.0	23.1	-	261.3	-	3437.2	-	-
bf_OBM3	200	5000	5.4	11.0	-	50.0	-	404.5	-	-
bf_OBM3	200	10000	2.6	4.9	-	11.9	-	1963.9	-	-
bf_OBM3	200	15000	1.2	10.4	-	13.3	-	391.5	-	-
bf_OBM3	200	20000	1.4	5.9	-	8.2	-	643.3	-	-
bf_OBM3	200	25000	1.5	4.2	-	2.0	-	98.1	40.3	52.2
bf_OBM3_gas	100	2000	3.9	12.8	-	28.0	-	-	-	-
bf_OBM3_gas	100	5000	1.6	5.0	-	5.0	-	-	111.5	90.1
bf_OBM3_gas	100	10000	1.7	7.2	-	8.2	-	204.3	-	-
bf_OBM3_gas	100	15000	0.6	4.6	-	1.1	-	334.2	-	-

Sample	Temp. (°F)	Press. (psig)	Shear stress uncertainty (%) at different angular velocities (RPM)							
			600	300	250	200	150	100	6	3
bf_OBM3_gas	100	20000	0.7	1.7	-	3.8	-	114.4	-	-
bf_OBM3_gas	150	2000	1.1	12.6	-	24.8	-	1315.1	-	-
bf_OBM3_gas	150	5000	2.5	20.8	-	94.0	-	-	-	-
bf_OBM3_gas	150	10000	4.7	5.8	-	24.3	-	-	-	-
bf_OBM3_gas	150	15000	2.6	3.7	-	11.5	-	441.5	-	-
bf_OBM3_gas	150	20000	1.0	6.2	-	3.5	-	-	233.1	302.9
bf_OBM3_gas	200	2000	2.5	71.6	-	-	-	-	-	-
bf_OBM3_gas	200	5000	1.3	8.5	-	25.2	-	181.8	77.4	52.5
bf_OBM3_gas	200	10000	0.7	12.5	-	23.5	-	256.2	-	-
bf_OBM3_gas	200	15000	3.8	4.7	-	8.5	-	266.3	98.4	107.6
bf_OBM3_gas	200	20000	1.1	7.4	-	5.6	-	177.9	114.3	670.8
bf_OBM3_gas	200	25000	3.3	1.9	-	5.8	-	177.6	87.6	71.8

Table B.2 Relative uncertainty of experimental measurements in relation to the mean value.

APPENDIX C

Here we list the experimental measurements and their respective standard deviations for the pipe flow loop (Table C.1), and the concentric (Table C.2) and eccentric (Table C.3) annuli flow loop tests.

Test number	u_{sg} , m/s		u_{sl} , m/s		$\frac{\Delta P}{\Delta L}$, kPa/m		Liquid holdup	
	Avg.	St. dev.	Avg.	St. dev.	Avg.	St. dev.	Avg.	St. dev.
2	0.64	0.024	0.69	0.006	0.65	0.015	6.64	0.17
3	0.47	0.027	0.69	0.006	0.74	0.016	7.12	0.17
4	0.53	0.039	0.69	0.006	0.68	0.013	6.86	0.16
5	0.40	0.038	0.69	0.007	0.76	0.015	7.30	0.14
6	0.31	0.031	0.69	0.006	0.79	0.014	7.56	0.12
7	0.20	0.027	0.69	0.006	0.87	0.015	7.96	0.08
8	0.10	0.025	0.71	0.006	0.94	0.016	8.43	0.04
9	0.07	0.024	0.69	0.006	0.95	0.016	8.61	0.03
10	0.59	0.050	0.51	0.009	0.65	0.012	6.30	0.21
11	0.68	0.056	0.51	0.008	0.60	0.012	6.09	0.25
12	0.73	0.059	0.51	0.008	0.60	0.011	5.97	0.23
13a	0.75	0.051	0.69	0.006	0.61	0.013	6.48	0.22
14	0.51	0.052	0.51	0.010	0.70	0.014	6.66	0.20
15	0.38	0.047	0.51	0.016	0.74	0.014	6.99	0.15
16	0.41	0.044	0.54	0.012	0.71	0.013	6.93	0.20
17	0.32	0.046	0.49	0.040	0.76	0.014	7.16	0.16
18	0.30	0.043	0.50	0.015	0.77	0.014	7.24	0.15
19	0.20	0.036	0.50	0.011	0.82	0.014	7.62	0.10
20	0.10	0.033	0.50	0.010	0.90	0.015	8.19	0.05
21	0.07	0.035	0.50	0.011	0.93	0.016	8.46	0.03
22	0.70	0.062	0.13	0.026	0.53	0.012	5.00	0.31
23	0.69	0.057	0.33	0.061	0.56	0.011	5.76	0.28
24	0.52	0.047	0.12	0.044	0.62	0.013	6.30	0.23
25	0.39	0.052	0.13	0.042	0.70	0.013	6.63	0.19
26	0.32	0.040	0.11	0.044	0.73	0.013	6.83	0.16
27	0.21	0.040	0.12	0.041	0.79	0.013	7.32	0.11

Test number	u_{sg} , m/s		u_{sl} , m/s		$\frac{\Delta P}{\Delta L}$, kPa/m		Liquid holdup	
	Avg.	St. dev.	Avg.	St. dev.	Avg.	St. dev.	Avg.	St. dev.
28	0.11	0.037	0.12	0.038	0.88	0.015	8.00	0.06
29	0.06	0.032	0.10	0.041	0.91	0.016	8.38	0.04
30	0.51	0.043	0.32	0.044	0.63	0.012	6.21	0.22
31	0.42	0.036	0.32	0.047	0.68	0.014	6.52	0.20
32	0.32	0.034	0.31	0.049	0.73	0.013	6.90	0.17
33	0.20	0.032	0.31	0.050	0.80	0.014	7.41	0.11
34	0.11	0.027	0.30	0.058	0.87	0.015	8.01	0.06
35	0.08	0.026	0.32	0.041	0.91	0.016	8.22	0.04

Table C.1 Experimental data for gas-liquid flow in pipe.

Test name	D_i , mm	u_{sg} , m/s		u_{sl} , m/s		$\frac{\Delta P}{\Delta L}$, kPa/m	
		Avg.	St.dev.	Avg.	St.dev.	Avg.	St.dev.
test_1c_new_15	33.4	0.54	0.059	0.69	0.011	7.69	0.30
test_1c_new_14	33.4	0.49	0.053	0.69	0.010	7.78	0.27
test_1c_new_13	33.4	0.35	0.045	0.69	0.012	8.06	0.20
test_1c_new_12	33.4	0.22	0.036	0.70	0.011	8.48	0.12
test_1c_new_11	33.4	0.09	0.031	0.70	0.013	8.84	0.06
test_1c_new_6	33.4	0.59	0.074	0.49	0.040	7.20	0.35
test_1c_new_7	33.4	0.52	0.077	0.50	0.037	7.35	0.31
test_1c_new_8	33.4	0.35	0.058	0.50	0.034	7.69	0.25
test_1c_new_9	33.4	0.20	0.048	0.50	0.046	8.18	0.14
test_1c_new_10	33.4	0.11	0.042	0.50	0.045	8.57	0.09
test_1.5c_10	48.3	0.59	0.073	0.51	0.031	8.07	0.17
test_1.5c_9	48.3	0.50	0.064	0.52	0.031	8.28	0.17
test_1.5c_8	48.3	0.35	0.065	0.51	0.036	8.61	0.14
test_1.5c_7	48.3	0.20	0.055	0.51	0.033	9.06	0.10
test_1.5c_6	48.3	0.10	0.054	0.50	0.036	9.42	0.06
test_1.5c_16	48.3	0.10	0.041	0.70	0.022	9.61	0.03
test_1.5c_17	48.3	0.21	0.043	0.71	0.016	9.31	0.07
test_1.5c_18	48.3	0.34	0.046	0.70	0.022	9.02	0.11
test_1.5c_19	48.3	0.50	0.055	0.70	0.020	8.73	0.14
test_1.5c_20	48.3	0.59	0.055	0.70	0.022	8.58	0.14
test_1.25c_20	42.2	0.59	0.052	0.69	0.007	7.65	0.25
test_1.25c_19	42.2	0.51	0.045	0.69	0.007	7.82	0.19
test_1.25c_18	42.2	0.34	0.040	0.69	0.008	8.17	0.14
test_1.25c_17	42.2	0.21	0.036	0.69	0.007	8.55	0.10

Test name	Di, mm	u _{sg} , m/s		u _{sl} , m/s		$\frac{\Delta P}{\Delta L}$, kPa/m	
		Avg.	St.dev.	Avg.	St.dev.	Avg.	St.dev.
test_1.25c_16	42.2	0.11	0.035	0.69	0.011	8.97	0.05
test_1.25c_15	42.2	0.61	0.061	0.51	0.020	7.32	0.23
test_1.25c_14	42.2	0.50	0.051	0.51	0.020	7.58	0.19
test_1.25c_13	42.2	0.34	0.044	0.52	0.035	7.92	0.15
test_1.25c_12	42.2	0.20	0.038	0.51	0.024	8.53	0.11
test_1.25c_11	42.2	0.10	0.051	0.49	0.051	8.96	0.06
test_0.75c_15	26.7	0.55	0.048	0.69	0.007	7.66	0.22
test_0.75c_14	26.7	0.49	0.042	0.69	0.006	7.74	0.20
test_0.75c_13	26.7	0.36	0.036	0.69	0.006	8.01	0.16
test_0.75c_12	26.7	0.20	0.031	0.69	0.007	8.45	0.10
test_0.75c_11	26.7	0.10	0.027	0.69	0.007	8.84	0.05
test_0.75c_10	26.7	0.56	0.055	0.51	0.012	7.21	0.27
test_0.75c_9	26.7	0.50	0.051	0.51	0.013	7.35	0.25
test_0.75c_8	26.7	0.35	0.042	0.50	0.019	7.72	0.20
test_0.75c_7	26.7	0.21	0.034	0.50	0.013	8.17	0.12
test_0.75c_6	26.7	0.10	0.031	0.50	0.018	8.61	0.07

Table C.2 Experimental data for gas-liquid flow in concentric annulus.

Test name	Di, mm	u _{sg} , m/s		u _{sl} , m/s		$\frac{\Delta P}{\Delta L}$, kPa/m	
		Avg.	St.dev.	Avg.	St.dev.	Avg.	St.dev.
test_1e_15	33.4	0.60	5.880	0.70	0.009	7.47	0.15
test_1e_14	33.4	0.50	5.010	0.71	0.010	7.68	0.13
test_1e_13	33.4	0.35	3.545	0.71	0.009	8.00	0.10
test_1e_12	33.4	0.20	2.202	0.71	0.010	8.42	0.06
test_1e_11	33.4	0.12	1.357	0.71	0.009	8.74	0.04
test_1e_10	33.4	0.60	6.027	0.51	0.042	7.25	0.17
test_1e_9	33.4	0.51	5.072	0.52	0.037	7.43	0.15
test_1e_8	33.4	0.35	3.667	0.51	0.042	7.78	0.11
test_1e_7	33.4	0.20	2.208	0.50	0.042	8.23	0.07
test_1e_6	33.4	0.12	1.501	0.50	0.047	8.57	0.05
test_1.5e_15	48.3	0.61	6.047	0.71	0.021	8.56	0.16
test_1.5e_14	48.3	0.51	5.110	0.70	0.024	8.64	0.12
test_1.5e_13	48.3	0.35	3.599	0.71	0.026	8.90	0.09
test_1.5e_12	48.3	0.21	2.286	0.71	0.022	9.15	0.06
test_1.5e_11	48.3	0.11	1.413	0.70	0.029	9.37	0.04
test_1.5e_10	48.3	0.61	6.112	0.51	0.033	8.07	0.18

Test name	D _i , mm	u _{sg} , m/s		u _{sl} , m/s		$\frac{\Delta P}{\Delta L}$, kPa/m	
		Avg.	St.dev.	Avg.	St.dev.	Avg.	St.dev.
test_1.5e_9	48.3	0.50	5.222	0.51	0.036	8.22	0.15
test_1.5e_8	48.3	0.35	3.743	0.51	0.038	8.44	0.10
test_1.5e_7	48.3	0.21	2.475	0.51	0.038	8.71	0.07
test_1.5e_6	48.3	0.09	1.366	0.50	0.039	9.08	0.04
test_1.25e_20	42.2	0.61	0.059	0.68	0.016	7.86	0.20
test_1.25e_19	42.2	0.53	0.057	0.69	0.014	7.98	0.19
test_1.25e_18	42.2	0.35	0.043	0.69	0.011	8.28	0.14
test_1.25e_17	42.2	0.19	0.036	0.69	0.010	8.66	0.08
test_1.25e_16	42.2	0.09	0.036	0.69	0.010	8.94	0.04
test_1.25e_15	42.2	0.61	0.055	0.51	0.016	7.25	0.22
test_1.25e_14	42.2	0.50	0.053	0.51	0.017	7.44	0.20
test_1.25e_13	42.2	0.36	0.047	0.51	0.018	7.80	0.16
test_1.25e_12	42.2	0.19	0.035	0.50	0.020	8.29	0.09
test_1.25e_11	42.2	0.11	0.034	0.50	0.018	8.61	0.06
test_0.75e_15	26.7	0.56	0.046	0.69	0.007	7.38	0.15
test_0.75e_14	26.7	0.52	0.040	0.69	0.007	7.44	0.13
test_0.75e_13	26.7	0.36	0.031	0.69	0.006	7.71	0.10
test_0.75e_12	26.7	0.20	0.031	0.69	0.007	8.11	0.06
test_0.75e_11	26.7	0.11	0.027	0.69	0.007	8.45	0.04
test_0.75e_10	26.7	0.60	0.051	0.50	0.009	6.77	0.19
test_0.75e_9	26.7	0.50	0.047	0.50	0.011	6.99	0.15
test_0.75e_8	26.7	0.35	0.044	0.50	0.009	7.34	0.12
test_0.75e_7	26.7	0.19	0.034	0.50	0.010	7.84	0.07
test_0.75e_6	26.7	0.11	0.033	0.50	0.010	8.23	0.04

Table C.3 Experimental data for gas-liquid flow in eccentric annulus.



Pedro Cavalcanti De Sousa <pedrosousa@tamu.edu>

AAUDE Doctoral Student Survey Completion Certificate

1 message

Pedro Cavalcanti De Sousa <noreply@qemailserver.com>

Wed, Apr 1, 2020 at 11:01 AM

Reply-To: Pedro Cavalcanti De Sousa <survey@tamu.edu>

To: pedrosousa@tamu.edu

TAMU Doctoral Student Exit Survey Completion Certificate

Pedro Cavalcanti De Sousa (UIN:219003060) submitted all pages of the TAMU Doctoral Student Exit Survey on 4/1/2020.

Thank you for answering TAMU Doctoral Student Exit Survey.

CERTIFICATE *of* COMPLETION

of the

Survey of Earned Doctorates

Questionnaire

This certifies that Pedro Cavalcanti de Sousa,
a student at Texas A&M University Graduate School,
has completed the Survey of Earned Doctorates
on 4/1/2020.

Confirmation Code:228723KTFN





Marketplace™

Copyright authorization for Figure 1.1

Society of Petroleum Engineers (SPE) - License Terms and Conditions

This is a License Agreement between Pedro Cavalcanti de Sousa / Texas A&M University ("You") and Society of Petroleum Engineers (SPE) ("Publisher") provided by Copyright Clearance Center ("CCC"). The license consists of your order details, the terms and conditions provided by Society of Petroleum Engineers (SPE), and the CCC terms and conditions.

All payments must be made in full to CCC.

Order Date	06-Apr-2020	Type of Use	Republish in a thesis/dissertation
Order license ID	1026962-1	Publisher	Society of Petroleum Engineers
ISBN-13	978-1-61399-263-0	Portion	Chart/graph/table/figure

LICENSED CONTENT

Publication Title	SPE Kuwait International Petroleum Conference and Exhibition	Country	United States of America
Author/Editor	Society of Petroleum Engineers	Rightsholder	Society of Petroleum Engineers (SPE)
Date	12/31/2011	Publication Type	e-Book
Language	English		

REQUEST DETAILS

Portion Type	Chart/graph/table/figure	Distribution	Worldwide
Number of charts / graphs / tables / figures requested	1	Translation	Original language of publication
Format (select all that apply)	Print, Electronic	Copies for the disabled?	No
Who will republish the content?	Academic institution	Minor editing privileges?	No
Duration of Use	Life of current edition	Incidental promotional use?	No
Lifetime Unit Quantity	Up to 499	Currency	USD
Rights Requested	Main product		

NEW WORK DETAILS

Title	THE DYNAMICS OF DRILLING FLUID RHEOLOGY, WELLBORE FLOW, AND FORMATION PRESSURE IN WELL CONTROL	Institution name	Texas A&M University
Instructor name	Dr. Jerome Schubert	Expected presentation date	2020-05-01

ADDITIONAL DETAILS

Order reference number	N/A	The requesting person / organization to appear on the license	Pedro Cavalcanti de Sousa / Texas A&M University
------------------------	-----	---------------------------------------------------------------	--------------------------------------------------

REUSE CONTENT DETAILS

Title, description or numeric reference of the portion(s)	Figure 1e	Title of the article/chapter the portion is from	HPHT 101: What Every Engineer or Geoscientist Should Know about High Pressure High Temperature Wells
Editor of portion(s)	N/A	Author of portion(s)	Society of Petroleum Engineers
Volume of serial or monograph	N/A	Issue, if republishing an article from a serial	N/A
Page or page range of portion	3	Publication date of portion	2012-12-10

CCC Republication Terms and Conditions

1. Description of Service; Defined Terms. This Republication License enables the User to obtain licenses for republication of one or more copyrighted works as described in detail on the relevant Order Confirmation (the "Work(s)"). Copyright Clearance Center, Inc. ("CCC") grants licenses through the Service on behalf of the rightsholder identified on the Order Confirmation (the "Rightsholder"). "Republication", as used herein, generally means the inclusion of a Work, in whole or in part, in a new work or works, also as described on the Order Confirmation. "User", as used herein, means the person or entity making such republication.
2. The terms set forth in the relevant Order Confirmation, and any terms set by the Rightsholder with respect to a particular Work, govern the terms of use of Works in connection with the Service. By using the Service, the person transacting for a republication license on behalf of the User represents and warrants that he/she/it (a) has been duly authorized by the User to accept, and hereby does accept, all such terms and conditions on behalf of User, and (b) shall inform User of all such terms and conditions. In the event such person is a "freelancer" or other third party independent of User and CCC, such party shall be deemed jointly a "User" for purposes of these terms and conditions. In any event, User shall be deemed to have accepted and agreed to all such terms and conditions if User republishes the Work in any fashion.
3. Scope of License; Limitations and Obligations.
 - 3.1. All Works and all rights therein, including copyright rights, remain the sole and exclusive property of the Rightsholder. The license created by the exchange of an Order Confirmation (and/or any invoice) and payment by User of the full amount set forth on that document includes only those rights expressly set forth in the Order Confirmation and in these terms and conditions, and conveys no other rights in the Work(s) to User. All rights not expressly granted are hereby reserved.
 - 3.2. General Payment Terms: You may pay by credit card or through an account with us payable at the end of the month. If you and we agree that you may establish a standing account with CCC, then the following terms apply: Remit Payment to: Copyright Clearance Center, 29118 Network Place, Chicago, IL 60673-1291. Payments Due: Invoices are payable upon their delivery to you (or upon our notice to you that they are available to you for downloading). After 30 days, outstanding amounts will be subject to a service charge of 1-1/2% per month or, if less, the maximum rate allowed by applicable law. Unless otherwise specifically set forth in the Order Confirmation or in a separate written agreement signed by CCC, invoices are due and payable on "net 30" terms. While User may exercise the rights licensed immediately upon issuance of the Order Confirmation, the license is automatically revoked and is null and void, as if it had never been

issued, if complete payment for the license is not received on a timely basis either from User directly or through a payment agent, such as a credit card company.

- 3.3. Unless otherwise provided in the Order Confirmation, any grant of rights to User (i) is "one-time" (including the editions and product family specified in the license), (ii) is non-exclusive and non-transferable and (iii) is subject to any and all limitations and restrictions (such as, but not limited to, limitations on duration of use or circulation) included in the Order Confirmation or invoice and/or in these terms and conditions. Upon completion of the licensed use, User shall either secure a new permission for further use of the Work(s) or immediately cease any new use of the Work(s) and shall render inaccessible (such as by deleting or by removing or severing links or other locators) any further copies of the Work (except for copies printed on paper in accordance with this license and still in User's stock at the end of such period).
- 3.4. In the event that the material for which a republication license is sought includes third party materials (such as photographs, illustrations, graphs, inserts and similar materials) which are identified in such material as having been used by permission, User is responsible for identifying, and seeking separate licenses (under this Service or otherwise) for, any of such third party materials; without a separate license, such third party materials may not be used.
- 3.5. Use of proper copyright notice for a Work is required as a condition of any license granted under the Service. Unless otherwise provided in the Order Confirmation, a proper copyright notice will read substantially as follows: "Republished with permission of [Rightsholder's name], from [Work's title, author, volume, edition number and year of copyright]; permission conveyed through Copyright Clearance Center, Inc. " Such notice must be provided in a reasonably legible font size and must be placed either immediately adjacent to the Work as used (for example, as part of a by-line or footnote but not as a separate electronic link) or in the place where substantially all other credits or notices for the new work containing the republished Work are located. Failure to include the required notice results in loss to the Rightsholder and CCC, and the User shall be liable to pay liquidated damages for each such failure equal to twice the use fee specified in the Order Confirmation, in addition to the use fee itself and any other fees and charges specified.
- 3.6. User may only make alterations to the Work if and as expressly set forth in the Order Confirmation. No Work may be used in any way that is defamatory, violates the rights of third parties (including such third parties' rights of copyright, privacy, publicity, or other tangible or intangible property), or is otherwise illegal, sexually explicit or obscene. In addition, User may not conjoin a Work with any other material that may result in damage to the reputation of the Rightsholder. User agrees to inform CCC if it becomes aware of any infringement of any rights in a Work and to cooperate with any reasonable request of CCC or the Rightsholder in connection therewith.
4. Indemnity. User hereby indemnifies and agrees to defend the Rightsholder and CCC, and their respective employees and directors, against all claims, liability, damages, costs and expenses, including legal fees and expenses, arising out of any use of a Work beyond the scope of the rights granted herein, or any use of a Work which has been altered in any unauthorized way by User, including claims of defamation or infringement of rights of copyright, publicity, privacy or other tangible or intangible property.
5. Limitation of Liability. UNDER NO CIRCUMSTANCES WILL CCC OR THE RIGHTSHOLDER BE LIABLE FOR ANY DIRECT, INDIRECT, CONSEQUENTIAL OR INCIDENTAL DAMAGES (INCLUDING WITHOUT LIMITATION DAMAGES FOR LOSS OF BUSINESS PROFITS OR INFORMATION, OR FOR BUSINESS INTERRUPTION) ARISING OUT OF THE USE OR INABILITY TO USE A WORK, EVEN IF ONE OF THEM HAS BEEN ADVISED OF THE POSSIBILITY OF SUCH DAMAGES. In any event, the total liability of the Rightsholder and CCC (including their respective employees and directors) shall not exceed the total amount actually paid by User for this license. User assumes full liability for the actions and omissions of its principals, employees, agents, affiliates, successors and assigns.
6. Limited Warranties. THE WORK(S) AND RIGHT(S) ARE PROVIDED "AS IS". CCC HAS THE RIGHT TO GRANT TO USER THE RIGHTS GRANTED IN THE ORDER CONFIRMATION DOCUMENT. CCC AND THE RIGHTSHOLDER DISCLAIM ALL OTHER WARRANTIES RELATING TO THE WORK(S) AND RIGHT(S), EITHER EXPRESS OR IMPLIED, INCLUDING

WITHOUT LIMITATION IMPLIED WARRANTIES OF MERCHANTABILITY OR FITNESS FOR A PARTICULAR PURPOSE. ADDITIONAL RIGHTS MAY BE REQUIRED TO USE ILLUSTRATIONS, GRAPHS, PHOTOGRAPHS, ABSTRACTS, INSERTS OR OTHER PORTIONS OF THE WORK (AS OPPOSED TO THE ENTIRE WORK) IN A MANNER CONTEMPLATED BY USER; USER UNDERSTANDS AND AGREES THAT NEITHER CCC NOR THE RIGHTSHOLDER MAY HAVE SUCH ADDITIONAL RIGHTS TO GRANT.

7. Effect of Breach. Any failure by User to pay any amount when due, or any use by User of a Work beyond the scope of the license set forth in the Order Confirmation and/or these terms and conditions, shall be a material breach of the license created by the Order Confirmation and these terms and conditions. Any breach not cured within 30 days of written notice thereof shall result in immediate termination of such license without further notice. Any unauthorized (but licensable) use of a Work that is terminated immediately upon notice thereof may be liquidated by payment of the Rightsholder's ordinary license price therefor; any unauthorized (and unlicensable) use that is not terminated immediately for any reason (including, for example, because materials containing the Work cannot reasonably be recalled) will be subject to all remedies available at law or in equity, but in no event to a payment of less than three times the Rightsholder's ordinary license price for the most closely analogous licensable use plus Rightsholder's and/or CCC's costs and expenses incurred in collecting such payment.

8. Miscellaneous.

8.1. User acknowledges that CCC may, from time to time, make changes or additions to the Service or to these terms and conditions, and CCC reserves the right to send notice to the User by electronic mail or otherwise for the purposes of notifying User of such changes or additions; provided that any such changes or additions shall not apply to permissions already secured and paid for.

8.2. Use of User-related information collected through the Service is governed by CCC's privacy policy, available online here: <https://marketplace.copyright.com/rs-ui-web/mp/privacy-policy>

8.3. The licensing transaction described in the Order Confirmation is personal to User. Therefore, User may not assign or transfer to any other person (whether a natural person or an organization of any kind) the license created by the Order Confirmation and these terms and conditions or any rights granted hereunder; provided, however, that User may assign such license in its entirety on written notice to CCC in the event of a transfer of all or substantially all of User's rights in the new material which includes the Work(s) licensed under this Service.

8.4. No amendment or waiver of any terms is binding unless set forth in writing and signed by the parties. The Rightsholder and CCC hereby object to any terms contained in any writing prepared by the User or its principals, employees, agents or affiliates and purporting to govern or otherwise relate to the licensing transaction described in the Order Confirmation, which terms are in any way inconsistent with any terms set forth in the Order Confirmation and/or in these terms and conditions or CCC's standard operating procedures, whether such writing is prepared prior to, simultaneously with or subsequent to the Order Confirmation, and whether such writing appears on a copy of the Order Confirmation or in a separate instrument.

8.5. The licensing transaction described in the Order Confirmation document shall be governed by and construed under the law of the State of New York, USA, without regard to the principles thereof of conflicts of law. Any case, controversy, suit, action, or proceeding arising out of, in connection with, or related to such licensing transaction shall be brought, at CCC's sole discretion, in any federal or state court located in the County of New York, State of New York, USA, or in any federal or state court whose geographical jurisdiction covers the location of the Rightsholder set forth in the Order Confirmation. The parties expressly submit to the personal jurisdiction and venue of each such federal or state court. If you have any comments or questions about the Service or Copyright Clearance Center, please contact us at 978-750-8400 or send an e-mail to support@copyright.com.



Marketplace™

Copyright authorization for Figure 1.2

Society of Petroleum Engineers (SPE) - License Terms and Conditions

This is a License Agreement between Pedro Cavalcanti de Sousa / Texas A&M University ("You") and Society of Petroleum Engineers (SPE) ("Publisher") provided by Copyright Clearance Center ("CCC"). The license consists of your order details, the terms and conditions provided by Society of Petroleum Engineers (SPE), and the CCC terms and conditions.

All payments must be made in full to CCC.

Order Date	06-Apr-2020	Type of Use	Republish in a
Order license ID	1026963-1		thesis/dissertation
ISBN-13	9781555631079	Publisher	Society of Petroleum Engineers
		Portion	Chart/graph/table/figure

LICENSED CONTENT

Publication Title	Mechanistic modeling of gas-liquid two-phase flow in pipes	Country	United States of America
		Rightsholder	Society of Petroleum Engineers (SPE)
Author/Editor	Shoham, Ovadia., Society of Petroleum Engineers of AIME.	Publication Type	Book
Date	12/31/2005		
Language	English		

REQUEST DETAILS

Portion Type	Chart/graph/table/figure	Distribution	Worldwide
Number of charts / graphs / tables / figures requested	1	Translation	Original language of publication
Format (select all that apply)	Print, Electronic	Copies for the disabled?	No
Who will republish the content?	Academic institution	Minor editing privileges?	No
Duration of Use	Life of current edition	Incidental promotional use?	No
Lifetime Unit Quantity	Up to 499	Currency	USD
Rights Requested	Main product		

NEW WORK DETAILS

Title	THE DYNAMICS OF DRILLING FLUID RHEOLOGY, WELLBORE FLOW, AND FORMATION PRESSURE IN WELL CONTROL	Institution name	Texas A&M University
		Expected presentation date	2020-05-01

Instructor name Dr Jerome Schubert

ADDITIONAL DETAILS

Order reference number	N/A	The requesting person / organization to appear on the license	Pedro Cavalcanti de Sousa / Texas A&M University
------------------------	-----	---------------------------------------------------------------	--------------------------------------------------

REUSE CONTENT DETAILS

Title, description or numeric reference of the portion(s)	Figure 1.5	Title of the article/chapter the portion is from	Mechanistic modeling of gas-liquid two-phase flow in pipes
Editor of portion(s)	N/A	Author of portion(s)	Shoham, Ovadia.; Society of Petroleum Engineers of AIME.
Volume of serial or monograph	N/A		
Page or page range of portion	9	Issue, if republishing an article from a serial	N/A
		Publication date of portion	2006-01-01

CCC Republication Terms and Conditions

1. Description of Service; Defined Terms. This Republication License enables the User to obtain licenses for republication of one or more copyrighted works as described in detail on the relevant Order Confirmation (the "Work(s)"). Copyright Clearance Center, Inc. ("CCC") grants licenses through the Service on behalf of the rightsholder identified on the Order Confirmation (the "Rightsholder"). "Republishing", as used herein, generally means the inclusion of a Work, in whole or in part, in a new work or works, also as described on the Order Confirmation. "User", as used herein, means the person or entity making such republication.
2. The terms set forth in the relevant Order Confirmation, and any terms set by the Rightsholder with respect to a particular Work, govern the terms of use of Works in connection with the Service. By using the Service, the person transacting for a republication license on behalf of the User represents and warrants that he/she/it (a) has been duly authorized by the User to accept, and hereby does accept, all such terms and conditions on behalf of User, and (b) shall inform User of all such terms and conditions. In the event such person is a "freelancer" or other third party independent of User and CCC, such party shall be deemed jointly a "User" for purposes of these terms and conditions. In any event, User shall be deemed to have accepted and agreed to all such terms and conditions if User republishes the Work in any fashion.
3. Scope of License; Limitations and Obligations.
 - 3.1. All Works and all rights therein, including copyright rights, remain the sole and exclusive property of the Rightsholder. The license created by the exchange of an Order Confirmation (and/or any invoice) and payment by User of the full amount set forth on that document includes only those rights expressly set forth in the Order Confirmation and in these terms and conditions, and conveys no other rights in the Work(s) to User. All rights not expressly granted are hereby reserved.
 - 3.2. General Payment Terms: You may pay by credit card or through an account with us payable at the end of the month. If you and we agree that you may establish a standing account with CCC, then the following terms apply: Remit Payment to: Copyright Clearance Center, 29118 Network Place, Chicago, IL 60673-1291. Payments Due: Invoices are payable upon their delivery to you (or upon our notice to you that they are available to you for downloading). After 30 days, outstanding amounts will be subject to a service charge of 1-1/2% per month or, if less, the maximum rate allowed by applicable law. Unless otherwise specifically set forth in the Order Confirmation or in a separate written agreement signed by CCC, invoices are due

and payable on "net 30" terms. While User may exercise the rights licensed immediately upon issuance of the Order Confirmation, the license is automatically revoked and is null and void, as if it had never been issued, if complete payment for the license is not received on a timely basis either from User directly or through a payment agent, such as a credit card company.

- 3.3. Unless otherwise provided in the Order Confirmation, any grant of rights to User (i) is "one-time" (including the editions and product family specified in the license), (ii) is non-exclusive and non-transferable and (iii) is subject to any and all limitations and restrictions (such as, but not limited to, limitations on duration of use or circulation) included in the Order Confirmation or invoice and/or in these terms and conditions. Upon completion of the licensed use, User shall either secure a new permission for further use of the Work(s) or immediately cease any new use of the Work(s) and shall render inaccessible (such as by deleting or by removing or severing links or other locators) any further copies of the Work (except for copies printed on paper in accordance with this license and still in User's stock at the end of such period).
- 3.4. In the event that the material for which a republication license is sought includes third party materials (such as photographs, illustrations, graphs, inserts and similar materials) which are identified in such material as having been used by permission, User is responsible for identifying, and seeking separate licenses (under this Service or otherwise) for, any of such third party materials; without a separate license, such third party materials may not be used.
- 3.5. Use of proper copyright notice for a Work is required as a condition of any license granted under the Service. Unless otherwise provided in the Order Confirmation, a proper copyright notice will read substantially as follows: "Republished with permission of [Rightsholder's name], from [Work's title, author, volume, edition number and year of copyright]; permission conveyed through Copyright Clearance Center, Inc. " Such notice must be provided in a reasonably legible font size and must be placed either immediately adjacent to the Work as used (for example, as part of a by-line or footnote but not as a separate electronic link) or in the place where substantially all other credits or notices for the new work containing the republished Work are located. Failure to include the required notice results in loss to the Rightsholder and CCC, and the User shall be liable to pay liquidated damages for each such failure equal to twice the use fee specified in the Order Confirmation, in addition to the use fee itself and any other fees and charges specified.
- 3.6. User may only make alterations to the Work if and as expressly set forth in the Order Confirmation. No Work may be used in any way that is defamatory, violates the rights of third parties (including such third parties' rights of copyright, privacy, publicity, or other tangible or intangible property), or is otherwise illegal, sexually explicit or obscene. In addition, User may not conjoin a Work with any other material that may result in damage to the reputation of the Rightsholder. User agrees to inform CCC if it becomes aware of any infringement of any rights in a Work and to cooperate with any reasonable request of CCC or the Rightsholder in connection therewith.
4. Indemnity. User hereby indemnifies and agrees to defend the Rightsholder and CCC, and their respective employees and directors, against all claims, liability, damages, costs and expenses, including legal fees and expenses, arising out of any use of a Work beyond the scope of the rights granted herein, or any use of a Work which has been altered in any unauthorized way by User, including claims of defamation or infringement of rights of copyright, publicity, privacy or other tangible or intangible property.
5. Limitation of Liability. UNDER NO CIRCUMSTANCES WILL CCC OR THE RIGHTSHOLDER BE LIABLE FOR ANY DIRECT, INDIRECT, CONSEQUENTIAL OR INCIDENTAL DAMAGES (INCLUDING WITHOUT LIMITATION DAMAGES FOR LOSS OF BUSINESS PROFITS OR INFORMATION, OR FOR BUSINESS INTERRUPTION) ARISING OUT OF THE USE OR INABILITY TO USE A WORK, EVEN IF ONE OF THEM HAS BEEN ADVISED OF THE POSSIBILITY OF SUCH DAMAGES. In any event, the total liability of the Rightsholder and CCC (including their respective employees and directors) shall not exceed the total amount actually paid by User for this license. User assumes full liability for the actions and omissions of its principals, employees, agents, affiliates, successors and assigns.
6. Limited Warranties. THE WORK(S) AND RIGHT(S) ARE PROVIDED "AS IS". CCC HAS THE RIGHT TO GRANT TO USER

THE RIGHTS GRANTED IN THE ORDER CONFIRMATION DOCUMENT. CCC AND THE RIGHTSHOLDER DISCLAIM ALL OTHER WARRANTIES RELATING TO THE WORK(S) AND RIGHT(S), EITHER EXPRESS OR IMPLIED, INCLUDING WITHOUT LIMITATION IMPLIED WARRANTIES OF MERCHANTABILITY OR FITNESS FOR A PARTICULAR PURPOSE. ADDITIONAL RIGHTS MAY BE REQUIRED TO USE ILLUSTRATIONS, GRAPHS, PHOTOGRAPHS, ABSTRACTS, INSERTS OR OTHER PORTIONS OF THE WORK (AS OPPOSED TO THE ENTIRE WORK) IN A MANNER CONTEMPLATED BY USER; USER UNDERSTANDS AND AGREES THAT NEITHER CCC NOR THE RIGHTSHOLDER MAY HAVE SUCH ADDITIONAL RIGHTS TO GRANT.

7. Effect of Breach. Any failure by User to pay any amount when due, or any use by User of a Work beyond the scope of the license set forth in the Order Confirmation and/or these terms and conditions, shall be a material breach of the license created by the Order Confirmation and these terms and conditions. Any breach not cured within 30 days of written notice thereof shall result in immediate termination of such license without further notice. Any unauthorized (but licensable) use of a Work that is terminated immediately upon notice thereof may be liquidated by payment of the Rightsholder's ordinary license price therefor; any unauthorized (and unlicensable) use that is not terminated immediately for any reason (including, for example, because materials containing the Work cannot reasonably be recalled) will be subject to all remedies available at law or in equity, but in no event to a payment of less than three times the Rightsholder's ordinary license price for the most closely analogous licensable use plus Rightsholder's and/or CCC's costs and expenses incurred in collecting such payment.
8. Miscellaneous.
 - 8.1. User acknowledges that CCC may, from time to time, make changes or additions to the Service or to these terms and conditions, and CCC reserves the right to send notice to the User by electronic mail or otherwise for the purposes of notifying User of such changes or additions; provided that any such changes or additions shall not apply to permissions already secured and paid for.
 - 8.2. Use of User-related information collected through the Service is governed by CCC's privacy policy, available online here:<https://marketplace.copyright.com/rs-ui-web/mp/privacy-policy>
 - 8.3. The licensing transaction described in the Order Confirmation is personal to User. Therefore, User may not assign or transfer to any other person (whether a natural person or an organization of any kind) the license created by the Order Confirmation and these terms and conditions or any rights granted hereunder; provided, however, that User may assign such license in its entirety on written notice to CCC in the event of a transfer of all or substantially all of User's rights in the new material which includes the Work(s) licensed under this Service.
 - 8.4. No amendment or waiver of any terms is binding unless set forth in writing and signed by the parties. The Rightsholder and CCC hereby object to any terms contained in any writing prepared by the User or its principals, employees, agents or affiliates and purporting to govern or otherwise relate to the licensing transaction described in the Order Confirmation, which terms are in any way inconsistent with any terms set forth in the Order Confirmation and/or in these terms and conditions or CCC's standard operating procedures, whether such writing is prepared prior to, simultaneously with or subsequent to the Order Confirmation, and whether such writing appears on a copy of the Order Confirmation or in a separate instrument.
 - 8.5. The licensing transaction described in the Order Confirmation document shall be governed by and construed under the law of the State of New York, USA, without regard to the principles thereof of conflicts of law. Any case, controversy, suit, action, or proceeding arising out of, in connection with, or related to such licensing transaction shall be brought, at CCC's sole discretion, in any federal or state court located in the County of New York, State of New York, USA, or in any federal or state court whose geographical jurisdiction covers the location of the Rightsholder set forth in the Order Confirmation. The parties expressly submit to the personal jurisdiction and venue of each such federal or state court. If you have any comments or questions about the Service or Copyright Clearance Center, please contact us at 978-750-8400 or send an e-mail to support@copyright.com.



Marketplace™

Copyright authorization for Figure 1.3

American Society of Mechanical Engineers ASME - License Terms and Conditions

This is a License Agreement between Pedro Cavalcanti de Sousa / Texas A&M University ("You") and American Society of Mechanical Engineers ASME ("Publisher") provided by Copyright Clearance Center ("CCC"). The license consists of your order details, the terms and conditions provided by American Society of Mechanical Engineers ASME, and the CCC terms and conditions.

All payments must be made in full to CCC.

Order Date	09-Apr-2020	Type of Use	Republish in a thesis/dissertation
Order license ID	1027615-1	Publisher	AMERICAN SOCIETY OF MECHANICAL ENGINEERS,
ISSN	0195-0738	Portion	Chart/graph/table/figure

LICENSED CONTENT

Publication Title	Journal of energy resources technology	Country	United States of America
Author/Editor	AMERICAN SOCIETY OF MECHANICAL ENGINEERS.	Rightholder	American Society of Mechanical Engineers ASME
Date	12/31/1978	Publication Type	Journal
Language	English		

REQUEST DETAILS

Portion Type	Chart/graph/table/figure	Distribution	Worldwide
Number of charts / graphs / tables / figures requested	2	Translation	Original language of publication
Format (select all that apply)	Print, Electronic	Copies for the disabled?	No
Who will republish the content?	Academic institution	Minor editing privileges?	No
Duration of Use	Life of current edition	Incidental promotional use?	No
Lifetime Unit Quantity	Up to 499	Currency	USD
Rights Requested	Main product		

NEW WORK DETAILS

Title	The Dynamics of Drilling Fluid Rheology, Wellbore Flow, and Formation Pressure in Well Control	Institution name	Texas A&M University
Instructor name	Dr. Jerome Schubert	Expected presentation date	2020-05-08

ADDITIONAL DETAILS

Order reference number	N/A	The requesting person / organization to appear on the license	Pedro Cavalcanti de Sousa / Texas A&M University
------------------------	-----	---------------------------------------------------------------	--------------------------------------------------

REUSE CONTENT DETAILS

Title, description or numeric reference of the portion(s)	Figure 9 and Figure 10	Title of the article/chapter the portion is from	Upward Vertical Two-Phase Flow Through an Annulus-Part I: Single-Phase Friction Factor, Taylor Bubble Rise Velocity, and Flow Pattern Prediction
Editor of portion(s)	N/A		
Volume of serial or monograph	114		
Page or page range of portion	10	Author of portion(s)	AMERICAN SOCIETY OF MECHANICAL ENGINEERS.
		Issue, if republishing an article from a serial	1
		Publication date of portion	1992-03-01

PUBLISHER SPECIAL TERMS AND CONDITIONS

Permission is granted for the specific use of Figures 9, 10 only as stated herein and does not permit further use of the materials without proper authorization. As is customary, we request that you ensure proper acknowledgment of the exact sources of this material, the authors, and ASME as original publisher.

CCC Republication Terms and Conditions

1. Description of Service; Defined Terms. This Republication License enables the User to obtain licenses for republication of one or more copyrighted works as described in detail on the relevant Order Confirmation (the "Work(s)"). Copyright Clearance Center, Inc. ("CCC") grants licenses through the Service on behalf of the rightsholder identified on the Order Confirmation (the "Rightsholder"). "Republication", as used herein, generally means the inclusion of a Work, in whole or in part, in a new work or works, also as described on the Order Confirmation. "User", as used herein, means the person or entity making such republication.
2. The terms set forth in the relevant Order Confirmation, and any terms set by the Rightsholder with respect to a particular Work, govern the terms of use of Works in connection with the Service. By using the Service, the person transacting for a republication license on behalf of the User represents and warrants that he/she/it (a) has been duly authorized by the User to accept, and hereby does accept, all such terms and conditions on behalf of User, and (b) shall inform User of all such terms and conditions. In the event such person is a "freelancer" or other third party independent of User and CCC, such party shall be deemed jointly a "User" for purposes of these terms and conditions. In any event, User shall be deemed to have accepted and agreed to all such terms and conditions if User republishes the Work in any fashion.
3. Scope of License; Limitations and Obligations.
 - 3.1. All Works and all rights therein, including copyright rights, remain the sole and exclusive property of the Rightsholder. The license created by the exchange of an Order Confirmation (and/or any invoice) and payment by User of the full amount set forth on that document includes only those rights expressly set forth in the Order Confirmation and in these terms and conditions, and conveys no other rights in the Work(s) to User. All rights not expressly granted are hereby reserved.
 - 3.2. General Payment Terms: You may pay by credit card or through an account with us payable at the end of the month. If you and we agree that you may establish a standing account with CCC, then the following terms apply: Remit Payment to: Copyright Clearance Center, 29118 Network Place, Chicago, IL 60673-1291.

Payments Due: Invoices are payable upon their delivery to you (or upon our notice to you that they are available to you for downloading). After 30 days, outstanding amounts will be subject to a service charge of 1-1/2% per month or, if less, the maximum rate allowed by applicable law. Unless otherwise specifically set forth in the Order Confirmation or in a separate written agreement signed by CCC, invoices are due and payable on "net 30" terms. While User may exercise the rights licensed immediately upon issuance of the Order Confirmation, the license is automatically revoked and is null and void, as if it had never been issued, if complete payment for the license is not received on a timely basis either from User directly or through a payment agent, such as a credit card company.

- 3.3. Unless otherwise provided in the Order Confirmation, any grant of rights to User (i) is "one-time" (including the editions and product family specified in the license), (ii) is non-exclusive and non-transferable and (iii) is subject to any and all limitations and restrictions (such as, but not limited to, limitations on duration of use or circulation) included in the Order Confirmation or invoice and/or in these terms and conditions. Upon completion of the licensed use, User shall either secure a new permission for further use of the Work(s) or immediately cease any new use of the Work(s) and shall render inaccessible (such as by deleting or by removing or severing links or other locators) any further copies of the Work (except for copies printed on paper in accordance with this license and still in User's stock at the end of such period).
- 3.4. In the event that the material for which a republication license is sought includes third party materials (such as photographs, illustrations, graphs, inserts and similar materials) which are identified in such material as having been used by permission, User is responsible for identifying, and seeking separate licenses (under this Service or otherwise) for, any of such third party materials; without a separate license, such third party materials may not be used.
- 3.5. Use of proper copyright notice for a Work is required as a condition of any license granted under the Service. Unless otherwise provided in the Order Confirmation, a proper copyright notice will read substantially as follows: "Republished with permission of [Rightsholder's name], from [Work's title, author, volume, edition number and year of copyright]; permission conveyed through Copyright Clearance Center, Inc. " Such notice must be provided in a reasonably legible font size and must be placed either immediately adjacent to the Work as used (for example, as part of a by-line or footnote but not as a separate electronic link) or in the place where substantially all other credits or notices for the new work containing the republished Work are located. Failure to include the required notice results in loss to the Rightsholder and CCC, and the User shall be liable to pay liquidated damages for each such failure equal to twice the use fee specified in the Order Confirmation, in addition to the use fee itself and any other fees and charges specified.
- 3.6. User may only make alterations to the Work if and as expressly set forth in the Order Confirmation. No Work may be used in any way that is defamatory, violates the rights of third parties (including such third parties' rights of copyright, privacy, publicity, or other tangible or intangible property), or is otherwise illegal, sexually explicit or obscene. In addition, User may not conjoin a Work with any other material that may result in damage to the reputation of the Rightsholder. User agrees to inform CCC if it becomes aware of any infringement of any rights in a Work and to cooperate with any reasonable request of CCC or the Rightsholder in connection therewith.
4. Indemnity. User hereby indemnifies and agrees to defend the Rightsholder and CCC, and their respective employees and directors, against all claims, liability, damages, costs and expenses, including legal fees and expenses, arising out of any use of a Work beyond the scope of the rights granted herein, or any use of a Work which has been altered in any unauthorized way by User, including claims of defamation or infringement of rights of copyright, publicity, privacy or other tangible or intangible property.
5. Limitation of Liability. UNDER NO CIRCUMSTANCES WILL CCC OR THE RIGHTSHOLDER BE LIABLE FOR ANY DIRECT, INDIRECT, CONSEQUENTIAL OR INCIDENTAL DAMAGES (INCLUDING WITHOUT LIMITATION DAMAGES FOR LOSS OF BUSINESS PROFITS OR INFORMATION, OR FOR BUSINESS INTERRUPTION) ARISING OUT OF THE USE OR INABILITY TO USE A WORK, EVEN IF ONE OF THEM HAS BEEN ADVISED OF THE POSSIBILITY OF SUCH DAMAGES. In any event, the total liability of the Rightsholder and CCC (including their respective employees and directors) shall not exceed

the total amount actually paid by User for this license. User assumes full liability for the actions and omissions of its principals, employees, agents, affiliates, successors and assigns.

6. Limited Warranties. THE WORK(S) AND RIGHT(S) ARE PROVIDED "AS IS". CCC HAS THE RIGHT TO GRANT TO USER THE RIGHTS GRANTED IN THE ORDER CONFIRMATION DOCUMENT. CCC AND THE RIGHTSHOLDER DISCLAIM ALL OTHER WARRANTIES RELATING TO THE WORK(S) AND RIGHT(S), EITHER EXPRESS OR IMPLIED, INCLUDING WITHOUT LIMITATION IMPLIED WARRANTIES OF MERCHANTABILITY OR FITNESS FOR A PARTICULAR PURPOSE. ADDITIONAL RIGHTS MAY BE REQUIRED TO USE ILLUSTRATIONS, GRAPHS, PHOTOGRAPHS, ABSTRACTS, INSERTS OR OTHER PORTIONS OF THE WORK (AS OPPOSED TO THE ENTIRE WORK) IN A MANNER CONTEMPLATED BY USER; USER UNDERSTANDS AND AGREES THAT NEITHER CCC NOR THE RIGHTSHOLDER MAY HAVE SUCH ADDITIONAL RIGHTS TO GRANT.
7. Effect of Breach. Any failure by User to pay any amount when due, or any use by User of a Work beyond the scope of the license set forth in the Order Confirmation and/or these terms and conditions, shall be a material breach of the license created by the Order Confirmation and these terms and conditions. Any breach not cured within 30 days of written notice thereof shall result in immediate termination of such license without further notice. Any unauthorized (but licensable) use of a Work that is terminated immediately upon notice thereof may be liquidated by payment of the Rightsholder's ordinary license price therefor; any unauthorized (and unlicensable) use that is not terminated immediately for any reason (including, for example, because materials containing the Work cannot reasonably be recalled) will be subject to all remedies available at law or in equity, but in no event to a payment of less than three times the Rightsholder's ordinary license price for the most closely analogous licensable use plus Rightsholder's and/or CCC's costs and expenses incurred in collecting such payment.
8. Miscellaneous.
 - 8.1. User acknowledges that CCC may, from time to time, make changes or additions to the Service or to these terms and conditions, and CCC reserves the right to send notice to the User by electronic mail or otherwise for the purposes of notifying User of such changes or additions; provided that any such changes or additions shall not apply to permissions already secured and paid for.
 - 8.2. Use of User-related information collected through the Service is governed by CCC's privacy policy, available online here:<https://marketplace.copyright.com/rs-ui-web/mp/privacy-policy>
 - 8.3. The licensing transaction described in the Order Confirmation is personal to User. Therefore, User may not assign or transfer to any other person (whether a natural person or an organization of any kind) the license created by the Order Confirmation and these terms and conditions or any rights granted hereunder; provided, however, that User may assign such license in its entirety on written notice to CCC in the event of a transfer of all or substantially all of User's rights in the new material which includes the Work(s) licensed under this Service.
 - 8.4. No amendment or waiver of any terms is binding unless set forth in writing and signed by the parties. The Rightsholder and CCC hereby object to any terms contained in any writing prepared by the User or its principals, employees, agents or affiliates and purporting to govern or otherwise relate to the licensing transaction described in the Order Confirmation, which terms are in any way inconsistent with any terms set forth in the Order Confirmation and/or in these terms and conditions or CCC's standard operating procedures, whether such writing is prepared prior to, simultaneously with or subsequent to the Order Confirmation, and whether such writing appears on a copy of the Order Confirmation or in a separate instrument.
 - 8.5. The licensing transaction described in the Order Confirmation document shall be governed by and construed under the law of the State of New York, USA, without regard to the principles thereof of conflicts of law. Any case, controversy, suit, action, or proceeding arising out of, in connection with, or related to such licensing transaction shall be brought, at CCC's sole discretion, in any federal or state court located in the County of New York, State of New York, USA, or in any federal or state court whose geographical jurisdiction covers the location of the Rightsholder set forth in the Order Confirmation. The parties expressly submit to the personal jurisdiction and venue of each such federal or state court. If you have any

4/9/2020 <https://marketplace.copyright.com/rs-ui-web/mp/license/abcdd3a4-b630-41b5-a704-4020129d834e/f0061fdc-871c-4359-82c8-cd7728484...>
comments or questions about the Service or Copyright Clearance Center, please contact us at 978-750-8400 or send an e-mail to support@copyright.com.

v 1.1